Search for high mass resonances decaying into electron-positron pairs in proton-proton collisions at $\sqrt{s}$ = 7 TeV with the ATLAS detector

Dissertation
zur Erlangung des Grades
DOKTOR DER NATURWISSENSCHAFTEN
am Fachbereich 08: Physik, Mathematik und Informatik
der Johannes Gutenberg-Universität
in Mainz

von
Christian Göringer
geboren in Mainz

Mainz, den 28. Januar 2013

Datum der mündlichen Prüfung: 25.4.2013

Abstract

The Standard Model of particle physics was developed to describe the fundamental particles, which form matter, and their interactions via the strong, electromagnetic and weak force. Although most measurements are described with high accuracy, some observations indicate that the Standard Model is incomplete. Numerous extensions were developed to solve these limitations. Several of these extensions predict heavy resonances, so-called Z' bosons, that can decay into an electron positron pair. The particle accelerator Large Hadron Collider (LHC) at CERN in Switzerland was built to collide protons at unprecedented center-of-mass energies, namely 7 TeV in 2011. With the data set recorded in 2011 by the ATLAS detector, a large multi-purpose detector located at the LHC, the electron positron pair mass spectrum was measured up to high masses in the TeV range. The properties of electrons and the probability that other particles are mis-identified as electrons were studied in detail. Using the obtained information, a sophisticated Standard Model expectation was derived with data-driven methods and Monte Carlo simulations. In the comparison of the measurement with the expectation, no significant deviations from the Standard Model expectations were observed. Therefore exclusion limits for several Standard Model extensions were calculated. For example, Sequential Standard Model (SSM) Z' bosons with masses below 2.10 TeV were excluded with 95% Confidence Level (C.L.).

Abstract

Das Standard Modell der Teilchenphysik wurde entwickelt, um die fundamentalen Teilchen, aus denen Materie gebildet wird, und ihre Wechselwirkungen durch die starke, elektromagnetische und schwache Kraft zu beschreiben. Auch wenn die meisten Messungen mit hoher Präzision beschrieben werden, deuten einige Beobachtungen darauf hin, dass das Standard Modell unvollständig ist. Zahlreiche Erweiterungen wurden entwickelt, um diese Problematik zu überwinden. Einige dieser Erweiterungen sagen schwere Resonanzen, sogenannte Z' Bosonen, voraus, welche in ein Elektron-Positron-Paar zerfallen können. Der Teilchenbeschleuniger Large Hadron Collider (LHC) am CERN in der Schweiz wurde gebaut um Protonen bei bisher unerreichten Schwerpunktsenergien, 7 TeV im Jahr 2011, zur Kollision zu bringen. Mit dem Datensatz, der im Jahr 2011 mit dem ATLAS-Detektor, einem großen Vielzweck-Detektor am LHC, aufgezeichnet wurde, ist das Elektron-Positron-Paar-Massenspektrum bis in den TeV-Bereich vermessen worden. Dabei wurden die Eigenschaften von Elektronen, sowie die Wahrscheinlichkeit, das andere Teilchen als Elektronen misidentifiziert werden, im Detail untersucht. Die dabei gewonnen Kenntnisse wurden in Daten- und Monte-Carlo-Simulations-gestützen Methoden genutzt, um eine ausgefeilte Abschätzung der Standard-Modell-Erwartung durchzuführen. Beim Vergleich der Messung mit der Erwartung wurden keine signifikanten Abweichungen von der Standard-Modell-Vorhersage festgestellt. Daher wurden Ausschlussgrenzen für schwerer Resonanzen einiger Standard-Modell-Erweiterungen berechnet. Zum Beispiel wurden Sequential Standard Model (SSM) Z' Bosonen mit Massen unterhalb von 2.10 TeV mit 95% Confidence Level (CL) ausgeschlossen.

Contents

1 Introduction

Discoveries of previously unknown particles have played a major role in the development of the Standard Model (SM) of particle physics. In the 1960s, numerous new particles, so-called hadrons, were discovered. Driven by the desire to explain this "zoo" of particles in a systematic way, Gell-Mann and Zweig introduced the quark model [1], which describes hadrons as bound states of quarks. Within this model, a previously not observed bound state, the Ω^-, was predicted and finally discovered in 1964 [2], which was a great success of the quark model.

Technical advances allowed to construct particle accelerators at higher energies, which lead to the discovery of further new particles. Prominent examples are the discovery of the strong and weak force carriers and the top quark. In 1979, the strong force carrier, the gluon, was discovered at the PETRA (Positron-Elektron-Tandem-Ring-Anlage) accelerator at the DESY (Deutsches Elektronen-SYnchrotron) research center in Hamburg, Germany, which was operated at a center-of-mass energy of 38 GeV [3, 4, 5, 6]. Four years later, the weak force carriers, the Z and the $W^{\pm}$ bosons, were discovered at the Super Proton Anti-Proton Synchrotron (Sp$\bar{\text{p}}$S) at CERN (Conseil Européen pour la Recherche Nucléaire[1]), Switzerland, which was operated at a center-of-mass energy of up to 900 GeV [7, 8, 9, 10]. The top quark was discovered in 1995 at the Tevatron accelerator at the Fermilab in Batavia, Illinois, USA, which was operated at a center-of-mass energy of up to 1960 GeV [11, 12].

In a successful interplay between experimental physicists, who discovered new particles and measured their properties, and theoretical physicists, who built models to explain the measurements and predicted further particles as well as fundamental properties of the interactions, the Standard Model (SM) of particle physics was established [13, 14, 15]. It describes the elementary particles and their electromagnetic, weak and strong interactions. Within the SM, predictions can be made with very high precision describing a large variety of measurements accurately. However, some observations indicate that the SM might be an effective model derived from a more complete one. These hints can be categorized into theoretical arguments and experimental observations. Three experimental hints will be discussed briefly.

According to the current understanding of the creation of the universe, the big bang theory, matter and anti-matter was produced originally in equal amounts. However, experimental investigations indicate that the "known" parts of the universe are matter dominated. Within the SM, so-called CP-violating processes lead to an imbalance between matter and anti-matter, but the predicted amplitude is orders of magnitude too low to explain the observed imbalance of matter and anti-matter. On the other hand, so far unknown particles could enhance the amplitude of CP-violating processes significantly.

In the SM, neutrinos are incorporated as massless particles. However, neutrino flavor oscillations, which are only possible for massive particles, have been observed [16, 17].

Further, from astrophysical observations, it can be concluded that the contribution of

[1] European Organization for Nuclear Research

known matter and energy to the total matter in the universe amounts to only approximately 4%, while approximately 23% consists of dark matter [18]. The remaining 73% are assigned to dark energy, which is beyond the scope of this thesis, but also not explained within the SM.

Dark matter is needed to explain the different mass distributions extracted from observations of luminous matter and of gravitational phenomena [18, 19, 20]. This discrepancy could be caused by the presence of so far unknown particles that in general do interact rarely and, in particular, do not interact electromagnetically or strongly at all.

Many of the models that try to solve the outstanding problems of the SM predict new particles with masses of $\mathcal{O}(1\,\text{TeV})$. Those particles can be searched for by performing indirect and direct measurements. One promising way to search for high-mass resonances is at the so-called high-energy frontier, that is with particle colliders operated at highest center-of-mass energies.

The Large Hadron Collider (LHC) at CERN is a novel hadron-hadron collider, which is designed to collide protons[2] with an unprecedented center-of-mass energy of 14 TeV. The ATLAS detector (A Toroidal LHC ApparatuS) is one of two large detectors built to search for such new phenomena [21].

The analysis described in this thesis is a search for high-mass resonances that decay into an electron and a positron[3]. A prominent class of such resonances are heavy gauge bosons, called Z's, as they behave similar as the known Z boson, but have masses in the TeV region.

The data set analyses in this thesis was taken with proton-proton collisions at 7 TeV and corresponds to an integrated luminosity[4] of $4.9\,\text{fb}^{-1}$. Although the LHC was operated at only half of its design center-of-mass energy, the electron pair mass distribution could be probed up to high masses, namely events with electron pair masses of up to 1.64 TeV were observed, which is far beyond of what was accessible in previous experiments. The largest part of this thesis covers the careful estimation of the SM expectation for the electron pair mass distribution. The search for new resonances is performed by comparing the SM expectation to the measured mass distribution. As no significant deviations were found, exclusion limits on two classes of Z' models, the Sequential Standard Model (SSM) Z' [22] and the E_6 based Z' bosons [22, 23] were set. The SSM Z' boson behaves like a heavy SM Z boson and is commonly used as benchmark model in searches for high mass resonances that decay into electrons, whereas the E_6 based Z' bosons are predicted by a Grand Unification Theory (GUT).

This analysis follows the methods used in the ATLAS dilepton resonance search [24], to which I contributed as one of the main analyzers and performed most of the background estimate in the di-electron channel. In the following, if a statement refers to the ATLAS dilepton resonance search without further specifications, it refers to this ATLAS analysis. Furthermore, I also provided the same background estimate to the ATLAS search for contact interactions and large extra dimensions in dilepton events [25].

This thesis is structured as follows. In Chapter 2, the theoretical foundations of the SM will be introduced with a focus on the Drell-Yan process and two beyond the SM models that predict a heavy Z'. The ATLAS detector as well as the reconstruction and identification of electrons will be discussed in Chapter 3. In Chapter 4, the simulation

[2] There is also a heavy ion program, where lead ions are collided.

[3] With the exception of the theory chapter, electrons and positrons are not distinguished, but both are referred to as electrons.

[4] The integrated luminosity is the unit commonly used to express data set sizes in particle physics.

of relevant physics processes, like the Drell-Yan process, as well as the simulation of the ATLAS detector will be described. The event selection as well as calibrations are described in Chapter 5, whereas the SM background estimate is explained in detail in Chapter 6. In Chapter 7, comparisons of data to the expectation are performed. Exclusion limits for a selected number of Z' bosons are calculated in Chapter 8. Further, the results of this analysis are compared to results of other analyses, and future prospects are discussed. Finally, in Chapter 9, the analysis is summarized and final conclusions are drawn.

2 Theory

In the first part of this chapter, the Standard Model (SM) of particle physics will be introduced. This is followed by a discussion of the formalism needed to describe the Drell-Yan process $pp \to Z/\gamma^* + X$. In the last part, limitations of the SM and possible extensions, which this analysis is sensitive to, will be discussed, and the current experimental status of those extensions will be briefly summarized.

In this thesis, the convention $c = \hbar = 1$ is used, therefore masses and momenta are quoted in units of an energy, electron volts (eV).

2.1 Standard Model of Particle Physics

The standard model of particle physics is a quantum field theory that describes the dynamics and interactions of all currently known particles. However, there are some caveats and limitations. At first an overview will be given, followed by a discussion of the components the SM is built of.

The SM describes the elementary particles of matter, quarks and lepton and their interactions via the exchange of bosons. Both, quarks and leptons, have a spin 1/2 and form the class of fermions. They interact by the exchange of spin 1 gauge bosons and the Higgs boson, which will be discussed later. The gluons mediate the strong interaction, while the W^+, W^- and Z as well as the γ bosons[1] mediate the electroweak force. The gravitation does not play role concerning the validity of the SM, because its strength is low compared to the other forces. On the other hand, an incorporation of gravity in the SM is difficult to achieve due to the different structures of the theories.

The SM allows to derive predictions on its particle content as well as on particle properties. In this respect, the SM has been very successful. For example, the existence and properties of the W^+ and W^- bosons [7, 8] and the Z [9, 10] boson, were postulated more than ten years before they were discovered at the Super Proton anti-Proton Synchrotron (Sp$\bar{\text{p}}$S) at CERN.

The SM also predicts a Higgs boson and recently a boson with properties, which are compatible with a SM Higgs, was discovered[2] by the ATLAS [21, 26] and CMS [27, 28] experiments. In this case, the discovery took place even several decades after its first prediction.

In terms of precision, the SM describes most of the measured data with high precision. For example, the anomalous magnetic moment of the electron has been measured with a relative precision of 2.4×10^{-10} [29], and agrees within 1.3 standard deviations with the SM prediction [30].

Furthermore, the SM predicts correlations between observables, which in the electroweak case can be measured very precisely. This allows for detailed consistency checks,

[1] The Z boson is also often referred to as Z^0 to indicate that it carries no electric charge.

[2] There are many models beyond the SM that predict a Higgs Boson and further careful studies of the observed boson's properties are required to determine, if it is the SM Higgs boson or not.

which have been carried out and confirm[3] the validity of the electroweak sector of the SM [31, 32, 33].

For all these reasons, the SM can be considered as a very successful model. In the following, first some concepts needed to describe the SM will be introduced followed by a description of the SM itself.

2.1.1 Lagrangian Formalism and Symmetries

In this section the Lagrangian will be introduced briefly as it is necessary to understand the following sections. The Lagrangian is defined as

$$L = T' - V', \tag{2.1}$$

where T' is the kinetic energy and V' the potential energy. In field theories, the Lagrangian density $\mathcal{L}$, defined via

$$L = \int \mathcal{L}\, dx \tag{2.2}$$

is used instead and particles are described by quantized fields.

The Noether-Theorem [34, 35] states that there exists a conserved quantity, if a physical problem is invariant under a symmetry operation. This can be transferred to field theory. If the physics of a field ψ is observed to be invariant under a symmetry operation, e.g., an $U(1)$ symmetry, it can be transformed as

$$\psi = e^{i\alpha(x)}\psi, \tag{2.3}$$

where $\alpha(x)$ is a phase. If $\alpha(x)$ is a constant for all values of x, the symmetry is called a global symmetry, while it is a local one, if $\alpha(x)$ depends on x. The Lagrangian density can be made invariant under this local symmetry transformation, if an additional massless bosonic gauge field is introduced, which couples to the charge conserved by this symmetry.

A symmetry can be spontaneously broken[4], e.g., if for a field a ground state can be found that is not invariant under this symmetry. According to the Goldstone Theorem [36], a massless scalar boson, called Goldstone Boson, exists for every broken generator of a symmetry group.

2.1.2 Fields and Symmetries of the Standard Model

The SM is a local gauge-invariant quantum field theory, which is invariant under the following combination of gauge symmetry groups:

$$SU(3)_C \times SU(2)_L \times U(1)_Y. \tag{2.4}$$

To guarantee the gauge symmetry of the SM Lagrangian density, a massless gauge boson is added for each generator of the symmetry groups. Each group will be discussed in the following.

The $SU(3)_C$ is a special unitary group of degree three, which is the fundamental symmetry of the quantum chromodynamics (QCD) theory. The conserved charge is the color

[3] However there is a certain tension between the measurement of one asymmetry at two different colliders.
[4] This will be explained in the next section with the example of the Higgs mechanism in the SM.

quantum number with values[5] red, green and blue. The coupling constant is denoted by g_s and the strong force-carriers are massless gauge bosons called gluons. Gluon color states have a color and an anti-color that do not add up to white, e.g., red anti-blue. The eight gluon states are constructed[6] as pure color states or linear combinations such that all gluons carry a net color anti-color charge that does not add up to white.

In a measurement, the individual contributions of the different gluons cannot be distinguished[7], therefore processes with gluon exchanges are described as a superposition of all contributions of all possible gluons. In the following discussions, a gluon contribution to a process is to be understood as such a superposition, although it will not be mentioned explicitly.

The $SU(2)_L$ is a special unitary group of degree two. It describes chiral couplings, therefore particles interact differently whether they are left- or right-handed. In particular, left-handed anti-particles and right-handed particles do not couple to the gauge bosons that are introduced to conserve the gauge symmetry of the $SU(2)_L$: W^1, W^2, and W^3. The conserved charge is the weak isospin T and the coupling constant is denoted by g.

The $U(1)_Y$ is a unitary group of degree one with one generator that gives rise to the B^0 boson. Its conserved charge is the hypercharge $Y = 2(Q - T_3)$, where Q is the electrical charge and T_3 is the third component of the weak isospin. The coupling constant is denoted by g'.

This ansatz does not fully describe the observed interactions. The bosons that couple to the weak charge, W^1, W^2, and W^3, are massless, while they have been observed to be massive. The photon, which couples only to the electric charge as suggested by experiments, cannot be identified with the B^0 boson which couples to the hypercharge instead of the electric charge.

The B^0 and W^3 have identical quantum numbers and can therefore mix. It can be shown that with a mixing, described by the weak mixing angle θ_W, two states

$$\begin{pmatrix} \gamma \\ Z \end{pmatrix} = \begin{pmatrix} \cos\theta_W & \sin\theta_W \\ -\sin\theta_W & \cos\theta_W \end{pmatrix} \begin{pmatrix} B^0 \\ W^3 \end{pmatrix}, \tag{2.5}$$

can be found, where Z and γ couple as observed in measurements; The γ couples only to the electric charge, and the Z to the weak isospin. The observed charged gauge bosons W^+, W^- can be recovered by the following linear combination of the W^1 and W^2 states:

$$W^{\pm} = W^1 \mp iW^2. \tag{2.6}$$

This common description of the weak and electromagnetic interaction is referred to as electroweak (EWK) unification.

However, the $W^{\pm}$ and the Z bosons are still massless. Gauge invariance forbids to introduce explicit mass terms in the Lagrangian density for gauge bosons and fermions, which also have been observed to be massive. In the next section, the fermions and their charges will be introduced. Afterwards, the concept of the Spontaneous Symmetry Breaking (SSB) will be discussed, which gives rise to the required non-zero masses.

[5] The choice of names is arbitrary, but follows the convention typically used.

[6] Three colors and three anti-colors can be arranged in a net color (not white) octet and a "white" or colorless singlet, where the latter state does not take part in the strong (or any other) interaction. The physical gluon states are constructed from the octet.

[7] Free colored gluons cannot exist, see Section 2.2.1.

Table 2.1: The fermionic fields of the Standard Model and their corresponding charges.

	Generation			Charges			
	1	2	3	Color	T_3	Y	Q
Quarks	$\begin{pmatrix} u \\ d \end{pmatrix}_L$	$\begin{pmatrix} c \\ s \end{pmatrix}_L$	$\begin{pmatrix} t \\ b \end{pmatrix}_L$	Yes	1/2	1/3	2/3
				Yes	-1/2	1/3	-1/3
	u_R	c_R	t_R	Yes	0	4/3	2/3
	d_R	s_R	b_R	Yes	0	-2/3	-1/3
Leptons	$\begin{pmatrix} \nu_e \\ e \end{pmatrix}_L$	$\begin{pmatrix} \nu_\mu \\ \mu \end{pmatrix}_L$	$\begin{pmatrix} \nu_\tau \\ \tau \end{pmatrix}_L$	No	1/2	-1	0
				No	-1/2	-1	-1
	e_R	μ_R	τ_R	No	0	-2	-1

Fermions

Table 2.1 summarizes the fermionic fields and their charges. For each generation, the quark fields are split into a left-handed doublet under $SU(2)_L$ and two right-handed singlets, where the latter do not take part in the weak interaction due to a weak isospin of zero. However, all quarks do carry a color charge and an electric charge and therefore take part in the electromagnetic and strong interactions.

The leptons are structured similarly. However all leptons are colorless, and there are no right-handed neutrinos. The left-handed neutrinos have no electric, but a weak isospin charge and therefore only participate in the weak interaction. The charged leptons carry both, an electric and a weak charge.

The (observed) masses of the fermions cannot be added to the Lagrangian density by hand, because this would break the gauge symmetry. Instead, fermion masses as well as gauge boson masses are introduced by SSB, which will be discussed below.

Spontaneous Symmetry Breaking

The idea of SSB in the SM is to break the $SU(2)_L \times U(1)_Y$ not by introducing gauge invariance violating terms in the Lagrangian density itself. Rather, additional fields are added to the Lagrangian density in a gauge invariant way, and a non-trivial ground state is chosen such that an expansion around it violates the gauge invariance.

In particular, two additional complex scalar fields ϕ^0 and ϕ^+,

$$\phi = \begin{pmatrix} \phi^+ \\ \phi^0 \end{pmatrix}, \tag{2.7}$$

are introduced, where their contribution to the Lagrangian density can we written as

$$\mathcal{L}_\phi = T(\phi) - V(\phi).$$

The potential $V(\phi)$ has the form

$$V(\phi) = \mu^2 \phi^\dagger \phi + \lambda (\phi^\dagger \phi)^2.$$

If $\lambda > 0$, a global minimum[8] of the potential exists at[9] $\phi_{min} = 1/\sqrt{2}\begin{pmatrix}0\\ \nu\end{pmatrix}$, where $\nu = \sqrt{-\mu^2/\lambda}$. For $\mu^2 < 0$, this ground state is degenerate. An expansion of the potential around this particular ground state

$$\phi = \frac{1}{\sqrt{2}}\begin{pmatrix}0\\ \nu + h(x)\end{pmatrix} \tag{2.8}$$

gives rise to terms that violate the $SU(2)_L \times U(1)_Y$ symmetry. If the quantum numbers of the ground state are chosen as $T = 1/2$, $T_3 = -1/2$ and $Y = 1$, the electric charge satisfies $Q = 0$. The ground state is therefore invariant under transformations of the $U(1)_Q$, where the electric charge is the generator. As a result, the gauge boson associated with the electromagnetic force acquires no mass, but the three other gauge bosons do. Additionally, a massive neutral scalar boson, the Higgs boson, is introduced. Fermion masses can be introduced by terms that couple fermions to the Higgs field via so-called Yukawa-couplings.

The pure electromagnetic interaction can also be described by defining a Lagrangian density that only contains electromagnetic contributions and is invariant under the $U(1)_Q$ symmetry. This theory treats fermions as massless and is referred to as Quantum Electrodynamics (QED).

The Standard Model Lagrangian Density

The Lagrangian density of the SM can be written as

$$\mathcal{L}_{SM} = \mathcal{L}_{Fermion} + \mathcal{L}_{Gauge} + \mathcal{L}_{Higgs} + \mathcal{L}_{Yukawa}, \tag{2.9}$$

where $\mathcal{L}_{Fermion}$ describes the interactions of fermions with gauge bosons as well as their kinetic energy. The second term, $\mathcal{L}_{Gauge}$, describes the kinetic energy of the gauge bosons as well as their self-interactions (not for the photon). $\mathcal{L}_{Higgs}$ describes the kinetic energy and interactions of the Higgs similar to $\mathcal{L}_{Gauge}$. The last term, $\mathcal{L}_{Yukawa}$, describes the fermion mass terms.

The corresponding mass terms[10] for, e.g., electrons are

$$\mathcal{L} = -m_e\,(\bar{e}_L e_R + \bar{e}_R e_L) - \frac{m_e}{\nu}(\bar{e}_L e_R + \bar{e}_R e_L)h = -m_e\,\bar{e}e - \frac{m_e}{\nu}\,\bar{e}e\,h, \tag{2.10}$$

where $m_e = \frac{G_e \nu}{\sqrt{2}}$ is directly proportional to the vacuum expectation value of the Higgs. The constant G_e is the Yukawa-Coupling for the electron, which is not predicted by the theory, but a free parameter. The second term in Eq. 2.10 shows that electrons couple to the Higgs boson proportional to their mass, which is a prediction. Similar expressions as in Eq. 2.10 can be derived correspondingly for all fermions.

[8] For $\lambda < 0$, a local minimum exists which leads to a meta-stable ground state.
[9] The phase of the state is conventionally chosen such that the minimum is located at ϕ_{min}.
[10] The mass term(s) are given at the lowest order. higher order terms are, e.g., radiation corrections to the mass. The expansion formalism will be introduced in the next section.

2.2 Feynman Formalism

Feynman rules can be derived from the Lagrangian density. They state how to calculate the amplitude for a process, e.g., a scatter between two fundamental particles. According to Fermi's Golden Rule, the square of a (Feynman) amplitude times a term that describes the size of the available phase space can be interpreted as the probability for a process to happen, that is its cross-section [37]. These rules can be visualized in form of Feynman graphs[11]. In this thesis, the time coordinate is shown along the abscissa and the space coordinate along the ordinate.

The Feynman rules will be introduced for the example of a $2 \to 2$ scatter, but they can be applied to any complex scatter or to a propagator or vertex alone. In the language of Feynman rules, each particle is represented by a line. A point, where three or more particle lines intersect, is called a vertex. If a particle is neither present in the initial nor the final state, it is considered an internal line and called propagator.

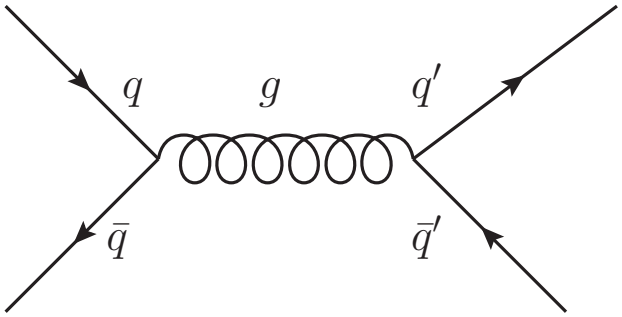

Figure 2.1: A scatter is shown, where a quark anti-quark pair, visualized on the left side, annihilates to a gluon, which decays into a quark anti-quark pair (possibly with different flavor).

The Feynman diagram shown in Fig. 2.1 shows the annihilation of a quark anti-quark pair into a virtual gluon that decays into a $q'\bar{q}'$ pair[12] again. The graph contains two vertices ($q\bar{q}g$ and $gq'\bar{q}'$), and the gluon propagator. At each vertex, an interaction takes place that is proportional to the square root of the corresponding coupling constant , e.g., the $q\bar{q}g$ vertex has a factor $\sqrt{\alpha_S}$ assigned to it. As the amplitude of a graph is proportional to the product of all vertex factors, in this case the amplitude is proportional to $\sqrt{\alpha_S} \times \sqrt{\alpha_S} = \alpha_S$. Furthermore, the amplitude is proportional to the propagator, in this case to $1/Q^2$, where $Q^2 := -q^2$ is the negative of the square of the gluon's 4-momentum.

The cross-section for this process can be calculated as an expansion series in the coupling constant α_S:

$$\sigma = \sum_i \alpha_S^i \, \sigma_i, \tag{2.11}$$

[11] Feynman graphs do not visualize trajectories or scattering angles. Simplified, Feynman graphs visualize which particle interacts with which. Here the convention is chosen that particles and anti-particles are labeled explicitly in contrast to the original convention that an anti-particle is indicated by an arrow that points into the negative time direction, but is still labeled as particle. The timelike axis is chosen to be the abscissa, and the spacelike axis points along the ordinate.

[12] The $'$ in q' indicates that the flavor of the final state quarks can differ from the initial state flavor, while the flavor of the quark anti-quark pairs need to be identical in order to couple to a gluon.

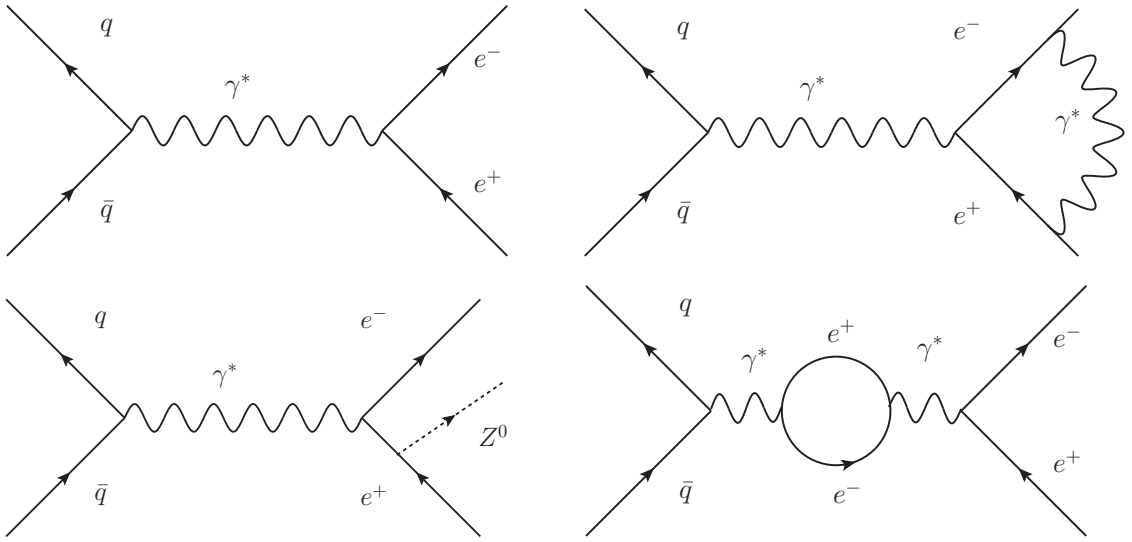

Figure 2.2: The top left diagram visualizes the process $q\bar{q} \to Z/\gamma^* \to ee$ at leading order, while the top right one shows a first order virtual correction. The bottom left diagram shows an example for initial state radiation and the bottom right one for a fermion loop.

where the σ_i denote the cross-section contributions of all graphs that are of $\mathcal{O}(\alpha_S^i)$, that means where the square of the amplitude is proportional to α_S^i. The contribution with the lowest $\mathcal{O}(\alpha_S^i)$ is called leading order (LO), the second lowest order is referred to as next to leading order (NLO) etc.

This can be generalized to all coupling constants:

$$\sigma = \sum_{i,j,k} \alpha_S^i \, \alpha_{em}^j \, \alpha_{weak}^k \, \sigma_{ijk}, \tag{2.12}$$

where α_{weak} is the weak coupling constant and α_{em} the electromagnetic coupling constant.

In the following, higher order corrections will be discussed using the example of the $q\bar{q} \to \gamma^* \to ee$ process. The top left graph of Fig. 2.2 shows the lowest order diagram, while the top right graph includes an additional photon that is emitted by one of the final state electrons and is absorbed by the other. In the bottom left diagram. a final state electron radiates off a Z boson. This contribution is referred to as Final State Radiation (FSR), while it is called Initial State Radiation (ISR) if emitted by an initial state particle. The bottom right plot shows a photon that splits into an transient electron positron pair, also referred to as (fermion) loop. Such loops can also be formed with bosons.

These corrections to the LO diagram(s) can be classified from two different perspectives. Firstly, the corrections can be split into virtual and real contributions. The first category contains all forms of additional intermediate particles that contribute to the amplitude of the process, but are not visible in the final state. In contrast, real contributions are visible in the final state, e.g., ISR and FSR. Secondly, corrections can be categorized by the part of the Feynman graph they modify, vertex and propagator corrections. The corrections shown in the top right and bottom left graphs in Fig. 2.2 belong to the first category, while the bottom right graph showns an example for a propagator correction.

Due to real emissions, the process should be denoted by $q\bar{q} \to \gamma^* \to ee + X$, with X

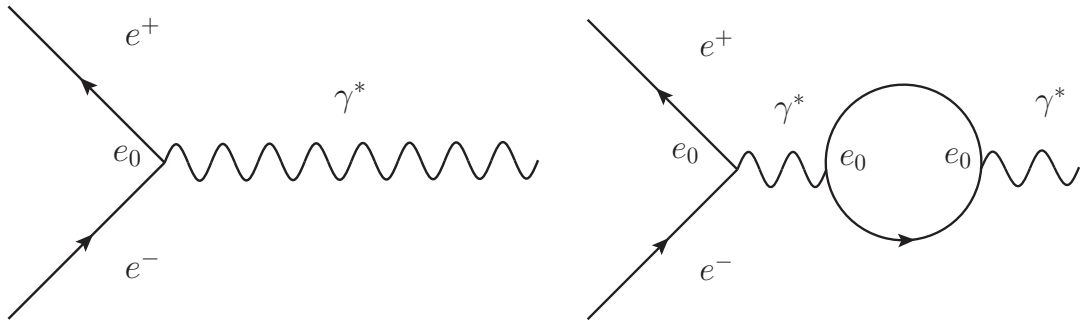

Figure 2.3: The left graph show a $e^-e^+\gamma$ vertex at LO in the bare charge e_0, whereas the right graph includes a loop correction in the propagator.

being any particle that appears in the final state[13], if no veto on additional particles is imposed. The case, where X is included, is referred to as inclusive, while it is referred to as exclusive otherwise. In the analysis presented in this thesis, only the inclusive case is considered. Furthermore, at the energy scales typically accessible in LHC collisions, the contribution of the Z as intermediate boson as well as its interference with the photon needs to be taken into account. This process, the Drell-Yan process, will be discussed later in more detail.

2.2.1 Running Coupling Constants

So far the coupling constants (or charges) and masses have been treated as constants. In the following, it will be discussed, why coupling constants vary with the scale they are being probed. The principles will be introduced using the example of the electric charge in QED and finally also applied to the weak and strong coupling constants.

Consider a vertex $e^-e^+\gamma$, where a photon couples[14] to an electron. The effective charge e in the amplitude, which is the charge an observer would measure, can be calculated as an expansion series in a bare charge e_0, which is defined as the charge assigned to a vertex without any loops considered [38]. In this notation, the lowest order graph is shown as the left graph of Fig. 2.3 and the one-loop correction, a vacuum polarization, in the right graph.

In each loop, the bosons that are produced may have any momentum. The contribution to the amplitude is to be calculated as an integral over all possible momenta from zero to infinity. However this contribution becomes infinite, when the momentum approaches infinity. This behavior, also referred to as ultraviolet divergence, can be (temporarily) avoided or "regularized" by introducing a arbitrary cut off scale.

To eliminate the dependence on this cut off scale, the amplitude as a function of e_0 can be re-parametrized ("renormalized") in terms of the measurable charge e, which is related to e_0 by

$$e^2(Q^2) = e_0^2 \left(\frac{1}{1 - I(Q^2)} \right). \tag{2.13}$$

Here $Q^2 := -q^2$ is the negative of the square of the virtual photon's 4-momentum and

[13] In the picture of pp scattering, the proton remnants can also contribute to X.
[14] In principle, there are two kinds of graphs for that vertex, Fig. 2.3 solves this ambiguity.

$I(Q^2)$ describes scale dependence. The coupling constants scale the same way as the charges do, because they are related by constants only, e.g., $\alpha_{em} = e^2/(4\pi)$.

In the formalism of renormalization, each loop contribution to the amplitude can be described as a difference of one term, where the momentum of the particles in the loop is integrated over, and another term, where the amplitude is evaluated at a fixed scale, the renormalization scale μ_R.

This difference is finite, even if the arbitrary cut-off scale is sent to infinity. As a result, the dependence on the cut-off scale can be eliminated and a finite prediction for the observable charge can be calculated, although the calculation itself includes terms that are divergent.

The choice of different values for μ_R corresponds to expansion series in numerically different values of the charge e. Therefore, the physical result ought to be independent of the choice of μ_R within the precision of the expansion, that is the number of orders calculated.

For practical calculations, the precision is limited and therefore an artificial dependence of a physical observable, e.g., an cross-section, on μ_R might exist. This is conveniently estimated by varying μ_R by a factor 1/2 and 2, recalculating the desired observable again. The differences are commonly quoated as a systematic uncertainty.

With this renormalization formalism, α_{em} can be evaluated at any desired scale Q^2 by inserting an experimentally measured value of α_{em} at a scale μ_R.

The effect of the "running" coupling constant can be interpreted as charge screening effect. In the electric field of a charged particle, vacuum polarization, that is the transient production of fermion pairs, is induced. The larger the distance to the particle, the more the effective charge of the particle (or $\alpha_{em}(Q^2)$) is reduced or "screened". This variation of α_{em} with Q^2 is small, its value at the Z pole mass amounts to approximately $\frac{1}{128}$, while it amounts to $\frac{1}{137}$ in the low energy limit of atomic physics, e.g., measured first at the hydrogen atom.

In QCD, the same effect can be observed as in QED, however with the exception that gluons can not only induce vacuum polarization into pairs of fermions but, due to the non-abelian structure of the $SU(3)_C$, also split into pairs of gluons. The latter effect overcompensates[15] the screening effect of the fermions and leads to an effective anti-screening effect, that is α_S increases with increasing distance or decreasing Q^2. This unique behavior is referred to as confinement, because no free color charged particles can exist, but only colorless bound states are formed instead. On the other hand, at high Q^2 or small distances the behavior is referred to as asymptotic freedom, because quarks and gluons can be treated as quasi free particles.

In order to expand, e.g., amplitudes in powers of the coupling constants, the latter has to be small with respect to one. For scales accessible at high energy physics experiments, this is true for the electromagnetic and weak coupling constants. In QCD however, the coupling constant α_S becomes $\mathcal{O}(1)$ at low scales of $\mathcal{O}(1\,\mathrm{GeV})$, which does not allow to perform perturbative calculations any more. The consequences will be discussed further in the next section.

[15] Whether there is a screening or anti-screening effect in QCD depends on the number of colors and the number of quark flavors. With the values realized in nature, there is an anti-screening effect.

2.3 Collider Physics

In this section, the concepts needed to describe proton-proton collisions will first be briefly introduced and then discussed further in subsequent sections.

The cross-section for a scatter, e.g., $q\bar{q} \to Z/\gamma^* \to ee + X$ can be calculated from its so-called matrix element, if the 4-momenta of the incoming and outcoming particles are known. At a pp-collider, two protons collide and the proton substructure needs to be taken into account to correctly describe the scattering.

A proton itself is a complex bound state. To explain quantum numbers like its electrical charge, it can be treated as if it were composed of three so-called valence quarks, *uud*. In order to describe the actual structure of a proton, the gluons, which are exchanged between these valence quarks, need to be taken into account. They can split up into quark anti-quark pairs again, which are called sea quarks. The quarks, anti-quarks and gluons within a proton are called partons. If the protons are so strongly boosted (along the beam axis) that transverse momenta of the partons can be neglected, the momentum of a parton can be described as the fraction[16] x of the total proton momentum.

In this picture, the parton momentum distributions can be described using Parton Density Functions (PDFs), which are extracted from measurements[17]. According to the Factorization Theorem [40], PDFs are universal and a (high momentum) proton-proton scattering $pp \to X$ can be written as the sum of all parton types over the convolution of the corresponding PDF with the partonic matrix element M, which can be calculated using Feynman rules:

$$\sigma(pp \to X) = \sum_{a,b} \int_0^1 dx_a \int_0^1 dx_b \, f_{a/p}(x_a, \mu_F^2) \, f_{b/p}(x_b, \mu_F^2) \, M(x_a, x_b, s, \mu_F^2, \mu_R^2). \quad (2.14)$$

Here a and b denote the incoming partons and x_a and x_b the corresponding parton momentum fractions, s the squared center-of-mass energy, μ_F the factorization scale and μ_R the renormalization scale. The PDF for a parton of type c is denoted by $f_{c/p}$ and the partonic matrix element by M. The (arbitrary) factorization scale μ_F determines up to which scale parton emissions are described by the PDFs instead of the matrix element and will be discussed together with PDFs in Section 2.3.1.

If a colored parton was scattered off, the remnants of the protons are no longer colorless. The partons of the remnant may interact as well, which is then referred to as underlying event. These interactions are dominated by $2 \to 2$ strong interactions with a low momentum exchange. Due to the confinement (see Section 2.2.1), partons will form colorless bound hadronic states. A single high momentum parton might typically create a handful up to a few dozen light mesons and baryons by interaction with other partons or emitting gluons that split into subsequent quark anti-quark pairs, which interact further. This process is called hadronization and the (typically collimated) set of hadrons formed is referred to as a jet. Jets might overlap or happen to be broad due to fluctuations, therefore a dedicated set of algorithms exists to define a jet, for example the anti-k_t algorithm [41] is commonly used within ATLAS. In this analysis, jets only contribute as background, e.g., if a jet mimics the experimental signature of an electron. In this case, jets are treated with electron reconstruction and identification algorithems, therefore jet

[16] The fraction x is also referred to as Bjorken-x, who introduced this description [39].
[17] The PDFs also depend on a energy scale or resolution, this will be discussed in Section 2.3.1.

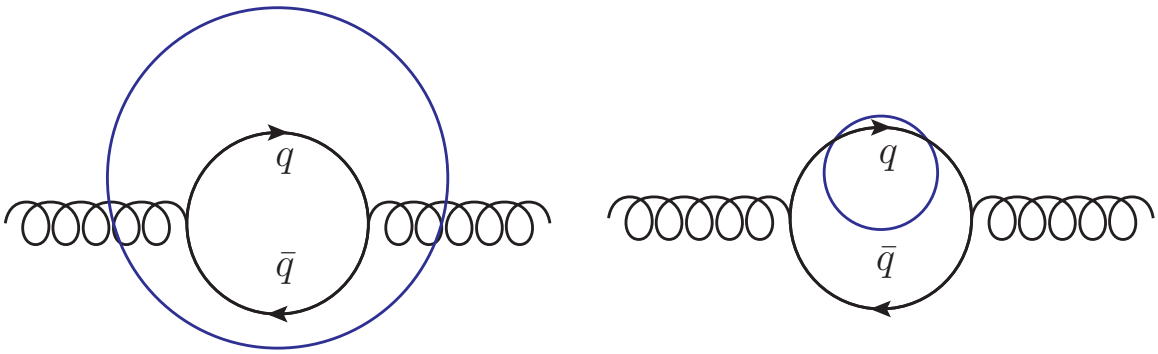

Figure 2.4: In both graphs, a gluon is shown that splits into a quark anti-quark pair, which annihilates back to a gluon (vacuum polarization). The blue circle on the left graph indicates that this process is probed with a low resolution that cannot resolve the intermediate gluon splitting, while the higher resolution indicated on the right graph is sufficient to resolve it.

algorithms are not discussed further.

Due to the high proton proton luminosities of the LHC, there is a high probability that multiple scatterings per bunch-crossing take place. Typically one hard scatter of interest is accompanied by a number of softer scatters of other proton-proton pairs. These soft proton-proton scatters are referred to as pile-up and can affect the measurement of other particles in a detector. Therefore pile-up effects will be discussed later in the chapters, where the measurement is described.

2.3.1 Parton Distribution Functions

In the following, the structure of protons described by PDFs will be discussed in more detail. Further, the PDF extraction and associated uncertainties will be explained.

The probability for a parton i to emit a parton f or to undergo a splitting that yields a parton f is described by the corresponding Altarelli-Parisi [42] splitting functions $P_{if}(z)$, where $1 - z$ is the momentum fraction that is carried by f. The splitting function that describes the probability for a quark q to emit a gluon with a momentum fraction $1 - z$ is given by

$$P_{qq}(z) = \frac{4}{3}\frac{1+z^2}{1-z}. \tag{2.15}$$

Soft splittings are favored due to infrared[18] divergences for the soft limit $z \to 1$. The softer the splittings, the higher the resolution required to resolve these low momentum gluons. Fig. 2.4 shows a sketch, where a gluon splitting cannot be resolved[19] in the left graph, while it can be resolved in the right one. With a lower resolution, the partons seem to carry a higher momentum fraction, because further splittings can, on average, not be resolved.

Fig. 2.5 shows an example of the MSTW2008LO PDF evaluated at two very different

[18] Conventionally, divergences in a low momentum limit are referred to as infrared, while divergences in high momentum limits are called ultraviolet. The terms reflect the low and high energy boundaries of visible light.

[19] This resolution effect can be interpreted as an analogon to an optical microscope.

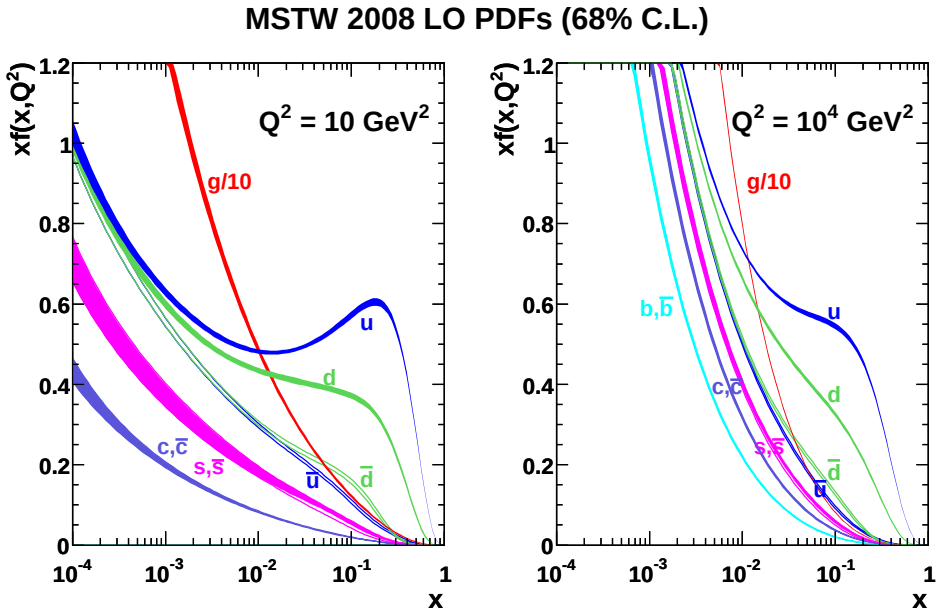

Figure 2.5: The left (right) plot shows the MSTW2008LO Parton Distribution Functions (PDFs) times the Bjorken-x for quarks and gluons at a scale of $Q^2 = 10\,\mathrm{GeV}^2$ ($Q^2 = 10^4\,\mathrm{GeV}^2$). Plots taken from Ref. [43].

scales, at $Q^2 = 10\,\mathrm{GeV}^2$ and $Q^2 = 10^4\,\mathrm{GeV}^2$. In both plots, the dominant contribution at high x is given by u and d quarks, which are dominantly valence quarks. At the higher scale, the contribution of sea quarks increases, because gluon splittings are more often resolved[20].

The evolution of the momentum distributions of partons to another scale can be calculated with the DGLAP equations [44], if they are known at any scale. The size of the strong coupling constant α_s at low resolutions or scales becomes $\mathcal{O}(1)$ and therefore the dynamics cannot be calculated pertubatively for scales smaller than a few GeV. By the factorization [40] of PDF and partonic hard matrix element at a factorization scale μ_F, the non-pertubative regime of QCD can be assigned to the PDFs, which are extracted from measurements. For practical applications, the factorization scale (as well as the normalization scale) is often set to the relevant scale of the partonic matrix element, e.g., to the Z pole mass, when studying Z production.

Extraction and Uncertainties

Experimental data of various collider and fixed-target experiments are sensitive to the parton momentum distribution in protons. The most common way to extract PDFs from these data is to introduce a functional form with free parameters and fix the free parameters by fitting an expectation derived with the PDF ansatz to data. The parametrization of the PDF is done at a Q^2 scale of $\mathcal{O}(1\,\mathrm{GeV}^2)$. For each experimental measurement to be included in the PDF extraction, the PDF ansatz is evolved with the DGLAP equations

[20] Also gluon splittings into two gluons are resolved.

to the scale the data was measured at. For example, if a cross-section measurement[21] of the Drell-Yan process $pp \to Z/\gamma^* \to ee + X$ at the Z pole mass is to be included, the ansatz is evaluated to the scale of the Z pole mass.

A convolution of this PDF ansatz with the partonic matrix element is then fitted to data. If a LO (NNLO) matrix element was used, the extracted PDF is referred to as LO (NNLO) PDF. The PDF collaborations include multiple measurements, performed at different scales Q^2 and sensitive to different values of x, and carry out a so-called global fit, which takes the whole set of measurements into account and determines the values of the PDF parameters. Therefore PDFs extracted from different groups vary due to the different data sets used and the different parametrization chosen. Common PDFs extracted this way are provided by the MSTW [43], and CTEQ [45] and HERA [46, 47] collaborations. An alternative ansatz is to use neural networks to extract PDFs as done by the NNPDF collaboration [48]. The following discussion focuses on the uncertainties of PDFs, which are extracted by a global fit, and how these are propagated to observables measured by experiments, e.g., cross-sections.

One limitation of the precision of the fit of the PDF model to data is introduced by the uncertainties of the data measured by experiments. Usually, these fit uncertainties are evaluated in a Hessian approach, where the fit parameters are transformed into a orthogonal eigenvector basis. Then each parameter can be varied independent of all others. For each parameter, the value determined in the fit is varied up and down by a shift corresponding to either a 68% C.L. or 90% C.L. uncertainty. Therefore, a PDF set typically includes additional $2n$ PDFs per confidence level, where n is the number of independent fit parameters. For each PDF a prescription is defined by the authors, how to calculate an uncertainty of an observable, e.g., a cross-section. In principle, the cross-section is calculated $2n$ times and all upward and all downward deviations with respect to the central cross-section are added up separately in quadrature, which results into an asymmetric uncertainty.

Another source of uncertainty is the choice of the value of α_S. It needs to be specified at one scale, typically at the Z pole mass, and is extracted with an uncertainty from a measurement. Uncertainties to cross-sections are propagated in a similar way as experimental uncertainties; the cross-section is calculated with different values of α_S (e.g. 68% or 90% C.L. uncertainty variations) consistently in the PDF and the matrix element, and the deviations with respect to the cross-section calculated with the nominal value are taken as systematic.

Furthermore, systematics or possible biases arising from the choice of the model can be studied. The MSTW collaboration recently reported a possible bias for valence quarks at low x [49]. Besides the HERA PDF, there is no common PDF set that allows to evaluate model variations on observables by end-users. A recent comparison of different PDFs can be found in [50].

2.4 The Drell-Yan Process

The Drell-Yan process [51], which was already briefly introduced, will be discussed in more detail in the following. It describes the annihilation of a quark-antiquark pair to

[21] The highest sensitivity to PDFs is typically seen in differential cross-sections in a variable that is related to x of the incoming partons. For example, the Drell-Yan cross-section differential in the Z rapidity $Y = 0.5\, ln(x_1/x_2)$, where x_1 and x_2 are the momentum fractions of the incoming partons.

a photon or Z boson, where the boson decays into a pair of oppositely charged leptons. The Drell-Yan process will be referred to as Z/γ^* exchange, although a wide mass range above the Z pole mass will be covered in this analysis, where the Z contributions are virtual. This notation follows the convention used by the ATLAS collaboration.

In the following the LO matrix element shall be described, which can be conveniently written in the following notation; The 4-momentum of the two initial state quarks shall be denoted by p_1 and p_2 and their polarization with σ_1 and σ_2, while the 4-momentum of the final state leptons shall be denoted by k_1 and k_2 and their polarization by τ_1 and τ_2. It is convenient to introduce the Mandelstam variables [52]

$$\hat{s} = (p_1 + p_2)^2, \quad \hat{t} = (p_1 - k_1)^2, \text{ and } \hat{u} = (p_1 - k_2)^2. \tag{2.16}$$

The amplitude in LO can be written as

$$M_{q\bar{q}}^{LO,\sigma\tau}(\hat{s}, \hat{t}, \hat{u}) = -\frac{e^2}{\hat{s}} \sum_{V=\gamma,Z} g_{qqV}^{\sigma} \; g_{llV}^{\tau} \; P_V(\hat{s}) \; A^{\sigma\tau}(\hat{u}, \hat{t}), \tag{2.17}$$

where e is the electric charge, g_{qqV}^{σ} and g_{llV}^{τ} are the couplings of the fermions to the gauge bosons, $P_V(\hat{s})$ the boson propagator and $A^{\sigma\tau}(\hat{u}, \hat{t})$ the "standard" matrix element. The individual fermion polarizations are replaced by one quantity σ (τ) that denotes the sign of the product $\sigma_1\sigma_2$ ($\tau_1\tau_2$).

The structure of the couplings is identical for quarks and leptons and is given with common indices ll for fermions

$$g_{ff\gamma}^{\pm} = -Q_f, \quad g_{ffZ}^{+} = \frac{\sin\theta_W}{\cos\theta_W} Q_f \quad \text{and } g_{ffZ}^{-} = \frac{T_{3,f} - \sin^2\theta_W \; Q_f}{\sin\theta_W \cos\theta_W}. \tag{2.18}$$

Here Q_f is the electric charge of the fermion, $T_{3,f}$ the third component of the weak isospin of the fermion and θ_W the weak mixing angle. The propagators are defined as

$$P_\gamma(\hat{s}) = 1, \quad P_Z(\hat{s}) = \frac{\hat{s}}{\hat{s} - M_Z^2 + i\hat{s}\Gamma_Z/M_Z}, \tag{2.19}$$

where $P_Z(\hat{s})$ is given in the running width scheme. The standard matrix elements are

$$A^{\pm\pm} = 2\,\hat{u} \quad \text{and } A^{\pm\mp} = 2\,\hat{t}. \tag{2.20}$$

2.4.1 K-Factors and Uncertainties

The calculation and parametrization of k-factors was performed by ATLAS members for [24] and is described in detail in [53]. It will be briefly summarized here.

It is assumed that higher order QCD and electroweak contributions factorize[22]. To account for higher order QCD corrections, a modified version of PHOZPR [55] was used together with the MSTW2008NNLO PDF [43]. The cross-section single differential in

[22] Before FEWZ3.1 [54] was released in late 2012, there was also no program available to perform the combined calculations. For the analysis of the ATLAS data taken in 2012, these new calculations are studied.

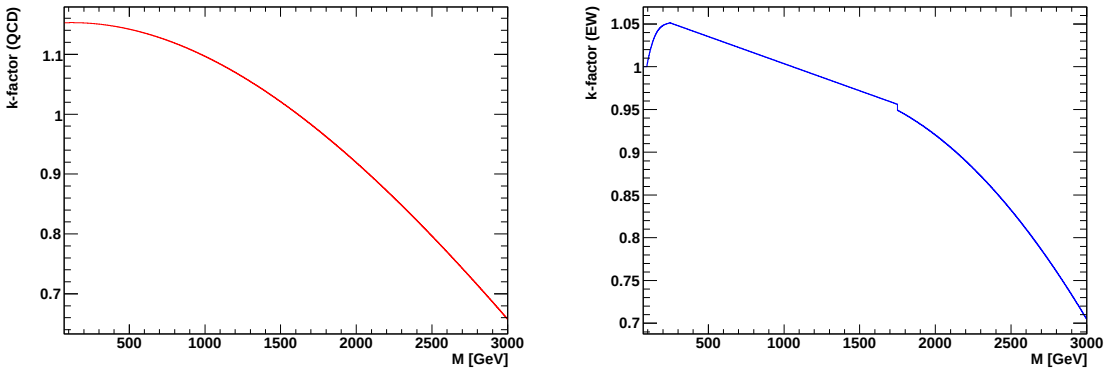

Figure 2.6: The left (right) plot shows the k-factors accounting for QCD (electroweak) higher order corrections to the Drell-Yan process as a function of the mass of the exchange particle [53]. The discontinuity visible in the right plot at 1700 GeV is due to the imperfect fit, which was performed in sections by the persons who provided the k-factors.

the mass of the exchange boson has been calculated at NNLO and LO[23], and the ratio is referred to as k-factor. The result has been parametrized and is shown in the left plot[24] of Fig. 2.6.

Uncertainties have been evaluated as a function of the invariant e^+e^- pair mass and include α_s and scale variations as well as the dominant PDF uncertainties. The 90% C.L. PDF eigenvector uncertainties were estimated using the MSTW2008NNLO PDF, which yields an asymmetric uncertainty[25]. Furthermore, the asymmetric envelope of the PDF uncertainties of NNPDF2.1, CT10[26] and CT10W has been calculated and was found in good agreement with the MSTW2008NNLO upward only uncertainty. The downward uncertainty of the envelope is typically larger than the MSTW2008NNLO only one. However, the uncertainty envelope of the other PDFs is well covered by taking the value of the MSTW2008NNLO only upward uncertainty as a symmetric uncertainty, which is therefore a valid choice to describe the total PDF uncertainty. It ranges from approximately 4% at the Z pole mass to 19% at 2 TeV. Further the NNLO cross-section has been calculated using separately only Z or Z' exchange, and the variation with respect to to the SM Drell-Yan process cross-section has been found to be below 1% up to 2 TeV.

Furthermore, using the MSTW2008NNLO PDF, the impact of different choices of α_s was evaluated and found to be within 1.7% up to 2 TeV. The renormalization and factorization scales were set to the Z pole mass, and scale uncertainties have been estimated by varying the renormalization (μ_r) and factorization scales (μ_F) independently by a factor of two with the constraint $0.5 \leq \mu_F/\mu_R \leq 2$. These uncertainties amount up to 2.1% at 2 TeV.

The total uncertainty is calculated as the quadratic sum of the three components. It

[23]For the LO prediction, the same PDF, MRSTMCal, as used in the Drell-Yan Monte Carlo sample generation was chosen, see Section 4.1.

[24]For the visualization of all distributions created for this thesis, the program ROOT [56] was used.

[25]The uncertainty derived with any C.L. for a upward cross-section fluctuation due to PDF eigenvector variations is in general different from a downward fluctuation.

[26]The CT10 and CT10W PDFs are available at NLO only, therefore a scaling method was used to compare their uncertainties with the ones from the other PDFs.

increases with mass and amounts to approximately 20% at 2 TeV.

NLO electroweak corrections are calculated using HORACE [57] version 3.1. The LO simulation of the Drell-Yan process used in this analysis already includes final state photon radiation, which is modeled with PHOTOS [58]. Therefore the k-factor derived is calculated as ratio of the cross-section (as a function of the invariant e^+e^- pair mass) at NLO over the cross-section at LO, in both cases with final state photon radiation turned off. The NLO corrections include electroweak loops, initial and final state radiation of real $W^\pm$ and Z bosons as well as initial state photon emissions. Furthermore, contributions from initial state photons as part of the proton PDF are considered ($\gamma\gamma \to e^+e^- + X$) using the MRST2004QED PDF [59]. The total uncertainty of electroweak corrections increases with mass and amounts to approximately 4.5% at 2 TeV.

2.5 Limitations and Selected Extensions of the Standard Model

Although the SM is very successful in describing most data, there are some observations that are not covered as well as some theoretical arguments that suggest that the SM is an effective model derived from a more complete one. A few selected of them will be briefly introduced.

Recently, neutrino oscillations have been observed [16, 17], which requires that neutrinos have a non-zero mass, while the SM is constructed[27] such that neutrino masses are zero.

According to the current understanding of the early phase of the formation of our universe, matter and anti-matter was produced in equal amounts. Due to CP violating weak decays, a matter anti-matter asymmetry arises, however the asymmetry predicted by the SM is not sufficient to explain today's matter dominated universe. New physics that introduce additional CP violating interactions could explain this observation.

There is also a number of theoretical aspects that cannot be satisfactorily explained by the SM. There is no explanation why the gravitation is so weak compared to the other forces. This issue is referred to as hierarchy problem. The Higgs mass at LO is fixed by the $W^\pm$ and Z masses, but quantum corrections through fermion and gauge boson loops contribute a significant amount. To be able to derive a Higgs mass close to the observed one, a significant amount of fine-tuning in terms of fermion masses or coupling constants needs to be performed. Therefore this issue is called the fine-tuning problem. Furthermore, there is no obvious reason why the lightest charged fermion weights 511 keV while the heaviest weights approximately 173 GeV, which is approximately six orders of magnitude heavier.

Many Beyond the Standard Model (BSM) models were developed to solve individual or several of the shortcomings of the SM. With experimental measurements, such as the result of this analysis, models can be verified or rejected, or the allowed phase space of a model can be restricted. Typically, there is an interplay between experimentators and theorists; new measurements might give hints to theorists, which direction might be promising or not. On the other hand, new models obeying recent experimental observations might lead to new measurements to judge the model in the light of what has been realized in nature.

In the following a selected class of models that predict new heavy resonances that decay into pairs of electrons shall be discussed.

[27] The SM has been constructed before neutrino oscillations were observed.

Several BSM models extend the symmetry group of the SM by an additional $U(1)_{BSM}$ group. If this higher symmetry is broken, e.g., by SSB, an additional neutral heavy gauge boson called Z′ emerges. In principle, this new gauge boson could mix with the Z in a similar way as the Z is constructed as a linear combination of W^3 and B^0. However, precision measurements of the Z boson at LEP set stringent limits on mass mixing, which can therefore neglected (see Ref. [60] and Section 2.5.4).

Correspondingly, the Z′ boson is incorporated in the Drell-Yan matrix element defined in Eq. 2.17 as follows:

$$M_{q\bar{q}}^{LO,\sigma\tau}(\hat{s},\hat{t},\hat{u}) = -\frac{e^2}{\hat{s}} \sum_{V=\gamma,Z,Z'} g_{qqV}^{\sigma}\ g_{llV}^{\tau}\ P_V(\hat{s})\ A^{\sigma\tau}(\hat{u},\hat{t}). \tag{2.21}$$

The couplings are model-dependent, but the propagator of the Z' is assumed to be identical to the Z propagator with the exception of the width. The latter may deviate, e.g., because the decay to $t\bar{t}$ is allowed, if the mass is above two times the t quark mass. Besides that the width also depends on couplings to additional new fermions, if the latter are predicted, and couplings of hypothetical Z' bosons to the known fermions might also differ from the SM Z boson's couplings. In the following, it is assumed that if new fermions exist, their mass is above half the Z' mass and a decay into these is therefore kinematically not possible. This is a reasonable assumption as there is no strong evidence for additional fermions at accessible masses. Due to the inclusion of the Z' in the matrix element, interference effects with the SM Drell-Yan process are possible.

2.5.1 Sequential Standard Model

The Sequential Standard Model (SSM) Z' [22] is a heavy gauge boson with the same quantum numbers and couplings to the SM fermions as the Z, but with a different pole mass and width, where the latter is approximately 3% of the pole mass. This model is somehow arbitrary as there is no deeper physics model that predicts these parameters of the Z'. It is rather a benchmark model that is commonly used in searches for dilepton resonances of many experiments to compare the sensitivity of the analyses.

In general, it can be shown that such a SSM Z' can exist, if it has non SM-like couplings to additional exotic fermions, or if it represents an excited state of the SM Z in case of additional dimensions at the TeV scale. It is assumed that the SSM Z' can only decay into SM particles.

2.5.2 E_6 Models

The E_6 based Z's [22, 23] are predicted by Grand Unifying Theories (GUTs), which attempt to unify the electroweak and strong forces by introducing a common gauge symmetry, E_6 in this case, at a very high energy scale, the GUT scale. The motivation for the E_6 ansatz comes from superstring theories. In order to describe physics at the TeV scale and below, the E_6 symmetry needs to be broken:

$$E_6 \rightarrow SO(10) \times U(1)_\psi \rightarrow SU(5) \times U(1)_\chi \times U(1)_\psi, \tag{2.22}$$

where the $SU(5)$ is broken further into the SM gauge group. The product of the two additional $U(1)$ is broken at the TeV scale and two massive gauge bosons are introduced,

Table 2.2: Z' models based on the E_6 symmetry group and their corresponding mixing angles [22, 23].

Model	Z'_χ	Z'_ψ	Z'_η	Z'_I	Z'_N	Z'_S
θ	0	$\pi/2$	$-\arctan\sqrt{5/3}$	$\pi+\arctan\sqrt{3/5}$	$\arctan\sqrt{15}$	$\arctan\sqrt{15}/9$

whose charges depend on the chirality σ of the fermion f and the mixing angle θ:

$$Q_f^\sigma(\theta) = q_{f\chi}^\sigma \cos\theta + q_{f\psi}^\sigma \sin\theta, \quad 0 \leq \theta \leq \pi. \tag{2.23}$$

In the notation of Eq. 2.17 for the matrix element. the coupling can be written as:

$$c_{ffZ'}^\sigma = \sqrt{\frac{5}{3}}\, g'\, Q_f^\sigma(\theta), \tag{2.24}$$

where g' is the SM coupling of the SM $U(1)_Y$. Using this parametrization, the Z' of various concrete GUT models obeying the symmetry of Eq. 2.22 can be retrieved by choosing the corresponding value for θ as given in Table 2.2. In terms of cross-section times branching ratio σBR at the LHC, Z'_ψ has the lowest and Z'_χ the highest value. The values of the other models are enclosed by these two for all accessible pole masses. The width of the resonances is predicted to be between 0.5% and 1.3% [61, 62].

2.5.3 Interference with the Drell-Yan Process

Fig. 2.7 shows the mass distributions (without any detector simulation) of the SSM Z' which is simulated together with the SM Drell-Yan process and the corresponding interference. For comparison, the mass distribution of the Drell-Yan process without the SSM extensions is also shown.

The interference at masses below the signal pole masses, that is the difference of the amplitude of the distribution with Z' signal included and without, is visible for the SSM Z'. However, the experimental signature is the resonance close to the pole mass. Typically the observed data will reach up to the mass region where approximately one event is expected for a given amount of data. The predicted number of events of the resonance close to the pole mass however is $\mathcal{O}(100)$ larger than the Drell-Yan prediction and lifts the prediction of the number of events to a level that is comparable to the mass region a few hundred GeV below. This resonance peak is what the analysis is sensitive to and therefore the interference can be neglected. This allows to simulate the Drell-Yan process and the Z' separately, where the latter needs to be simulated at one pole mass only and can be reweighted to any other desired pole mass. Details on this procedure will be given in Section 8.2.

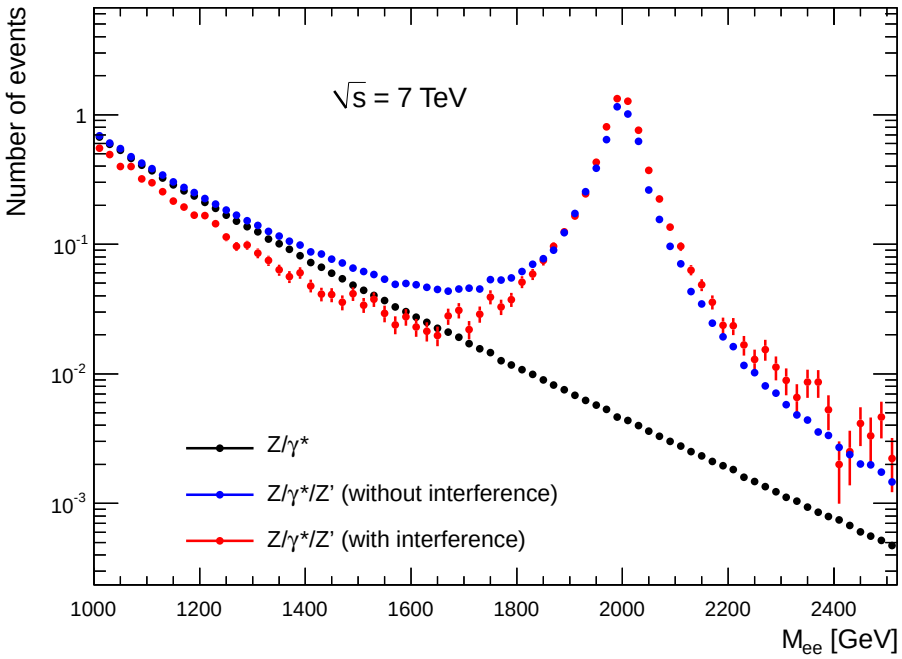

Figure 2.7: The mass distribution of the SM Drell-Yan process itself is shown in black, while the red (blue) marker show the corresponding distribution when a SSM Z' of pole mass 2000 GeV is included in the matrix element with interference with the Drell-Yan process turned on (off). The distributions are derived on generator level with no cuts applied and are scaled to the expectations of the data set used in this analysis. The SSM Z' Monte Carlo sample with interference turned on was generated with a significantly lower number of events than the sample with interference included.

2.5.4 Experimental Status

At the beginning of 2011, before the data for this analysis was taken, the strongest (indirect) exclusion limits on possible SSM Z''s were set by the LEPII[28] experiments. The Z width as well as angular correlations of the pair of charged fermions it can decay into were measured with high precision. In the presence of an additional heavy gauge boson, these quantities would differ from the SM prediction. A possible Z' could mix with the Z such that new mass eigenstates are formed in analogy to the B^0 and W^0. If a possible Z' did not mix, it would still contribute to (and therefore alter) the observed width and angular correlations. In the absence of significant deviations from the SM predictions, indirect limits can be set for a model by calculating the highest possible contribution, which is still compatible with the measured distribution. This amplitude can be converted back into a mass of the individual model. Therefore this kind of limit is very model-dependent. With this method, SSM Z' masses were excluded up to 1787 GeV with 95% C.L.

[28] Large Electron Positron Collider (LEP) was the precessor of the LHC installed in the same tunnels at CERN. Four large detectors were installed, see [63, 64, 65, 66] for more information on the detectors, the measurements done and the limits set on the existence of a SSM Z'.

Table 2.3: ATLAS 95% C.L. limits for the Z' bosons predicted by the E_6 models [69].

Model	Z'_χ	Z'_ψ	Z'_η	Z'_I	Z'_N	Z'_S
Mass limit [GeV]	900	738	771	842	763	871

Direct exclusion limits[29] were set by experiments located at hadron colliders. Here mass spectra were scanned for deviations ("bumps") and the highest possible cross-section that is still compatible with the data can be converted into a excluded mass by using the cross-section predicted by the model.

The Tevatron is a proton anti-proton collider with $\sqrt{s} = 1.96\,\text{GeV}$ located at Fermilab, Batavia, USA. It was successfully operated for 18 years until it was finally shut down in late 2011. Data was taken using two large multi-purpose detectors, the DØ and the CDF detectors. Both experiments performed searches for the SSM Z' and CDF [67] (DØ [68]) excluded with 95% C.L. masses below 1071 GeV (1023 GeV). The latter search was performed in the dielectron final state, while CDF searched in the dimuon final state.

Similar results were obtained by the LHC experiments; ATLAS [69] and CMS [70] excluded with 95% C.L. masses below 1048 GeV and 1140 GeV, respectively, using the data sets taken in 2010. Both results are derived from the combination of the analyses in the dielectron and dimuon finals states. Due to the higher center-of-mass energy of the LHC, the results derived with a data set taken in three months in two final states are competitive with the Tevatron results derived from a data set taken over years in one final state. The 95% C.L. exclusion limits for the E_6 models derived by ATLAS [69] are shown in Table 2.3. The corresponding results from the other three experiments [67, 68, 70] are of similar size.

[29] How to calculate direct exclusion limits will be discussed in detail in Chapter 8.

3 Experimental Setup

The Large Hadron Collider (LHC) is a hadron-hadron synchrotron collider located in a tunnel of 27 km circumference on the grounds of the European Organization for Nuclear Research (CERN) near Geneva, Switzerland. There are six experiments located at the LHC. Four of them are built for specific physics purposes (ALICE [71], LHCb [72], LHCf [73] and TOTEM [74]) and two of them are general purpose detectors, CMS and ATLAS. In this chapter, the LHC and the ATLAS experiment itself will be briefly described, followed by a description of particle reconstruction with ATLAS.

3.1 Large Hadron Collider

The LHC can be operated with two types of beams, proton beams and heavy ion[1] beams. It is designed to operate at unprecedented energies and luminosities, namely a center-of-mass energy of 14 TeV and an instantaneous luminosity $\mathcal{L} = 10^{34}\,\mathrm{s}^{-1}\mathrm{cm}^{-2}$ in proton-proton (pp) collisions. The number of protons per bunch amounts to approximately $1.1 \cdot 10^{11}$. In lead-lead collisions 5.5 TeV center-of-mass energy per nucleon pair can be achieved. The following discussion will focus on pp-collisions, because the data analyzed in this thesis involve only pp-collisions. Further information on the heavy ion operation mode can be found in [75].

For colliders, the instantaneous luminosity $\mathcal{L}$ is a measure for the number of particles in the beam, e.g. protons, that pass through a unit area per time. For a physical process with a cross-section σ, it correlates the cross-section to the rate of the process R: $R = \mathcal{L}\sigma$.

The luminosity integrated over time, $\int \mathcal{L}dt$, is a measure for the number of events. For a fixed center-of-mass energy, the size of the instantaneous luminosity is the key to provide as much data as possible for the experiments in a fixed amount of time.

The LHC beams are structured in up to 2808 filled bunches of protons, where each bunch consists of $\mathcal{O}(10^{11})$ protons. At so-called interaction points, the bunches are focused such that the transverse position distribution of the protons in the bunches is as narrow as possible to maximize the instantaneous luminosity. Due to the high proton density and large inelastic cross-section in such collisions of bunches (also called bunch-crossings), there are multiple pp-interactions per bunch-crossing, which are referred to as pile-up. The bunch-crossing rate amounts to 40 MHz and makes data-taking a challenge for the experiments. In the following, a brief summary of the LHC operation will be given.

In September 2008, proton beams were circulated for the first time. Unfortunately, there was an accident end of September 2008 with the super-conducting dipole magnets. Liquid Helium, used to cool down the magnets to a temperature of 1.8 K, evaporated instantaneously. This incident showed that time-consuming upgrades were necessary to safely operate the LHC.

After successful installation, the LHC was started up again and first proton-proton collisions at a center-of-mass energy of 900 GeV took place in November 2009. In 2010,

[1] Typically lead or gold ions are used.

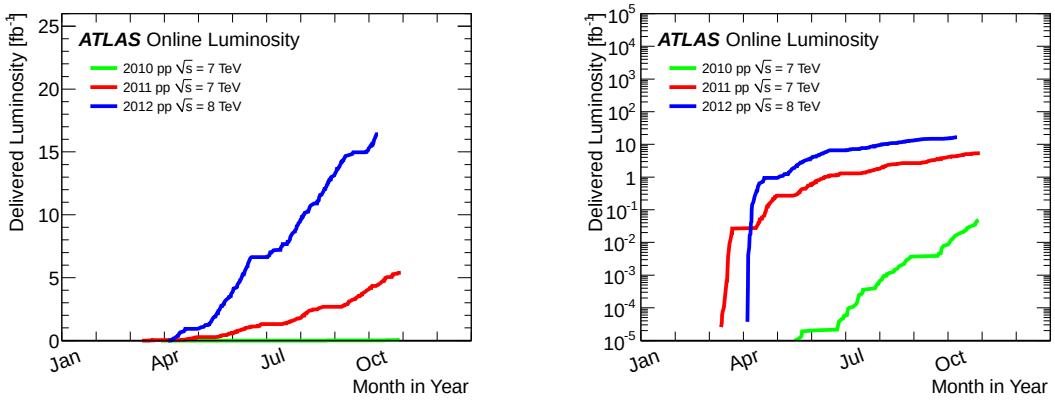

Figure 3.1: On the left plot, the integrated luminosity delivered for proton-proton collisions at ATLAS is shown as a function of time for the data taken in the years 2010, 2011 and 2012 on a linear scale, while the right plot shows the same distributions on a logarithmic scale. Plots taken from Ref. [77].

the center-of-mass energy was increased to 7 TeV at a low instantaneous luminosity (up to $2.1 \cdot 10^{32}\,\mathrm{s^{-1}cm^{-2}}$) and a data set was taken successfully over the whole year, which corresponds to to an integrated luminosity of $45\,\mathrm{pb^{-1}}$. The data set, which is analyzed in this thesis, was taken in 2011 with a center-of-mass energy of still 7 TeV, but with a significantly higher instantaneous luminosity of up to $3.7 \cdot 10^{33}\,\mathrm{s^{-1}cm^{-2}}$. Further information on the luminosity determination for the 2011 data set can be found in [76].

In 2012, the center-of-mass energy was increased to 8 TeV and an instantaneous luminosity of almost $8{\cdot}10^{33}\,\mathrm{s^{-1}cm^{-2}}$, which is very close to the design luminosity of $10^{34}\,\mathrm{s^{-1}cm^{-2}}$, was achieved. The average number of interactions per bunch-crossing increased to approximately 20, while the maximum increased to approximately 40. This is nearly the double amount of pile-up interactions than observed in 2011.

The development of the integrated luminosity for ATLAS[2] as a function of time is shown in Fig. 3.1. The different growth rates for the data taken in 2010, 2011 and 2012 are clearly visible. In 2011, $5.81\,\mathrm{fb^{-1}}$ were delivered by the LHC and $5.25\,\mathrm{fb^{-1}}$ were recorded by ATLAS. The data-taking efficiency is higher than the 90% that could be derived from these two numbers because beam-dump and other machine related studies are included in the recorded integrated luminosity. Further general information can be found in [77].

The next section will cover the ATLAS detector itself.

3.2 The ATLAS Detector

The ATLAS detector is a high-energy physics multi-purpose detector. It consists of an inner detector, which is able to measure tracks of charged particles, of calorimeters and of a muon system. Fig. 3.2 gives an overview of the detector. In the following, first the coordinate system and conventions will be discussed, followed by a description of the individual detector systems with focus on the components used in this thesis.

[2]The instantaneous luminosity is, amongst others, a function of the transverse beam width achieved at the interaction point. Therefore the instantaneous luminosity of the same LHC fill is different for

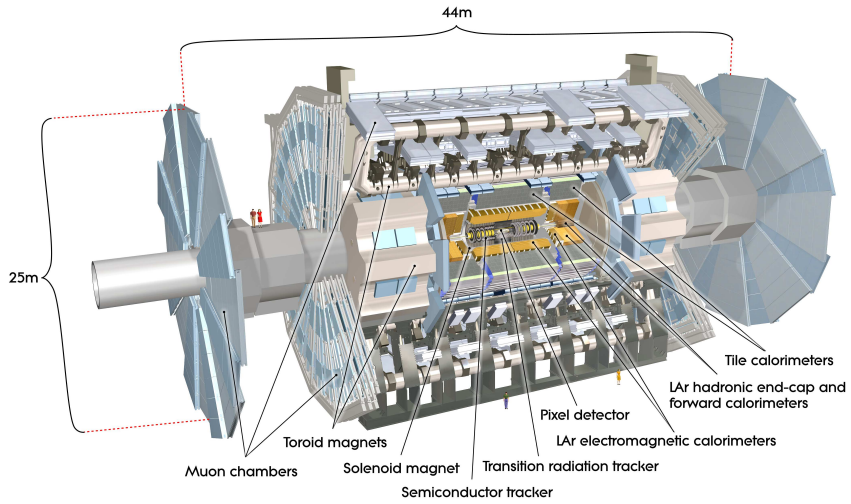

Figure 3.2: An overview over the detector components of ATLAS is shown [21].

3.2.1 Coordinate System and Conventions

A right handed, Cartesian coordinate system is used within ATLAS. The positive x-axis points towards the center of the LHC ring and the y-axis points upwards. The z-axis is oriented counter-clockwise along the beam axis. The nominal interaction point defines the origin of the coordinate system. In the following, derived coordinates, which are conveniently used, are defined:

- Radial distance to beam: $r = \sqrt{x^2 + y^2}$.
- Azimuthal angle: $\phi = \arctan(x/y)$.
- Polar angle: $\theta = \operatorname{arccot}(z/r)$.
- Pseudorapidity: $\eta = -\ln(\tan\theta/2)$.
- Rapidity: $Y = \frac{1}{2}\ln\left(\frac{E + p_z}{E - p_z}\right)$, where E denotes the energy and p_z the projection of the 3-momentum to the z-axis.
- Distance in the $\eta - \phi$-plane: $\Delta R = \sqrt{\Delta\eta^2 + \Delta\phi^2}$.
- Quantities with a T subscript are projections of the quantity to the (transverse) x-y-plane. They are referred to as absolute numbers unless stated otherwise.

Most mass distributions that are covering masses from 70 GeV to 3000 GeV are shown in a logarithmic display in the abscissa. Therefore the binning is chosen such that it is equidistant in a logarithmic display. It is split into 72 bins.

A remark concerning the notation: in general, the term electrons is used for the set of electrons and positrons unless stated otherwise.

each experiment, e.g. ATLAS and LHCb.

3.2.2 Inner Detector

The inner detector is immersed in a solenoidal magnetic field of 2 T, which bends the trajectory of charged particles. It is designed to measure the (transverse) momentum with a resolution of $\sigma_{p_T}/p_T = 0.05\,\% \, (p_T/GeV) \oplus 1\%$ within a coverage of up to $|\eta| < 2.5$. This covers all particles with an opening angle with respect to the beam of greater than 9.4°. To achieve this precision, three different systems, each in two different configurations, barrel and end-cap, are installed as shown in Fig. 3.3.

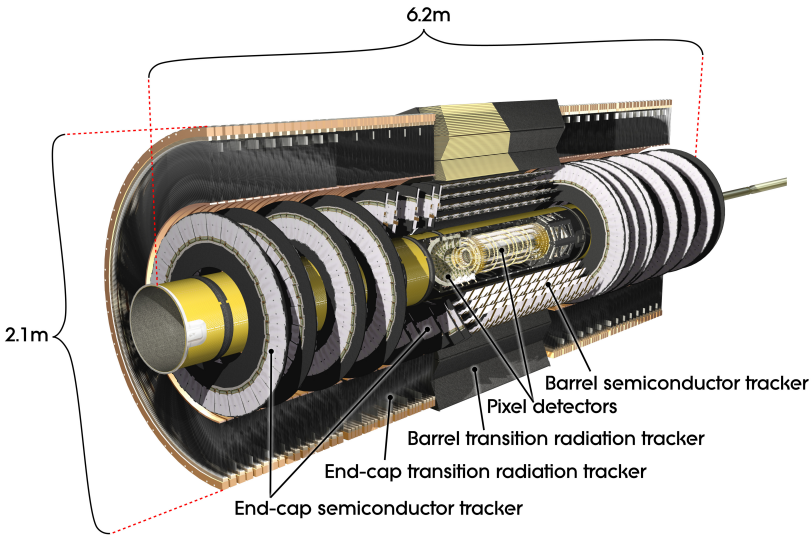

Figure 3.3: Overview of the ATLAS inner detector and its sub-systems [21].

The system closest to the beam pipe, starting at an radial distance of approximately only 45 mm, is the silicon pixel detector. It consists of three layers[3] in the barrel and three wheels in the end-caps. Its nominal position resolution amounts to 10 μm in the $R-\phi$ and to 115 μm in the z (R) measurement in the barrel (end-cap). The pixel detector is surrounded by the silicon microstrip detector (SCT), which is arranged in four double layers in the barrel and nine double wheels in the end-caps. It is designed such that each particle traversing the SCT ($|\eta| < 2.5$), traverses four double layers. Because the density of tracks coming from the interaction point is not as high as in the pixel detector, lower resolutions are sufficient. In $R-\phi$, 17 μm are achieved and in the z (R) direction 580 μm. The two silicon detectors are enclosed by the transition radiation tracker (TRT). It consists of gas filled straw tubes that are aligned parallel to the beam pipe in the barrel in 73 layers and perpendicular in the end-cap in 160 layers. The ionization signal of traversing charged particles is detected. Due to its geometrical form, the TRT measures only the $R-\phi$ component with a resolution of 130 μm in the barrel, whereas it measures the $Z-\phi$ component in the end-cap. Additionally, fibers with different refraction indices are arranged between the straw tubes. Here particles with a sufficiently high Lorenz factor will emit transition radiation, that means they emit additional photons, when traversing the boundary between two materials with different refraction indices. These photons excite the gas in the straw tubes, which leads to a larger signal amplitude than the ionization signal only. This can be used to e.g. separate electrons from pions at low momentum

[3]The innermost layer is also referred to as b-layer.

scales, because the light hadrons contained in many jets do not emit transition radiation. For momenta of a few hundred GeV, as of interest in this analysis, the separation power is low, because most of the relevant light hadrons do also emit transition radiation.

3.2.3 Calorimeter System

In this section, the relevant calorimetry principles will be introduced. Afterwards the individual ATLAS calorimeter subsystems will be discussed.

When incident particles, like electrons, taus, hadrons or photons, traverse the calorimeter, they interact with the material and deposit their energy until they are finally stopped. There are multiple types of calorimeters and sandwich calorimeters are a common type, which was chosen for ATLAS.

Sandwich calorimeters consist of alternating layers of absorber material, where incident particles have a high probability to deposit energy, and active layers, where the deposited energy of the incident and subsequently produced particles is measured. Incident particles form a shower of particles when they traverse the calorimeter, e.g. high energy electrons dominantly emit Bremsstrahlung photons, which convert into electron positron pairs again, which can again emit Bremsstrahlung and so on. This process is stopped, when the emitted photons do not have sufficient[4] energy to convert.

The energy of particles can be measured the more precise, the thinner each individual layer is. On the other hand, there are technical restrictions on the layer thickness (of the active layer), and the price increases with increasing granularity as well. In practice, a compromise needs to be found. In order that incident particles deposit as much energy as possible per way length, the absorber layers are built with materials, where the average energy deposition per way length is high. Typical choices are materials with high atomic numbers like lead[5] or iron because the interaction cross-sections increase with the atomic number, e.g. the probability to emit Bremsstrahlung scales with the square of the atomic number.

Calorimeters are typically splitted into an electromagnetic (em.) and a hadronic (had.) sub-system. An electron can be stopped with a much smaller amount of material as a (heavier) hadron of same momentum, because the probability to emit Bremsstrahlung decreases with one over the mass of the particle squared. The process that are relevant for energy losses of hadrons in matter, e.g. elastic and inelastic nuclear scatters, have a lower cross-section than Bremsstrahlung has for electrons. Therefore, the em. calorimeters are typically built with a higher granularity than the had. ones to reflect the different amount of energy deposited per way length.

The depth of em. calorimeters is expressed in terms of the so-called radiation length, which is defined by the following relation[6]: $E(x) = E_0 e^{-x/X_0}$, where $E(x)$ is the energy of a particle after it has traversed a length x in the material. Its initial energy is E_0 and the radiation length X_0 is the length after which a energy fraction of $1 - 1/e$ was on average deposited. For had. calorimeters, the depth is specified in terms of interaction length, which is the average length a particle can traverse inside a material before an interaction takes place. The radiation length for lead, the absorber material used in most ATLAS

[4] An energy of at least two times the electron rest mass is required.

[5] In most ATLAS calorimeters, lead is used as absorber material. In the forward calorimeters however, copper and tungsten are used as absorber material to cope with the high radiation [21].

[6] The actual energy loss of particles in matter due to ionization is described by a more complex function that depends (amongst others) on the energy of the particle, see e.g. the Bethe equation in Ref. [44].

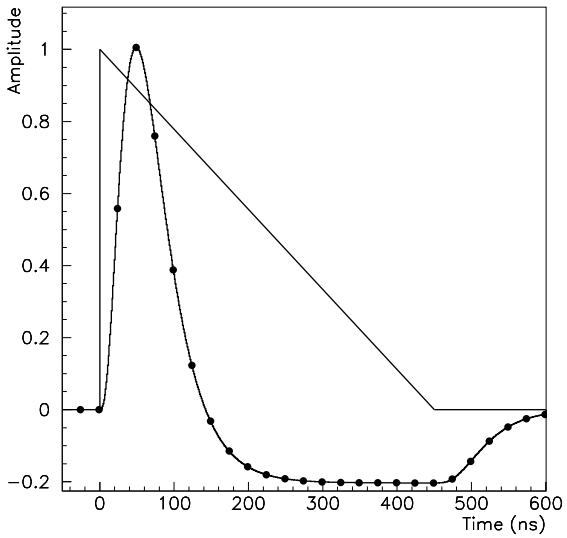

Figure 3.4: This plot shows a representative signal of an electromagnetic calorimeter barrel cell. The triangle shaped signal is the signal before shaping, the other line represents the signal after shaping. The dots indicate successive bunch crossings in a 25 ns spacing. Plot taken from Ref. [78].

calorimeters, amounts to 0.56 cm while its interaction length amounts to 17.1 cm [44].

The active layer is optimized to measure precisely the energy and shower shape of the incident particle and the subsequent particles produced. Typically, this layer is realized as a gas or liquid filled capacitor with a high voltage applied. Traversing electrons (charged particles) ionize the gas and the additionally released electrons are accelerated towards the anode, where the current $I(t)$ is measured. Simplified, this current signal is converted in a voltage $U(t)$ by integrating it over time: $U(t) = C^{-1}\, Q(t) = C^{-1} \int I(t)dt$, where C is the capacity and t the time. This voltage is proportional to the amount of ionization charge released by the incident electron.

Each calorimeter needs to be adapted to the environment it is operated within. In ATLAS, the average separation (in time) of two incident particles is smaller than the time all[7] of the ionization electrons need to drift to the anode. So if a few bunch-crossings before or after the incident particle of interest another particle traverses the same calorimeter cells, the signals superimpose. This effect is called out-of-time pile-up, while multiple interactions in the same bunch-crossing can also lead to superimposed signals referred to as in-time pile-up.

The impact of out-of-time pile-up on the calorimeter signal can be minimized by reducing the integration time and by shaping the signal. On the other hand, the smaller the integration time, the smaller the amplitude and the larger the impact of noise in the (pre-)amplifiers. The signal amplitude can be increased by choosing an active material with a high atomic number, because the ionization signal strength scales with the atomic number. When the ATLAS calorimeters were designed, these items were carefully studied and optimized [78].

[7] Of course, electrons might recombine with ions or be absorbed by impurities. All refers here to all electrons that can be detected.

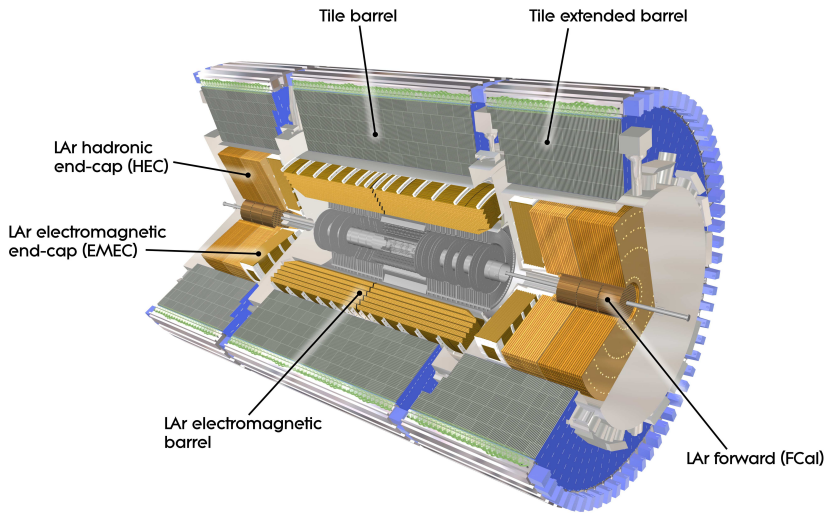

Figure 3.5: Sectional view of the ATLAS calorimeter system [21].

The ATLAS calorimeter system consists em. and had. sub-systems. All sub-systems except the ATLAS forward calorimeters are realized as sandwich calorimeters. Liquid Argon is used as active material for all calorimeters except the had. barrel calorimeters, which use scintillating tiles. Argon is liquid at temperatures between 83.80 K and 87.30 K, therefore the liquid Argon calorimeters are enclosed within cryostates.

Fig. 3.4 shows the calorimeter signal before and after shaping for the em. barrel calorimeter. In the majority of the data taken, the bunch spacing, that is the time[8] between two bunch crossings amounts to 50 ns. The signal before shaping has a total "width" of approximately 450 ns, while the shaped signal is much narrower and almost the full amplitude is contained within a window of 150 ns. The so-called undershoot, the tail of the signal that falls below the zero line, helps to minimize the out-of-time pile-up impact of the energy measurement. Further information can be found in [78, 79].

Both, the em. and the had. sub-systems, are splitted in η into a sub-set of calorimeters that is also covered by the tracking system, called central calorimeters, and a sub-set outside the tracking system coverage. Fig. 3.5 gives an overview over the individual sub-systems.

In the following the individual calorimeter sub-systems will be discussed, first the liquid Argon based sub-systems, then the tile based one.

The electromagnetic Barrel Calorimeters

The em. barrel calorimeter consists of two half-barrels adjoint at $\eta = 0$ and covers up to $|\eta| < 1.475$. Its structure is shown in detail in Fig. 3.6. It consists of three samplings, where the absorber layers are aligned in an accordeon shaped form. This form allows a hermetic coverage in the azimuthal angle.

[8] The nominal bunch spacing for the data set taken in 2011 is 50 ns, half of the design value. However, not all possible bunch positions can be filled, e.g. due to beam dump restrictions, therefore the actual bunch spacing is larger for a minority of the bunches. Further, in a small part of the early data taken, only a limited amount of bunches was filled at all.

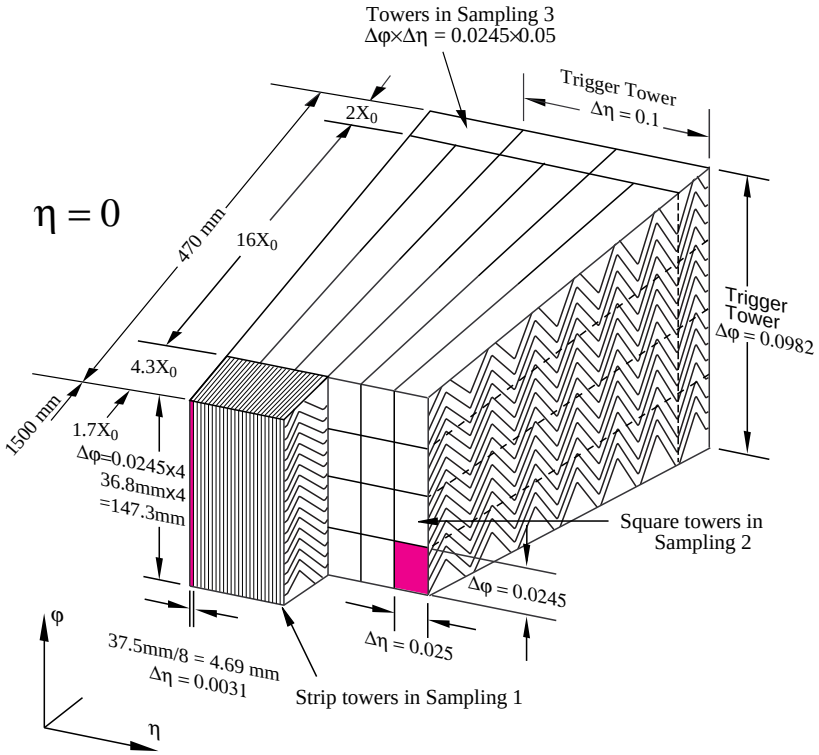

Figure 3.6: Schematic view of the em. barrel calorimeter, which shows the different granularity for the three calorimeter layers [21].

The first sampling has a very fine segmentation in η to distinguish closeby particles that enter the calorimeter, e.g. two photons from a π_0 decay. The second sampling covers most of the calorimeter depth in terms of radiation length and has a fine segmentation in both, η and ϕ, to precisely measure the shower shape. The third layer is less granular in η, because it does not significantly contribute to the measurement of the pointing of the shower. It is primarily used to estimate the longitudinal leakage of a shower. To be able to estimate energy depositions in not instrumented material between the solenoid magnet and the first calorimeter layer, a so-called presampler is installed. It consists of one active liquid Argon layer only, but is segmented in η and ϕ. The energy resolution of the central em. calorimeters will be discussed in detail in Section 3.3.2.

The End-Cap Calorimeters

The end-cap calorimeters consists of two wheels (em. and had.), which are themselves divided into an inner and an outer part. The outer em. wheel covers $1.375 < |\eta| < 2.5$ and is structured in three layers, too, where the second layer has a η and ϕ segmentation comparable to the barrel. The inner wheel covers $2.5 < |\eta| < 3.2$ and is structured in two layers which are less granular than the central calorimeters. The had. end-cap calorimeters cover $1.5 < |\eta| < 3.2$ and are segmented more coarsely than its em. counterparts.

The Forward Calorimeters

The forward calorimeters cover $3.2 < |\eta| < 4.9$, which covers angles with respect to the beam axis of 4.7° down to 0.85°. In this forward region, the requirements in terms of

radiation hardness are much higher than for other calorimeter parts. Therefore a different geometry was chosen; the calorimeters consists of three large absorber blocks, where in each of them cylindrical holes parallel to the beam axis were drilled. Each hole is filled with a rod of a smaller diameter than the hole; this gap is filled with liquid Argon. This structure leads to a coarse granularity.

The Tile Calorimeters

The had. barrel calorimeter is also a sandwich calorimeter, but uses scintillating tiles instead of liquid Argon as active layer. It is divided into two parts, the barrel covering $|\eta| < 1.0$ and the extended barrel covering $0.8 < |\eta| < 1.7$. Like the em. barrel calorimeters, it is structured in three layers, where each of them has a different granularity in η and ϕ.

Calorimeter Overlap and Gaps

Fig. 3.7 shows the η coverage of the different calorimeter sub-systems of the central calorimeters, which shows "gaps" of uninstrumented areas in the calorimeter transition regions. There exist additional devices, as shown in the figure, to estimate the energy deposits, but, in general, in those transition regions the precision of the energy measurements is lower than in the not-interrupted η ranges.

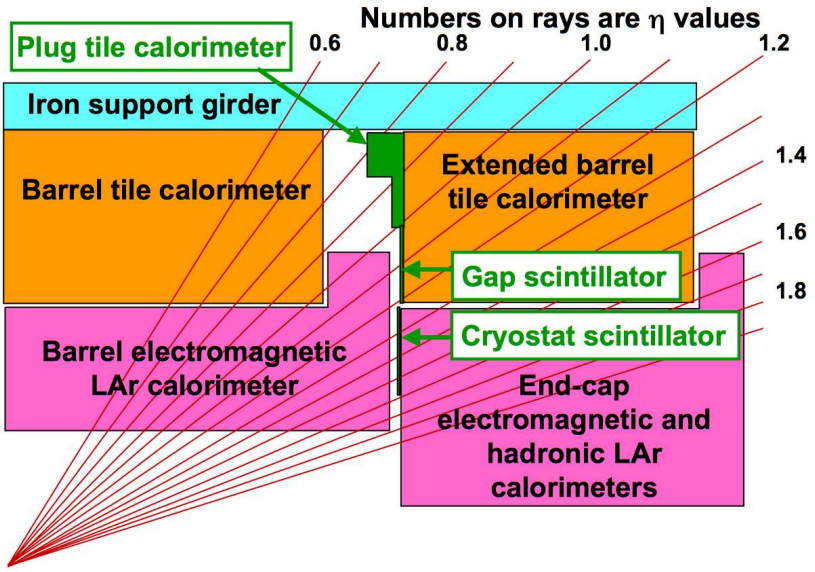

Figure 3.7: This display shows the coverage of the individual central calorimeter subsystems [21].

Calorimeter Readout

The readout of the energies measured in the liquid Argon operated calorimeter subsystems is done in two steps. The analogue raw signal of a calorimeter cell is send to the Front End Boards (FEBs), which are located in the detector on the outside of the corresponding calorimeter cryostat. Here the signal is amplified and shaped. If the event is to be recorded, the signal is converted into a digital signal, which is send via optical

fibers to the data acquisition system (DAQ). Further, for the trigger system, the signal of several cells is added up to a so-called trigger tower of typical size 0.1×0.1 in $\eta \times \phi$ and send to the trigger, which will be described later in this chapter.

3.2.4 Muon Spectrometer

The muon spectrometer is located in the outer part of the ATLAS detector, outside of the calorimeters. The large toroidal magnets of ATLAS provide the magnetic field, which bends particle trajectories that leave the calorimeters and traverse the muon system. It covers absolute pseudorapidities up to 2.7 and consists of four different detector types. Precision measurements are performed with the monitored drift tubes (MDT) in the central region, while cathode strip chambers (CSCs) are used in the end-caps. In the latter region, the requirements in terms of radiation hardness are higher, therefore a different detector type is used.

The second category of muon systems are the Resistive Plate Chambers (RPCs) in the central region and the Thin Gap Chambers (TGCs) in the end-caps. These systems are less precise in the momentum measurement, but can be read out quickly. Therefore, those chambers are used for triggering purposes. The trigger system will be described in the next section.

3.2.5 Di-electron Event Display

To illustrate how a typical di-electron event looks like, if measured with the detector components introduced so far, a so-called event display of a high mass event recorded in 2011 is shown in Fig. 3.8. Two electrons indicated in orange by (1) and (2) were observed. Electron (1) traversed the inner detector, namely the pixel barrel detector (3), the SCT barrel detector (4) and the TRT barrel detector (5), and was stopped in the em. barrel calorimeter (6). The second electron (2) traversed the pixel barrel detector (3), the SCT barrel and end-cap detector (4, 4a) and the TRT end-cap detector (5a) and was stopped in the em. barrel calorimeter (6). The reconstructed tracks are indicated by orange lines, which point to the em. energy clusters indicated as orange areas in the calorimeters. For readability, tracks and energy depositions of other particles are only shown if the track transverse momentum exceeds 200 MeV respectively the energy of a cluster exceeds 400 MeV.

For orientation, also further detector components are labeled. The barrel tile calorimeter is denoted by (7), the em. end-cap calorimeter by (8), the had. end-cap calorimeter by (8a) and the forward calorimeters by (9). The calorimeter cryostates are indicated in cyan and enclose the em. barrel calorimeters respectively the end-cap and forward calorimeter (8)-(9). The zoom in of the detector shown here can easily be identified in the detector overview shown in Fig. 3.2, when the position of the end-cap torroid magnets (10) is compared. The zoom shows less than half of the detector in diameter and less than one third in length along the z-axis. The muon systems located in the outer parts of the ATLAS detector are therefore not visible in the zoom in.

3.2.6 Trigger System

As discussed when introducing the LHC, the bunch crossing rate amounts to 40 MHz when running with design parameters. However, only a small subset of the occurring processes

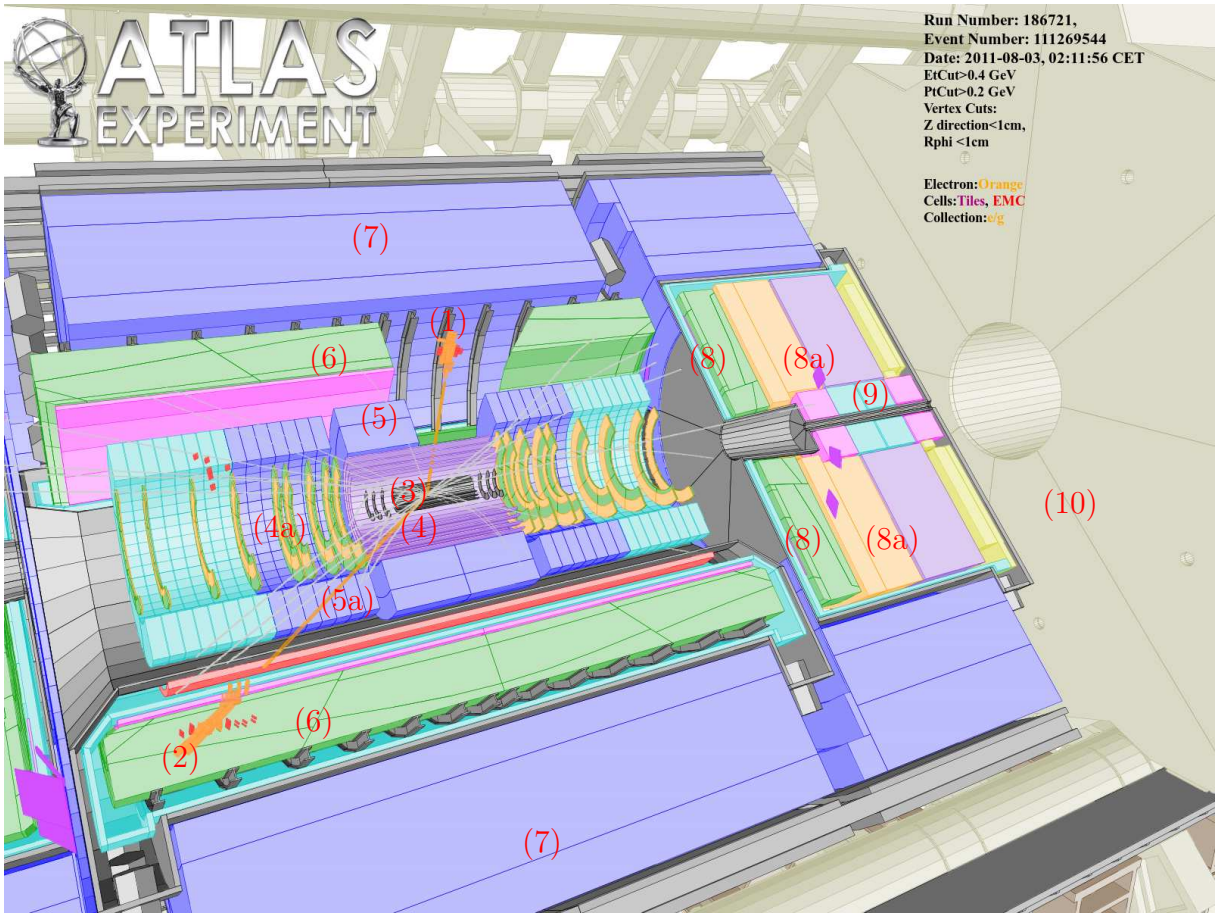

Figure 3.8: Display of an di-electron event with a pair mass of 1214 GeV. Taken from Ref. [53].

are of interest. Additionally, the typical size data size of one complete detector readout, approximately 1.5 MB, sets a limit on the event rate that can be recorded. Therefore, a trigger system is needed to select events of interest in a very short amount of time [21].

This is realized as a three level trigger system. The reason for this multi-level concept is that the event rate is reduced in steps at each level. Therefore more time is available to decide whether an event will be recorded or not at the next level. The first level (L1) trigger uses data from the calorimeters and the trigger chambers of the muon systems, which are read out with the full rate of 40 MHz, but with a coarse granularity and energy resolution for triggering purposes. Within 2.5 μs, the L1 trigger has to decide if and where possible interesting signatures are, so-called regions of interest (ROIs). The High Level Trigger (HLT), divided into L2 trigger and event filter[9], then investigates those ROIs further within a less stringent time limit, which allows a more elaborate analysis as base of the trigger decision.

In the following, the three trigger levels will be discussed.

[9]In a purely logical numbering scheme, it would have been called third level trigger, but the convention within ATLAS developed otherwise.

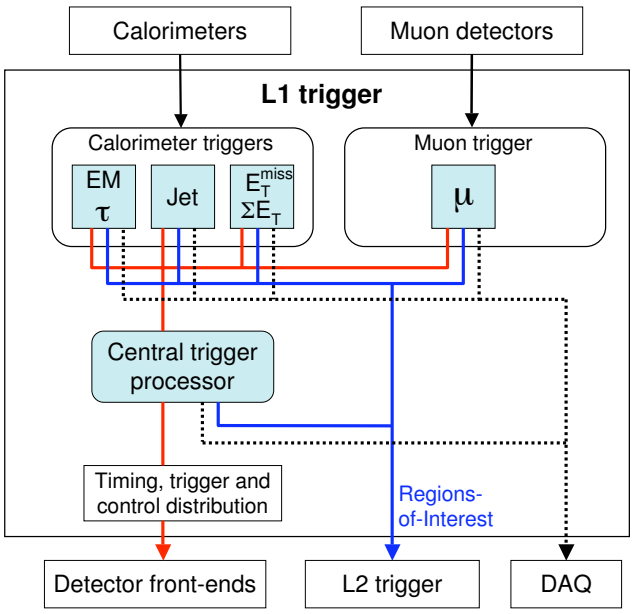

Figure 3.9: An overview over the Level-1 Trigger is shown [21].

The Level-1 Trigger

A schematic of the L1 trigger is illustrated in Fig. 3.9. It consists of two logical subsystems that determine multiplicities of particles of interest, e.g. how many electron candidates with an E_T above a certain threshold were found. These candidate multiplicities are sent to the Central Trigger Processor (CTP), where all active trigger signatures are implemented. One signature is, e.g., L1_2EM15, which requires two electron/photon candidates with an E_T of at least 15 GeV.

Additionally, each signature may have a so-called prescale p assigned to. It is an integer specifying that every p-th event with this signature is taken. If the multiplicities received at the CTP match a signature's requirements, the so-called Level-1 Accept (L1A) is distributed via the Timing, Trigger and Control distribution (TTC) system.

This triggers the readout of all detector systems used for later offline analysis. For this purpose, each detector component has an on-detector buffer pipeline, which allows to buffer the data readout for at least 2.5 μs. Upon reception of the L1A, the content of each buffer is read out into the Data AcQuisition (DAQ) system, which is located off-detector. Furthermore the information, which multiplicities were found at which geometrical position, is encoded in form of ROIs and sent to the Level-2 trigger.

In the next section, the calorimeter trigger will be discussed in more detail with the focus on the electron/photon candidate determination. Further information on the muon trigger system can be found here [21].

The Level-1 Calorimeter Trigger

The calorimeter trigger works on basis of two η-ϕ maps, one for the em. and one for the had. calorimeters, that provide the measured calibrated transverse energies. These maps are segmented in form of so-called trigger towers, which have a size of 0.1×0.1 in $\eta \times \phi$ in the central calorimeters, and larger sizes at higher pseudorapidities.

The calorimeter electronics provide analogue signals in the trigger signal path. They are digitized in the Pre-Processor (PP), which also applies an transverse energy calibration at the so-called em. scale. The calibration is performed such that if an electron or photon with a given transverse energy is detected, the incident transverse energy is recovered. For hadrons, the fraction of the energy actually observed in the calorimeters is lower and depends on the energy of the incident particle. An object-based calibration is not possible at the first trigger level as it consumes too much time. Therefore it is applied only within the HLT.

The calibrated trigger towers, 3584 in each the em. and the had. calorimeters, are sent[10] to the Cluster Processor (CP), which searches for electrons, photons and τ's, and to the Jet and Energy Sum Processor[11] (JEP), which searches for jets and calculates the sum of the transverse energy $\sum E_T$ in jets and in the total event as well as the missing energy $\not{E}_T$.

In the following, the principles of operation of the CP will be described, followed by a description of the JEP.

The Cluster Processor

To determine electron and photon candidates with the CP, the following algorithm is used, which exploits that electrons and photons form typically narrow showers which are contained in the em. calorimeters. Because no tracking information can be used, electrons and photons are treated in the same way.

In a window of 2×2 trigger towers in the em. layer, the sum E_T of two neighboring trigger towers is calculated as shown in the left plot of Fig. 3.10. The maximum of these four sums is the E_T^{max} assigned to this 2×2 window. If E_T^{max} exceeds one of the configurable E_T-thresholds, it is considered as a candidate. To prevent ambiguities, the same algorithm is applied to the eight 2×2 windows neighboring the window of interest. The central window is confirmed if its E_T^{max} is larger[12] than the ones of the neighboring window as shown in the right plot of Fig. 3.10.

The depth of the em. calorimeter is chosen such that electrons are typically stopped. Therefore no energy, besides calorimeter noise and pile-up, is expected to be measured in the hadronic inner core, that is the 2×2 windows at the position of the central window, but calculated with the had. layer instead of the em. layer of trigger towers. Typical values of this hadronic inner core isolation are a few[13] GeV. Electron and photon showers are also expected to be narrow, that is not broader than the width of two trigger towers. Therefore a possibility is foreseen to require that the transverse energy in the surrounding twelve trigger towers in the em. layer does not exceed a certain isolation value. However, because this value needs to be a fixed number, it is not possible to specify a isolation value that e.g. increases with E_T. To avoid possible inefficiencies for high E_T electrons, a trigger was chosen without this fixed isolation requirement for this analysis.

[10] To be precise, the trigger towers are summed up to jet inputs of size 0.2×0.2 in $\eta \times \phi$ still separate in em. and had. energy before transmitting them to the JEP.

[11] Officially, the JEP is called Jet Energy Sum Processor, but the additional "and" was inserted to make clear that the determination of jet and energy sums are two separate tasks.

[12] The reason for the use of $>$ and $\geq$, as shown in the figure, is that E_T^{max} is an integer quantity and two neighboring windows with the same E_T^{max} would result in the rejection of both windows otherwise.

[13] The noise level in trigger towers is much higher than in the full granularity precision readout, which is used when the actual event is recorded.

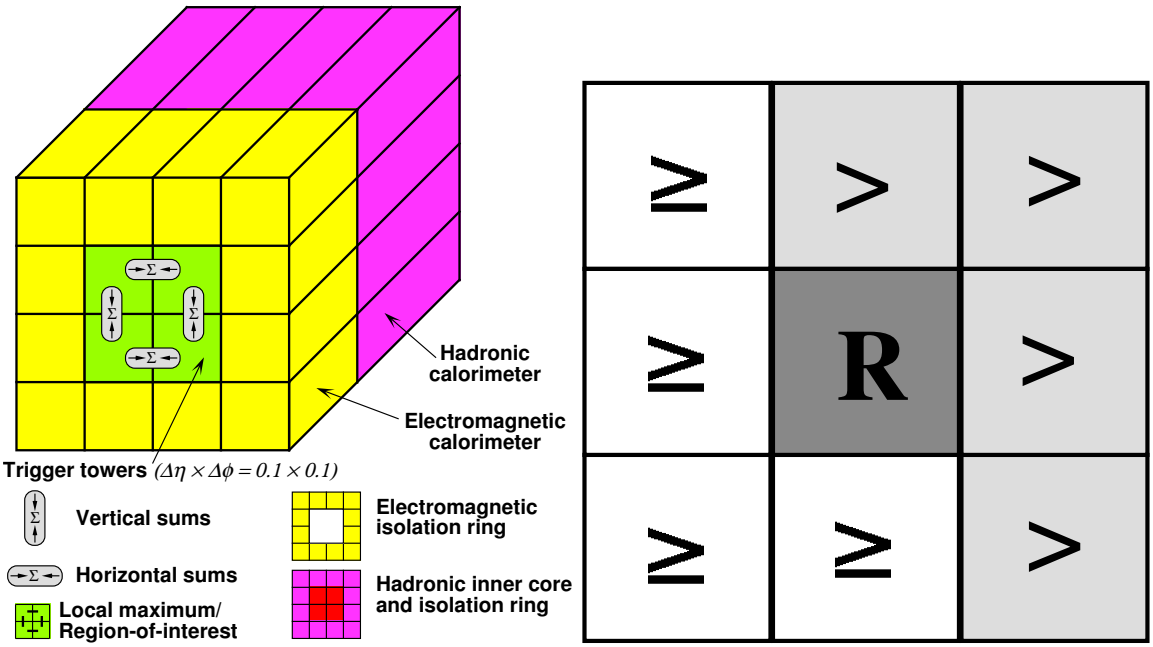

Figure 3.10: The left illustration shows the elements used for the electron/photon/tau identification algorithms in the cluster processor, where as the right sketch shows the requirements used in the algorithm that determines local transverse energy maxima [21].

The hadronic decay products of τ are typically highly boosted pions with small spatial opening angles, which allows to use the same algorithm as for electrons and photons, but with adapted parameters. The 2×2 windows are derived with the sum of the transverse energy of the em. and had. trigger towers. Additionally, the sum of the E_T of the twelve had. trigger towers that surround the central window can be required to be below a fixed isolation value.

The CP has the possibility to set 8 different E_T thresholds for electrons and photons as well as 8 additional ones which can be assigned either to the electron/photon sector or to the τ sector. The number of candidates found that pass each individual threshold are reported to the CTP.

The Jet Energy Sum Processor

The JEP has two purposes; to determine the jet multiplicities in an event and to calculate transverse energy sums. There is no need to treat the em. and had. layer separately, therefore the JEP sums up the transverse energy of these to so-called jet elements of size 0.2×0.2 in $\eta \times \phi$. The total transverse energy sum measured is the sum of the E_T of each jet element.

The second global event quantity determined is the missing transverse energy $\not{E}_T$. The quantity has to be interpreted as following: Assuming that the colliding protons have a transverse momentum of zero, the sum of the signed transverse momenta of all particles produced in the collision should be equal to zero. All deviations[14] from zero are assigned

[14] Due to the 2.5 μs total Level-1 decision time, it is not possible to apply detailed hadronic energy scales as done at higher trigger levels or in offline analyses. Therefore these deviations are also affected by

to decay products that do not deposit their energy in the detector, e.g. neutrinos, muons or new physics particles with certain interaction restrictions. To determine this quantity, the JEP converts the E_T of each jet element into an signed E_x and E_y component that is summed up separately in x and y and combined again afterwards.

To determine jet candidates, a similar principle as in the CP is used; the E_T in windows of various sizes, 2×2, 3×3 and 4×4 jet elements, is calculated. Then the window is determined that contains the local maximum in E_T.

Furthermore, the third global event quantity is an estimation of the sum of all transverse energy associated to jets candidates. For each jet trigger threshold, the calculated multiplicity is multiplied with a transverse energy close to the threshold. Finally the sum of these contributions is calculated. Further details can be found in [21].

The High Level Trigger

The methods used in the L2 trigger and the event filter are are very similar, therefore both together are referred to as High Level Trigger (HLT). For the L2 trigger, the detector data at the position of the ROIs is available in full granularity, while at the event filter level the data of the full event is available. In both cases, tracking information[15] is available, and reconstruction and identification algorithms similar to those used offline for the data recorded can be employed. This allows to reduce the event rate using sophisticated algorithms that select events with physical signatures of interest.

The L2 trigger is able to process incoming event data with rates up to 75 kHz and reduces the rate to below 3.5 kHz for the event filter within an average event processing time of approximately 40 ms. In the event filter, this rate is further reduced to approximately 300 Hz within an average event processing time of four seconds. Both systems are realized as large computer farms in dedicated buildings on the surface. Upon acceptance of an event by the event filter, the event raw data is finally recorded.

For this analysis, the photon trigger is of special interest. The shower shapes for electrons and photons are similar and therefore electrons and photons use the same identification algorithms at the so-called loose identification level. The electron identification as well as the reasons for the exact choice of the trigger will be discussed in detail later in this chapter, whereas this section focuses on the technical implications for the trigger. On trigger level, it is therefore possible to define a shared trigger that requires two electrons or photons, identified by common requirements on the shape of the em. shower in the calorimeters. Photons can later be distinguished from electrons by checking whether a track points to the energy cluster in the calorimeter.

One of the triggers derived this way is called 2g20_loose. The name of the trigger signature contains the imposed requirements: It requires that two particles (2) are either electron- or photon-like (g), have $E_T > 20$ GeV (20) and satisfy the shared electron and photon loose identification level (loose). This trigger signature is very similar for the L2 trigger, where it is named L2_2g20_loose, and for the event filter, where it is named EF_2g20_loose. The corresponding L1 signature is called L1_2EM12. It requires to electron- or photon-like energy depositions in the em. calorimeters with a transverse momentum of at least 12 GeV for each particle. The reason for the lower E_T threshold at L1 is that a trigger is only fully efficient above its E_T threshold and therefore the

the different fractions of visible energy in em. and had. showers.

[15] Due to bandwidth limitations, tracking information from the inner detector can only be used for a small fraction of events at L2.

threshold needs to be lowered to avoid the loss of events that might pass at the high level trigger.

The combination of (at least one) trigger signature per level is called trigger chain. In order to trigger an event by this chain, the L1_2EM12 trigger signature needs to be satisfied and a L1A needs to be issued. The corresponding ROIs are evaluated further at L2 and if these match the L2_2g20_loose signature, the event is considered further. At the event filter, it needs to satisfy the EF_2g20_loose signature to trigger the final trigger decision.

The next section of this chapter will describe how particles, with a focus on electrons, are reconstructed and identified.

3.3 Reconstruction of Particles with ATLAS

ATLAS event data consist of raw detector information, e.g. hits in the tracking system and individual energy deposits in calorimeter cells. Dedicated algorithms are used to reconstruct attributes of the incident particle, such as its 4-momentum. In the next sections, the track reconstruction in general will be explained briefly, followed by a more detailed description of the electron reconstruction and identification.

3.3.1 Track and Vertex Reconstruction

In this section the general concept of the track reconstruction is briefly summarized. For more details, also on reconstruction algorithms not described here, see [21]. In order to construct tracks, the hit information of the pixel detector and the SCT are converted into 3-dimensional space points. Two space points in successive layers of the pixel detector are taken as seed for a track. Additional space points in the area, where the current set of points is approximately pointing to, are successively added. Each time a point is added, the corresponding track candidates are fitted with a parametrized track function to judge whether or not the set of points is compatible with a particle trajectory. After the space points of the silicon detectors are incorporated, the track reconstruction is extended to the TRT.

When all tracks in an event are reconstructed, they are assigned to vertices, common geometrical origins in the interaction zone inside the beam pipe. All tracks that approximately point to a common origin are fitted again with the additional constraint that these tracks have a common origin.

Further, these tracks are extrapolated beyond the inner detector to predict their impact position in the calorimeters.

3.3.2 Electron Reconstruction and Identification

The seeds for electron candidates in the central calorimeters are so-called clusters in the second layer of the electromagnetic calorimeters. The window size of these clusters is 3×5 calorimeter cells in $\eta \times \phi$ and the energy assigned to a cluster is the sum of the energies of all cells within the window. Using a so-called sliding-windows algorithm [21], the calorimeter is scanned for such clusters. If the sum of the energies in a cluster exceeds 2.5 GeV, the candidate is considered further.

From all tracks pointing to a cluster within a cone of with size $R = 0.05$, the one with the smallest value of ΔR is chosen[16]. The energy of the cluster is then recomputed by summing up the individual energy in a 3×7 (5×5) window in the second layer for the barrel (end-caps). The granularity in the other layers is different. Here a matching algorithm, which considers the fractions of the cells lying within the window, is used to calculate the energy contributions.

Several energy corrections and pre-calibrations are applied that account for geometrical effects or inefficiencies. However, the final energy calibration is applied on analysis level and will be discussed later in Section 5.2.3. The 3-momentum of an electron candidate is derived from the energy calculated in the described way and its measured η and ϕ positions. The latter two are taken from the track measurement, if the track has at least four hits in the silicon detectors assigned to. Otherwise they are calculated from the energy weighted cluster position in the calorimeter for low quality tracks. Electrons are treated as massless particles[17].

The electron identification is divided in three levels with increasing quality requirements, namely loose, medium, and tight. The loose identification level, which is identical to the corresponding loose photon identification level, has three requirements on a candidate. The ratio of E_T in the first layer of the had. calorimeter to E_T of the em. cluster must be below a certain η-dependent threshold. Further, the ratio of the energy sum in a window of size 3×7 cells to the energy of a window of size 7×7 cells is required to be above a threshold. Finally there is a cut on the shower width in η. The thresholds are typically large matrices binned in E_T and η and are not listed here for space reasons.

The medium identification level adds additional requirements on top of the loose level. The track-cluster matching is by a factor of five stricter, namely $\Delta R < 0.01$ is required. Furthermore, there must be at least one hit in the pixel detector and the sum of the number of hits in the pixel detector and the SCT is required to be ≥ 4. The latter requirement ensures that the track quality is such that the track position measurements in η and ϕ are more precise than the calorimeter measurements.

There are two more requirements for energy depositions in the first layer of the em. calorimeters. If two local maxima are found in the energy depositions in the first layer within the electron candidate window, the difference of the largest to the second largest energy deposit over the sum of these energies must not exceed a certain threshold. This cut is particularly effective in suppressing neutral pions that decay into two photons. Additionally also the total shower width in the second layer has to be below a threshold.

The tight identification level, which is not used in this analysis, demands stricter requirements on track matching and quality and requests that transition radiation was observed in the TRT. Further, it suppresses photons that convert into a electron positron pair in the inner detector. The latter cut is applied in this analysis on top of the medium identification level. It requires that the track assigned to the electron candidate has a hit in the first layer of the pixel detector, the b-layer.

Further, in parts of the analysis, an isolation cut is applied. The calorimeter isolation is calculated as the sum of all transverse energies within a cone of size $\Delta R = 0.2$ around the cluster position minus the energy assigned to the corresponding electron candidate window of 3×7 (5×5) cells in the barrel (end-caps).

[16] If no track is found, the candidate is rejected.

[17] The electron rest mass of 511 keV is about 50,000 times smaller than the lowest transverse energies considered in this analysis and can therefore be neglected. Furthermore, this mass cannot be resolved with the ATLAS detector.

Electron Trigger

There are two classes of triggers for electrons, single particle triggers and two particle triggers. The first class imposes strict requirements on the particle identification level to enhance the purity of the triggered data. This is important as trigger rates are limited and jets that mimic electron signatures are abundantly produced in proton-proton collisions. The second trigger class requires two particles, which decreases naturally, at the same identification level, the trigger rate without e.g. loosing interesting di-electron events.

This approach has the additional advantage that a trigger with a modest particle identification level can be used as trigger for data-driven background determinations at the same time. The trigger that matches all described requirements is the 2g_20_loose trigger. It requires two photons with loose identification level and an E_T above 20 GeV. Because the photon and electron loose identification level are identical, this trigger can be interpreted as trigger that requires two energy depositions caused by an electromagnetic shower with at a transverse energy of at least 20 GeV. There are also di-electron triggers available, but they require the medium identification level, which does not allow to perform background studies with the signal trigger.

Electron Energy Resolution

The relative energy resolution in sampling calorimeters can be described by

$$\sigma(E)/E = a/\sqrt{E} \oplus b/E \oplus c, \tag{3.1}$$

where E is the energy in GeV and $\oplus$ refers to a summation in quadrature. The three contributions to the resolution, listed in the order of their appearance in the formula, are the stochastic term, the pile-up and noise term, and the constant term.

The constant a represents the stochastic term, which describes a resolution deterioration due to fluctuations of the energy deposits in the absorber layers. Although the average energy deposition in an absorber layer can be determined rather accurately, the actual deposit might deviate from that average. Therefore the stochastic term decreases, if the number of samplings per radiation length is increased. Depending on the $|\eta|$ region of the em. calorimeter, a amounts to $8 - 11\%$.

The second term has two contributions, the root mean square (RMS) of the thermal noise distribution[18] and of the pile-up energy distributions. The latter can be interpreted as the RMS of the average energy deposited by particles originating from soft scatters. Typical values for b at central η are approximately 270 MeV.

The third term is the most important one for high energy electrons. It accounts for all energy losses in uninstrumented material and therefore it depends on the goodness of their estimation as well as on the intercalibration of the calorimeter sub-systems. The value of c varies from 0.009 to 0.021 as a function of η in the central calorimeters. The values are taken from [80], which provides the best knowledge of the energy resolution for the data set analyzed in this thesis.

Using these values, the energy resolution for a transverse energy[19] of 500 GeV amounts

[18] The combined system of the calorimeter readout and the amplifier has an intrinsic noise level. Even if no input signal is applied, the output signal is not exactly zero, but follows a (typically Gaussian) distribution around zero or any other value it is gauged to. This distribution is referred to as the thermal noise distribution.

[19] The transverse energy was chosen, because it is the quantity of interest for this analysis.

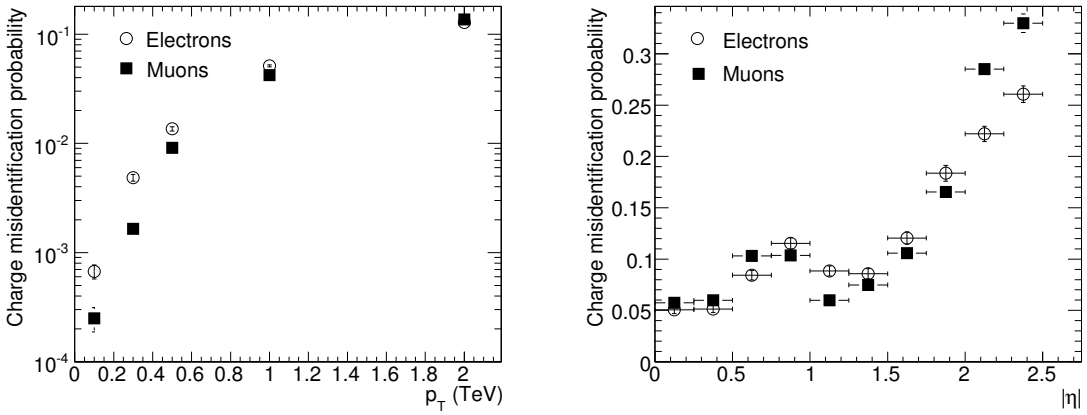

Figure 3.11: The left plot shows the charge mis-identification probability as function of p_T, whereas the right plot shows the charge mis-identification for particles with $p_T = 2000\,\text{GeV}$ as a function of $|\eta|$. All distributions are derived from Monte Carlo simulations. Plots taken from Ref. [21].

to 0.9% to 1.3% for $|\eta| < 2.47$ except the barrel end-cap transition region in $1.37 < |\eta| < 1.52$, where the resolution increases up to 2.7%. For comparison, in the inner detector a transverse momentum of 200 GeV is expected to be resolved with an relative uncertainty of approximately 8% [81]. In calibration runs with electronic pulses, it has been shown that high energy signals up to 2 TeV are measured without an unexpected deterioration of the resolution [82].

Di-electron Mass Resolution

The di-electron mass resolution has been estimated using SSM Z' Monte Carlo simulations with a pole mass of 2 TeV. On truth level, a mass window from 1995 GeV to 2005 GeV has been selected. From the reconstructed mass m_{reco} and the truth mass m_{truth}, the resolution given by

$$r = \frac{m_{reco} - m_{truth}}{m_{truth}} \tag{3.2}$$

has been calculated for all events. A Gaussian was fitted to the resolution distribution. The size of one standard deviation of the determined Gaussian distribution corresponds to the relative resolution. It amounts to 0.9%. To evaluate the stability of this result, a fit has been performed, where only positive values of r were considered to minimize the impact of electron Bremsstrahlung. This approach leads to a relative resolution of 0.8%. Furthermore, the size of the considered truth mass window was varied. The results fluctuate around 0.9% to 1%. Concluding from these results, the mass resolution at 2 TeV amounts to approximately 1%.

Charge Mis-identification

The electrical charge of electrons is determined from the curvature of the track measured in the inner detector. There are two main reasons for a possible wrong charge sign assignment. When an electron traverses the inner detector, it might emit Bremsstrahlung. If the Bremsstrahlung photon converts into a electron positron pair, the track of the

positron can be confused or incorporated into the track of the incident electron, which can lead to a wrong charge assignment. This effect increases with absolute pseudorapidity, because the amount of material traversed in the inner detector increases. Further, the curvature decreases with increasing momentum, and therefore the intrinsic resolution of the curvature measurement dominates the uncertainty of the charge assignment at high momenta.

The charge mis-identification, as estimated in Monte Carlo based simulations [21], is shown in the left plot of Fig. 3.11 and amounts to approximately 0.7% (5%) for electrons with a transverse momentum of 100 GeV (1000 GeV). The right plot of Fig. 3.11 shows the charge mis-identification probability as a function of the absolute pseudorapidity for electrons with a transverse momentum of 2000 GeV. It varies by a factor of approximately 5 as a function of absolute pseudorapidity and is, as expected, largest for high absolute pseudorapities. Recent comparisons [83, 84] have shown a reasonable agreement between Monte Carlo based and data based estimates within the transverse momentum range considered[20].

[20] The highest transverse momentum bin evaluated started at 75 GeV.

4 Monte Carlo Simulation

Physical processes like the Drell-Yan process are simulated to predict the outcome of a measurement. This is performed on an event-by-event basis in three steps.

In the first step, the event generation, the four vector of each particle involved in a process is drawn by means of random number sampling according to the corresponding probability density. The latter is formed by the convolution of the matrix elements with a Parton Distribution Function (PDF), see Eq. 2.14. Optionally, additional phase space restrictions[1] are imposed. Due to the random number sampling method used, the generators are also referred to as Monte Carlo generators. By generating a large number of events, smooth spectra, e.g. mass distributions, can be simulated. These results, without any detector simulation performed, are referred to as generator level results.

The second step is the detector simulation, which is performed using GEANT4 [85]. It simulates the interactions of the final state particles with the detector, e.g. how electrons interact with the material of the tracking system and the calorimeters. The result of the detector simulation is stored in a format that is compatible to the format used for recorded data. Therefore the same reconstruction algorithms are used as for data in the third step, the reconstruction step, which was already discribed in Section 3.3. In contrast to simulations on truth level, simulated data on reconstruction level, that is after step three, always include the detector simulation on top of the event generation step, which includes effects like electron energy losses due to Bremsstrahlung or the finite detector energy resolution.

In the following, a brief introduction of the used Monte Carlo generators and of GEANT4 will be given, and the data sets generated for this analysis, called samples, will be introduced.

4.1 Generators

There are several different generators available. Each of them has strengths and weaknesses in describing different processes. The main working-horse is PYTHIA [86], but for certain processes it turned out that other generators describe data better. Table 4.1 shows which generator was used for which process. In the following the generators and the reasons for their choice will be briefly discussed.

PYTHIA, like HERWIG [87], is a general purpose generator. The matrix element is implemented in LO, but additional radiations in the initial and final state are incorporated. E.g., if a gluon is emitted, it can split up into quarks which cannot exist unbound and will form hadrons. Additional real photon radiation is incorporated by using PHOTOS [58]. ALPGEN [88] follows, in principle, also this concept, but it uses explicit LO matrix

[1] Filter requirements can be applied, e.g., final state particles are required to be produced within the sensitive regions of the detector.

Table 4.1: The simulated processes, the corresponding generator and its matrix element order are listed.

Process	Generator	Matrix element order in α_S
$pp \to Z/\gamma^* + X$	Pythia	LO
$pp \to Z/\gamma^* + X$	MC@NLO	NLO
$pp \to WW + X, WZ + X, ZZ + X$	Herwig	LO
$pp \to t\bar{t} + X$	MC@NLO	NLO
$pp \to W + jets + X$	Alpgen	LO

element calculations for the production of W or Z bosons in association with n jets[2] for $n \in [0..5]$.

MC@NLO [89], on the other hand, uses NLO matrix elements in α_S, which allows a more precise description. The use of generators with higher than LO matrix elements would be ideal. However, the NLO or even NNLO description of processes involves numerous Feynman diagrams that contribute to the cross-section. Therefore these calculations and their implementation requires much more effort. Besides that, the overlap between radiations considered in the matrix element and in the showering, that is radiations applied to the colored particles generated by the matrix element, is larger and therefore more difficult to handle. In general, this also increases the time needed to generate events, but with today's computers this becomes feasible for NLO generators.

Furthermore, new generators also need to be tuned and adapted in order to describe the observed data. For the 2011 data set, just a few processes were generated and validated with NLO generators, while the ATLAS Monte Carlo production for the data taken in 2012 uses almost exclusively NLO matrix element generators.

For kinematic distributions of final state particles in a process that is calculated or simulated with a matrix element at finite order, the shape can deviate from the shape of distributions produced at the next-higher order. Since thee calculations are performed in a perturbation series, the deviations should become on average smaller at higher orders. Distributions, e.g. produced with LO or NLO generators, can be corrected for in two ways, a dedicated reweighting via k-factors and/or the use of special PDFs. For the LO matrix element generators, the MRSTMCal[3] PDF [90], is used. This PDF is constructed such that it mimics the shapes of distributions as derived from NLO calculations, but can be used consistently in a LO generator.

The normalization in terms of cross-section, however, needs to be corrected by so-called k-factors, defined as the ratio

$$k = \frac{\sigma_{\text{higher order}}}{\sigma_{\text{generator level order}}}, \tag{4.1}$$

where higher order is either NLO or NNLO depending on the highest order calculations available for each process[4]. Besides for the normalization, k-factors can also be used to

[2]The exact requirement is that a W boson is produced in association with n partons, which have $p_T > 20\,\text{GeV}$. Further details can be found in Section 6.5.1, where this background is discussed.

[3]This PDF is also referred to as LO**

[4]The phase space considered in the theoretical calculations needs to match the one for the Monte Carlo

predict more accurate distributions of observables, if the k-factors are calculated as a function of one or multiple of these observables. For the dominant background in this analysis, the Drell-Yan process, the k-factors are binned in the invariant mass of the Z/γ^* exchange particle, whereas for the other processes, the k-factors are a single number, which is equivalent to scaling to the best known cross-section.

Each Monte Carlo sample used in this analysis is listed together with its cross-section and the number of events generated in the Appendix in Table A.2 to Table A.6. For several processes, there are Monte Carlo samples binned in mass. The details, how these have to be combined, will be given in the discussion of this background (see Chapter 6) or signal (see Section 8.2).

For the 2011 data set, the Drell-Yan process was simulated with high statistical accuracy using Pythia. Nevertheless, there exist also Drell-Yan Monte Carlo samples generated with MC@NLO, but they contain only a small fraction of the events generated with Pythia, typically 20%, and there are no MC@NLO samples available for masses above 2 TeV. Therefore these samples cannot be used for the main analysis, but are used for only one cross-check performed in Section 6.5.2.

In general, each Monte Carlo sample is scaled to the luminosity observed in data, L_{data}, the following way:

$$s = \frac{L_{data}}{L_{MC}} = L_{data}\frac{\sigma B}{N}, \tag{4.2}$$

where s is the scale factor, L_{MC} the integrated luminosity of the Monte Carlo sample, N the number of events generated with a given cross-section times branching ratio, σB.

However, there is one Monte Carlo sample that behaves differently due to its modified cross-section, namely the so-called flat SSM Z' sample. It has been generated with a modified, approximately flat cross-section in the mass range of 100 GeV to a few TeV. This allows to reweight the sample to any desired SSM Z' pole mass, which is described in Section 8.2.

Furthermore, this Monte Carlo sample contains a large number of simulated electrons with high E_T and is therefore used for several Monte Carlo studies. There is no bias in using this sample to study SM electron properties, as electron properties do not depend on their mother particle as soon as the electron's 4-momentum is fixed. Besides that, the electron 4-momenta are quite close to those from the SM Drell-Yan process, because the SSM Z' has a spin of one and SM couplings.

One remark must be made on the Pythia Drell-Yan sample starting at a mass of 70 GeV. The cross-section of this sample, calculated by applying k-factors for the QCD and electroweak corrections, is 3% below the cross-section calculated at NNLO, which is 989 nB. The uncertainty of the k-factors, approximately 5%, covers the discrepancy. Nevertheless, this difference is being investigated[5], but not solved yet. Therefore the k-factors were used as they are, which is identical to the choice taken in the ATLAS dilepton resonance search [24].

sample.

[5]The most likely reason for this discrepancy is the fact that the k-factors were derived by comparing to the LO predictions of the corresponding program (horace or phozpr), but not to the Pythia prediction directly. Slightly different LO predictions of these programs, e.g., due to different definitions of what is included at LO and what not or due to the tuning of Pythia, might explain the effect.

4.2 GEANT

GEANT4 [85] is a powerful software toolkit to simulate the complex interactions of particles with matter, e.g. in the ATLAS detector. For this purpose, a detailed model of the ATLAS detector is implemented that includes each geometric detail of the structure, the materials used and their aggregate state as well as electric and magnetic fields. It is interfaced with the ATLAS software, and the propagation of each particle generated in a Monte Carlo event is thoroughly simulated. Furthermore, the numerous additionally produced particles, e.g. the particles produced in an em. shower induced by an electron traversing the calorimeters, are also tracked and simulated. The result of this simulation step is a record of "hits", which contains the information about of the amount of energy deposited in which part of the detector at which time.

In a second step, the response of the active detector components to the "hits" is simulated, e.g. the analogue signal of a calorimeter cell in response to the ionization signature of an electron as well as its digitization. Thereby, calibrations, dead channels etc. are taken into account to reproduce the data taking conditions as exactly as possible, see also Section 5.2.1.

Due to the large number of calculations performed, the typical time for the GEANT4 "hit" simulation of one event of the process[6] $pp \to W(\to e\nu) + X$ amounts to 19 min on average, whereas the digitization and the reconstruction steps take on average only 24 s and 8 s, respectively, [91]. The time needed for the event generation with PYTHIA itself is negligible, it amounts to 79 ms. In order to accelerate the event simulation without loosing a significant amount of accuracy, parts of the simulation, e.g. parts of the showering in the calorimeters or the digitization of detector responses, are parametrized. Besides that, large signal libraries are generated once and used repeatedly for further event simulation.

The output format of the detector simulation is transformed such that it is compatible with the format of the data. Therefore the same reconstruction algorithms can be applied to data and simulated events. Further details on the ATLAS detector simulation can be found in [91].

4.3 Pile-up Treatment

Due to the high luminosity of the LHC bunches, on average more than one scattering process occurs per bunch crossing. Typically only one of these scatters is a hard scatter, which produces particles with significant transverse momentum, while the other process are typically soft scatters producing particles in the range of O(100 MeV) and below[7] [92]. However, though with a significantly lower probability, also particles with momenta in the GeV region are produced. These additional soft scatters are referred to as pile-up and are studied in dedicated ATLAS analyses [92, 93]. Because of contributions from non-perturbative QCD, pile-up cannot be exactly predicted. To reproduce the measurements of pile-up, the PYTHIA generator is tuned such that it describes these pile-up data. With these settings, a large library of pile-up events is generated and mixed together with the hard scatter generated for the process of actual interest during the hit phase of the GEANT4 simulation [91].

Each Monte Carlo sample used was generated using pile-up that matches the data

[6] The numbers are averaged over the contributions of negatively and positively charged W bosons.
[7] ATLAS is not sensitive to tracks below approximately 100 MeV.

conditions rather well. Additional fine tuning was performed with a dedicated reweighting procedure to match the average number of (pile-up) interactions on an event-by-event basis in Monte Carlo to data. This procedure is described in Section 5.2.1.

5 Event Selection

In this chapter, the data set analysis in this thesis will be introduced. Furthermore, the cuts used to select the di-electron signal will be described and their impact on selected distributions will be discussed. For this purpose, data distributions will be compared to distributions derived from Drell-Yan Monte Carlo, because the Drell-Yan process is the major source of pairs of electrons in the mass range around the Z boson pole mass. The agreement between the data and the simulated prediction needs to be improved by applying calibrations and corrections. They will be discussed in the second part of this chapter.

5.1 Selection

Data Set and Trigger

Events in data are assigned to so-called streams depending on the triggers they originate from, e.g. all events that pass at least one photon or electron trigger are assigned to the stream used in this analysis, the so-called EGamma stream. To select data that have been taken under good beam quality conditions and detector conditions with respect to relevant detector components, a so called "good runs list" is used. In particular, a certain quality level is required for the inner detector, the central calorimeters[1], and the proton bunches in the LHC beam as recommended by the ATLAS EGamma performance group for electron-based analyses. The same good runs list[2] is used as for the corresponding ATLAS dielectron resonance search [24]. For disk space reasons, only a preselection of data, called "skim", is used. It requires at least one electron candidate with $E_T > 23\,\text{GeV}$ and another one with $E_T > 15\,\text{GeV}$. Additionally the signal trigger (see below) is required to be online in the selected data set. After application of these requirements, $4.9\,\text{fb}^{-1}$ out of the totally recorded $5.25\,\text{fb}^{-1}$ are available[3].

The EF_2g20_loose trigger (see Section 3.2.6) is chosen to select events that might contain pairs of interesting electron candidates. It requires two localized energy deposits, each of them with $E_T > 20\,\text{GeV}$, in the central em. calorimeters. Furthermore the two candidates have to satisfy the loose electron identification criteria, which include amongst others the requirement that the shower shape is compatible with the signature of an electron or photon[4].

[1] On top of the good runs list, there is a per event information available that flags so-called noise bursts in the calorimeter. It rejects 0.7% of the total events but none that passes the full selection.

[2] The exact name of the GRL is data11_7TeV.periodAllYear_DetStatus-v36-pro10_CoolRunQuery-00-04-08_Eg_standard.xml and all data listed there are used.

[3] The integrated luminosity does not depend on the E_T cut applied, but logically it is applied before the trigger requirement.

[4] The loose identification criteria are identical for electrons and photons since they are only based on shower shapes in the calorimeters. The trigger itself does not require a track pointing to the calorimeter energy deposit and therefore selects electrons and photons.

Phase Space and Identification Level Selection

To match this data taking requirements in the selection used in this analysis, only pairs of electron candidates that satisfy at least the trigger requirements are considered. Therefore they have to satisfy the loose identification level, which implicitly requires $|\eta| < 2.47$. Explicitly, the calorimeter transition region between barrel and end-cap ($1.32 < |\eta| < 1.57$), which is poorly instrumented, is vetoed. Furthermore, each electron candidate is required to have $E_T > 25\,\text{GeV}$. The trigger does not work fully efficient for electron candidates with an E_T at the trigger threshold, therefore the higher value of E_T is chosen as recommended by the EGamma performance group. This preselection is passed by all events at the current cut stage.

For all remaining candidate pairs the invariant mass M_{ee} is calculated and required to satisfy $M_{ee} > 70\,\text{GeV}$. The mass distribution at lower masses is strongly effected by a kinematic turn-on due to the E_T requirements[5] and is therefore not considered in this high-mass focused analysis. In the following, additional cuts on top of this base selection will be introduced and discussed, and a qualitative estimate of the real electron efficiency at certain cut stages will be evaluated.

To show the real electron efficiency of the selection, a mass window close to the Z boson pole mass (70 GeV to 110 GeV) is chosen. With an appropriate selection, it is possible to select a "pure" sample in this "benchmark" region that consists of nearly 100% electron pairs from Z boson decays. This will be shown in the next Chapter or see, e.g., Ref. [94]. To illustrate the purity of the selected data at the trigger stage, the number of events selected in data is compared to the number of events predicted using the simulated Drell-Yan samples. For this purpose, the same selection at each cutstage as in data is applied to the electron pair that originates from the Z boson decay[6]. The prediction derived from the simulation is scaled to the same luminosity as in data according to Eq. 4.2.

Fig. 5.1 shows the mass distribution after the base selection on the left plot and the E_T distribution of the single electrons on the right side. In both distributions one can see that the shape in data follows already roughly the shape of the predicted Drell-Yan distribution, although in the E_T distribution the impurity is dominant at low values of E_T. The purity amounts to approximately 76% in the window around the pole mass after this basic selection. On top of the cuts that ensure consistency with the trigger, stricter requirements on the electron identification are imposed. Both electron candidates are required to satisfy the medium identification level and have a pixel hit in the innermost layer of the tracking system, the b-layer, to veto photon conversions in the tracking system. At this point the purity amounts to approximately 96%. As will be shown in Section 5.2, there are corrections for data and Monte Carlo simulation on the percent level, therefore conclusions from further comparisons can only be drawn after the corrections are introduced.

The electron pairs from Z boson decays as well as from considered Z' bosons have an opposite electrical charge sign, that is are an electron positron pair. In contrast, the sign of the charge of any two jets[7], which mimic electrons can be considered as uncorrelated. Therefore these contributions could be suppressed with an opposite charge requirement.

[5] For electrons produced in the Drell-Yan process, the average E_T is typically close to half of the mass of the exchange boson. Therefore the electron E_T threshold should be below half the M_{ee} threshold to avoid this kinematical turn-on.

[6] To ensure this, the truth information of the event record of the decay is used.

[7] Also in W+jets events, where the W boson decays into an electron and a neutrino, there is no significant correlation between the sign of the charge of the jet and the electron.

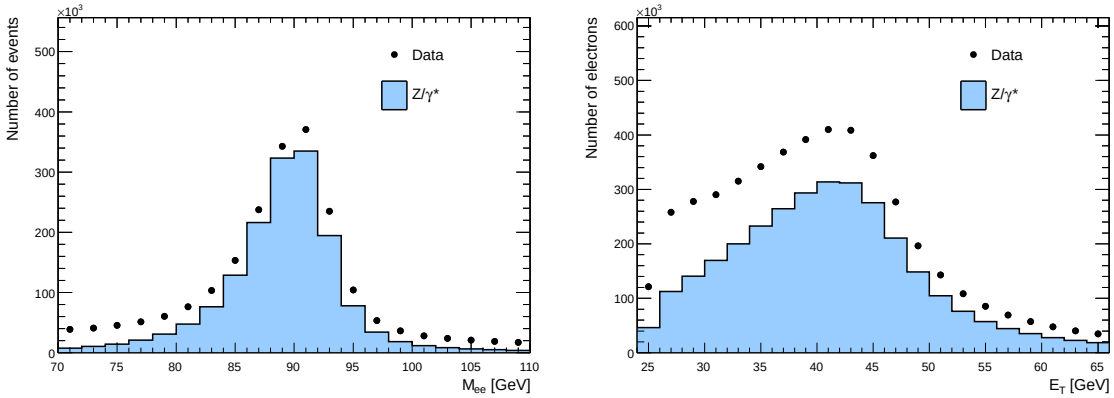

Figure 5.1: The electron candidate pair mass distribution is shown on the left side with trigger, $E_T > 25\,\text{GeV}$ and loose electron identification requirements applied. On the right plot, the individual E_T of both electron candidates is shown with the same cuts applied as in the previous plot. Results from data are shown in black, whereas the simulated Drell-Yan contribution, scaled to the integrated luminosity of the data, is shown in blue. Only electron pairs with a mass in the window from 70 GeV to 110 GeV are considered for the plots.

This has been studied in [53] and due to the increased charge mis-identification probability at high energies (see Section 3.3.2), the acceptance for a SSM Z' with a pole mass of 2 TeV would be reduced by approximately 7%. Therefore this cut was not considered further.

Isolation

The left (right) plot of Fig. 5.2 shows the leading (subleading) E_T distribution with the so far described cuts applied, but no isolation requirement imposed. There is a noticeable difference in the shape of the two distributions: the leading distribution follows the form of a rather symmetric peak with a maximum at half the Z pole mass, while the subleading distribution has a asymmetric form with a significantly larger population at lower E_T. The reason for this shape is that the electron with the lower E_T has a high chance to be the electron that has emitted Bremsstrahlung, if one of the two electrons emitted Bremsstrahlung. This difference is important for the correct calculation of the isolation variable. The value of the isolation corresponds to the energy deposited in a cone around the electron core region, see Section 3.3.2. Electrons with a isolation value below a fixed threshold of 7 GeV pass the cut. This isolation cut efficiency therefore decreases with increasing transverse momenta. However, a correction was derived, which approximately cancels the decrease in efficiency. The details of the corrections and efficiencies will be discussed in Section 5.2.4. As result only the leading electron is required to be isolated, because the efficiency correction for the subleading electron has some limitations at high E_T and would reject too many signal events.

Highest E_T Pair Selection

Out of the 1,277,106 events in data that pass the selection described, 331 events remain, which have more than one pair per event satisfying all cuts described so far. Out of these 331 events, 325 times three pairs (due to three electron candidates) were observed and

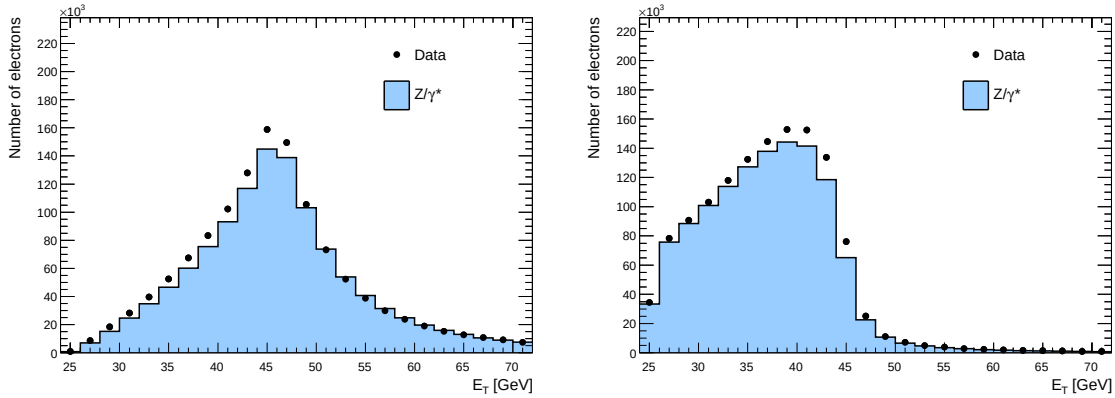

Figure 5.2: The leading (subleading) E_T distribution on the left (right) side is shown with trigger, $E_T > 25\,\text{GeV}$, medium electron identification requirements and photon conversion veto applied. Results from data are shown in black, whereas the simulated Drell-Yan contribution, scaled to the integrated luminosity of the data, is shown in blue. Only electron pairs with a mass in the window from 70 GeV to 110 GeV are considered for the plots.

5 times six pairs (due to four electron candidates). In those rare cases, the pair with the highest sum[8] of the individual electron candidate E_T is taken. Table 5.1 shows the cutflow table as derived from data[9]. It summarizes the cuts applied and shows the event yield as well as the cut survival fraction of each cut with respect to its precessor and with respect to all events triggered. After good runs list, skim, which includes already E_T cuts, and trigger about 1.5% of the events in the EGamma stream remain. Out of these approximately 25% pass the full selection.

Summary

The resulting mass distribution with all cuts applied is shown in the top left plot of Fig. 5.3. Here the imperfect Z boson resonance lineshape is visible in the Monte Carlo simulation. The p_T distribution of the pair, that is the p_T^Z shown in the top right plot shows a bad agreement at low values of p_T^Z. The η (bottom left) and ϕ (bottom right) distributions in data seem to agree already rather well with the expectation besides a global offset, which is visible in η and ϕ, and the inefficiency around $\phi \approx -0.8$. The second part of this chapter will deal with the calibrations and corrections needed to improve the quality of the distributions derived from data and the simulation. Especially important are the energy calibration for data and the Z boson p_T modeling in the simulation.

[8] E_T is always considered as a signless quantity, therefore this sum adds the absolute values of the transverse momenta.

[9] No electron energy or isolation calibration has been applied.

Table 5.1: The cutflow derived from data, where no electron energy and isolation calibration has been applied, is shown. The third column shows the survival fraction of the cut with respect to the previous one while the survival fraction in the fourth column is calculated with respect to all events triggered. If a survival fraction is not defined, it is denoted by an N/A for not applicable. The numbers of the last cut are denoted by *, because this cut reduces the number of pairs per event to one, but does not reject events. In 331 events, the number of pairs were reduced to one. The first line labeled "EGamma stream" refers to all events taken, where at least one electron or photon trigger has fired, which is the basis data set for all electron analyses.

Cut name	Number of events after cut	Local survival fraction	Total survival fraction
EGamma stream	342,727,749	N/A	N/A
Good runs list + skim	86,839,599	25.3 %	N/A
Trigger	4,935,886	5.7 %	N/A
Loose electron identification	4,370,554	88.5 %	88.5 %
Exclude barrel endcap transition	3,789,825	86.7 %	76.8 %
Electron $E_T > 25\,\mathrm{GeV}$	2,347,103	61.9 %	47.6 %
Electron pair mass $> 70\,\mathrm{GeV}$	2,078,562	88.6 %	42.1 %
Medium electron identification	1,360,679	65.5 %	27.6 %
Electron b-layer hit	1,285,868	94.5 %	26.1 %
Leading electron isolation $< 7\,\mathrm{GeV}$	1,277,106	99.3 %	25.9 %
Select highest E_T electron pair	1,277,106*	100.0 %*	25.9 %*

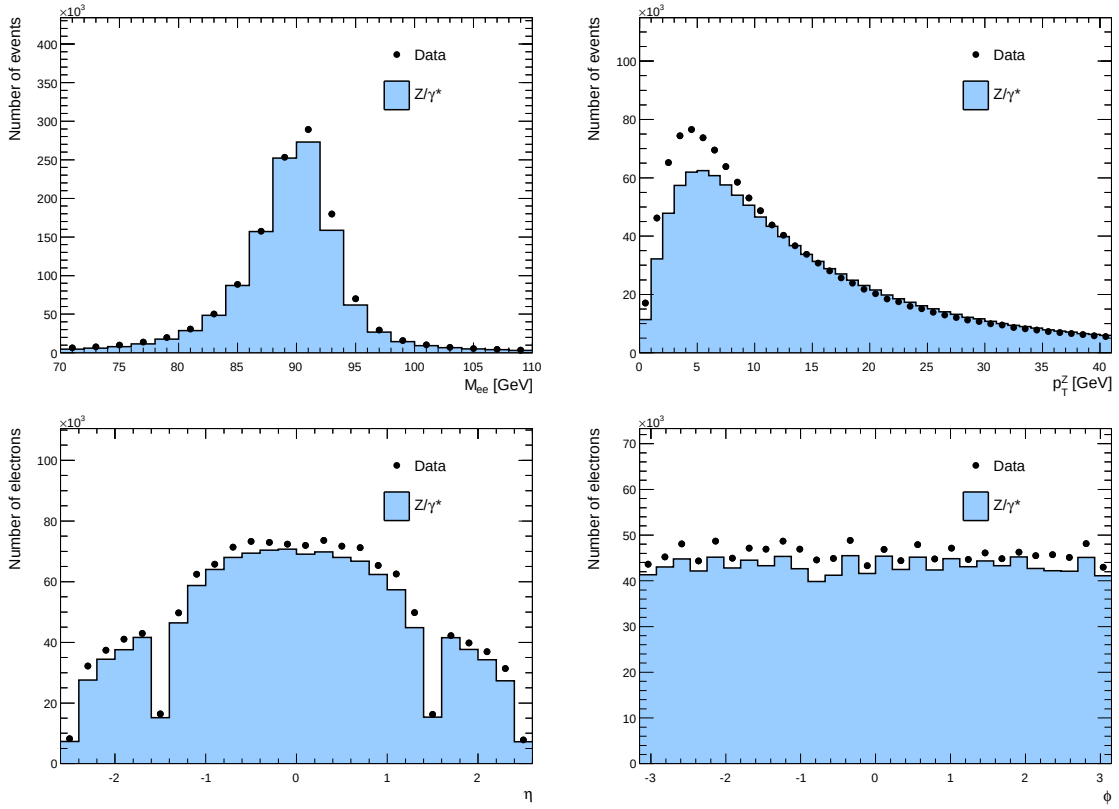

Figure 5.3: The top left plot shows the mass distribution and the top right one p_T^Z distribution while the bottom left (right) plot shows the η (ϕ) distribution of the leading electron. All four distributions are derived with all cuts but no corrections applied. In each plot, results from data are shown in black, whereas the simulated Drell-Yan contribution, scaled to the integrated luminosity of the data, is shown in blue. Only electron pairs with a mass in the window from 70 GeV to 110 GeV are considered for the plots.

5.2 Efficiencies and Corrections for Monte Carlo and Data

In this section, calibrations and corrections to be applied to data and the simulated samples will be discussed. For data, the energy measurement in the calorimeters and the isolation calculations need to be calibrated. Additionally, the readout modules for certain calorimeter regions were defect for a limited time, which is taken into account by the ATLAS reconstruction software.

Those data-taking conditions have to be reproduced exactly in the simulation which will be discussed in the next subsection. The description of Z bosons produced with a low p_T does not match data very well and needs to be corrected. Also the efficiencies to trigger, reconstruct and identify electrons need to be studied in data and simulation. Differences are accounted for by efficiency scale factors that have been derived in an iterative process by the EGamma performance group [95]. Further information, beyond what will be discussed with respect to scale factors and efficiencies in the following sections, can be found in the Appendix in Appendix A.1 and Appendix A.2.

In the following, the calibrations and corrections will be discussed individually (if possible) with all other corrections switched off. At the end of the section, a comparison of data and the Drell-Yan prediction around the Z boson pole mass with all corrections applied will be shown. However this comparison will not be the final word in this respect, because the contributions from other physics processes are neglected so far. They will be discussed in the next chapter.

5.2.1 Pile-up and Calorimeter Corrections

Data was taken in 2011 in so-called "periods" during which the data taking conditions were approximately constant. These data periods can be merged into four larger blocks in which the conditions are still very similar. They are listed in Table 5.2. To reproduce these four different sets of detector and machine conditions, one representative run for each block was chosen[10] and its conditions were used to simulate the Monte Carlo samples with. This is a good approximation, which can be improved by a reweighting procedure described in the following.

Pile-up Reweighting

The average number of pile-up interactions for the four different blocks are shown in the left plot of Fig. 5.4. The comparison of the average number of pile-up interactions as simulated and as measured in data can be found in the right plot and shows a good agreement. Nevertheless a reweighting of the pile-up distribution in each simulated sample to the one measured in data is performed to achieve the best possible agreement.

The reweighting is performed by applying weights $w(\mu)$ to each simulated event as follows

$$w(\mu) = \frac{p_{data}(\mu)}{p_{sim}(\mu)}, \tag{5.1}$$

where μ is the number of average interactions per bunch crossing. For data. $p_{data}(\mu)$, and for the simulation $p_{sim}(\mu)$ denote the average number of interactions per bunch crossing scaled such that the integral over the distribution amounts to unity. This reweighting preserves the number of events predicted in the Monte Carlo simulation.

Defect FEB Treatment

The second important feature that needs to be reproduced in the simulation is the failure of a few calorimeter readout modules, so-called Front-End Boards (FEBs). In the second data block, four FEBs which are responsible for the readout of parts of the second layer of the electromagnetic calorimeter were defect. Since typically 80% of the electron energy is deposited in this layer, electrons cannot be reconstructed any more with those cells' energy information being unknown. Therefore they are masked out during the reconstruction step of the simulation and additionally all electrons that are reconstructed close to that region are vetoed. Fig. 5.5 shows the electron distribution in η and ϕ derived from the simulated Drell-Yan samples for the first and second block. In the distribution for the second block, the masked region ($0 < \eta < 1.475$ and $-0.791 < \phi < -0.595$) can be clearly seen. As a result of the pair selection, the corresponding electron partner with a typical $\Delta\phi \approx \pi$ is

[10] These four runs were selected by the ATLAS collaboration and used for all regular Monte Carlo productions for the data set from 2011.

Table 5.2: The fractions of data taken in each of the four blocks of data taking are listed. Additionally the information about the fraction of events simulated with the corresponding conditions in the Monte Carlo samples are listed. The last column states the status of the calorimeter readout modules.

Period	fraction of data	fraction in simulation	FEB conditions
B-D	3.7%	3.3%	all OK
E-H	20.2%	17.8%	6 defect (4 second layer, 2 third layer)
I-K	25.0%	24.2%	2 defect (both third layer)
L-M	51.1%	54.7%	2 defect (both third layer)

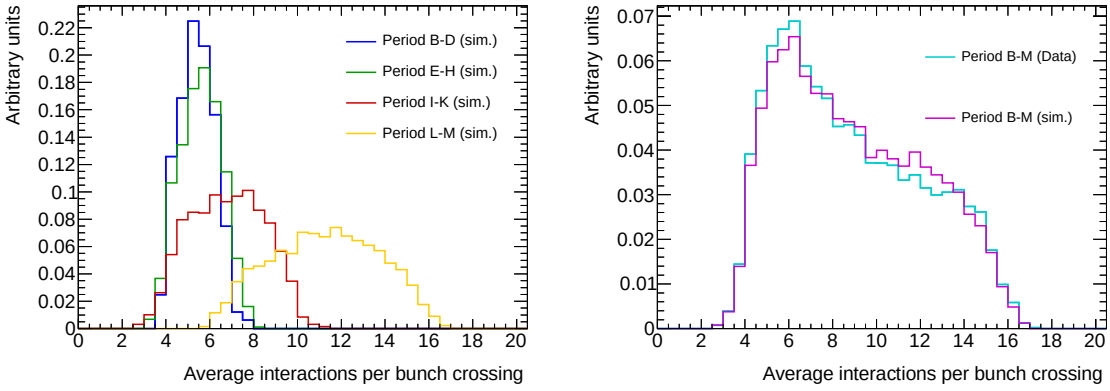

Figure 5.4: The left plot shows the average number of interactions per bunch crossing for the four different blocks of data periods as simulated in the Monte Carlo samples. The right plot shows the average number of interactions per bunch crossing for the full dataset as measured in cyan and as simulated (before reweighting) in magenta. All distributions are normalized to unity.

also vetoed which leads to the band of low population at $\phi \approx 2.5$. The defect FEBs of the third layer are treated differently. They were switched off during the reconstruction stage of the simulated samples to match the conditions in data, but there is no electron veto, if an electron is reconstructed close to it. The reason is that electrons with an E_T of 600 GeV typically[11] deposit at most 5% and on average below 2% of their energy in the third layer (see Fig. A.9 in the Appendix), so the uncertainty introduced on the energy measurement is small. However the acceptance loss, if the veto was imposed on the electron candidates predicted from Drell-Yan decays with $1500\,\text{GeV} < M_{Z/\gamma^*} < 1750\,\text{GeV}$, amounts to approximately 3.5%. Therefore it has been decided to introduce no veto in the third layer, which is the same decision as taken in the ATLAS dilepton resonance search [24].

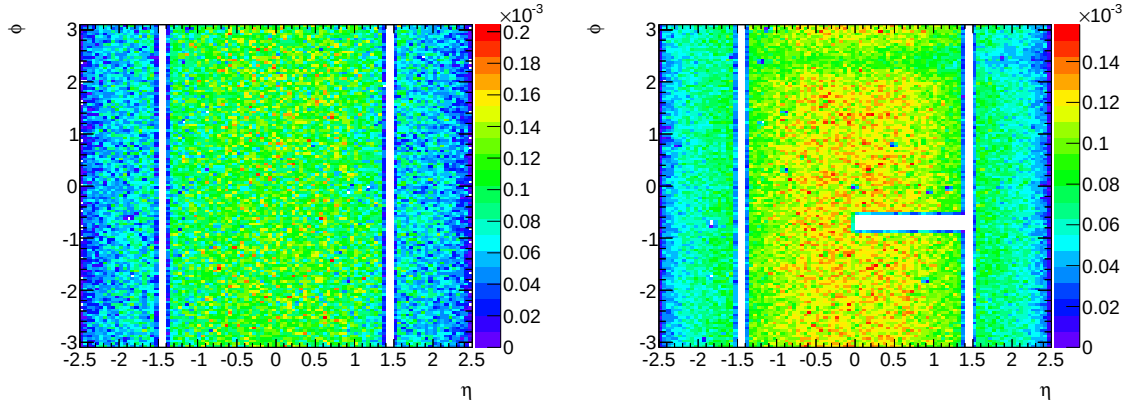

Figure 5.5: The two plots shows subsets of the two-dimensional η,ϕ distribution with all cuts applied as simulated for the Drell-Yan process. The left (right) plot shows the subset of the distribution that corresponds to the data taking conditions in period B-D (E-H). Both plots are normalized to unity.

5.2.2 Z Boson Transverse Momentum Reweighting

The prediction of Z boson production with p_T^Z of a few GeV cannot be calculated pertubatively. Instead Monte Carlo generators use models which need to be tuned to the distribution measured in data to get a reasonable prediction. In the tune used for the simulation to describe the data taken in 2010 [96], the ATLAS-wide tune for PYTHIA was more successful to describe the p_T^Z measured in data than the one performed for 2011 [97]. Therefore a reweighting of the p_T^Z distribution of the Drell-Yan samples used to describe the data of this analysis to the corresponding p_T^Z distribution simulated in the 2010 Drell-Yan samples was performed on truth level. The reweighting procedure takes into account that the p_T^Z distribution is a function of the mass of the boson, which is calculated as the invariant mass of the two daughter electrons on generator level before FSR. It is the same procedure as used in the ATLAS dilepton resonance search and has been developed by the EGamma performance group.

The result of the reweighting procedure can be seen in Fig. 5.6 where the p_T^Z distribution is shown after the full selection for masses between 70 GeV and 120 GeV with and without the reweighting applied. The distribution with reweighting gives a significantly better description of the data, although it is still not perfect. Since none of the other corrections[12] are applied in the figure, the agreement is not expected to be perfect. The comparison with all corrections applied will be shown at the end of this chapter. Comparisons including electron candidates from other processes than only the Drell-Yan process can be found in Section 6.6, when data is compared to the final background expectation.

5.2.3 Data Energy Calibration

The electron energy scale in data is determined by comparing the measured Z boson mass in data to the one predicted by the simulation. The mass can be expressed as $M = \sqrt{2E_1E_2(1-\cos(\theta_{12}))}$, where E_1 and E_2 are the energies of the two electrons and

[11] The highest observed E_T were around 600 GeV, therefore this is a worst case estimation.

[12] For example, applying the data energy scale calibration or the E_T and η dependent electron identification efficiency scale factors will alter the shown distributions.

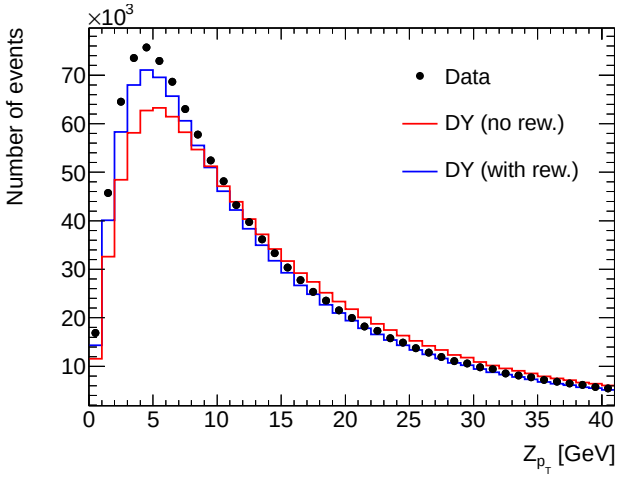

Figure 5.6: The p_T of the the electron pair in data is shown in black, and compared to the p_T^Z as predicted in the Drell-Yan simulation with (without) the p_T^Z reweighting applied in blue (red). The Drell-Yan prediction is scaled to the integrated data luminosity of $4.9\,\mathrm{fb}^{-1}$.

θ_{12} is the angle between the two electrons measured in the tracking system. The latter measurement can be assumed to have a negligible uncertainty compared to the electron energy measurement. The actual calibration constant is introduced in the relation $E_{meas} = E_{true}(1+\alpha)$, where E_{meas} is the energy measured in data, E_{true} the predicted energy from the simulation and α the calibration constant. Combining those two formulas, the measured mass of a Z boson can be related to the energy of the two electrons and their calibration constants given a proper selection. The methods used in ATLAS to perform the calibration are described in detail in [98]. The result of this calibration as a function of η is shown in the left plot of Fig. 5.7. The largest correction amounts to 0.8%. The small corrections of the energy calibration are a result of multiple calibration iterations over the whole ATLAS data taking period. Furthermore, the current calibration constants are relative to the ones made in a previous iteration with the data set taken in 2010. This calibration has already been applied during data reconstruction of the data set taken in 2011.

The right plot of Fig. 5.7 shows the comparison of the Drell-Yan prediction (with reweighted p_T^Z) close to the Z boson pole mass compared to data (without and with the energy calibration applied). In the latter case, the main improvement lies in the better description of the falling edge of the Z resonance peak.

5.2.4 Isolation E_T and Pile-Up Corrections

The isolation definition used here has a dependence on the transverse momentum of the corresponding electron and on the number of pile-up interactions in the event. The higher the E_T of the electron, the broader the electron shower. Since the value of the isolation is defined as the energy deposited in a cone of size $\Delta R = 0.2$ minus the energy deposited in the fixed size electron window (3×7 or 5×5 in $\eta \times \phi$), this broadening of the shower is not taken into account.

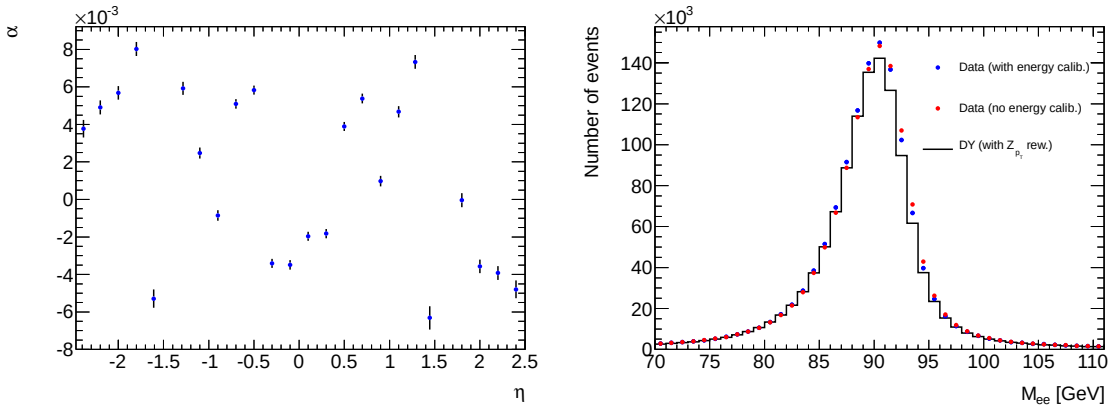

Figure 5.7: The left plot shows the energy scale calibration constant α as a function of η. On the right side, the Drell-Yan prediction close to the Z boson pole mass is compared to data with (in blue) and without (in red) the energy calibration applied.

Isolation Corrections

To make the value of the isolation variable independent of the electron E_T, the mean of the isolation distribution is calculated as a function of electron E_T up to 200 GeV. A linear dependence has been found and a linear function has been adapted via a χ^2 fit. It has been verified that the RMS of the isolation distribution as a function of E_T is approximately constant. The same procedure has been performed as a function of the number of vertices (as a measure for the number of pile-up interactions per event) instead of E_T. A quadratic dependence has been found and also parametrized. In the following, the term isolation will always refer to the isolation corrected for its E_T and pile-up dependence.

The isolation corrections described have been derived by the EGamma performance group on data and are cross-checked using simulated Drell-Yan samples in the same kinematic range [53].

Isolation Efficiencies

Whereas the isolation corrections and efficiency scale factors have been derived for an electron E_T up to 200 GeV, electrons with an E_T of up to 600 GeV have been observed in this analysis. The quality of the E_T correction at high E_T was studied using the large SSM Z' Monte Carlo simulation. which contains simulated electrons with a reasonable yield up to an E_T of approximately 1000 GeV. For this study, the two reconstructed electrons[13] of the Z′ decay are considered after the full selection. This number of electron pairs N_{pass} (binned in η and E_T of the subleading electron) is divided by the number of electron pairs N_{all} with all but the isolation cut on the leading electron applied.

The resulting efficiency $\epsilon_{iso} = \frac{N_{pass}}{N_{all}}$ is shown in Fig. 5.8 as a function of the E_T of the subleading electron. Additionally the efficiency is shown for the case that N_{pass} is derived with the isolation requirement applied only to the subleading or to both electrons. The efficiency decreases as a function of E_T in the two η bins around the calorimeter barrel end-cap transition region (top right and bottom left plot), where the lateral energy leakage cannot be measured and corrected for as precise as in the fully instrumented parts of the

[13]Besides the isolation corrections themselves, no corrections or scales have been applied.

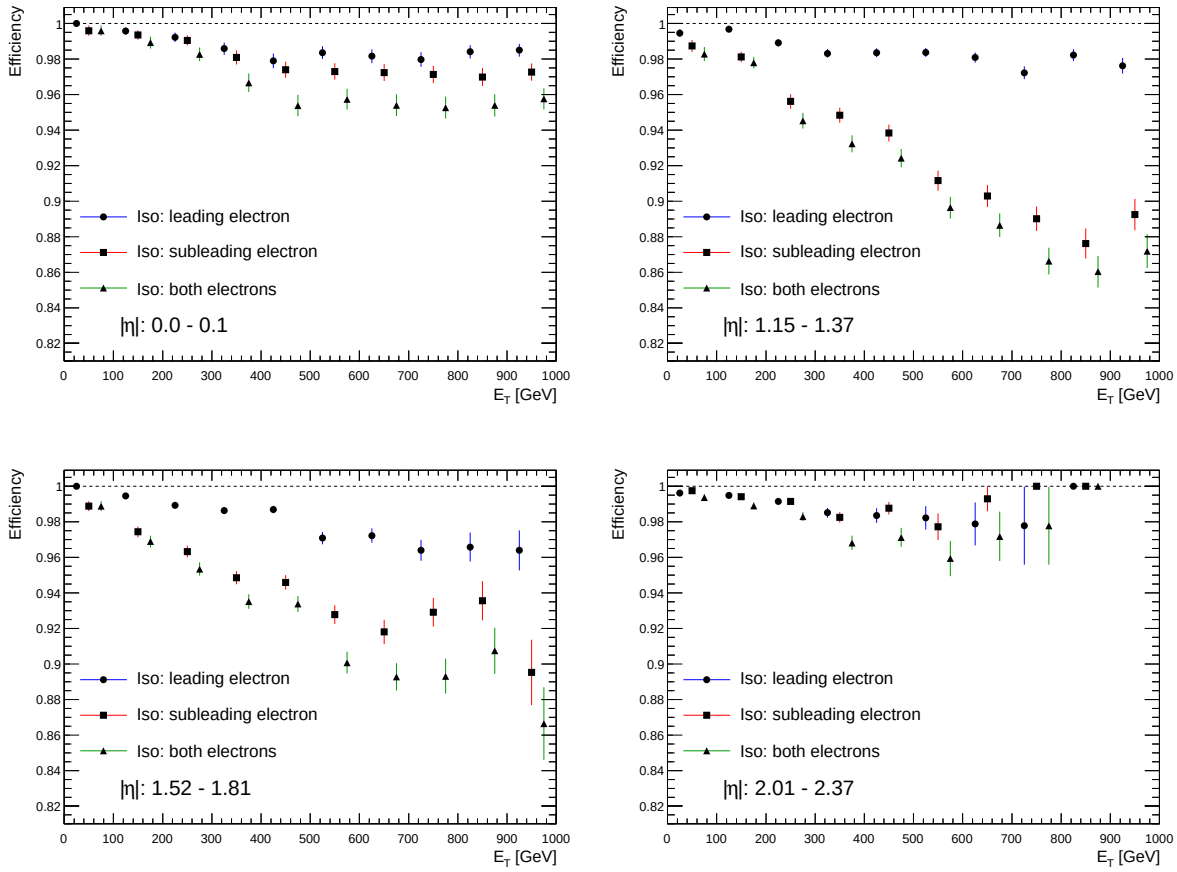

Figure 5.8: The isolation efficiency ϵ_{iso} is shown as a function of the subleading electron E_T in four of the nine bins in $|\eta|$, whereas the full set is shown in the Appendix in Fig. A.8. In blue the efficiency is shown in case that only the leading electron is required to be isolated, while in red the corresponding case for the subleading electron is shown. The case that both electrons are required to be isolated is shown in green. If an efficiency is exactly one, that is numerator and denominator are identical, binomial statistics do not predict a meaningful uncertainty. Therefore the uncertainty is set to zero. The number of pairs in those bins never exceeds three.

calorimeter. In not-interrupted calorimeter regions (top left and bottom right plot), the efficiency shows a weak dependence on E_T. In case only the leading electron is required to be isolated, the absolute efficiency ϵ_{iso} is significantly higher than in case that only the subleading electron is required to be isolated. If both electrons are required to be isolated, the resulting efficiency is the "product" (taking correlations into account) of the two efficiencies and therefore even lower.

This lead to the decision to apply the isolation only to the leading electron to avoid the efficiency loss as well as to minimize possible biases if the simulation does not describe the isolation in data well at high E_T. The appropriate corrections cannot be derived from data, because there are not enough events left after the tight selections needed in calibrations to guarantee the purity of the sample. Corrections derived from simulations are being studied, however no final results were available. Also corrections, which cannot be cross-checked with data, need to be used with care.

5.2.5 Reconstruction Efficiency

The efficiency or probability to reconstruct an electron, that is to reconstruct an energy cluster in the calorimeter with at least 2.5 GeV and a track pointing towards it within $|\Delta\eta| < 0.05$, is measured in data and in simulated Drell-Yan samples as a function of η. The ratio of these efficiencies is called the reconstruction scale factor and deviates no more than 2% from one. This measurement [53] has been performed by the EGamma performance group. The scale factor distributions can be found in the Appendix in Fig. A.1.

5.2.6 Identification Efficiency

The medium identification efficiency is defined as the efficiency of a reconstructed electron candidate to pass the medium identification cuts. The corresponding scale factor as a function of η and E_T deviates at most 2% from one. The scale factors were derived with an E_T range from 25 GeV to 45 GeV and cross-checks indicate no strong hints for deviations at higher E_T, where statistics are strongly limited[14]. This measurement [53] has been performed by the EGamma performance group and the scale factor distributions can be found in the Appendix in Fig. A.2.

Relative to this scale factor, the scale factor for the electron efficiency to pass the b-layer hit requirement and the efficiency to pass both the b-layer hit and the isolation requirement were derived for the ATLAS dilepton resonance search [53]. The latter scale factor concerning the b-layer hit requirement has been derived independently as a function of η and of E_T up to 80 GeV. The scale factor deviates from unity by at most 4% at large $|\eta|$ and at most by 2% as a function of E_T. The scale factor with the isolation requirement included differs by at most 0.5% from the scale factor without isolation. The scale factor distributions are shown in the Appendix in Fig. A.2 to Fig. A.3.

5.2.7 Trigger Efficiency

The trigger efficiency, that is the probability for an electron pair, which passes the full selection without looking at the trigger criterion, to pass the trigger criterion, is shown in Fig. 5.9. It has been derived using the flat Z' Monte Carlo and amounts to approximately 99% with no significant dependence on the electron pair mass.

The trigger efficiency in data and the corresponding scale factor have been derived for the ATLAS dilepton resonance search [53] separately as a function of η and E_T up to 100 GeV. In that context, it has been shown that the trigger efficiency derived for a trigger, which requires only one electron with the same threshold, can be used to describe the efficiency of the di-object trigger. This allows to derive scale factors with a higher statistical precision. The scale factor as a function of η (E_T) deviates no more than 1% (0.6%) from unity and is shown in the Appendix in Fig. A.5.

[14] These scale factors need to be derived from clean electron samples in data. The cleanest sources are electrons from W or Z boson decays close to the pole mass, therefore the reach in electron E_T is limited.

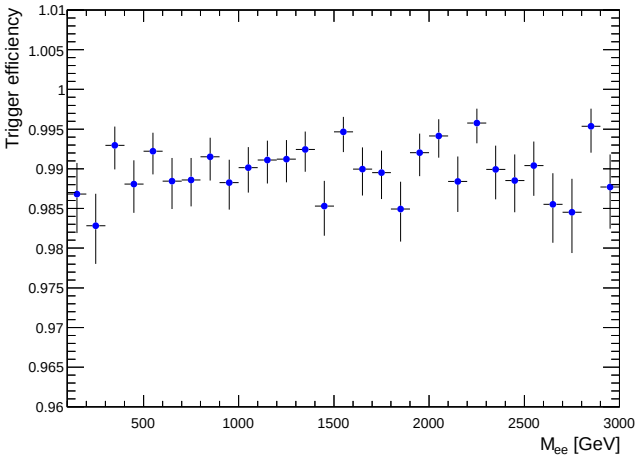

Figure 5.9: The trigger efficiency for an electron pair, which passes the full selection without looking at the trigger criterion, to pass the trigger criterion is shown as derived from Monte Carlo simulations.

5.2.8 Summary

The following comparisons of data with the Monte Carlo simulation contain all calibrations and corrections discussed in this section, but no background other than the Drell-Yan background[15].

The Drell-Yan prediction is scaled to the number of events in data in the considered mass range 70 GeV to 110 GeV. The corresponding scale factor of 1.05 is expected to be approximately 1.03 due to the k-factor, see Section 4.1, and agrees within the k-factor uncertainty of 4.5% and the luminosity uncertainty of 1.8% with the expectation.

The top left plot in Fig. 5.10 shows the mass distribution of the electron pair. The ratio between data and the Drell-Yan prediction differs by less than 5% from unity for masses below 105 GeV. The top right plot shows the p_T distribution of the electron pair. It indicates a good agreement between data and prediction for p_T above 5 GeV. Below, the difference of the ratio from unity increases up to 13%. This behavior is expected, since the p_T distribution of the Z boson is reweighted to the corresponding distribution as simulated for the 2010 data set, which also had this flaw. However the agreement is significantly better then without this reweighting as shown in Section 5.2.2.

The bottom left plot shows the η distribution of the leading electron and also indicates a good agreement between data and prediction. The same is true for the ϕ distribution of the leading electron shown in the bottom right figure with the exception that the region around $\phi \approx 0.9$, the region with the defect readout modules during a couple of periods, is not modeled perfectly. The reason is the approximation chosen, when the Monte Carlo samples were produced: Each of the four blocks of data periods are modeled by one representative run which results into a limited precision of this modeling. This effects also the ϕ distribution outside the $\phi \approx -1$ region, because the two electrons of a Z boson decay are typically back-to-back in ϕ. If one electron traverses the calorimeter in the effected ϕ region, the electron is vetoed and therefore the event is typically[16] rejected.

[15] Further background contributions will be discussed in the next chapter.

[16] There is a small probability that another particle is mis-reconstructed as good electron and this pair of one real and one fake electron passes the selection.

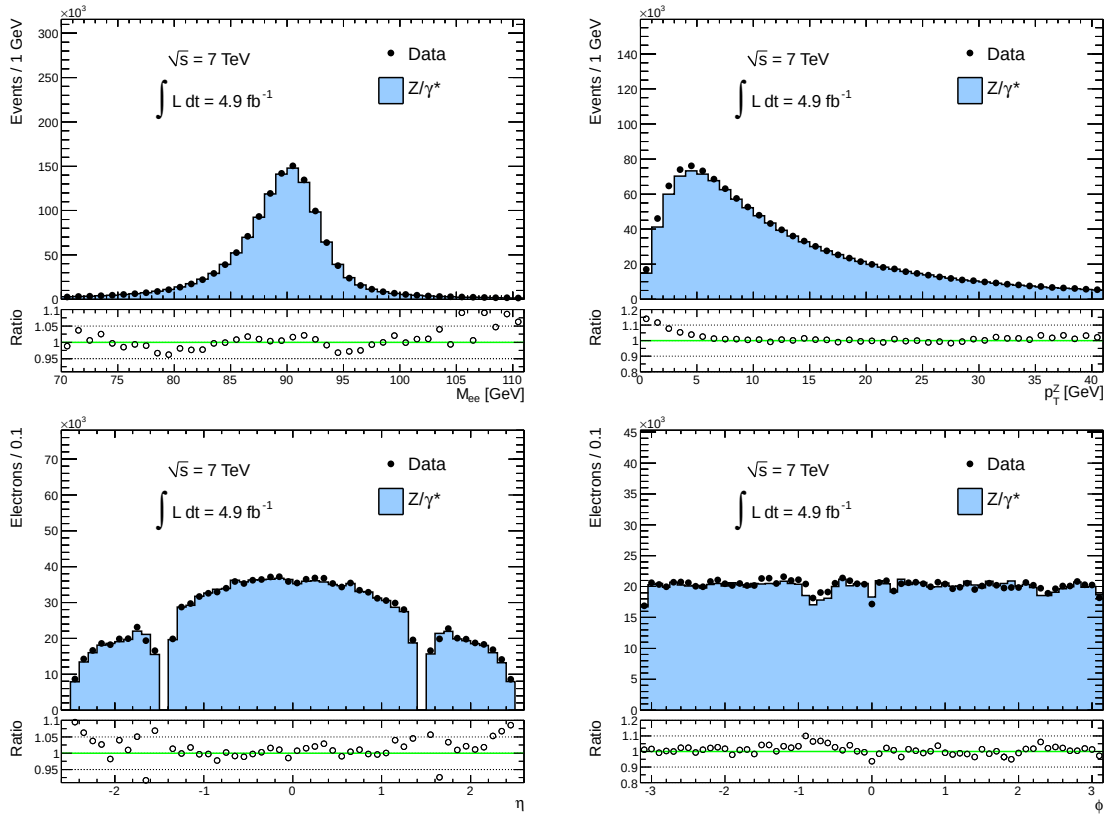

Figure 5.10: The distributions shown are restricted to pair masses between 70 GeV and 110 GeV. The Drell-Yan predictions are normalized to the number of data events in this mass window. The top left plot the measured mass distribution shown in black is compared to the Drell-Yan prediction shown in blue. The top right plot shows the p_T distribution of the electron pair and the bottom left (right) plot shows the leading electron η (ϕ) distribution. In the bottom panel, the ratio of the number of events observed in data over the number of events predicted is shown. Other background contributions, but from the Drell-Yan process are not included here.

This also results in an "mirrored" electron deficit in ϕ displaced by π. The same effects, but no additional features are visible in the corresponding η and ϕ distributions of the subleading electron, therefore these distributions are not shown here[17].

These predictions at low mass close to the Z pole mass will be extended to high mass in the next chapter. Here also contributions from other backgrounds than from the Drell-Yan process will be discussed.

[17]However, these distributions are shown with all backgrounds included at the end of Chapter 6.

6 Background Expectations

In the following, additional conventions used in this and the following chapters will be introduced. Then an overview of the background composition will be given, followed by a dicussion of the individual background contributions and their extrapolation to high masses.

All Monte Carlo and data results shown correspond to an integrated luminosity of $4.9\,\mathrm{fb}^{-1}$ and include all corrections described in Section 5.2. The electrical charge indices of, e.g., W bosons or top quarks are not shown, when the result can be treated as independent of the charge. Furthermore, the term mass in the context of a pair of electrons (candiates) refers to the mass calculated from the sum of the individual 4-momenta of the the two particles.

The background contributions can be split up into three categories: real electron backgrounds, fake backgrounds and mixed backgrounds with one real electron and one fake particle. The term real electron refers to electrons that are identified as electrons. In contrast, the term fake refers to the case, when a particle, which is not an electron, is mis-identified as an electron. These fakes are mainly mis-identified jets with certain topologies, e.g., when the majority of the energy within a jet is carried by a single π^0. The pion decays almost exclusively into two photons, which create em. showers in the calorimeters similar to the showers induced by electrons.

In the following, an overview of the contributions to the three background categories will be given. Three contributions are relevant for the real electron background, the contributions of the Drell-Yan process, the contributions of diboson processes ($pp \to ZZ + X$, $pp \to WZ + X$ and $pp \to WW + X$) with at least two electrons in the final state, and the $pp \to t\bar{t} + X$ process, when the W bosons decay into an electron and a neutrino or into a neutrino and a tau, where the tau decays into an electron and a neutrino. These backgrounds are determined using Monte Carlo simulations.

The fake background consists dominantly of mis-identified jets from multijet processes. The main contributions to the mixed fake background are contributions from $pp \to t\bar{t} + X$ and $pp \to\ W + jets + X$ processes. In the W+jets case, the W boson decays into an electron and a neutrino and one of the jets is mis-identified as electron. The $t\bar{t}$ contribution originates from so-called semi-leptonic decays, where one W boson decays[1] into an electron and a neutrino, whereas the other W boson decays into a quark anti-quark pair.

Both, the fake and the mixed fake background contributions are estimated with a data-driven approach, denoted by *method I*. This method is cross-checked by a second approach, *method II*, where the contribution of events with two fakes is estimated by a data-driven method, while the W+jets and the $t\bar{t}$ contributions originating from a real electron and a fake are determined using Monte Carlo simulations.

In the following, the real electron background contributions will be discussed, followed by the discussion of the fake and mixed fake contributions. Afterwards, the individual results will be combined to the total background expectation and compared to data.

[1] Also W bosons decays into a neutrino and a tau, where the tau decays into an electron and a neutrino, are included here.

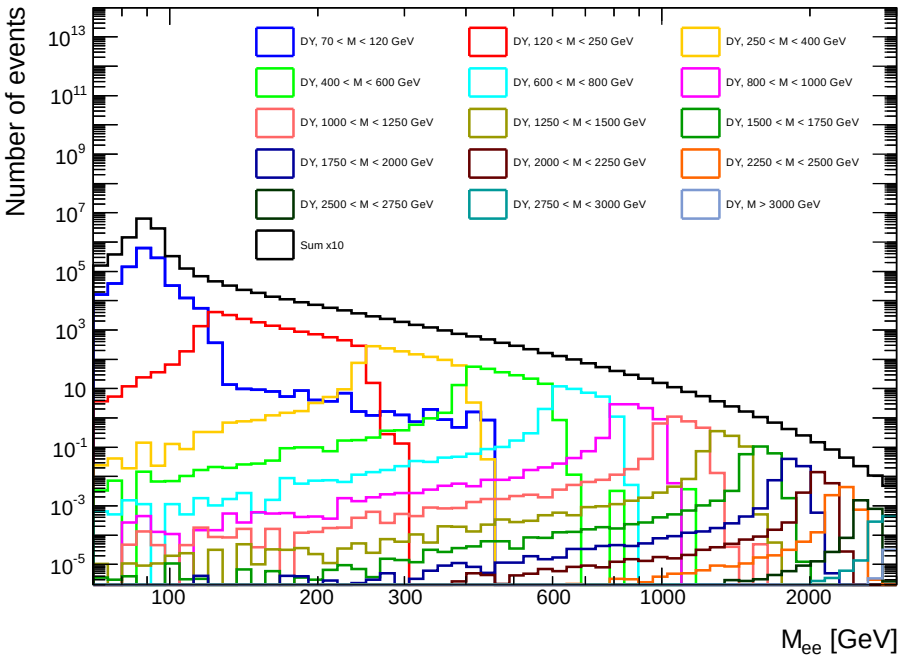

Figure 6.1: This figure shows how the Drell-Yan spectrum is constructed from the spectra of the different mass-filtered samples, which are scaled to the integrated luminosity of the data, $4.9\,\mathrm{fb}^{-1}$. Also the sum of the individual distributions, scaled by an additional factor of ten, is shown in black. None of the distributions is stacked with another.

6.1 Drell-Yan Prediction

The Drell-Yan process is simulated for the mass range from 70 GeV to 3000 GeV in 15 Monte Carlo samples, which cover successive mass ranges. Distributions derived from the individual samples are combined as follows. For each event, the k-factor defined in Section 2.4.1 is applied as event weight depending on the Z/γ^* mass the event was generated with. Then distributions, e.g. the electron pair mass distribution, are calculated separately for each of the 15 samples, and are scaled according to the luminosity scale factor of the sample as described in Eq. 4.2. The result of this procedure for the pair mass distribution is shown in Fig. 6.1. The transition between the contribution from each sample seems to be smooth by eye except for one sample, the one covering the mass range of 800 GeV to 1000 GeV on truth level. It has been checked that this effect is not real, the combination of binning and population misleads the eye. Finally, the 15 individual distributions are summed up to a combined Drell-Yan distribution. This procedure is carried out for every distribution derived for the Drell-Yan process. In the following only these combined distributions are referred to.

The Drell-Yan background prediction including the uncertainties is shown in Table 6.1 as a function of the pair mass. The dominant uncertainty is the combined PDF, α_s and scale uncertainty[2], which is smaller than 5% for masses below 400 GeV and increases to 25% for masses above 2000 GeV. As intended by the use of dedicated mass-binned Monte

[2]The details of PDF, α_s and scale uncertainties and the electroweak k-factor uncertainty were already discussed in Section 2.4.1.

Table 6.1: This table shows the predictions and uncertainties of the Drell-Yan background as a function of mass. The number of events predicted are scaled to an integrated luminosity of $4.9\,\mathrm{fb}^{-1}$. The PDF, α_S and scale uncertainty as well as the EWK k-factor uncertainty are discussed in Section 2.4.1.

Mass range [GeV]	70 - 110	110 - 130	130 - 150	150 - 170
Number of events	1169637 ± 51714	14813 ± 635	5492 ± 231	2782 ± 115
Statistical uncertainty [%]	$< 0.5\,\%$	$< 0.5\,\%$	$1\,\%$	$1\,\%$
PDF, α_s and scale uncertainty [%]	$4\,\%$	$4\,\%$	$4\,\%$	$4\,\%$
EWK k-factor uncertainty [%]	$< 0.5\,\%$	$< 0.5\,\%$	$< 0.5\,\%$	$< 0.5\,\%$
Combined uncertainty [%]	$4\,\%$	$4\,\%$	$4\,\%$	$4\,\%$

Mass range [GeV]	170 - 200	200 - 240	240 - 300	300 - 400
Number of events	2229 ± 91	1424 ± 59	890 ± 37	496 ± 21
Statistical uncertainty [%]	$1\,\%$	$1\,\%$	$1\,\%$	$1\,\%$
PDF, α_s and scale uncertainty [%]	$4\,\%$	$4\,\%$	$4\,\%$	$4\,\%$
EWK k-factor uncertainty [%]	$< 0.5\,\%$	$< 0.5\,\%$	$1\,\%$	$1\,\%$
Combined uncertainty [%]	$4\,\%$	$4\,\%$	$4\,\%$	$4\,\%$

Mass range [GeV]	400 - 800	800 - 1200	1200 - 2000	2000 - 3000
Number of events	252 ± 12	11.56 ± 0.79	1.37 ± 0.15	0.0323 ± 0.0081
Statistical uncertainty [%]	$1\,\%$	$< 0.5\,\%$	$< 0.5\,\%$	$< 0.5\,\%$
PDF, α_s and scale uncertainty [%]	$5\,\%$	$6\,\%$	$10\,\%$	$25\,\%$
EWK k-factor uncertainty [%]	$1\,\%$	$2\,\%$	$3\,\%$	$5\,\%$
Combined uncertainty [%]	$5\,\%$	$7\,\%$	$11\,\%$	$25\,\%$

Carlo samples, the statistical uncertainty is negligibly small.

6.2 Diboson Prediction

Three processes contribute to the total diboson background: $pp \to ZZ + X$, $pp \to WZ + X$ and $pp \to WW + X$ with at least two electrons in the final state[3]. For each process, three Monte Carlo samples are available, which cover successive mass ranges. In the following, the predictions of the individual processes will be discussed as well as how they are combined to the total diboson background prediction. This is followed by the description of the extrapolation of the mass distributions to high masses.

6.2.1 Combination of Samples

In contrast to the Drell-Yan background with exactly two electrons from the hard scatter, the term "mass" is more difficult to define here, because in the considered processes up to four electrons are produced in the final state. In this analysis the pair of electrons in an event is taken, which passes all selection criteria and has the highest sum of the individual transverse momenta. The term mass refers to the mass of this pair.

The phase space simulated for each process is split into three samples by applying filters on the properties of the electrons originating from the hard scatter on truth level as shown in Table 6.2. The samples are classified according to the mass range they cover as a low mass, a medium mass and a high mass sample. These samples were meant to be complemented by a fourth one covering the masses above 1600 GeV, but this was impossible to produce due to technical restrictions. Since the background needs to be extrapolated to 3000 GeV in any case, this only limits the mass up to which the spectrum can be used as input to the extrapolation fit procedure.

WW Contributions

The mass distribution derived from the three WW Monte Carlo samples is shown in Fig. 6.2. It is a smooth spectrum that decreases as the mass increases. There is a sharp "turn on" of the mass distributions of the medium and high mass samples, respectively, because there are only two electrons from the WW decays. The contributions below the corresponding mass filter thresholds are mainly due to energy loss via Bremsstrahlung of (at least) one of the electrons of the W decay.

The medium and high mass WW Monte Carlo samples were simulated by the ATLAS collaboration with the requirement that both W bosons decay into a electron and a neutrino. This does not include the topology, e.g., where one W boson decays into a neutrino and tau, which decays into an electron and a neutrino. The size of the contribution of such topologies was studied with the low mass sample, which includes all leptonic decay modes of the W bosons. Of the total WW background, 9.6% of the events are topologies, where one electron originates from a tau decay, and 0.4% are topologies, where both electrons originate from tau decays. Therefore only approximately 90% of the WW background is simulated in the medium high mass sample. To compensate this deficit, the prediction of the medium and high mass samples are scaled by $1/0.9 \approx 1.11$.

Table 6.2: An overview over the filter criteria applied to the diboson Monte Carlo samples. For all Monte Carlo samples, electron η and E_T cuts were applied during the event generation step. For the medium and high mass samples, further restrictions were imposed, when the samples were generated by the ATLAS collaboration. For the WW samples, both W bosons are forced to decay to an electron and a neutrino. For the WZ and ZZ samples, one Z boson is forced to decay into an electron positron pair.

Sample name	Single electron filter	Di-electron mass filter
Low mass	$E_T > 10\,\text{GeV}, \lvert\eta\rvert < 2.8$	$M_{ee} < 400\,\text{GeV}$
Medium mass	$E_T > 15\,\text{GeV}, \lvert\eta\rvert < 2.6$	$400\,\text{GeV} < M_{ee} < 1000\,\text{GeV}$
High mass	$E_T > 15\,\text{GeV}, \lvert\eta\rvert < 2.6$	$1000\,\text{GeV} < M_{ee} < 1600\,\text{GeV}$

ZZ Contributions

The mass distribution derived from the three ZZ Monte Carlo samples is shown in Fig. 6.3. At $\approx 91\,\text{GeV}$ the Z boson resonance peak is visible, followed by the falling continuum. This spectrum is composed in a more complicated way than the WW mass spectrum, because up to four electrons are available from the hard scatter, from which the pair with the highest sum of the individual transverse momenta is selected. The mass of this pair is denoted by M_{reco}. On basis of the medium mass sample, the contributions to the mass distribution will be discussed in more detail.

The left plot of Fig. 6.4 shows the correlation of the two Z boson masses at truth level. The Z with the lower mass (called "subleading" Z from here on) is dominantly produced on-shell, while the Z with the higher mass ("leading") has a significant probability to be produced either on-shell or at masses directly above the mass filter applied, in this case 400 GeV. This means that a large fraction, namely 55%, of the selected electron pairs with a mass of 400 GeV and above do not originate from the same Z mother particle ("mixed electron pair"). This is illustrated in the right plot of Fig. 6.4, which shows M_{reco} as a function of the leading Z truth mass. In the high mass sample, the corresponding mixed electron pair fraction amounts to only 36%, because it is kinematically less likely to find two electrons (from two different Z bosons with a mass close to the pole mass) that have a mass above 1000 GeV as it is required for the high mass sample.

The contribution from mixed electron pairs explains the non-zero population of lower masses down to the Z pole mass from the medium and high mass samples, see Fig. 6.3. If an electron is rejected[4], which is part of the pair that has a truth level mass above the mass filter threshold, a different pair of electrons might be chosen out of the remaining electrons. If this electron pair originiates from the same Z boson, it is very likely that the pair mass is close to the Z pole mass as was discussed before, see Fig. 6.4. Due to bremsstrahlung, also M_{reco} on reconstruction level can be shifted towards lower values compared to its truth mass, but this is a small contribution to the population of the mass distributions below the mass filter threshold.

[3]The relevant individual decay modes of the bosons will be discussed individually for each of the three processes in the corresponding sections.

[4]In the filter, electrons in the calorimeter barrel end-cap transition region are not vetoed, while they are vetoed in this analysis.

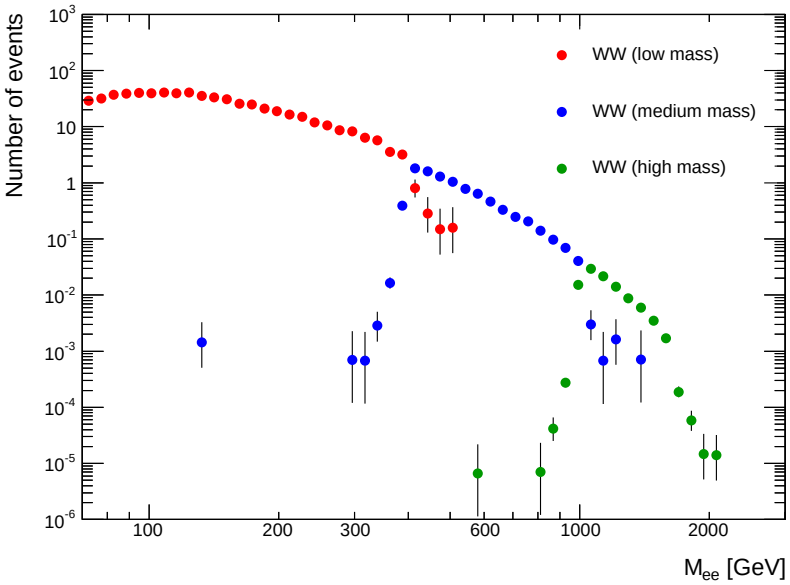

Figure 6.2: The composition of the mass distribution for the WW background is shown. The contribution derived from the low mass sample is shown in blue, whereas the distributions in red and blue show the contributions derived from the medium and high mass samples, respectively. The distributions are scaled to an integrated luminosity of $4.9\,\mathrm{fb}^{-1}$.

In the following, the impact of the filter requirements on the medium and high mass samples will be discussed. It is required that at least one Z boson decays into an electron positron pair. The only relevant topology that is vetoed this way are events, where both Z bosons decay to a tau anti-tau pair and one tau or anti-tau of each Z boson decays into an electron and a neutrino. The fraction of selected events with this topology in the low mass sample amounts to 0.1%. Therefore no bias with this respect is expected for the estimate derived from the medium and high mass samples.

WZ Contributions

Fig. 6.5 shows the mass distributions derived from the three WZ Monte Carlo samples. The shapes of the mass distributions are similar to the shapes of the ZZ mass distributions, which will be explained in the following.

The left plot of Fig. 6.6 shows the truth level W mass as a function of the truth level Z mass for the medium mass sample. In approximately 50% of the events, both the W and the Z boson are produced on-shell. In this case, only mixed electron pairs can fullfil the mass filter requirement of 400 GeV. The same effect is visible in the right plot of Fig. 6.6, where the correlation of M_{reco} with the Z boson truth mass is shown. This large fraction of mixed electron pairs explains the small contributions at the Z boson resonance mass in Fig. 6.5: If the truth filter requirement is satisfied by an mixed electron pair and the electron originating from the W decay is rejected on reconstruction level, the electron pair originating from the Z boson can be selected. The same effect was observed in the ZZ mass distributions.

The fraction of mixed electron pairs decreases from 53% in the medium mass sample

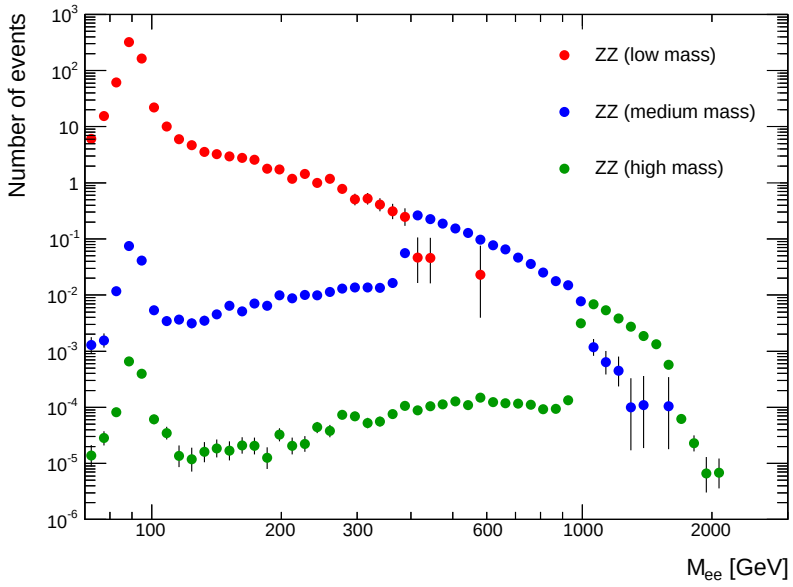

Figure 6.3: The composition of the mass distribution for the ZZ background is shown. The contribution derived from the low mass sample is shown in blue, whereas the distributions in red and blue show the contributions derived from the medium and high mass samples, respectively. The distributions are scaled to an integrated luminosity of $4.9\,\mathrm{fb}^{-1}$.

to 23% in the high mass sample, because, similar to the ZZ case, it is kinematically less likely to find two electrons from an on-shell Z and W boson with an electron pair mass of at least 1000 GeV than of at least 400 GeV.

In the following, the impact of the filter requirements on the medium and high mass samples will be discussed. It is required that at least one Z boson decays into an electron positron pair. The only relevant topologies that are vetoed this way are events, where the Z boson decays into a tau and an anti-tau, where at least one tau decays into an electron and a neutrino, and the W boson either decays directly into an electron and a neutrino or via a tau into an electron and two neutrinos. The fraction of events with this topologies in the low mass sample amounts to 1%, therefore no bias with this respect is expected for the predictions of the mass distributions derived from the medium and high mass samples.

The combined diboson mass distributions are calculated by summing up the individual contributions derived from the WW, ZZ and WZ Monte Carlo samples.

6.2.2 Extrapolation to high Masses

The prediction for each background is needed up to masses of 3 TeV. Therefore the mass distribution of the diboson background and other backgrounds needs to be extrapolated to high masses. This procedure will be described in general terms first, followed by a discussion of the results for the combined diboson mass distribution.

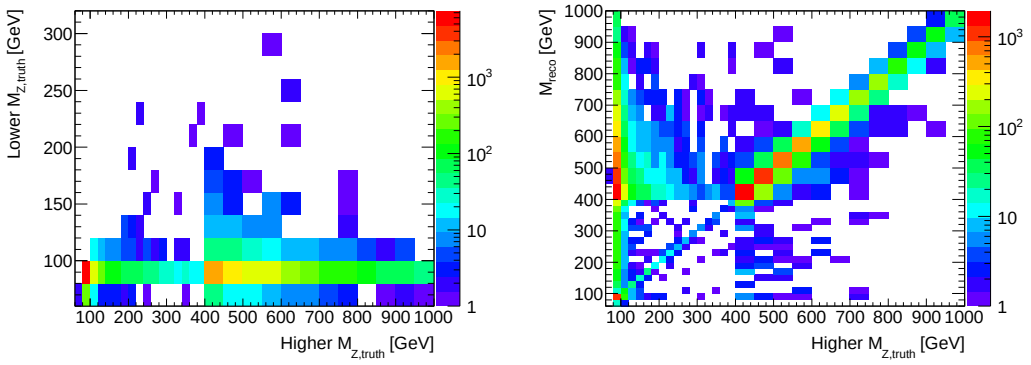

Figure 6.4: The left plot shows the truth level mass of the subleading Z as a function of the truth level mass of the leading Z for the ZZ medium mass sample. The mass of the selected electron pair on reconstruction level is shown as a function of the leading Z truth level mass in the right plot. The color code indicates the number of events on a logarithmic scale. The number of events is not scaled to luminosity.

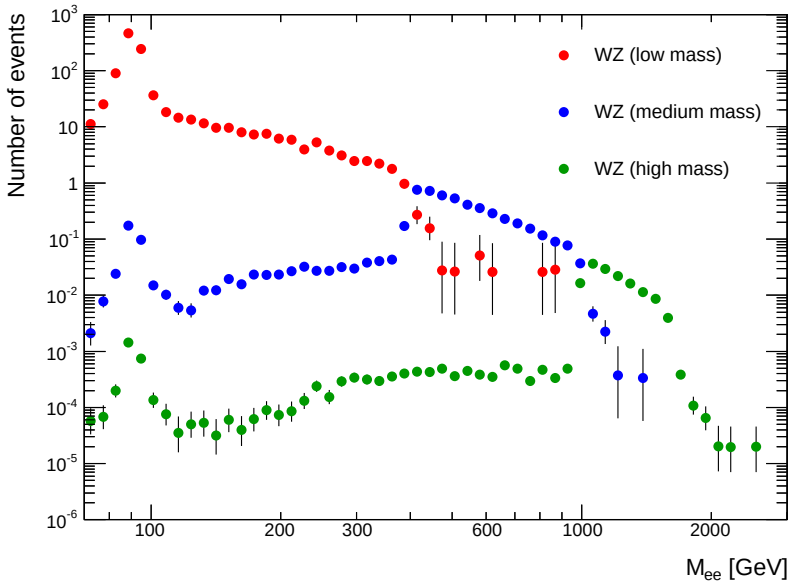

Figure 6.5: The composition of the mass distribution for the WZ background is shown. The contribution derived from the low mass sample is shown in blue, whereas the distributions in red and blue show the contributions derived from the medium and high mass samples, respectively. The distributions are scaled to an integrated luminosity of $4.9\,\mathrm{fb}^{-1}$.

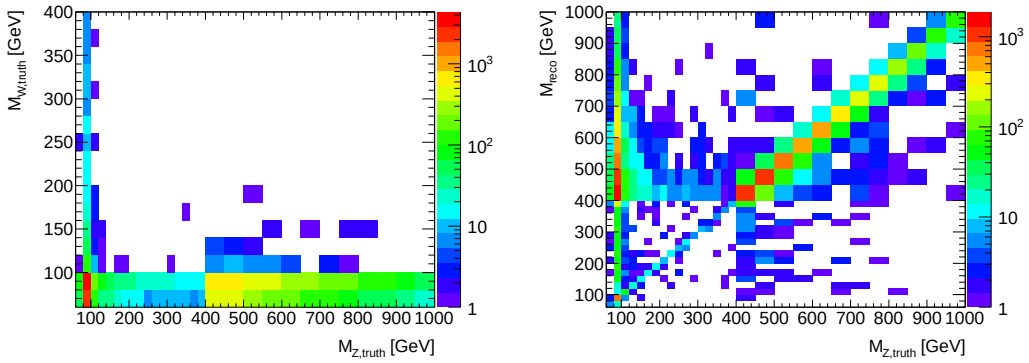

Figure 6.6: For the medium mass WZ sample, the truth level mass of the W boson is shown as a function of the truth level mass of the Z boson in the left plot, and the mass of the selected electron pair on reconstruction level is shown as a function of the Z truth level mass in the right plot. In both plots, the color code indicates the number of events on a logarithmic scale. The number of events is not scaled to luminosity.

The Extrapolation Method

Two different functions are used for the extrapolation,

$$f_0(m) = e^{-p_0} \cdot m^{p_1} \cdot m^{p_2 \cdot \ln(m)} \text{ and} \tag{6.1}$$

$$f_1(m) = \frac{p_0}{(m + p_1)^{p_2}}. \tag{6.2}$$

The function f_0 is a modified version of the function used by the ATLAS collaboration to describe the dijet mass spectrum in the search for high mass resonances in the di-jet mass spectrum [99]. The second function, f_1, has no direct physical motivation, but it turned out that the mass spectra can be described well with this function. Both functions were also used for this purpose in the ATLAS dilepton resonance search.

To evaluate the stability of the fit results, and to get a handle on the uncertainties, the following method was developed, which extends the simpler procedure already used in the ATLAS dilepton resonance search. Instead of using one fit range as a default and a few others as a systematic variation, a large number of fit ranges is considered. The average prediction of all fits, which pass certain quality criteria, is calculated and used as the result of the fit procedure.

Technically, this is realized as follows. For both, the lower and upper fit ranges, an interval is defined, which is sampled with a certain step size. An example is an interval of [100 GeV, 200 GeV], which is sampled with a step size of 50 GeV. This results into three values, 100 GeV, 150 GeV and 200 GeV, which are used, e.g., as lower fit range border. A second interval is defined for the upper fit range and each possible combination of lower and upper fit borders is considered. The fits are performed using a χ^2 method[5] implemented in ROOT [56]. The input for the fits are histograms with a finite bin width. It is checked that each fit range considered corresponds to a unique set of bins. If two fit

[5] A weighted log-likelihood fit was considered as an alternative, but finally dropped, because ways to perform a log-likelihood fit with weighted events are controversely discussed, and it is difficult to define a good criterion to evaluate the quality of the fit.

ranges specified in terms of masses correspond to the same set of bins, the fit is performed only once. Furthermore each considered bin is required to contain at least 12 events (before weights are applied) to ensure that a χ^2 fit approach is valid. For each fit range, both fit functions are evaluated. Each fit is required to converge and needs to have a probability value of at least 5%.

The set of fits is combined to one result as follows: The mean

$$\bar{m} = \frac{1}{n} \sum_{i=1}^{n} m_i \tag{6.3}$$

of all n successful fit results is calculated for each mass point m_i in a 1 GeV binning. The calculated Root Mean Square (RMS)

$$\sigma = \sqrt{\frac{1}{n-1} \sum_{i=1}^{n} (\bar{m} - m_i)^2} \tag{6.4}$$

is used to estimate the spread or the uncertainty of the mean value $\bar{m}$.

The main purpose of this procedure is to extrapolate mass distributions to high masses. Therefore a (to a certain extend arbitrary) mass threshold, m_{Fit}, is defined, above which the fit result is used to replace the original mass distribution. The fit result at lower masses is used to verify that the original mass distribution is well described.

Extrapolation of the Diboson Mass Distribution

The fit range intervals used for the extrapolation of the diboson fits were chosen based on the following considerations.

The lower fit range needs to start above the Z pole mass, because the functions used to perform the fit cannot describe the resonance. A mass of 130 GeV was chosen. The highest value considered as lower fit range border was chosen such that a large number of ranges is considered, but its exact value is arbitrary to a certain extend. A mass of 650 GeV was chosen. The same considerations apply to the lowest value considered for the upper fit range. It was chosen to be 1200 GeV. The diboson mass spectrum was simulated up to masses of 1600 GeV on truth level. Due to, e.g., Bremsstrahlung, events can be reconstructed at a lower mass than they were generated with. Therefore masses up to 1450 GeV are considered for the upper fit range. The lower and upper intervals for the fit ranges are sampled using a 20 GeV and 50 GeV step size, respectively.

The result of this fitting procedure is shown in Table 6.3. For masses below 170 GeV, the fit results do not describe the mass distribution, because the fit functions do not take the Z boson resonance at 91 GeV into account. For masses between 170 GeV and 1200 GeV, the mass distribution is well described. The agreement is better than expected from the size of the uncertainties of the fit procedure, which indicates slightly overestimated uncertainties. For higher masses, no meaningful comparison can be performed, because masses above 1600 GeV are not simulated.

To evaluate that the RMS, which is used as extrapolation uncertainty, does not depend on the choice of, e.g., the lowest mass border used for the lower fit range, the following consistency check was carried out. The lowest mass considered as lower fit border was increased from 130 GeV to 200 GeV. The results of all fits that passed the quality requirements were compared at various mass points. Two examples, at 500 GeV and at

Table 6.3: The prediction for the diboson background is shown as a function of mass with and without the extrapolation procedure applied. The large deviations of the result for low masses and masses above 1600 GeV are expected and discussed in the text. The number of events listed is scaled to an integrated luminosity of 4.9 fb^{-1}.

Mass range [GeV]	70 - 110	110 - 130	130 - 150	150 - 170
Prediction (no extrapolation)	1731.3 ± 7.8	145.6 ± 3.1	100.6 ± 2.7	72.0 ± 2.2
Prediction (with extrapolation)	400 ± 361	108 ± 60	76 ± 46	59 ± 29
Mass range [GeV]	170 - 200	200 - 240	240 - 300	300 - 400
Prediction (no extrapolation)	75.1 ± 2.3	60.3 ± 2.0	47.6 ± 1.8	31.5 ± 1.4
Prediction (with extrapolation)	72 ± 25	59 ± 16	48.3 ± 9.4	29.9 ± 3.9
Mass range [GeV]	400 - 800	800 - 1200	1200 - 2000	2000 - 3000
Prediction (no extrapolation)	16.20 ± 0.37	0.96 ± 0.11	0.1120 ± 0.0017	0.000082 ± 0.000027
Prediction (with extrapolation)	16.40 ± 0.78	0.938 ± 0.013	0.1202 ± 0.0084	0.0069 ± 0.0022

2500 GeV, are shown in Fig. 6.7. No hint for a bias due to the choice of the lowest fit border has been found. The same procedure was evaluted for the upper fit border, which was lowered to 1350 GeV instead of 1450 GeV.

The final mass distribution can be seen in Fig. 6.8 and is obtained the following way: For mass region where the Monte Carlo statistics are sufficient and no extrapolation is needed, the direct Monte Carlo prediction is used. Above a mass threshold, $m_{\text{Fit}} = 1400\,\text{GeV}$, the prediction from the fit procedure is used.

6.2.3 Summary

The final mass-dependent diboson prediction including the uncertainties is shown in Table 6.4. The cross-section has an theoretical uncertainty of 5% [100]. For masses above m_{Fit}, the extrapolation uncertainty is used instead of the statistical uncertainty For masses below 800 GeV, the cross-section uncertainty is the dominating uncertainty, while for higher masses the statistical respectively fit procedure uncertainty is the most important uncertainty. For masses above 2 TeV, the total uncertainty amounts to 32%.

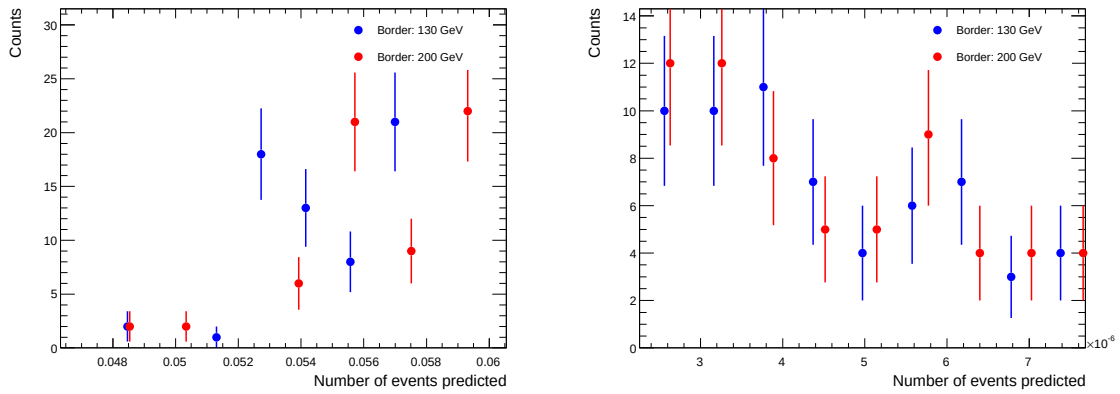

Figure 6.7: The distribution of the predicted number of events in a 1 GeV window for all successful fits evaluated at a mass of 500 GeV is shown on the left side, while the same distribution evaluated at 2500 GeV is shown on the right side. The blue points show the predictions for all fits with the lower fit range interval [130 GeV, 650 GeV], while the distribution shown in red shows the fit results after the lower border of 130 GeV is moved to 200 GeV. The distributions correspond to an integrated luminosity of 4.9 fb^{-1}.

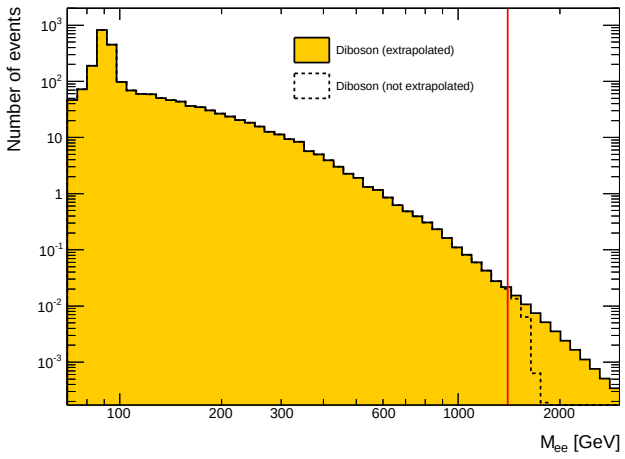

Figure 6.8: The final diboson mass distribution including the extrapolation to high masses is shown in orange, whereas the result without the extrapolation is shown as dashed line. The red vertical line indicates the threshold of 1400 GeV, where-from the extrapolation is used. The distributions are scaled to an integrated luminosity of 4.9 fb^{-1}.

Table 6.4: The predictions and uncertainties of the diboson background are shown as a function of mass. The number of events predicted are scaled to an integrated luminosity of $4.9\,\mathrm{fb}^{-1}$.

Mass range [GeV]	70 - 110	110 - 130	130 - 150	150 - 170
Number of events	1731 ± 87	145.6 ± 7.9	100.6 ± 5.7	72.0 ± 4.2
Statistical uncertainty [%]	$< 0.5\,\%$	$2\,\%$	$3\,\%$	$3\,\%$
Fit uncertainty [%]	$0\,\%$	$0\,\%$	$0\,\%$	$0\,\%$
Cross-section uncertainty [%]	$5\,\%$	$5\,\%$	$5\,\%$	$5\,\%$
Combined uncertainty [%]	$5\,\%$	$5\,\%$	$6\,\%$	$6\,\%$

Mass range [GeV]	170 - 200	200 - 240	240 - 300	300 - 400
Number of events	75.1 ± 4.4	60.3 ± 3.6	47.6 ± 3.0	31.5 ± 2.1
Statistical uncertainty [%]	$3\,\%$	$3\,\%$	$4\,\%$	$5\,\%$
Fit uncertainty [%]	$0\,\%$	$0\,\%$	$0\,\%$	$0\,\%$
Cross-section uncertainty [%]	$5\,\%$	$5\,\%$	$5\,\%$	$5\,\%$
Combined uncertainty [%]	$6\,\%$	$6\,\%$	$6\,\%$	$7\,\%$

Mass range [GeV]	400 - 800	800 - 1200	1200 - 2000	2000 - 3000
Number of events	16.20 ± 0.89	0.96 ± 0.12	0.1172 ± 0.0086	0.0069 ± 0.0022
Statistical uncertainty [%]	$2\,\%$	$11\,\%$	$1\,\%$	$0\,\%$
Fit uncertainty [%]	$0\,\%$	$0\,\%$	$5\,\%$	$31\,\%$
Cross-section uncertainty [%]	$5\,\%$	$5\,\%$	$5\,\%$	$5\,\%$
Combined uncertainty [%]	$6\,\%$	$12\,\%$	$7\,\%$	$32\,\%$

6.3 $t\bar{t}$ Prediction

The $t\bar{t}$ Monte Carlo simulation includes semi-leptonic and dileptonic decays into electrons, muons and taus, while full-hadronic decays are absent. The latter are covered by the data-driven multijet methods. Top quarks decay almost exclusively into a bottom quark and a W boson. If both W bosons decay into an electron and a neutrino or into a neutrino and a tau, which decays into an electron and a neutrino, two electrons are observed in the final state. These events are refered to as *type ee* events. If only one W boson decays, direct or via a tau, into an electron and a neutrino, the event is referred to as *type ef* event. In this topology, one of the jets need to be mis-identified as an electron in order to contribute to the background of this analysis. These *type ef* events are a small fraction of the $t\bar{t}$ background, approximately 5%. However, this contribution is needed for one of the two methods that determine the mixed fake background. In principle, the *type ee* and the combined *type ee* and *type ef* mass distributions could be determined and extrapolated separately. But with this approach, the two fake background methods could not be compared directly, but only with the full $t\bar{t}$ estimate included. Therefore this approach was not considered further.

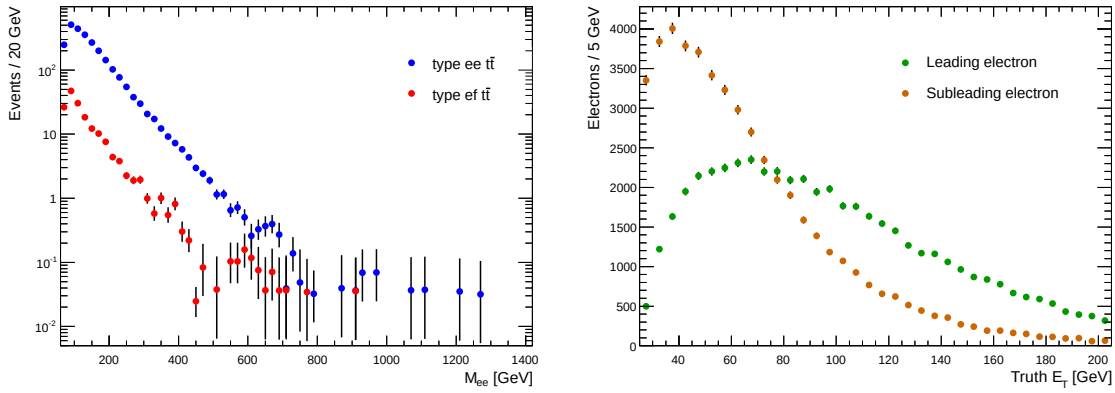

Figure 6.9: The mass distribution for both, *type ee* and *type ef* $t\bar{t}$ events, is shown separately in the left plot. For *type ee* events, the E_T distributions of the leading and the subleading electrons on truth level are shown in the right plot. The distributions are scaled to an integrated luminosity of $4.9\,\mathrm{fb}^{-1}$.

In the left plot of Fig. 6.9, the mass distribution for both, *type ee* and *type ef* events, is shown separately. The shapes of both distributions are very similar in the mass range up to approximately 500 GeV, where a sufficient number of events is available for the comparison. Furthermore, in the lowest mass bin of both distributions, from 70 GeV to 90 GeV, a deficit is visible. It can be understood from the deficit at low values of E_T in the E_T distribution of the leading and subleading electron shown in the right plot of Fig. 6.9. The distributions are derived on truth level[6] for *type ee* events that pass the full selection. The leading electron distribution is significantly shifted towards higher values with respect to the distribution of the subleading electron. The reason is the two step production and the, on average, strong transverse boost of the W bosons. This will be explained in the following.

The rest mass of the top quark of approximately 173 GeV [101] is about twice as heavy as the sum of the bottom quark and the W boson mass. This results into a large average p_T of the W bosons of approximately[7] 60 GeV, if the transverse momentum of the top quark was zero. A W boson has a probability of approximately 30% to be observed in a left-handed helicity state, whereas the probability for a longitudinal helicity state amounts to approximately 70% [102]. A W boson in a left-handed helicity state emits the charged lepton in direction of its 3-momentum. Due the typically significant transverse boost of W bosons produced in top quark decays, the charged lepton is emitted in flight direction[8] in the labaratory frame in 76% of the *type ee* $t\bar{t}$ events that pass the selection. This explains the large average E_T of the leading electron. On average, at least one of the two electrons is (positively) boosted and this electron is selected as the leading electron. Furthermore, the "mother" particles of the electrons, the W bosons are produced in two different two-body decays, and decay in turn in a second two-body decay, which leads to an additional spread of the size of the E_T of the two electrons.

[6] This was studied on truth level, because there these spectra are not distorted by the effects of Bremsstrahlung.

[7] The average W boson p_T quoted was calculated from the events that pass the *type ee* selection.

[8] There is of course an opening angle distribution. The statement refers to all openening angles smaller than $\pi/2$.

Table 6.5: The $t\bar{t}$ *type ee* estimation and the results of the extrapolation procedure are shown The number of events listed is scaled to an integrated luminosity of $4.9\,\mathrm{fb}^{-1}$.

Mass range [GeV]	70 - 110	110 - 130	130 - 150	150 - 170
Prediction (no extrapolation)	988.5 ± 6.9	397.5 ± 4.3	308.7 ± 3.7	232.9 ± 3.2
Prediction (with extrapolation)	1123 ± 482	388 ± 107	292 ± 61	216 ± 34

Mass range [GeV]	170 - 200	200 - 240	240 - 300	300 - 400
Prediction (no extrapolation)	236.1 ± 3.2	179.5 ± 2.8	122.3 ± 2.4	66.4 ± 1.7
Prediction (with extrapolation)	222 ± 24	173 ± 11	123.1 ± 2.8	66.74 ± 0.79

Mass range [GeV]	400 - 800	800 - 1200	1200 - 2000	2000 - 3000
Prediction (no extrapolation)	23.5 ± 1.0	0.28 ± 0.13	0.032 ± 0.032	0.0 ± 0.0
Prediction (with extrapolation)	23.49 ± 0.96	0.30 ± 0.10	0.0129 ± 0.0083	0.00013 ± 0.00015

6.3.1 Extrapolation of the *type ee* Mass Distribution

For the extrapolation of the $t\bar{t}$ background, the same procedure as used for the diboson background is applied, although with different parameters. The values for the lower and upper fit ranges are sampled with a 25 GeV step size from the intervals [130 GeV, 400 GeV] and [500 GeV, 700 GeV], respectively. The extrapolation result is used for masses above 500 GeV.

The result of the fit procedure for the *type ee* contribution is shown in Table 6.5. The mass distribution is well described by the fit for masses between 110 GeV and 1200 GeV. The deficit for masses between 70 GeV and 90 GeV cannot be described by the functions used in the fit. For higher masses, the number of simulated are insufficient to make a meaningful comparison. Due to the limited number of events to base the extrapolation upon, the extrapolation uncertainty is large for masses above 2000 GeV, namely 111%.

6.3.2 Extrapolation of the *type ef* Mass Distribution

The *type ef* contribution amounts to approximately 5% of the total $t\bar{t}$ contribution. The resulting mass distribution is based upon too few events to be extrapolated reliably up to masses of 3000 GeV. Therefore another approach was used. The ratio of the number of *type ef* events with respect to the total number of $t\bar{t}$ events was calculated as a function of the mass. The $t\bar{t}$ mass distribution for the sum of the *type ef* and *type ee* events can be extrapolated to high masses. By multiplying this result with the fraction of *type ef* events, an absolute estimate of the *type ef* contribution at high masses can be derived, as will be shown in the following.

The fraction of *type ef* events is shown in the left plot of Fig. 6.10. For masses above 120 GeV, the ratio can be described with a horizontal line. The value of the ordinate,

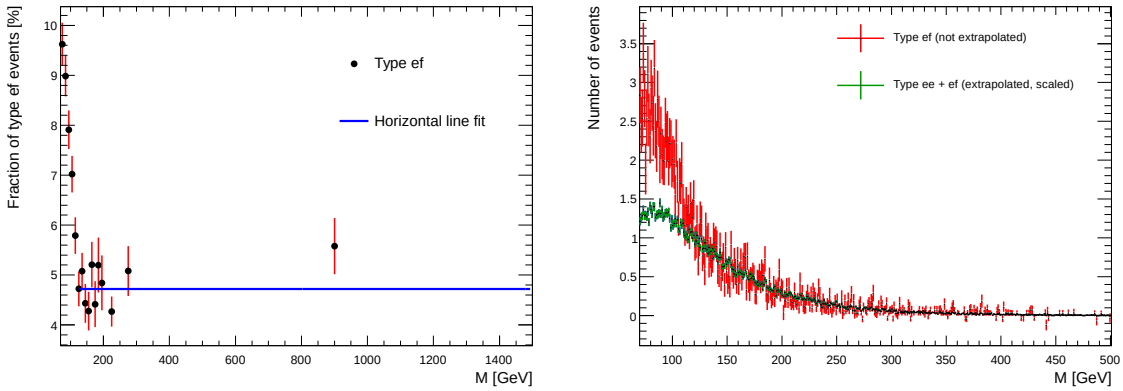

Figure 6.10: The fraction of *type ef* events with respect to all $t\bar{t}$ events is shown as a function of mass in the left plot. The result of a straight line fit to this fraction in the mass range 120 GeV to 1500 GeV is indicated by the blue line. The last bin covers masses from 300 GeV to 1500 GeV. In the right plot, the *type ef* mass distribution is shown in red, whereas the corresponding combined *type ef* and *type ee* distribution as calculated with the fit procedure and scaled with s_{II} is shown in blue. The distribution is scaled to an integrated luminosity of 4.9 fb^{-1}.

s_{II}, was determined using a χ^2 fit in the mass range 120 GeV to 1500 GeV. The extracted fraction is $s_{II} = (4.74 \pm 0.13)\%$. Given that the fraction of the total $t\bar{t}$ background with respect to the total background expectation is at most 10%, the *type ef* contribution is smaller than 0.5%. Therefore, no further investigation on systematic uncertainties of s_{II} has been performed.

The mass distribution for the sum of the *type ef* and *type ee* events was extrapolated to high masses with the same parameters for the fit ranges as for the *type ee* events. As expected, the fit result agrees on the same good level as the *type ee* result does. The tabulated results with and without extrapolation are shown in the Appendix in Table A.7.

The combined *type ef* and *type ee* mass distribution as calculated with the fit procedure and scaled with s_{II} is shown in the right plot of Fig. 6.10. For comparison, the *type ef* mass distribution without any extrapolation is shown. The two distributions agree well within uncertainties for masses above 125 GeV. There is no hint of an systematic shift or bias for the approximation with the constant scale factor s_{II}.

Therefore, the final *type ef* mass distribution is composed as follows. For masses below 150 GeV, the distribution as derived directly from the simulation is used. For higher masses, the fit result of the combined *type ef* and *type ee* mass distribution scaled with s_{II} is used. The relative uncertainty of s_{II} is used as normalization uncertainty.

6.3.3 Summary

The final *type ee* $t\bar{t}$ prediction including their uncertainties is shown in Table 6.6. The theoretical cross-section uncertainty of 9.5% [103] dominates the uncertainty for masses below 800 GeV, whereas for higher masses the extrapolation uncertainty dominates. The total uncertainty for masses above 2000 GeV amounts to 111%.

The results for the *type ef* prediction basically correspond to the results for the *type ee*

Table 6.6: This table shows the predictions and uncertainties of the *type ee* $t\bar{t}$ background as a function of mass. The number of events listed is scaled to an integrated luminosity of $4.9\,\mathrm{fb}^{-1}$.

Mass range [GeV]	70 - 110	110 - 130	130 - 150	150 - 170
Number of events	988 ± 94	398 ± 38	309 ± 30	233 ± 22
Statistical uncertainty [%]	1 %	1 %	1 %	1 %
Fit uncertainty [%]	0 %	0 %	0 %	0 %
Cross-section uncertainty [%]	10 %	10 %	10 %	10 %
Combined uncertainty [%]	10 %	10 %	10 %	10 %

Mass range [GeV]	170 - 200	200 - 240	240 - 300	300 - 400
Number of events	236 ± 23	179 ± 17	122 ± 12	66.4 ± 6.5
Statistical uncertainty [%]	1 %	2 %	2 %	3 %
Fit uncertainty [%]	0 %	0 %	0 %	0 %
Cross-section uncertainty [%]	10 %	10 %	10 %	10 %
Combined uncertainty [%]	10 %	10 %	10 %	10 %

Mass range [GeV]	400 - 800	800 - 1200	1200 - 2000	2000 - 3000
Number of events	23.5 ± 2.4	0.30 ± 0.11	0.0129 ± 0.0083	0.00013 ± 0.00015
Statistical uncertainty [%]	0 %	0 %	0 %	0 %
Fit uncertainty [%]	4 %	34 %	64 %	110 %
Cross-section uncertainty [%]	10 %	10 %	10 %	10 %
Combined uncertainty [%]	10 %	35 %	65 %	111 %

prediction scaled down by a factor of approximately 20. Therefore they are only listed in the Appendix in Table A.8.

6.4 Multijet and W+Jets Estimation: Method I

In this section, the first of two methods to estimate the background contribution of fakes, denoted as *method I*, will be discussed. This method is used for the final background estimation, whereas *method II* has some conceptual limitations and will therefore be used as cross-check, only.

The signatures of jets that fake electron signatures will be briefly outlined, followed by an introduction of the fake factor formalism. Further, the calculation of fake factors and the resulting mass distribution as well as their extrapolation and uncertainties will be discussed.

6.4.1 Fake Signatures

The electron identification cuts are derived such that the efficiency to identify a real electron as an electron is balanced versus the probability that other particles are mis-identified as electron[9]. Such mis-identified particles are denoted by the term fake. These fakes are primarily mis-identified jets, which consist dominantly of pions and kaons. Neutral pions decay primarily into two photons, which induce em. showers when traversing the calorimeters. Therefore, a jet, where most of the energy is carried by a single π^0, will create a signature in the calorimeters that is similar to that of an electron. However neither of the photons do produce a track in the inner detector. Therefore, a track of an additional charged hadron contained in the jet, e.g., of a charged pion, needs to point loosely to the main energy deposition in the calorimeter to complete the signature.

Jets with the fake signatures discussed can be selected by inverting parts of the electron identification criteria (see Section 3.3.2), which aim at suppressing these signatures. The track match variable describes the spatial deviation of the barycenter of the energy deposition in the calorimeter from the point, where it should hit the calorimeter according to the track extrapolation. In the medium electron identification, the track match tolerance is tightened[10] by a factor of five with respect to the basic requirement for all electron candidates.

The strip cuts reject electron candidates, where two closeby local energy maxima are found in the first layer of the em. calorimeter, which is the typical signature of a π^0 that decayed into two photons. Therefore a sample of jets, which are likely to fake electrons, can be selected by inverting one of these two cuts.

6.4.2 Fake Factor Formalism

For the following discussion, the electron-like particles are labeled with an "T" for "tight", while the more jet-like particles are denoted by an "L" for "loose". In this section, the fake factor ansatz will be derived with these general terms "T" and "L" which will be matched to the exact cuts used afterwards. Only pairs of particles of interest. They are denoted by N_{xy} with $x, y \in \{T, L\}$, where the first index corresponds to the leading electron and the second one to the subleading electron.

In this notation, four categories, N_{TT}, N_{TL}, N_{LT} and N_{LL}, can be defined, which are measurable quantities. Those are related via

$$\begin{pmatrix} N_{TT} \\ N_{TL} \\ N_{LT} \\ N_{LL} \end{pmatrix} = \begin{pmatrix} r_1 r_2 & r_1 f_2 & f_1 r_2 & f_1 f_2 \\ r_1(1-r_2) & r_1(1-f_2) & f_1(1-r_2) & f_1(1-f_2) \\ (1-r_1)r_2 & (1-r_1)f_2 & (1-f_1)r_2 & (1-f_1)f_2 \\ (1-r_1)(1-r_2) & (1-r_1)(1-f_2) & (1-f_1)(1-r_2) & (1-f_1)(1-f_2) \end{pmatrix} \begin{pmatrix} N_{RR} \\ N_{RF} \\ N_{FR} \\ N_{FF} \end{pmatrix} \tag{6.5}$$

to the "true" quantities, N_{ab} with $a, b \in \{R, F\}$, which classify, whether an object was an actual electron or not. The index "R" refers to real electrons while "F" refers to fakes. The vector on the right hand side of the equation describes truth quantities, which are

[9] In the limit of a a negligible fake probability, also only a small fraction of the real electrons would pass those criteria.

[10] All electron candidates are required to have a track match within a cone of radius $R = 0.05$. This threshold is left unchanged for the loose identification level, but tightened at the medium identification level.

not accessible in data. For the coefficients f_i and r_i, the index $i = 1$ ($i = 2$) refers to the first (second) index of the corresponding quantity N. The coefficients f denote the probability that a fake is reconstructed as a electron-like "tight", while $1 - f$ denotes the probability that a fake is reconstructed as fake-like "loose". The coefficients r represent the probability that a real electron is reconstructed as a tight electron, whereas $1 - r$ denotes the probability that a real electron is reconstructed as a fake. N_{TT} is the number of particles, which is reconstructed as electron-like:

$$N_{TT} = r_1 r_2 N_{RR} + r_1 f_2 N_{RF} + f_1 r_2 N_{FR} + f_1 f_2 N_{FF}. \tag{6.6}$$

The quantity of interest is the contribution to N_{TT}, which originates from pairs of particles with at least one fake. Therefore N_{RR} will not be considered further in this method[11].

By inverting the matrix in Eq. 6.5, the inaccessible truth quantities on the right side of Eq. 6.8 can be replaced by measurable quantities. The direct inversion of Eq. 6.5 leads to complicated expressions for the matrix elements. Inserting these into Eq. 6.8 results into a lot of terms of similar size, which are subtracted from each other. Such terms are expected to lead to significant statistical uncertainties on N_{TT}. To avoid this, an approximation was used. The real electron efficiency r is set to one and the neglected inefficiency is corrected for with the use of Monte Carlo simulations later. More details will be discussed below. With the $r = 1$ assumption, Eq. 6.5 becomes

$$\begin{pmatrix} N_{TT} \\ N_{TL} \\ N_{LT} \\ N_{LL} \end{pmatrix} = \begin{pmatrix} 1 & f_2 & f_1 & f_1 f_2 \\ 0 & 1 - f_2 & 0 & f_1(1 - f_2) \\ 0 & 0 & 1 - f_1 & (1 - f_1) f_2 \\ 0 & 0 & 0 & (1 - f_1)(1 - f_2) \end{pmatrix} \begin{pmatrix} N_{RR} \\ N_{RF} \\ N_{FR} \\ N_{FF} \end{pmatrix}, \tag{6.7}$$

and therefore Eq. 6.6 can be written as

$$N_{TT} = N_{RR} + f_2 N_{RF} + f_1 N_{FR} + f_1 f_2 N_{FF}. \tag{6.8}$$

The deviations of approximated matrix elements in Eq. 6.7 to the exact values are expected to be largest for three subsets of matrix elements, which will be discussed further. The first subset contains the second and third matrix element in the first row (highlighted in green), the second subset contains the first to third matrix element in the first column (highlighted in blue), whereas the third subset contains the second and third matrix element of the fourth row (highlighted in red). In the first subset, r enters linearly. For electrons with a $E_T > 25\,\text{GeV}$, r amounts to 0.93 and for $E_T > 50\,\text{GeV}$, r amounts to 0.97. This might lead to an slight overestimation of the real electron plus fake background component. However the double fake contribution dominates and there the leading matrix element is identifical in the exact and the approximated calculation. The corrections for the second subset are real electron corrections and are dominated by mis-identified electrons from the Drell-Yan process, which are well described in the simulation. The correction for the third subset describes cases, where a real electron is mis-identified as a fake and a real fake is mis-identified as an electron. The main source of such signatures are W+jets events. The goodness of this combination of approximation and Monte Carlo simulation based corrections will be evaluated later.

[11] The contribution of N_{RR} to N_{TT} is predicted precisely by the simulation of the background processes discussed in Sections 6.1 to 6.3.

In the following, the derivation of the formalism with the $r = 1$ approximation will be continued. The corresponding inverted matrix with the $r = 1$ approximation is

$$\begin{pmatrix} N_{RR} \\ N_{RF} \\ N_{FR} \\ N_{FF} \end{pmatrix} = \begin{pmatrix} 1 & \frac{f_2}{f_2-1} & \frac{f_1}{f_1-1} & \frac{f_1 f_2}{(f_1-1)(f_2-1)} \\ 0 & \frac{1}{1-f_2} & 0 & -\frac{f_1}{(f_1-1)(f_2-1)} \\ 0 & 0 & \frac{1}{1-f_1} & -\frac{f_2}{(f_1-1)(f_2-1)} \\ 0 & 0 & 0 & \frac{1}{(f_1-1)(f_2-1)} \end{pmatrix} \begin{pmatrix} N_{TT} \\ N_{TL} \\ N_{LT} \\ N_{LL} \end{pmatrix}. \tag{6.9}$$

By using Eq. 6.9 and the fake factor definition $F_i = \frac{f_i}{1-f_i}$, the expressions in Eq. 6.8 can be replaced as follows:

$$f_2 N_{RF} = F_2 N_{TL} - F_1 F_2 N_{LL}, \tag{6.10}$$
$$f_1 N_{FR} = F_1 N_{LT} - F_1 F_2 N_{LL} \text{ and} \tag{6.11}$$
$$f_1 f_2 N_{FF} = F_1 F_2 N_{LL}. \tag{6.12}$$

These equations can be written as a contribution of one real electron and one fake, $N_{\ell+jets}$, and a contribution of two fakes, $N_{multijets}$:

$$N_{\ell+jets} = F_2 N_{TL} + F_1 N_{LT} - 2 \cdot F_1 F_2 N_{LL} \text{ and} \tag{6.13}$$
$$N_{multijets} = F_1 F_2 N_{LL}. \tag{6.14}$$
$$\tag{6.15}$$

The final result, the sum of these two contributions, can be written as.

$$N_{\ell+jets\,\&\,QCD} = F_2 N_{TL} + F_1 N_{LT} - F_1 F_2 N_{LL}. \tag{6.16}$$

It is important to note that $N_{\ell+jets}$ and the resulting $N_{\ell+jets\,\&\,QCD}$ are defined as a difference of two numbers (or mass distributions), which are of similar size. Such terms lead to large uncertainties in the result. If r was not set to one in Eq. 6.5, the corresponding equations would contain complicated coefficients instead of fake factors F in front of N_{LT}, N_{TL} and N_{TT}, which cannot be interpreted in a straightforward way as the fake factors F can be. Furthermore, without the $r = 1$ approximation, larger statistical uncertainties due to the additional subtractions are expected.

In terms of the actual analysis, "f" and "F" can be expressed as:

$$f = \frac{\text{Number of particles passing "tight"}}{\text{Number of particles passing "loose"}} \text{ and} \tag{6.17}$$
$$F = \frac{\text{Number of particles passing "tight"}}{\text{Number of particles passing "loose" but fail "tight"}}. \tag{6.18}$$

Due to the different selection criteria for the leading and subleading electron the two fake factors, F_1 and F_2 are replaced by F_{lead} and F_{subl} to relate them closer to the analysis. This allows to express the final background formulas follows:

$$N_{\ell+jets} = F_{subl}N_{TL} + F_{lead}N_{LT} - 2 \cdot F_{lead}F_{subl}N_{LL}, \tag{6.19}$$
$$N_{multijets} = F_{lead}F_{subl}N_{LL} \text{ and} \tag{6.20}$$
$$N_{\ell+jets\,\&\,multijets} = F_{subl}N_{TL} + F_{lead}N_{LT} - F_{lead}F_{subl}N_{LL}. \tag{6.21}$$

Although $N_{\ell+jets}$ contains all contributions from signatures with one real electron and one fake, this will be referred to by its main contribution, the W+jets contribution, according to the convention also used in the ATLAS dilepton resonance search.

6.4.3 Electron Fake Factor Estimation

The fake factors F are estimated via an "inverse" Tag and Probe method in a jet-enriched sample using all reconstructed electron candidates. Ideally the sample was pure, e.g., contained no real electrons, which were mis-identified as jet-like. However, a sample with a very high purity can only be derived with a selection that has a low efficiency. In order to have a sufficient number of events, a balance between purity and efficiency needs to be found. With a Tag and Probe method, a sufficient purity and efficiency can be achieved. The idea of Tag and Probe is to choose an electron candidate as a tag, which has a high probability to be a jet, and to consider all other electron candidates in the event as probes. By imposing further requirements on the properties of the tag and probe pair, the probability that the probe is also jet-like, is increased to a sufficient level. Remaining contributions, e.g., of mis-identified electrons, are corrected for by the use of Monte Carlo simulations.

In the following, the selection used for the tag and probe method is described. The considered phase space in this method needs to be compatible with the signal selection of this analysis. To achieve this, the basic selection criteria like data quality, phase space cuts and trigger requirement are the same as in the signal selection. The tag electron candidate is required to satisfy the loose electron identification level, but required to fail the track match criterion, which is part of the medium identification level. In case of multiple tags, all tags are considered[12]. All other electron candidates are considered as probes and it is checked whether they satisfy the full signal selection criterion ("tight")[13] or the loose electron identification but fail the track match requirement ("loose fail tight"). The ratio of the number of probe candidates satisfying the two categories corresponds to the fake factor as defined in Eq. 6.18.

This basic selection is refined to suppress contributions from real electrons coming from W+jets decays or Drell-Yan decays at the Z pole mass. To suppress the first category of electrons, a missing transverse energy cut is applied. Cut values of 15 GeV to 35 GeV were tested using Monte Carlo simulations, and finally $\not{E}_T < 25\,\text{GeV}$ was chosen to obtain the best balance between purity and the number of probes remaining after the cut. Lowering this cut to 15 GeV reduces the available number of probes by approximately 40% while

[12] Each pair of tag and probe is evaluated, but if the same probe passes the selection with multiple probes, it is counted only once.

[13] The full signal selection requires the leading electron to be isolated, whereas there is no such requirement on the subleading electron. The same requirements are imposed for the "tight" requirements in this method. For the "loose fail tight" candidates, the results where identical within statistical uncertainties, when imposing an isolation requirement on the leading electron or not. Therefore this requirement has been dropped to increase the number of available probes.

the estimated size of W+jets contributions is reduced by approximately 5%. A higher cut value of 35 GeV increases the estimated size of W+jets contributions significantly by about an factor of two, whereas the available number of probes is increased by an insignificant amount.

The largest contribution to the real electron dilution are electrons from decays of Z bosons, where one of the electrons is mis-identified. To suppress this contribution, the mass of the candidate pair of tag and probe has to satisfy $|m_{\text{tag and probe}} - 91\,\text{GeV}| > 20\,\text{GeV}$. Furthermore both electron candidates are required to have the same charge. The reason is as follows: Two electrons originating from a Z boson decay have an opposite charge sign, whereas the probability to assign a positive or negative charge to a jet, which is mis-identified as an electron, is of same size. Therefore only every second fake jet should be rejected, whereas almost all contributions of mis-identified electrons from the Drell-Yan process should be rejected. However, there is a small charge mis-identification probability. Averaged over η, it amounts for electrons with an E_T of 100 GeV to below 0.1%, and can increase up to about 1% at highest $|\eta|$. The corresponding scale factor, the ratio of the mis-identification efficiency in data and Monte Carlo simulation, has not been studied explicitly. However, the size of a possible bias due to an incorrect simulation of the charge mis-identification, is assumed to be of order 0.1% to 1% times the deviation of the scale factor from one. This is expected to be a sub percent effect that can be neglected.

The remaining dilution must be corrected for by Monte Carlo simulations[14]. Most simulated samples have filters applied, which require certain minimum transverse energies or invariant masses. To match these requirements, a minimum invariant mass of 40 GeV is required for the Tag and Probe pairs.

The probe E_T distributions are shown in Fig. 6.11. The dilution in the case of the "loose fail tight" distributions is small, as expected, because real electrons have a high probability to satisfy the medium identification criterion. In case of the "tight" distributions, the corrections range from below 5% at 25 GeV to approximately 40% for $E_T > 120\,\text{GeV}$. The corresponding distributions, single-differential in η and double-differential in η and p_T, show a similar behavior with respect to the diluation. Therefore, they are listed in the Appendix in Fig. A.10 to A.12 and are not discussed further.

From the dilution corrected distributions, the fake factors are derived according to Eq. 6.18. The results are shown in Fig. 6.12. The leading fake factor F_{lead} shows only a weak dependence on E_T and amounts to $\approx 15\%$, while F_{subl} increases with E_T from $\approx 17\%$ to $\approx 27\%$. The reason for this different behavior with E_T comes from the fraction of leptons in the hadronic shower, which increases with E_T and makes hadronic showers look more similar to electromagnetic ones. The electron identification requirements are evaluated in fixed windows in η and ϕ, which are surrounded by a region which is checked for energy depositions to evaluate the isolation of the electron. An isolation requirement is imposed on the leading electron only, and dampens the principal rise of the fake factor with E_T, because it rejects broad hadronic showers.

The fake factors as a function of η are shown in the two bottom plots of Fig. 6.12. They depend only weakly on η in the calorimeter barrel ($|\eta| < 1.37$). In the calorimeter end-caps, a strong dependence is observed, the fake factors increase significantly with $|\eta|$. In this high $|\eta|$ region, the granularity of the calorimeter is coarser than in the barrel, and the electrons traverse more not-instrumented material before entering the calorimeter.

[14]The Tag and Probe method is also evaluated for the relevant simulated samples. The resulting distributions can be subtracted from the distributions derived from data to correct for the dilution.

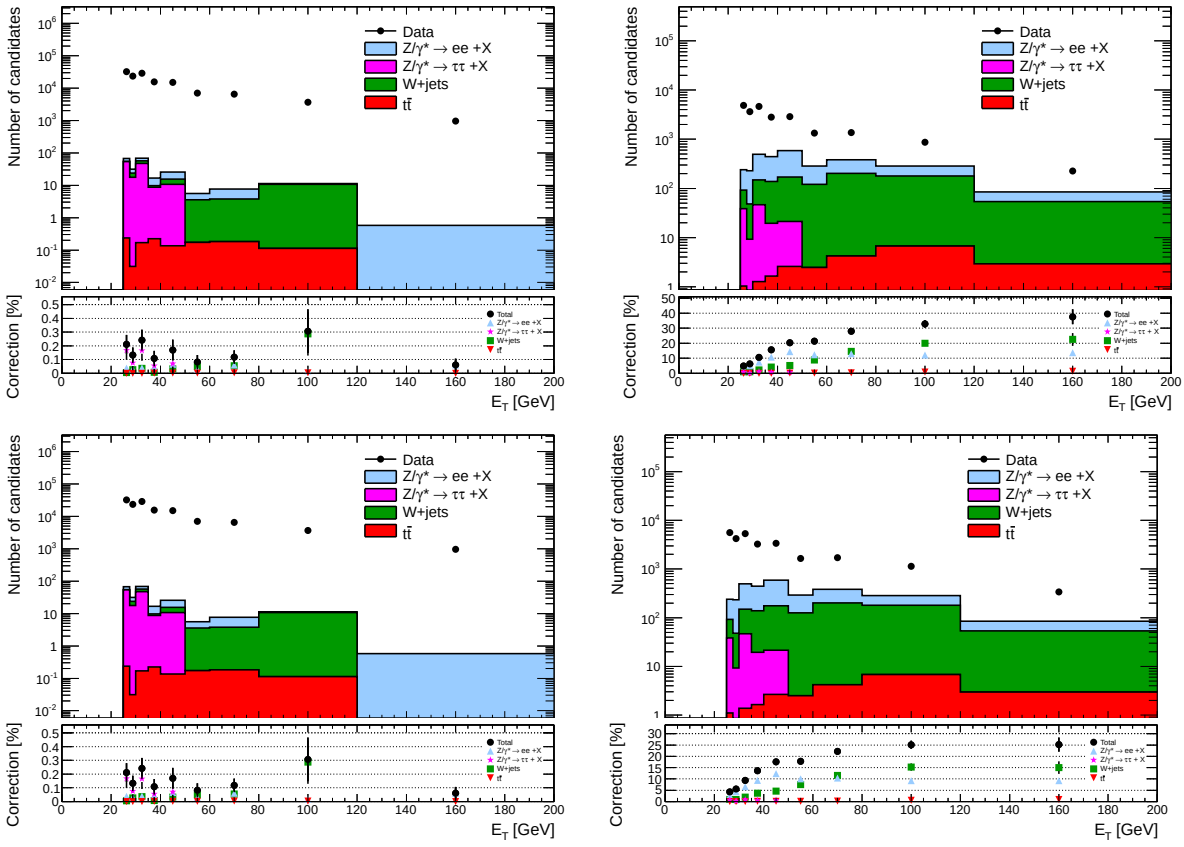

Figure 6.11: The E_T distribution of the leading "loose fail tight" probes and the leading "tight" probes are shown in the top left and top right plot, respectively. The corresponding distributions for the subleading case are shown in the bottom left and right plots. Data is shown by black markers, and the corrections are shown as a colored stack of histograms. In the bottom panel, the relative size of the Monte Carlo corrections are shown. The distributions are scaled to an integrated luminosity of $4.9\,\mathrm{fb}^{-1}$.

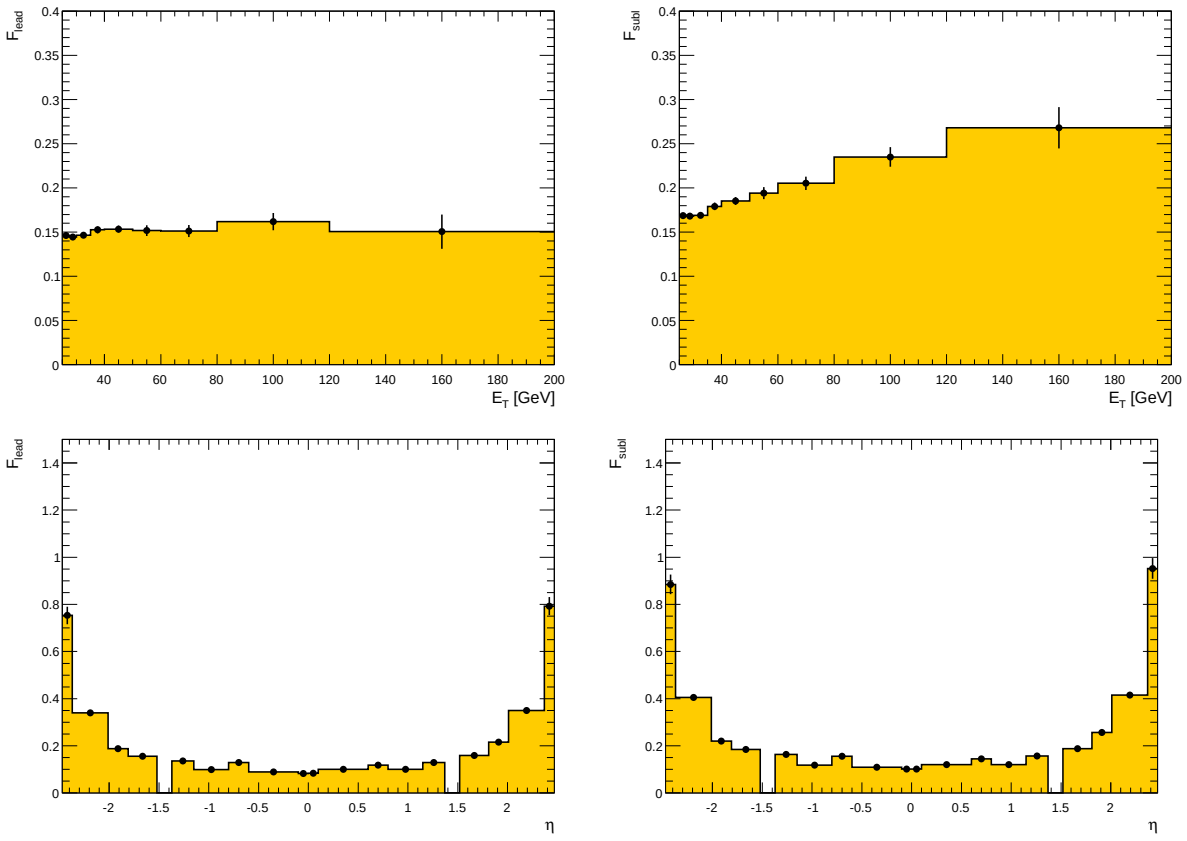

Figure 6.12: The fake factor binned in E_T is shown for the leading electron on the top left plot and for the subleading electron on the top right. The corresponding fake factors binned in η are shown in the bottom row. The error bars indicate statistical uncertainties only.

Therefore the properties of electrons can only be measured less precise[15] than in the calorimeter barrel, which lead to an increase of the probability to mis-reconstruct a jet as an electron up to $\approx 90\%$. The fake factor binned in η and E_T is constructed as follows: It is binned in three different η regions[16]: $|\eta| < 2.01$, $2.01 \leq |\eta| < 2.37$, $2.37 \leq |\eta| < 2.47$. In each η region a binning in E_T is chosen, whose granularity depends on the number of events available in that η bin. The shape of the fake factor distribution as a function of E_T in each η bin is similar to the distribution binned in E_T only and is therefore not discussed further. It can be found in the Appendix in Fig. A.13.

6.4.4 Fakeable Object Selection

In the following, the measurement of the distributions the fake factors are to be applied to, the so-called fakeable object distributions, are discussed. First, the abstract definitions of the three event categories, N_{TL}, N_{LT} and N_{LL} as introduced in Section 6.4.2, will be matched to the actual cuts used. A "T" as first letter stands for a leading electron as defined in the signal definition, that is amongst others an isolated electron. A "T" as second letter denotes an electron, which is subleading "tight"and therefore not necessarily isolated. The "L" as first (second) letter stands for a leading (subleading) "loose fail tight" candidate, where no isolation requirement is imposed on the leading electron, see Section 6.4.3. In each event, all pairs are evaluated according to the described criteria. It is not possible to reproduce exactly the algorithm used for the signal selection by taking only the highest E_T pair per event, because every candidate pair has a probability to be mis-identified as a pair of electrons. The impact is expected to be small, because the fake factors are smaller than one, and therefore the method does not predict that, e.g., on average two pairs per event are expected to pass the signal selection. Besides this highest E_T cut and the electron identification criteria, the selection is the same as the signal selection.

The mass distributions of the three categories N_{TL}, N_{LT} and N_{LL} without the Monte Carlo simulation based dilution correction and without any weights applied, e.g., no fake factors, are shown in the left plot of Fig. 6.13. The dilution from mis-identified real electrons in the N_{TL} and N_{LT} distributions around the Z pole mass is clearly visible while the N_{LL} shows no deviation from a monotonic falling curve in that region. This indicates that the probability that both real electrons from a Z decay are mis-identified at once is negligible.

The right plot shows the result of the convolution of the mass distributions with the fake factors. The Monte Carlo simulation based corrections are calculated with the $r = 1$ approximation used to derive Eq. 6.7. They amount to approximately 50% at the Z pole mass and decrease rapidly with mass to 3.7% at 120 GeV. The Drell-Yan and $t\bar{t}$ *type ee* corrections account for the approximation of the matrix elements highlighted in blue in Eq. 6.7, whereas the W+jets corrections account for the ones highlighted in red.

Further, the percent size of these corrections to the final mass spectrum was confirmed by a second fake factor method, which was developed by a colleague for the ATLAS dilepton resonance search[17]. The size of real electron contributions to the mass spec-

[15] The electron identification cuts were derived such by the EGamma performance group that the probability to identify a real electron as electron is approximately independent of η. Therefore the fake probability increases with η.

[16] The barrel end-cap calorimeter transition region $1.37 < |\eta| < 1.52$ is always excluded.

[17] In contrast to the method described in this thesis, the fake factors were derived on a data sample that

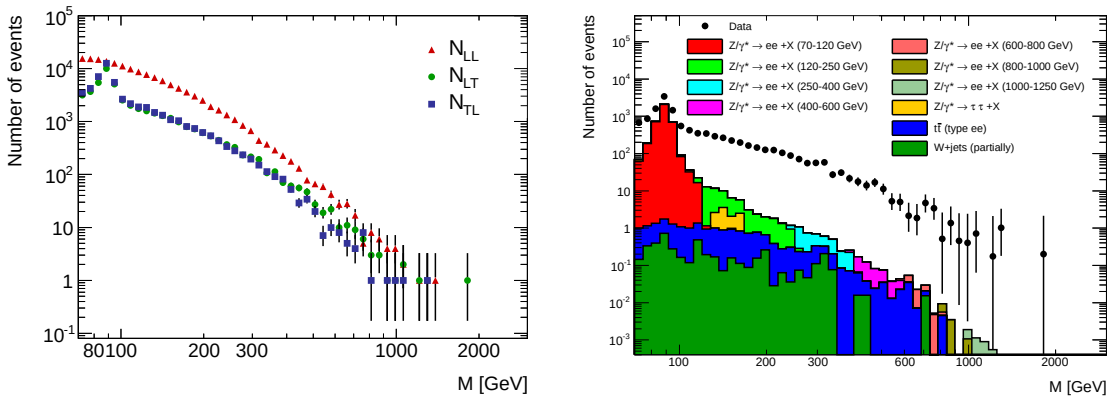

Figure 6.13: The mass distributions for the three categories N_{TL}, N_{LT} and N_{LL} are shown in the left plot. No dilution correction or weights, e.g., fake factors are applied. The mass distribution derived with the E_T and η dependent fake factors is shown in the right plot. The black markers represent the data without dilution corrections. The latter are stacked on top of each other. The W+jets corrections is only partially as described in the text.

trum was estimated by comparing the number of electron candidate pairs, N_{OS}, which have an opposite electrical charge sign, to the number of electron candidate pairs with the same electrical charge sign, N_{SS}. For dijet and W+jets events, $N_{OS} - N_{SS}$ should be approximately zero, because the probability for a jet to have a positive or negative charge sign assigned to can be considered as equal for this purpose. In contrast, electron pairs produced via the Drell-Yan process always have an opposite charge sign and are reconstructed almost exclusively[18] as opposite sign pair. Therefore, the quantity $(N_{OS} - N_{SS})/(N_{OS} + N_{SS})$ can be used to estimate the relative fraction of the real electron contribution. It was found to be compatible with the percent level Monte Carlo corrections derived in this thesis.

In the following, the dependence of the background estimate on η is evaluated. The pure multijet contribution is chosen for the discussion, because comparisons with and without fake factors can be performed in a meaningful way[19]. Fig. 6.14 shows the absolute value of the pseudorapidity difference between the leading and the subleading electron candidate, $|\Delta\eta|$, for different pair mass thresholds with no fake factors applied. For masses above 70 GeV, the distribution is dominated by small values of $|\Delta\eta|$, whereas at masses above 500 GeV, large values of $|\Delta\eta > 2.5|$ are dominant, which indicate that both candidates traverse the detector in opposite z-direction. The latter is the typical signature for multijet production, e.g., via quark gluon scattering in the t-channel, while small $|\Delta\eta|$ are dominant for annihilation processes in the s-channel.

This increase in $|\Delta\eta|$ for higher masses leads to an increased fraction of electron candidates with $|\eta > 2.01|$, where the fake factor is approximately a factor 2 to 5 higher than at lower values of $|\eta|$. This effect is shown in the two top plots of Fig. 6.15 for the

was triggered by jet triggers instead of electron triggers. Nevertheless, the fake factors derived there are of similar size.

[18] At a transverse momentum of 100 GeV, the charge mis-identification is below 0.1% and therefore neglected.

[19] The W+jets contribution is calculated from three distributions, each with a different fake factor weight applied to, which does not allow a direct comparison with and without fake factors, see Eq. 6.19.

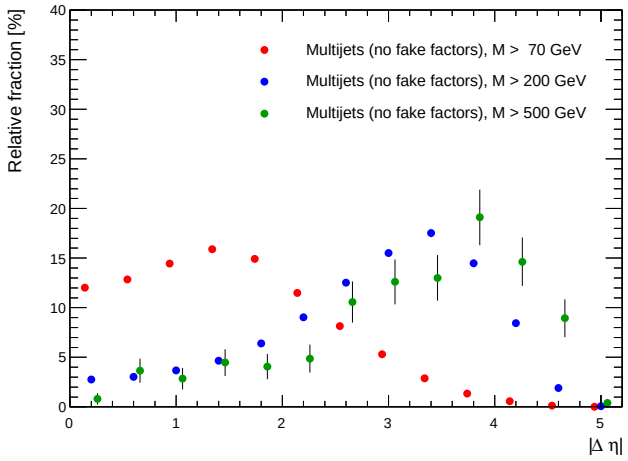

Figure 6.14: The relative fraction of $|\Delta\eta|$ is shown for the multijet background with no fake factors applied, where $|\Delta\eta|$ is the absolute value of the pseudorapidity difference between the leading and the subleading electron candidate. The distributions are shown for three pair mass thresholds. The error bars indicate statistical uncertainties, only.

leading and subleading electron candidate. At masses above 70 GeV, more than 90% of the candidates satisfy $|\eta| < 2.01$, whereas only approximately 70% satisfy $|\eta| < 2.01$ for pair masses above 500 GeV. With fake factors applied, this picture changes drastically as shown in the two bottom plots of Fig. 6.15. The number of candidates with $|\eta > 2.01|$ decreases from approximately 75% to half this value. This demonstrates how important it is to take the fake factor η dependence into account.

6.4.5 Extrapolation of the Mass Distribution

The mass spectrum after dilution correction is extrapolated with the same method, which was already used for the extrapolation of the Monte Carlo-driven background predictions. However, one additional step was added here to increase the fit range that can be used. If a bin needs to be very broad, e.g. 50 GeV, to satisfy the criterion that at least 12 not-weighted events are contained, there is a bias, if the position of the bin center is used in the fit. For "rapidly" decreasing curves, most entries within a bin are located close to the left bin border. This effect becomes the more important, the broader the bins are in relation to their population. To take this into account, the average abscissa (mass) position in each bin is calculated as the average of the positions (masses) of the events contained in this bin. The ordinate of this point is calculated as the sum of the individual event weights divided by the width of the bin. This set of points is then fitted instead of the original histogram, which could only have been used up to lower masses.

The lower fit range interval is [120 GeV, 160 GeV] and sampled in 5 GeV steps, while the upper fit range interval is [500 GeV, 1000 GeV] and sampled with a step size[20] of 20 GeV. The resulting fit uncertainty is smaller than 7% in the mass range from 130 GeV to 500 GeV while the extrapolation to, e.g., 2000 GeV yields a fit uncertainty of 102%. The extrapolation to low masses is used to estimate the contribution in the region of

[20] Double counting of fit ranges is avoided, see Section 6.2.2.

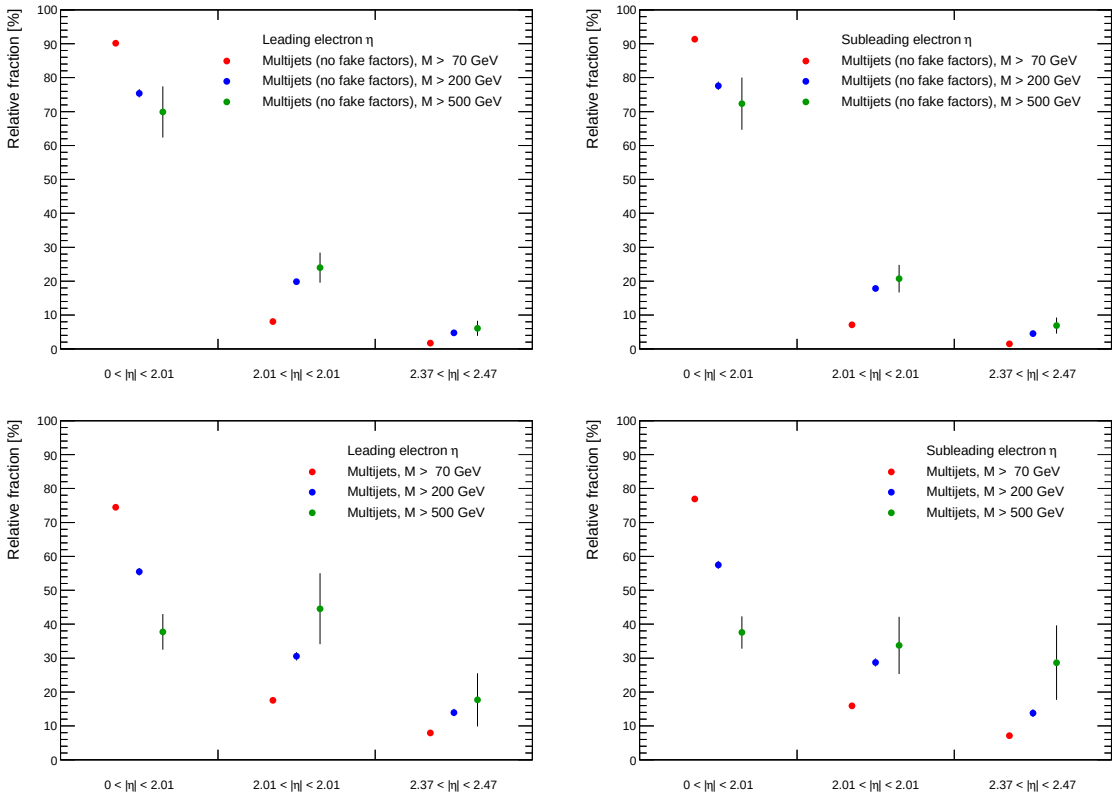

Figure 6.15: The relative fraction of the multijet background as a function of $|\eta|$ is shown for three pair mass thresholds. The top (bottom) plots show the distributions without (with) fake factors applied. The left (right) plot corresponds to the distributions for to the leading (subleading) electron candidate. These distributions are shown for three pair mass thresholds. The error bars indicate only statistical uncertainties.

the Z boson pole mass, where no precise direct estimation is possible. This approach results in 20% extrapolation uncertainty. In the following, the normalization used to compare the background expectation to data is described, followed by the comparison itself to demonstrate that the W+jets and multijet background can be well described with *method II*.

6.4.6 Normalization

The background expectation is normalized to data in the mass range 70 GeV to 110 GeV. This avoid a systematic shift due to the luminosity scale, which has an uncertainty of 1.8%, and the observed 3% difference between the theory cross-section calculated for the Drell-Yan process and the extracted cross-section from the simulation with k-factors applied. In this normalization region, the total background consists to more than 99.5% of Drell-Yan background only. The normalization is calculated as follows. The number of W+jets and multijet estimated, $N_{\text{W+jets and multijets}}$, is derived from data. Therefore no additonal normalization is needed. A scale

$$s = \frac{N_{\text{Data}} - N_{\text{W+jets and multijets}}}{N_{\text{MC based}}} \tag{6.22}$$

is applied to the number of events estimated using Monte Carlo simulations, $N_{\text{MC based}}$. The scale $s =$ amounts to 1.05, which is close to the factor of 1.03 expected from the Drell-Yan cross-section, if a luminosity scale is not taken into account. The value of s is well covered by the cross-section and luminosity uncertainties.

Fig. 6.16 shows the mass distribution measured in data compared to the full background estimation. The ratio in the mass range above the Z boson pole mass up to 200 GeV typically fluctuates within statistical uncertainties around unity. No hint for a systematic deviation is observed.

6.4.7 Systematic Uncertainties

To evaluate the uncertainty of this fake factor estimate, the impact of variations, e.g., using different cut values or different reverse identification criteria, is propagated into the extrapolated mass spectrum. The relative deviation of these mass spectra with respect to the estimate derived with the default cuts is shown in Table 6.7. In the following, the individual variations will be discussed, followed by the explanation of the recipe the total uncertainty is calculated with.

The largest uncertainty arises, when the strip cuts requirement was used as reverse identification criterion instead of the fail track match requirement. For 130 GeV $< M <$ 1200 GeV, the deviations are below 20%, while they increase to 64% for masses above 2000 GeV.

The impact of the cut on the missing transverse energy, which was introduced to suppress W+jets Monte Carlo corrections during the fake factor calculations, has been studied. If this cut is removed, the final estimate is affected by up to 3.2% (14%) for masses of up to 800 GeV (above 2000 GeV). If the default cut value of 25 GeV is increased to 35 GeV, the variation of the background estimate is below 3%. Lowering the cut value to 15 GeV has an impact below 3% for masses up to 400 GeV and increases up to 30% for masses above 2000 GeV. This cut value of 15 GeV can be considered as an extreme or aggressive variation, as it reduces the W+jets by an negligible amount, while it reduces

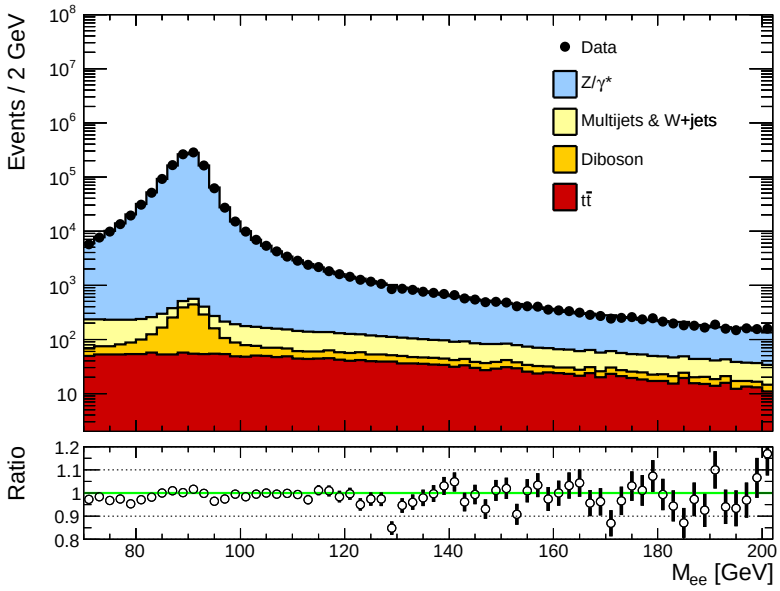

Figure 6.16: The mass distribution for data in black is compared to the total background estimation where the multijet and W+jets contribution is estimated using *method I*. The Monte Carlo predictions are normalized to data as described in the text. The inset on the bottom shows the ratio of the number of events in data over the one in the background prediction.

the number of fake factor probes by approximately 40%. This indicates that the missing transverse energy of the W+jets contribution is well described in the simulation. The (per bin) largest deviation observed when variing the value of the missing transverse energy cut is taken as uncertainty on the fake background estimate.

Furthermore, the E_T cut on the tag candidates was raised from 20 GeV to 25 GeV, which alters the background estimation by less than 3% up to 400 GeV and by 29% for masses above 2000 GeV. Due to the trigger requirement, the cut value cannot be lowered.

To evaluate the dependence of the fake factors on the dilution, the cross-sections of the processes, which are used for the corrections, are varied up and down by one standard deviation, see Section 4.1. This results into an uncertainty of 2% to 3% of the mass-dependent fake factor estimate. This is plausible, because the dilution corrections are small in the low E_T bins of the fake factors. Although the dilution corrections are larger at higher E_T, the fake factors at high E_T do not contribute dominatly, because high fake pair masses are typically formed by fakes, which have large opening angles in η with respect to each other, but only moderate individual E_T.

Furthermore, the impact of neglecting the η and/or E_T dependence of the fake factor has been studied. This is expected to lead to wrong results and is therefore not included in the uncertainty. Nevertheless, it is evaluated, because the second W+jets and multijet method, which will be discussed in the next section, does not take these dependences fully into account. The results are as expected, starting at medium masses (400 GeV), all estimates with neglected dependences predict a lower number of events.

The total uncertainty is calculated as quadratic sum of the discussed contributions. It is dominated by the extrapolation and the reverse identification criterion uncertainty and amounts to less than 20% for masses between 130 GeV and approximately 800 GeV, while

it increases up to 128% for masses above 2000 GeV.

Table 6.7: This table shows the number of events estimated for the multijet and W+jets background contribution derived with *method I*. Furthermore, the relative impact of variations in the analysis method on the estimate are shown. The total uncertainty is calculated as described in the text. The number of events listed is scaled to an integrated luminosity of $4.9\,\mathrm{fb}^{-1}$.

Mass [GeV]	70 - 110	110 - 130	130 - 150	150 - 170	170 - 200	200 - 240
Fake factor estimate	2434	708	505	364	371	295
Fit uncertainty	20 %	11 %	6.8 %	4.2 %	2.3 %	1.9 %
Fail strip cuts (η, E_T)	45 %	24 %	16 %	16 %	12 %	11 %
No $\not\!\!E_T$ cut	1.4 %	1.5 %	1.5 %	1.4 %	1.3 %	1.2 %
$\not\!\!E_T > 15$	2.9 %	1.0 %	0.32 %	0.15 %	0.50 %	0.75 %
$\not\!\!E_T > 35$	2.5 %	1.5 %	1.0 %	0.66 %	0.30 %	0.10 %
Tag $E_T > 25\,GeV$	2.9 %	1.1 %	0.45 %	0.10 %	0.38 %	0.63 %
MC correction cross-section	1.6 %	1.6 %	1.6 %	1.7 %	1.7 %	1.7 %
Fake factor (E_T)	15 %	15 %	13 %	12 %	9.5 %	6.4 %
Fake factor (η)	9.5 %	6.1 %	4.8 %	4.0 %	3.5 %	3.3 %
Fake factor (not differential)	13 %	11 %	9.7 %	7.5 %	4.7 %	1.3 %
Total uncertainty	50 %	27 %	18 %	16 %	12 %	12 %

Mass [GeV]	240 - 300	300 - 400	400 - 800	800 - 1200	1200 - 2000	2000 - 3000
Fake factor estimate	224	142	74	3.1	0.42	0.025
Fit uncertainty	2.2 %	1.8 %	8.6 %	39 %	67 %	102 %
Fail strip cuts (η, E_T)	10 %	11 %	8.0 %	7.4 %	28 %	64 %
No $\not\!\!E_T$ cut	0.97 %	0.66 %	0.38 %	3.2 %	7.4 %	14 %
$\not\!\!E_T > 15$	0.75 %	0.35 %	1.5 %	7.9 %	16 %	30 %
$\not\!\!E_T > 35$	0.37 %	0.55 %	0.45 %	0.12 %	0.86 %	2.9 %
Tag $E_T > 25\,GeV$	0.63 %	0.26 %	1.9 %	9.0 %	17 %	29 %
MC correction cross-section	1.8 %	1.9 %	2.1 %	2.5 %	2.8 %	3.0 %
Fake factor (E_T)	2.3 %	3.7 %	14 %	36 %	53 %	72 %
Fake factor (η)	3.8 %	5.5 %	11 %	24 %	37 %	55 %
Fake factor (not differential)	5.1 %	13 %	27 %	53 %	70 %	85 %
Total uncertainty	11 %	11 %	12 %	42 %	76 %	128 %

6.5 Multijet and W+Jets Estimation: Method II

This method determines the multijet background in a data-driven way and the electron+jets component using Monte Carlo simulations. The latter component consists of the W+jets contribution, which will be described here, and the part of the $t\bar{t}$ background with one real electron and one fake particle, which was already described in Section 6.3.

In comparison to *method I*, this method has certain limitations and is used as a cross-check only. Nevertheless, it is a fully evaluated estimate, which gives additional insights into the composition of the W+jets contribution, which cannot be extracted in the fully data-driven method.

In the following, the W+jets estimation and the multijet estimation will be discussed separately followed by a comparison of *method II* to *method I*.

6.5.1 Monte Carlo W+Jets Estimation

For the determination of the W+jets background, Monte Carlo samples with the simulation of the process $pp \rightarrow W + n$ jets $+ X$ with $0 \leq n \leq 5$ and $E_{T,Jet} > 20\,\text{GeV}$ on parton level are available[21]. In general, it is difficult to estimate backgrounds, which contain electron fakes from Monte Carlo simulations, because of the high rejection factor of $\approx 10^5$ for jets mis-identified by the medium identification criteria. While it is helpful in the search that only one out of ten thousand jets is mis-identified as an electron, it is hard to simulate enough events to get a well described mass spectrum, which can be extrapolated to high mass.

To cope with this situation, not only the estimation using the full selection is looked at, but also looser selections are evaluated. The *loose* selection differs from the full selection by the following requirements: Both electrons need to be loose instead of medium and no requirements on the isolation and b-layer hit properties are made. An even looser selection, called *no-ID* selection, with no electron identification level required, is also evaluated.

The mass distributions, derived with the *loose* and the *no-ID* selections, are normalized to the same number of events in the mass range 70 GeV to 200 GeV as in the mass distribution derived with the full selection. This allows to compare the shapes of the distributions. The impact of the normalization will be discussed later.

For each of the three selections, the mass distributions, separate for each jet multiplicity, are shown in Fig. 6.17. The dominant feature of those spectra is the different slope of the mass distributions for different jet multiplicities. The lower the jet multiplicity, the steeper the spectrum. For low invariant electron + fake jet masses, low p_T jets contribute dominantly. Therefore the topologies with only one jet dominate due to the high cross-section. At higher masses, the higher multiplicities of jets overcompensate the lower cross-section of these topologies. This behavior can be seen very clearly in the case of the two loose selections, but only to a limited extend in the case of the full selection. In the latter case, the number of available events for the derivation of the mass distribution

[21] The contribution of $W + 0$ jets has been found to be negligible and is not considered further. The contributions of W bosons that decay into a τ and a neutrino, where the τ decays into an electron, are approximately 3% to 5% of the size of the contribution, where the W decays directly into an electron and a neutrino. Due to the small size of the contribution and the insufficient number of events available to extrapolate the mass distribution of these process to high masses, these decays have been neglected in this analysis.

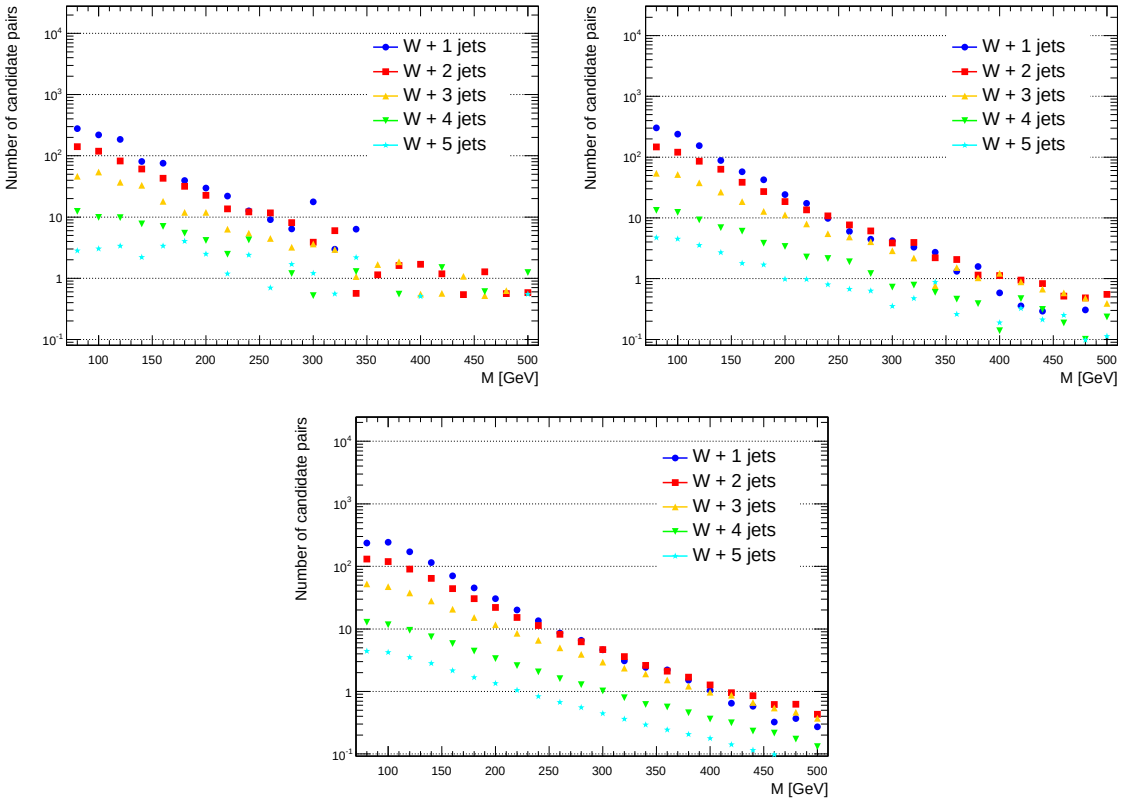

Figure 6.17: The top left plot shows the mass distribution for different jet multiplicities derived with the full selection, whereas the top right (bottom) plot shows the same distribution derived with the *loose* (*no-ID*) selection. The statistical uncertainties are suppressed to clearly show the shape of the distributions. The 100% uncertainty level for $W + 1$ jets is reached at approximately 0.6 scaled events for the top left plot, while the relative uncertainty of the highest mass entry for $W + 1$ jets in the top right (bottom) plot has an uncertainty of approximately 33% (22%). The distributions in the top left plot are scaled to an integrated luminosity of $4.9\,\mathrm{fb}^{-1}$, while the distributions in the top right and bottom plot are scaled such (for each multiplicity individually) that they contain the same number of events in the mass window 70 GeV to 200 GeV as the corresponding distribution in the top left plot.

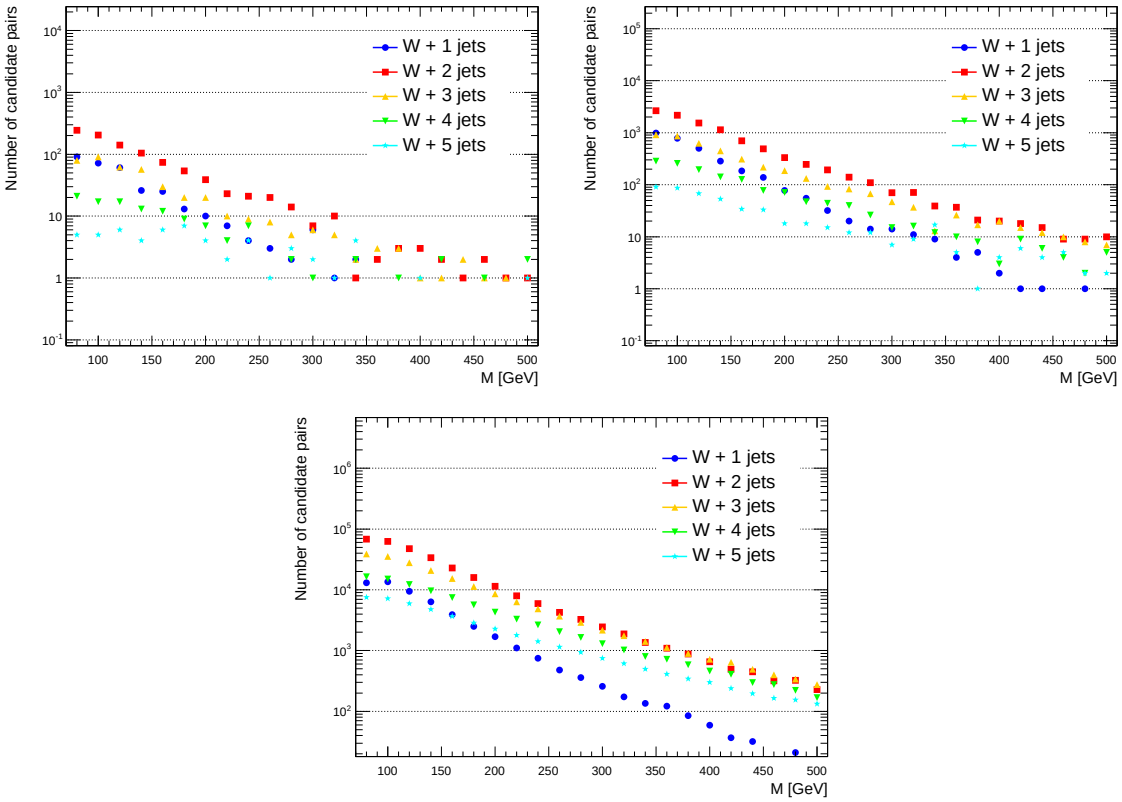

Figure 6.18: The top left plot shows the mass distribution for different jet multiplicities in case of the full selection while the top right (bottom) plot shows the same in case of the *loose* (*no-ID*) selection. The statistical uncertainties are suppressed to clearly show the shape of the distributions. The entries in all plots are the raw number of events available in the simulated sample and are neither scaled to luminosity or normalized.

is significantly lower, and the distribution fluctuate too strongly too define a slope. The raw number of events, without any weight or scaling applied, is shown in Fig. 6.18. By using the *loose* (*no-ID*) selection an order (two orders) of magnitude of available events is gained.

The different slopes of the mass distributions make extrapolations to high masses difficult, because each W+jets multiplicity contributes differently to the total W+jets background as a function of mass. Therefore, the mass distributions have to be extrapolated individually for each jet multiplicity. This is only possible for the two looser selections, where a sufficient number of events is available. The $W + 1$ jets Monte Carlo sample has the lowest statistical uncertainties and is used as example for the following discussion.

The mass distribution derived with the full selection has no events left above 260 GeV. In case of the *loose* selection, there are three events left above 400 GeV, while there are more than a hundred events left in the *no-ID* case. This favors the *no-ID* selection for the extrapolation, if the shapes are similar. This will be evaluated in the following.

In Table 6.8, the number of events predicted for the full selection is compared with the prediction using the *no-ID* selection normalized in two different ranges[22], 70 GeV to

[22]The normalization is performed for each multiplicity separately, therefore five normalizations are per-

200 GeV and 130 GeV to 200 GeV. In case of the first (second) normalization range, the number of events in the first two bins for the *no-ID* and the full selection agree within one (two) standard deviation(s). The different results for the two normalization ranges at low masses can be explained as follows: The jet E_T filter used in the production of the Monte Carlo samples requires that each jet has $p_T > 20\,\text{GeV}$. For higher multiplicities, there are more candidate jets available. In events with more than two jets, at least three pairs can be formed. Due to the highest E_T pair cut[23], always the pair with the highest mass is chosen, which results into a bias towards higher masses. For example, to form an invariant mass of 70 GeV, a jet E_T of 20 GeV allows a large opening angle range with respect to the electron. But for masses of e.g. 200 GeV, the phase space in terms of possible opening angles for the same jet E_T of 20 GeV decreases significantly. Therefore the number of pairs per event decreases with increasing mass.

In mass regions between 200 GeV and 800 GeV, the impact of the different normalization ranges is negligible and the difference to the result using the full selection is within one standard deviation. At even higher masses, there are not enough events left to make a meaningful comparison. In general, this demonstrates that the shape approximation is not perfect, but still reasonable. The *no-ID* selection is chosen as default estimate, because the high number of events is needed for the extrapolation.

The statistical uncertainty of the normalization factors scaling the number of events of the *no-ID* selection to the number of events of the full selection is taken as additional normalization uncertainty. It amounts to 9% to 12% depending on the jet multiplicity.

Extrapolation to high Masses

The extrapolation to high masses is done with the same fit procedure as the other Monte Carlo driven background estimates. The fit range intervals used are $[70\,\text{GeV}, 400\,\text{GeV}]$ for the lower range for all multiplicities. The upper interval ranges up to the last bin with at least twelve not weighted entries. In the $W + 1$ jets case, the upper fit range interval is $[400\,\text{GeV}, 550\,\text{GeV}]$, $[400\,\text{GeV}, 950\,\text{GeV}]$ for the $W + 3$ jets case and $[400\,\text{GeV}, 1000\,\text{GeV}]$ for all other cases. The minimum distance between lower and upper fit range is required to be at least 250 GeV, and the extrapolation is used for masses above 400 GeV.

The results[24] of the extrapolation procedure are shown in Table 6.8 and agree for masses of up to 800 GeV within one standard deviation with the mass distributions before extrapolation. For higher masses, the low number of events available allows no significant comparisons[25].

Summary

Table 6.9 shows the final W+jets estimate and its uncertainties. The dominating uncertainty for masses below 1200 GeV is the cross-section uncertainty of 27.5% [53]. At higher

formed per normalization range.

[23] Jets that are reconstructed with the electron reconstruction algorithms have by definition a mass of zero, therefore E_T and p_T can be used equivalently here.

[24] The result shown is the combination (sum) of the five separate extrapolations of the mass distribution derived for each jet multiplicity.

[25] The statistical uncertainty in the table does not reflect the fact that the mass distributions for some jet multiplicities are formed by an insufficient number of events in this high mass region. If there are no events left to estimate the contribution of a jet multiplicity, the contribution to the combined uncertainty (summed over all multiplicities) is zero.

Table 6.8: The background estimates for W+jets (all multiplicities combined) are shown as a function of mass. In each section of the table, the first row shows the number of events estimated with the full selection, scaled to an integrated luminosity of $4.9\,\mathrm{fb}^{-1}$ and with no extrapolation performed. The second and third rows show the estimation using the *no-ID* selection normalised to the given normalization range as specified in parenthesis. In these rows, the uncertainties are statistical only. In the last section of the table, the two rows marked by an * show the results of the extrapolation for masses above 400 GeV.

Selection	70 - 110	110 - 130	130 - 150	150 - 170
Full	886 ± 42	318 ± 26	185 ± 18	147 ± 16
No-ID (70-200 GeV)	861.3 ± 3.1	312.1 ± 1.8	217.5 ± 1.5	143.2 ± 1.2
No-ID (130-200 GeV)	799.6 ± 2.7	290.3 ± 1.6	203.1 ± 1.3	134.6 ± 1.0

Selection	170 - 200	200 - 240	240 - 300	300 - 400
Full	134 ± 15	92 ± 12	78 ± 11	48.0 ± 8.7
No-ID (70-200 GeV)	134.8 ± 1.1	96.98 ± 0.92	66.13 ± 0.71	38.07 ± 0.50
No-ID (130-200 GeV)	127.45 ± 0.98	92.45 ± 0.81	63.78 ± 0.63	37.19 ± 0.45

Selection	400 - 800	800 - 1200	1200 - 2000	2000 - 3000
Full	18.1 ± 3.3	1.66 ± 0.96	0.0 ± 0.0	0.0 ± 0.0
No-ID (70-200 GeV)	18.13 ± 0.31	0.595 ± 0.039	0.0476 ± 0.0081	0.00067 ± 0.00067
No-ID (130-200 GeV)	18.09 ± 0.28	0.619 ± 0.037	0.0503 ± 0.0083	0.00093 ± 0.00093
No-ID (70-200 GeV)*	18.0 ± 4.1	0.658 ± 0.092	0.075 ± 0.022	0.0032 ± 0.0019
No-ID (130-200 GeV)*	17.94 ± 0.40	0.687 ± 0.084	0.081 ± 0.022	0.0036 ± 0.0020

masses the fit uncertainty becomes important as well and dominates for very high masses. The reason for the low statistical uncertainty is the high number of events available with the *no-ID* selection. The normalization and shape uncertainty do not cover the full systematics that would be needed. The goodness of the *no-ID* approximation was only tested with respect to the full selection, which has not sufficient statistics in order to be used as a proper reference. Furthermore, it cannot be evaluated whether or not the W+jets estimate with the full selection as derived from Monte Carlo simulations describes data. Therefore it is unclear, if, e.g., the fake factor, which is implicitly derived, is correct. These limitations of the W+jets estimate will be discussed further in the summary of *method II* in Section 6.5.3.

Table 6.9: The estimate and uncertainties of the W+jets background are shown as a function of mass. The number of events listed is scaled to an integrated luminosity of $4.9\,\mathrm{fb}^{-1}$.

Mass range [GeV]	70 - 110	110 - 130	130 - 150	150 - 170
Number of events	861 ± 265	312 ± 96	218 ± 67	143 ± 44
Statistical uncertainty [%]	0 %	1 %	1 %	1 %
Shape uncertainty [%]	8 %	8 %	7 %	6 %
Fit uncertainty [%]	0 %	0 %	0 %	0 %
Cross-section uncertainty [%]	28 %	28 %	28 %	28 %
Normalization uncertainty [%]	11 %	11 %	11 %	11 %
Combined uncertainty [%]	31 %	31 %	31 %	31 %

Mass range [GeV]	170 - 200	200 - 240	240 - 300	300 - 400
Number of events	135 ± 41	97 ± 29	66 ± 20	38 ± 11
Statistical uncertainty [%]	1 %	1 %	1 %	1 %
Shape uncertainty [%]	6 %	5 %	4 %	2 %
Fit uncertainty [%]	0 %	0 %	0 %	0 %
Cross-section uncertainty [%]	28 %	28 %	28 %	28 %
Normalization uncertainty [%]	11 %	11 %	11 %	11 %
Combined uncertainty [%]	30 %	30 %	30 %	30 %

Mass range [GeV]	400 - 800	800 - 1200	1200 - 2000	2000 - 3000
Number of events	18.0 ± 6.9	0.66 ± 0.22	0.075 ± 0.031	0.0032 ± 0.0021
Statistical uncertainty [%]	0 %	0 %	0 %	0 %
Shape uncertainty [%]	3 %	5 %	1 %	0 %
Fit uncertainty [%]	24 %	14 %	29 %	59 %
Cross-section uncertainty [%]	28 %	28 %	28 %	28 %
Normalization uncertainty [%]	11 %	11 %	11 %	11 %
Combined uncertainty [%]	38 %	33 %	42 %	66 %

6.5.2 Multijet Reverse Identification Method

This method uses the same reverse identification criteria as *method I* to extract the shape of the mass distribution of the multijet background. In this context, such mass distributions are called multijet templates. In contrast to *method I*, the templates are not normalized by fake factors separate for leading and subleading electrons as a function of E_T and η, but are normalized by a so-called template fit to data, which determines the fraction of multijet background in the Z boson pole mass region. Finally, the templates are extrapolated to high masses. Each of the three steps will be discussed in the following.

Template Selection

The selection used to derive the multijet templates is identical to the one used for *method I*. The full selection, as described in Chapter 5, is used with the exception of the medium electron identification level for both electrons, which is lowered to loose. Two different templates are derived. For the first template, both electrons are required to fail the track match criterion "fail track match template", whereas they are required to fail the strip cuts for the second template refered to as "fail strip cuts template".

The dilution of these templates is small. The most important contribution are misidentified electrons from the Drell-Yan process at masses close to the Z boson pole mass. In the mass range between 70 GeV and 110 GeV, the relative dilution amounts to 1.7% (6.4%) for the fail track match (fail strip cuts) template and decreases to the per mill level for higher masses. The dilution from W+jets and $t\bar{t}$ topologies is below one per cent.

Template Normalization

The normalization constant c_1 of the multijet mass templates, which are denoted by $d_{multijets}(m)$, is determined by a template fit to data according to

$$d_{data}(m) = c_0 \cdot d_{MC}(m) + c_1 \cdot d_{multijets}(m). \tag{6.23}$$

Here, $d_{data}(m)$ is the measured mass distribution with the full selection, and $d_{MC}(m)$ is the sum of the mass distributions derived for the Drell-Yan, diboson, $t\bar{t}$ and W+jets background as discussed in Sections 6.1 to 6.3 and Section 6.5.1. This template or fraction fit is implemented in ROOT in the TFractionFitter class [104] and determines the two normalization constants c_0 and c_1. The discrimination power of the fit is due to the different shapes of the Monte Carlo background template, which is dominated by the Z resonance at low masses and of the multijet template, which follows a monotonically falling form. The mass region used for this procedure is 70 GeV to 200 GeV. To avoid biases due to the imperfect Z lineshape description, the binning of the mass distribution for the fit consists of one broad bin from 70 GeV to 110 GeV followed by 5 GeV broad bins up to 200 GeV. The resulting distributions are shown in the left plot of Fig. 6.19. The different shapes are clearly visible.

In the following, the results for the normalization constants will be discussed. The normalization constant c_0 is expected to be close to unity, because the Monte Carlo driven background estimate is scaled to the corresponding luminosity, whereas c_1 for the multijet templates is expected to be similar to the fake factor for the N_{LL} distribution as derived in Section 6.4.3: $F_{lead} \cdot F_{subl} \approx 0.15^2 = 0.023$.

For the fail track match template, the results are $c_0 = 1.05 \pm 0.02$ and $c_1 = 0.026 \pm 0.006$.

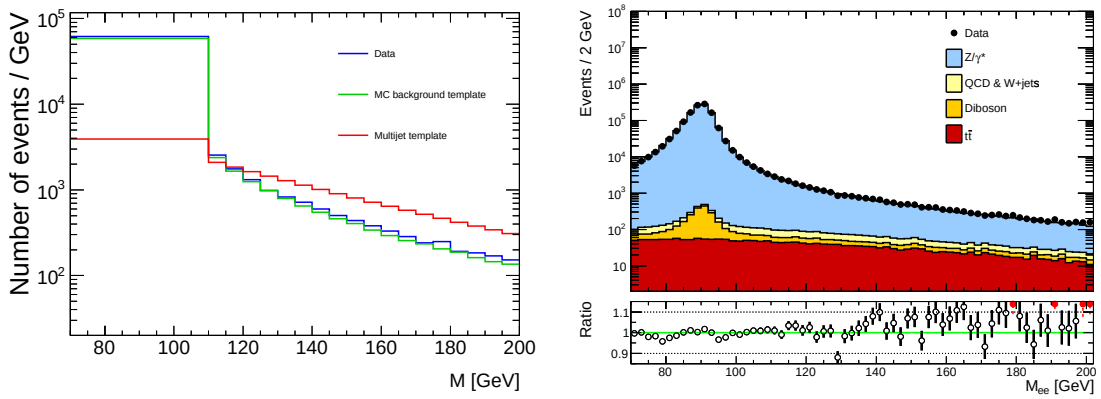

Figure 6.19: The mass distributions used to perform the template fit are shown in the left plot. The multijet template distribution is shown in red, the background template derived from Monte Carlo simulations in green, and data in blue. All three distributions are normalized to events per GeV despite the different bin widths to pronounce the shape differences. On the right plot, the mass distribution for data, shown in black, is compared to the total background estimation, where the multijet and W+jets contributions are estimated using *method II*. Both, the Monte Carlo predictions and the multijet estimation, are scaled by the scale factors of the template fit to data. The plot in the bottom panel shows the ratio of the number of events in data over the number of events of the background prediction. Ratios greater than 1.15 are shown in red. The largest value observed is 1.25.

As described in Section 4.1, the theory calculation of the cross-section of the Drell-Yan process is approximately 3% higher than the extracted cross-section of the Drell-Yan Monte Carlo sample with the corresponding k-factors applied. Therefore, an scaling factor of 1.03 is expected, which is covered by the Drell-Yan k-factor uncertainty of 4.5% and the luminosity uncertainty of 1.8%. The template normalization c_1 is compatible with the expectation from *method I* within uncertainties. The relative uncertainty of c_1 amounts to 23%, which is much higher than in case of c_0. The reason is that the multijet contribution is small in the mass region used, e.g. on per mill level at the Z boson pole mass, and therefore more difficult to estimate than the normalization of $d_{MC}(m)$, which contributes $\approx 99,9\%$ to $d_{data}(m)$.

The final background estimate using *method II* for the W+jets and multijets estimation, both scaled according to Eq. 6.23, is shown in the right plot of Fig. 6.19 and compared to data. The ratio of the number of events in data over the number of events predicted shows typically deviations of at most 10% from one. However, there seems to be a slight trend of an underestimation of the background, which was not observed for *method I* in the corresponding comparison shown in Fig. 6.16.

In the following, systematic uncertainties of the normalization constant c_1 will be discussed. For the template fit, the upper bin edge of the first bin in the mass distributions has been changed from 110 GeV to 130 GeV, which results in a difference of 37.5% for c_1. The Drell-Yan prediction, which dominates $d_{MC}(m)$, was replaced by a prediction derived from a Monte Carlo sample simulated with MC@NLO instead of Pythia. The normalization constant c_1 decreased significantly by 30%. Both checks demonstrate that

the normalization is quite sensitive to the shape of the Drell-Yan mass distribution. Additionally the cross-section of the Drell-Yan Monte Carlo simulations was varied by one standard deviation (5%) up and down when scaling to luminosity. The impact on the normalization constant c_1 is 6%. The sum of the fit normalization uncertainty, the first bin edge variation, the Monte Carlo generator variation and the cross-section variation added in quadrature reflects the total normalization uncertainty and amounts to 53%. The results for the fail strip cuts template are of similar size.

Extrapolation to high Mass

A binned log-likelihood in a binning of 1 GeV size was performed to extrapolate the mass distribution to high masses. The fit function $f_0(m)$ as defined in Eq. 6.1 was used. In contrast to all other mass distributions, the multijet mass templates do not contain weighted events[26], which allows to perform a log-likelihood fit. The result of the extrapolation in the default fit range from 110 GeV to 800 GeV is shown in Fig. 6.20. The fit result agrees with the data distribution within the statistical uncertainties of the data. Further extrapolations using the lower part (70 GeV to 600 GeV) and the upper part of the mass distribution (200 GeV to 1200 GeV) were performed. Also the full available range from 70 GeV to 1200 GeV was evaluated. The fail track match template was chosen as the default template due to its smaller dilution. For the default template, all four fit ranges are considered for the systematic variations, whereas for the fail strip cuts template only the default range was considered. The results of these variations are shown in Table 6.10. In the mass range from 70 GeV to 300 GeV, the different estimates agree within 15%. At higher masses, the estimates using the extrapolation of the fail strip cuts estimate start to deviate significantly from the extrapolation of the default template. Especially, the deviations are much larger than the impact of the fit range variations.

Due to the use of one fake factor that neither depends on η nor on E_T nor incorporates differences between leading and subleading electrons, the correct evolution of the mass distribution cannot be taken into account correctly. To achieve a correct description at masses above the normalization region, a new normalization would be needed, which can be understood as the convolution of the corresponding fake factors with the η and E_T distributions valid in this higher mass region. Multiple normalizations are not possible with this method, because there exists only one resonance in the mass region considered. This is a conceptual limitation of this method.

Due to this caveat, the extrapolation uncertainty is rather large at high masses. It is calculated as the maximum deviation of the estimates shown in Table 6.10, that is the largest deviation (per 1 GeV bin) when performing the fit in a different mass range or with a different multijet template. At 2000 GeV, this uncertainty amounts to 272%, while it is less than 25% for masses below 400 GeV.

6.5.3 Summary and Comparison to Method I

In Table 6.11, the background estimate for the multijet and W+jets background derived with *method II* are shown together with the uncertainties. At low masses, e.g. in the first mass bin, the ratio of the multijet contribution to the W+jets contribution is approximately 2 : 1, while it is 1 : 2 in the next to last mass bin. The total uncertainty is approximately 30% for masses up to 400 GeV and increases to 67% at 2000 GeV, where

[26] Technically, the extrapolation is performed before the global normalization scale factor is applied.

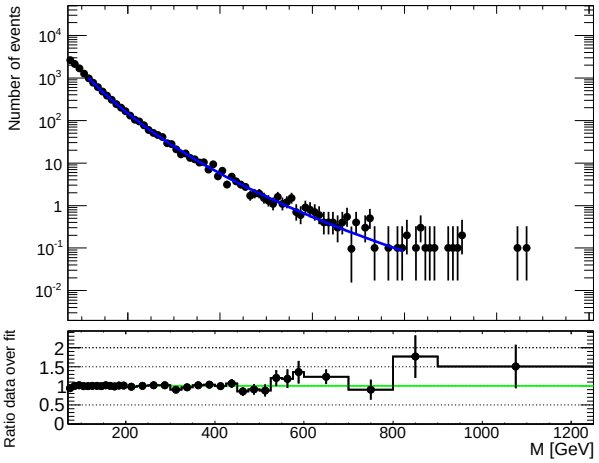

Figure 6.20: The mass distribution of the fail track match template is shown by the black markers, while the fit in the default range 110 GeV to 800 GeV is shown as blue line. Although the fit was done with a binning with 1 GeV bin width, this illustration uses a bin width of 5 GeV for better readability. In the bottom panel, the ratio of the number of events in data over the number of events predicted by the fit is shown. The uncertainties of the ratio are derived from the statistical uncertainties of the mass distribution without extrapolation.

Table 6.10: The individual extrapolation results used to derive the total extrapolation uncertainty are shown as a function of invariant mass. The estimate derived from the fit of the fail track match is shown in the row labeled default fit. The following three lines show the relative deviations with respect to the default result due to variations of the fit range. The last row shows the relative deviations of the estimate taken from the fit of the fail strip cuts template.

Mass range [GeV]	70 - 110	110 - 130	130 - 150	150 - 170	170 - 200	200 - 240
Default fit [number of events]	2067	462	286	181	160	108
Fit range: 70 - 600 GeV	4 %	1 %	0 %	0 %	0 %	1 %
Fit range: 200 - 1200 GeV	15 %	6 %	2 %	0 %	1 %	3 %
Fit range: 70 - 1200 GeV	4 %	1 %	0 %	0 %	0 %	0 %
Fail strip cuts (default range)	6 %	1 %	0 %	0 %	1 %	3 %

Mass range [GeV]	240 - 300	300 - 400	400 - 800	800 - 1200	1200 - 2000	2000 - 3000
Default fit [number of events]	67	33	12	0.27	0.020	0.00045
Fit range: 70 - 600 GeV	2 %	5 %	10 %	23 %	33 %	46 %
Fit range: 200 - 1200 GeV	3 %	2 %	2 %	19 %	40 %	80 %
Fit range: 70 - 1200 GeV	1 %	3 %	8 %	19 %	27 %	39 %
Fail strip cuts (default range)	6 %	13 %	28 %	80 %	141 %	272 %

the multijet contribution amounts to only 12%. Therefore the high extrapolation uncertainty of the multijet template has a minor impact on the total uncertainty for masses above 2 TeV. In contrast, the extrapolation uncertainty of the W+jets estimate is rather small, as the mass distributions derived with the *no-ID* selection reach up to high masses even before the extrapolation. These are normalized by one fake factor in the low mass region 70 GeV to 200 GeV, which neglects the evolution of the fake factors. This is also true for the multijet estimate, and is a severe limitation of *method II*, because it results into biased predictions at high masses. The size of a such a bias cannot be estimated within the method itself. However, the comparison of the mass distributions derived with *method I* and *method II* allows to study the bias problem.

The final results of the two methods are compared in Table 6.12. In the mass bin 70 GeV to 110 GeV, *method II* predicts a 25% higher number of events than the default estimate with *method I*, which is well within the individual uncertainties of 39% and 50%, respectively. But there is a systematic trend: with increasing mass, the prediction of *method II* starts to become lower than the prediction of *method I*. For masses above 400 GeV, *method II* predicts less than 50% of the events predicted with *method I*, and for masses above 2000 GeV less than 1/6. This trend in *method II* is due to the neglected η and E_T dependence of the fake factors. As can be seen from the table, also the results with *method I* predict a systematically lower background, that is underestimate the background, if one or both dependences of the fake factor are not taken into account. The estimates of both methods converge in the case of non-differential fake factors for high masses. The absolute background prediction, especially at low masses, is different, because in *method II* the fake factors[27] are derived in the mass range 70 GeV to 200 GeV, whereas in *method I*, an average fake factor over all masses, separate for leading and subleading electron, is calculated. In these comparisons, especially at high masses, the amplification by the extrapolation procedure needs to be taken into account. Already without the extrapolation, the deviations of the estimate, which takes no fake factor dependences into account, with respect to the estimate, which takes the η and E_T dependences into account, increase with mass. Therefore the "wrongness" of this estimate increases with mass. This wrong slope, which indicates a much steeper decrease, is extrapolated to higher mass, which amplifies the underestimation.

The trend that *method II* underestimates the background can also be seen, when the data is compared to the full background estimate derived with *method II* (see Fig. 6.19) and with *method I* (see Fig. 6.16). The first estimate shows a systematic trend, which indicates a background underestimation, whereas the latter shows no systematic trend. This suggests that the conceptual more sophisticated, data-driven approach of *method I* seems to predict the correct amount of W+jets and multijets in the mass region considered. Due to this result, but also due the conceptual problems and related incomplete systematics, *method II* is considered as a cross-check method only and is not used further.

[27] In *method II*, there is one fake factor for both, the leading and the subleading electron. However, there are two different fake factors for the W+jets and the multijet background.

Table 6.11: The combined estimate and the uncertainties of the multijet and W+jets background derived with *method II* are shown as a function of mass.

Mass range [GeV]	70 - 110	110 - 130	130 - 150	150 - 170
Number of events	3037 ± 1171	807 ± 266	526 ± 167	341 ± 106
Statistical uncertainty [%]	$< 0.5\,\%$	$< 0.5\,\%$	$< 0.5\,\%$	$< 0.5\,\%$
W+jets shape uncertainty [%]	2 %	3 %	3 %	3 %
Fit uncertainty [%]	10 %	4 %	2 %	1 %
Cross-section uncertainty [%]	8 %	11 %	12 %	12 %
Normalization uncertainty [%]	36 %	31 %	29 %	28 %
Combined uncertainty [%]	39 %	33 %	32 %	31 %

Mass range [GeV]	170 - 200	200 - 240	240 - 300	300 - 400
Number of events	312 ± 95	217 ± 65	142 ± 42	76 ± 23
Statistical uncertainty [%]	$< 0.5\,\%$	$< 0.5\,\%$	1 %	1 %
W+jets shape uncertainty [%]	3 %	2 %	2 %	1 %
Fit uncertainty [%]	1 %	4 %	7 %	10 %
Cross-section uncertainty [%]	13 %	13 %	14 %	14 %
Normalization uncertainty [%]	28 %	27 %	26 %	24 %
Combined uncertainty [%]	30 %	30 %	30 %	30 %

Mass range [GeV]	400 - 800	800 - 1200	1200 - 2000	2000 - 3000
Number of events	32 ± 11	0.97 ± 0.35	0.099 ± 0.045	0.0039 ± 0.0026
Statistical uncertainty [%]	0 %	0 %	0 %	0 %
W+jets shape uncertainty [%]	2 %	3 %	1 %	$< 0.5\,\%$
Fit uncertainty [%]	23 %	24 %	37 %	61 %
Cross-section uncertainty [%]	16 %	20 %	22 %	24 %
Normalization uncertainty [%]	21 %	17 %	14 %	12 %
Combined uncertainty [%]	35 %	36 %	45 %	67 %

Table 6.12: The estimate of the W+jets and multijets background derived with *method I* and *method II* is shown. In the first row of each block, the default estimate for *method I* including all systematic uncertainties is shown, whereas in the next three rows, results with fake factors are shown, which do not take into account the η and/or E_T dependence. These results are listed with their extrapolation uncertainties, only. The result of *method II* is shown including all systematic uncertainties. The ratio shown is the ratio of the results of *method II* over *method I* with fake factors binned in η and E_T.

Mass range [GeV]	70 - 110	110 - 130	130 - 150	150 - 170
Method I (η, E_T)	2434 ± 1207	708 ± 189	505 ± 90	364 ± 60
Method I (η)	2202 ± 442	665 ± 67	481 ± 30	350 ± 13
Method I (E_T)	2809 ± 365	812 ± 52	572 ± 23	407 ± 10
Method I (not differential)	2739 ± 347	790 ± 48	554 ± 22	391.9 ± 9.5
Method II (not differential)	3037 ± 1177	807 ± 267	526 ± 167	341 ± 106
Ratio II/I	1.25	1.14	1.04	0.94

Mass range [GeV]	170 - 200	200 - 240	240 - 300	300 - 400
Method I (η, E_T)	371 ± 46	295 ± 34	224 ± 24	142 ± 15
Method I (η)	358.2 ± 8.1	285.5 ± 6.4	215.7 ± 5.2	133.9 ± 2.5
Method I (E_T)	406.2 ± 5.6	314.2 ± 3.4	229.2 ± 3.1	136.4 ± 1.9
Method I (not differential)	388.3 ± 5.3	296.8 ± 3.1	212.7 ± 2.8	123.0 ± 1.8
Method II (not differential)	312 ± 95	217 ± 66	142 ± 43	76 ± 23
Ratio II/I	0.84	0.74	0.63	0.54

Mass range [GeV]	400 - 800	800 - 1200	1200 - 2000	2000 - 3000
Method I (η, E_T)	73.7 ± 9.8	3.1 ± 1.3	0.42 ± 0.32	0.025 ± 0.032
Method I (η)	65.9 ± 5.8	2.36 ± 0.84	0.26 ± 0.15	0.0111 ± 0.0092
Method I (E_T)	63.1 ± 3.6	1.98 ± 0.53	0.194 ± 0.093	0.0069 ± 0.0057
Method I (not differential)	53.7 ± 2.8	1.46 ± 0.36	0.125 ± 0.057	0.0037 ± 0.0028
Method II (not differential)	32 ± 12	0.97 ± 0.35	0.099 ± 0.045	0.0039 ± 0.0026
Ratio II/I	0.44	0.31	0.24	0.15

6.6 Discussion of the total Background Expectation

In this section the agreement of the observed data with the full background expectation for masses up to 500 GeV will be discussed, whereas the discussion for higher masses follows in Chapter 7.

The full background estimate consists of the real electron contributions from the Drell-Yan, $t\bar{t}$ and diboson processes, which are normalized to data as described in Section 6.4.6, and the W+jets and multijet estimate using *method I*.

Fig. 6.21 shows the comparison of data to expectation for several variables in the mass range above 70 GeV. Fig. 6.21(a) shows the mass distribution of the electron pair and Fig. 6.21(b) the pair rapidity. For both distributions, data and expectation within better than 5%. Fig. 6.21(c)-(h) show the three[28] variables that define the 4-vector (E_T, η, and ϕ) for the leading and subleading electron. They also show a good agreement within 5%. These deviations cannot be explained by statistics, they are of systematic nature. The reasons were already discussed in the previous chapter, e.g., the imperfect p_T^Z description in the Drell-Yan simulation as well as the data-taking conditions, which were only modeled as four different blocks and do not perfectly reproduce the calorimeter readout inefficiencies seen in ϕ. Nevertheless, an agreement of data with the expectation within 5% for masses close to the Z pole mass can be seen as a good result for a high-mass search.

To demonstrate that the data is still well described at higher masses, the same distributions for masses above 200 GeV are shown in Fig. 6.22. A good agreement within statistical uncertainties is observed. The electron E_T distributions are shown in Fig. 6.22(c)-(d). The W+jets and multijet contribution is enriched at low E_T. In the following, the possibility to reduce this background further by exploiting the observed enrichment will be discuseed. Adding a cut to suppress the low E_T tail as a function of the electron pair mass, would improve the signal to background ratio, but also reduce the acceptance for real di-electron events. However, a high acceptance is crucial for a sensitive search given that the background is well described. To estimate the acceptance loss, the following cut was evaluated: The minimum E_T cut[29] was set to $35\% \cdot \frac{M_{ee}}{2}$. The most probable electron E_T value[30] is close to $\frac{M_{ee}}{2}$ and this cut rejects all electron pairs where one electron has an E_T below 35% of the half pair mass. The acceptance loss calculated [31] using the simulated Drell-Yan samples amounts to 4.1% at 1 TeV, 5.3% at 2 TeV, and 6.0% at 3 TeV. The percentage being cut on has been varied, but the order of magnitude of the acceptance loss did not change. Due to the size of the acceptance loss, such a cut was not considered further. For the ATLAS dilepton resonance search [24], this cut was not studied. Furthermore, the enrichment of the W+jets and multijet contribution at low E_T for a given pair mass is another justification for the selection criterion to chose the electron pair with the highest sum of the individual electron E_T, if more than one pair passes all other selection criteria.

Table 6.13 shows, binned in mass, the number of events expected from the individual background contributions as well as their sum. Electrons created in the Drell-Yan process dominate the background expectation. The relative importance of the multijet and W+jets contribution increases with mass and the number of events expected amounts to approximately 2/3 of the Drell-Yan contribution at 2000 GeV. In contrast to the pre-

[28] The fourth component, the electron mass, is set to zero.
[29] The threshold is only raised but never lowered below the original E_T threshold of 25 GeV.
[30] This holds for processes like Drell-Yan or Z' production, if the electrons do not emit Bremsstrahlung.
[31] In a mass window starting at the quoted mass with a width of 50 GeV.

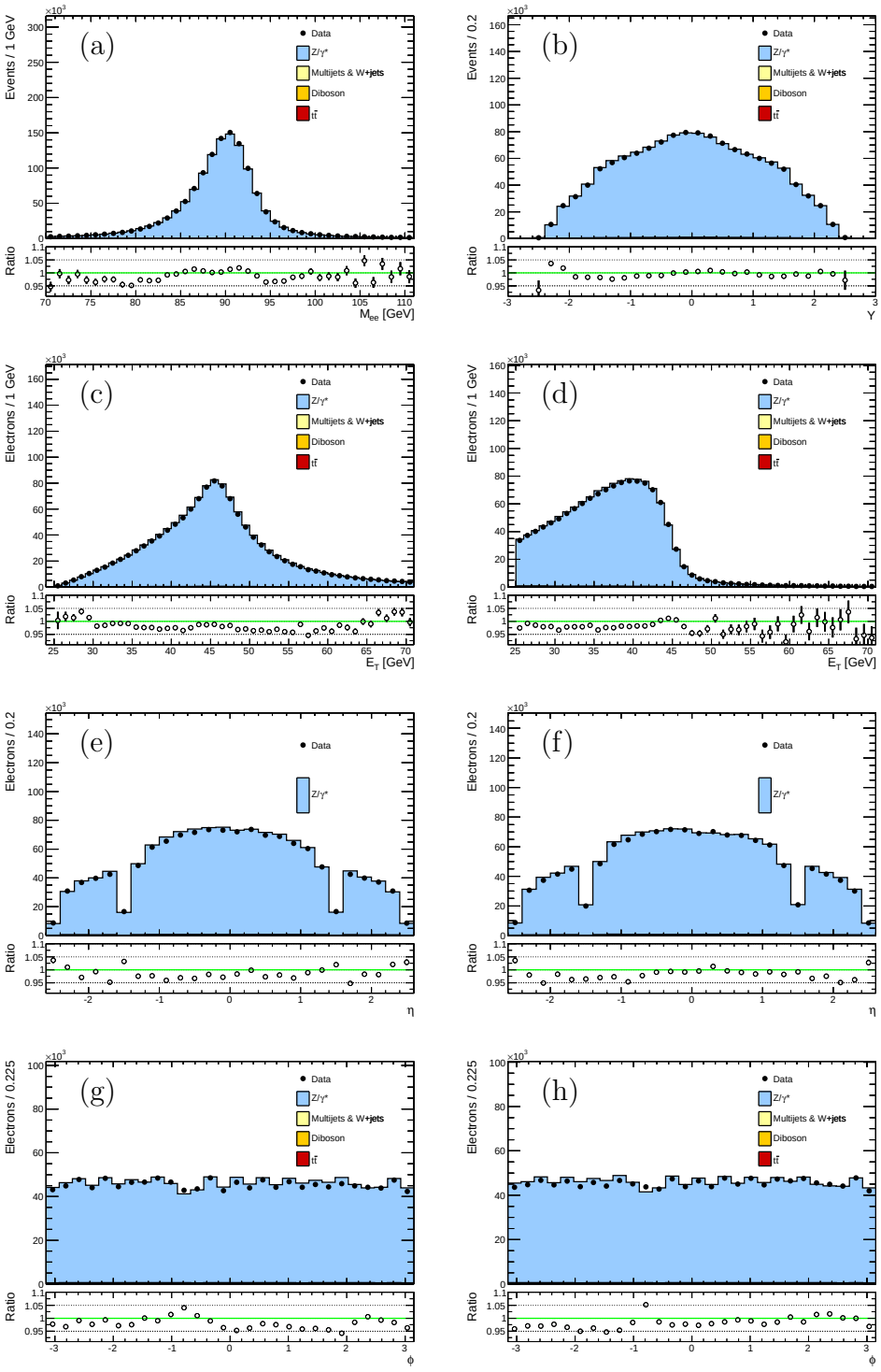

Figure 6.21: This figure shows from top to bottom and from left to right the mass, di-electron rapidity, leading electron E_T, subleading electron E_T leading electron η, subleading electron η, leading electron ϕ and subleading electron ϕ distribution for masses greater than 70 GeV. In each plot, data is represented by black markers, while the background expectation is shown as the colored stack of histograms. The background expectation is normalized to the number of events in data in the mass region 70 GeV to 110 GeV. In the bottom panel, the ratio of the number of events in data over the total number of events of the background expectation is shown. The green horizontal line indicates a ratio of one.

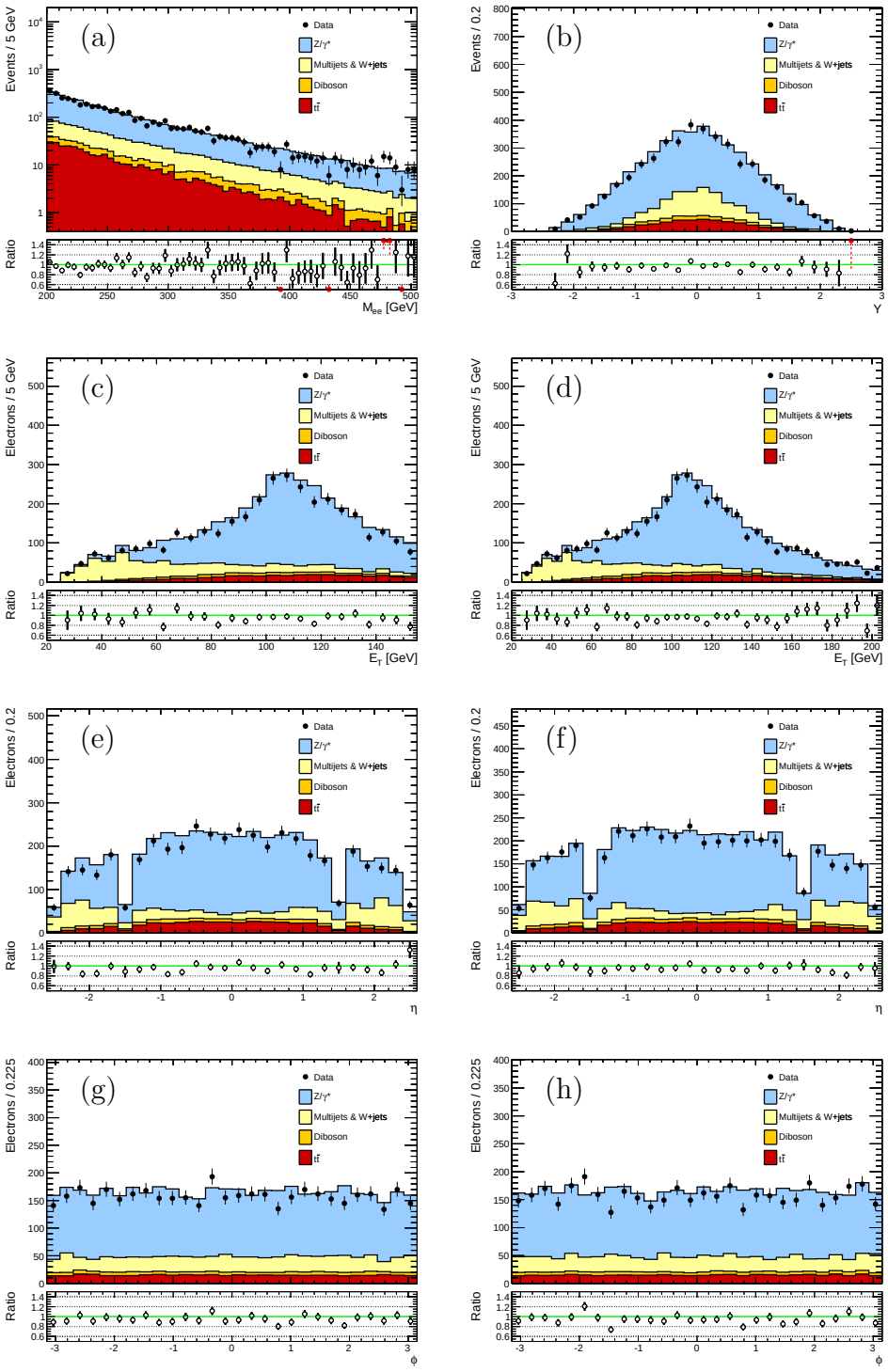

Figure 6.22: This figure shows from top to bottom and from left to right the mass, di-electron rapidity, leading electron E_T, subleading electron E_T leading electron η, subleading electron η, leading electron ϕ and subleading electron ϕ distribution for masses greater than 200 GeV. In each plot, data is represented by black markers, while the background expectation is shown as the colored stack of histograms. The background expectation is normalized to the number of events in data in the mass region 70 GeV to 110 GeV. In the bottom panel, the ratio of the number of events in data over the total number of events of the background expectation is shown. The green horizontal line indicates a ratio of one.

Table 6.13: The individual background contributions and the total background expectation is shown together with their uncertainties. The total background expectation is calculated as the linear sum of the individual components, while the total background uncertainty is derived by adding the individual background uncertainties in quadrature. The expectation is normalized to the number of events in data in the mass window from 70 GeV to 110 GeV.

$m_{e^+e^-}$ [GeV]	70 - 110	110 - 130	130 - 150	150 - 170
Z/γ^*	1231068 ± 54431	15591 ± 668	5780 ± 243	2928 ± 121
$t\bar{t}$	1040 ± 99	418 ± 40	325 ± 31	245 ± 24
Diboson	1822 ± 91	153.2 ± 8.3	105.9 ± 6.0	75.8 ± 4.4
Multijets + W+jets	2434 ± 1207	708 ± 189	505 ± 90	364 ± 60
Total	1236365 ± 54444	16871 ± 696	6716 ± 261	3613 ± 137

$m_{e^+e^-}$ [GeV]	170 - 200	200 - 240	240 - 300	300 - 400
Z/γ^*	2346 ± 96	1499 ± 62	937 ± 39	522 ± 23
$t\bar{t}$	249 ± 24	189 ± 18	129 ± 12	69.9 ± 6.9
Diboson	79.0 ± 4.6	63.5 ± 3.8	50.2 ± 3.1	33.1 ± 2.2
Multijets + W+jets	371 ± 46	295 ± 34	224 ± 24	142 ± 15
Total	3044 ± 110	2047 ± 73	1340 ± 47	767 ± 28

$m_{e^+e^-}$ [GeV]	400 - 800	800 - 1200	1200 - 2000	2000 - 3000
Z/γ^*	265 ± 13	12.17 ± 0.83	1.44 ± 0.16	0.0340 ± 0.0085
$t\bar{t}$	24.7 ± 2.6	0.32 ± 0.11	0.0136 ± 0.0088	0.00014 ± 0.00015
Diboson	17.05 ± 0.94	1.01 ± 0.12	0.1234 ± 0.0091	0.0073 ± 0.0023
Multijets + W+jets	73.7 ± 9.2	3.1 ± 1.3	0.42 ± 0.32	0.025 ± 0.032
Total	380 ± 16	16.6 ± 1.6	1.99 ± 0.35	0.066 ± 0.033

cise Drell-Yan prediction, the multijet and W+jets contribution is extrapolated, and the related high systematic uncertainty dominates the total background uncertainty at high masses. The total background uncertainty amounts to below 5% for masses up to 400 GeV, whereas it increases to approximately 10% for masses above 800 GeV, and to 50% for masses above 2000 GeV.

6.6.1 Improvements with respect to the ATLAS Dilepton Resonance Search

The major improvements of the SM background estimate in this analysis with respect to the ATLAS dilepton resonance search will be discussed in the following.

In the ATLAS dilepton resonance search the extrapolation of mass distributions towards high masses was done in different ways. One default fit range was chosen and typically 3 to 10 fit range variations as well as 2 fit function variations were evaluated to estimate the stability of the extrapolation. However, it is difficult to specify objective criteria for

the choice of these few selected fit ranges. Therefore this procedure has been replaced in this thesis by a different ansatz, which tries to cover all possible fit ranges as described in Section 6.2.2.

Furthermore, the treatment of the small fake contribution of the $t\bar{t}$ background (one real electron plus one fake) has been improved. It was explicitly studied and it could be shown that the mass distribution of this contribution can be described with the combined *type ee* and *type ef* mass distribution scaled down by a constant factor of approximately 20. This contribution is only relevant for the multijet and W+jets *method II*, which covers only one electron plus one fake contributions from W+jets processes. In the ATLAS dilepton resonance search, this contribution was counted twice, once in the $t\bar{t}$ contribution and once in the fake factor methods (*method I*), but was accounted for with a systematic uncertainty equal to the size of the double counting. In this analysis, the $t\bar{t}$ fake contribution has been explicitly studied and was therefore not double counted. Furthermore, the $t\bar{t}$ electron E_T spectra were studied to explain the deficit at low electron pair masses.

For the multijet and W+jets background cross-check method, *method II*, the W+jets contribution was estimated with simulated Monte Carlo samples, which are binned in the number of associated jets[32] produced in addition to the W boson. In the ATLAS dilepton resonance search, the mass distribution of all jet multiplicities has been summed up and this merged distribution was extrapolated. Due to the low number of events available, also there a loose electron identification level was used. In this analysis, the shape of the individual W+jets mass distributions, separate for each multiplicity, has been studied. For this purpose, two looser electron identification levels were used. While the $W+1$ jets and $W+2$ jets contributions dominate the mass spectrum at lower masses, the $W+3$ jets contribution becomes the major contribution at higher masses due to different "slopes". Therefore the contribution of each multiplicity was extrapolated separately in this analysis.

In the ATLAS dilepton resonance search, also a second fake factor method, calculated by a colleague, was used. The method uses jet triggers to define the data set used to calculate the fake factors. Both fake factor results are compatible within better than 20%. Due to time restrictions for the ATLAS dilepton resonance search, only parts of the planned systematics were evaluated for the *method I*. Therefore in the ATLAS dilepton resonance search, a systematic uncertainty of 30% was conservatively assigned to each bin, where the uncertainty was lower. In the improved version of *method I* in this thesis, the full list of systematics was evaluated. This allows the estimation of the uncertainties on a solid basis, and also reduced the uncertainty by approximately a factor of two at low masses. Further the extrapolation method was refined; two instead of one fit functions were evaluated with the extrapolation method described in this thesis.

For the final multijet and W+jets estimate of the ATLAS dilepton resonance search, both fake factor results were combined with the results of *method II* by an un-weighted average. As uncertainty the envelope of the one standard deviation uncertainty bands of the three methods was used. Within uncertainties, the multijet and W+jets estimate of the ATLAS dilepton resonance search is compatible with the estimate of this analysis. At high masses, the averaged estimate predicts a lower multijet and W+jets contribution due to the inclusion of the estimate with *method II*, which underestimates at high masses.

The total expectation derived in the ATLAS dilepton resonance search for masses above 1200 GeV amounts to 1.86 ± 0.35, whereas the expectation derived in this thesis amounts

[32] Each jet (parton) is required to have a minimum transverse momentum of 20 GeV.

to 2.06 ± 0.35. The uncertainty values are identical by chance, as both are calculated in a different manner. The expectations are compatible within uncertainties, but the estimate derived in this thesis is 11% higher.

7 Search for a New Physics Signal

In this chapter the comparison of the measured mass distribution data with the expectation will be discussed. In the first section, the mass distribution will be presented and discussed in terms of the ratio of the number of events observed and of the number of events expected. In the second part, local significances will be discussed, while in the third part, global significances derived with BumpHunter [105] will be presented.

The mass distribution over the full range that is covered by data is shown in the left plot of Fig. 7.1. The ratio of the number of events in data over the number of events expected typically deviates at most by 5% from unity for masses below 400 GeV. At higher masses, deviations from a ratio of unity are covered by the large statistical uncertainties for all bins but two in the mass region around 900 GeV. Here, the agreement of data and the expectation needs to be discussed further in terms of significances.

The right plot of Fig. 7.1 shows the electron pair p_T^{ee} distribution. Caution is required in the interpretation of this plot, because the background expectations for the diboson, $t\bar{t}$, W+jets and multijets contributions are extrapolated in mass, but not in p_T^{ee}. Therefore, these individual contributions have large statistical uncertainties and eventually there are no events left for the estimate, which leads to an underestimation of the background. Nevertheless, with having this in mind, the figure still can be used to judge the agreement of data with respect to the expectation in a qualitative way. It shows, by eye, no strong hint of an excess in data. However, due to the mentioned caveats of the p_T^{ee} distribution[1], only the mass distribution is considered further for the result interpretation.

In Table 7.1, the number of events observed in data are compared with the background expectation. Below 1200 GeV, the data agree with the expectation within the background uncertainties. However, in the mass range from 1200 GeV to 2000 GeV, 1.99 ± 0.35 events are expected, while three are observed. To judge the agreement in a more profound way, statistical significances are discussed in the following sections.

7.1 Search using local Significances

To evaluate quantitatively how likely the observed fluctuations in the measured mass distribution with respect to the expectations are, the so called p-value assuming Poisson distributed data is calculated. In a second step, also the systematic uncertainties of the background expectation are taken into account. The prescription and code is taken from Ref. [106].

The probability to observe D events in data for an expectation value of B is

$$P(D, B) = \frac{B^D e^{-B}}{D!}. \tag{7.1}$$

The p-value is defined as the probability to observe D_0 or more events in data for a given

[1] Of course, the same applies for the individual electron E_T distributions.

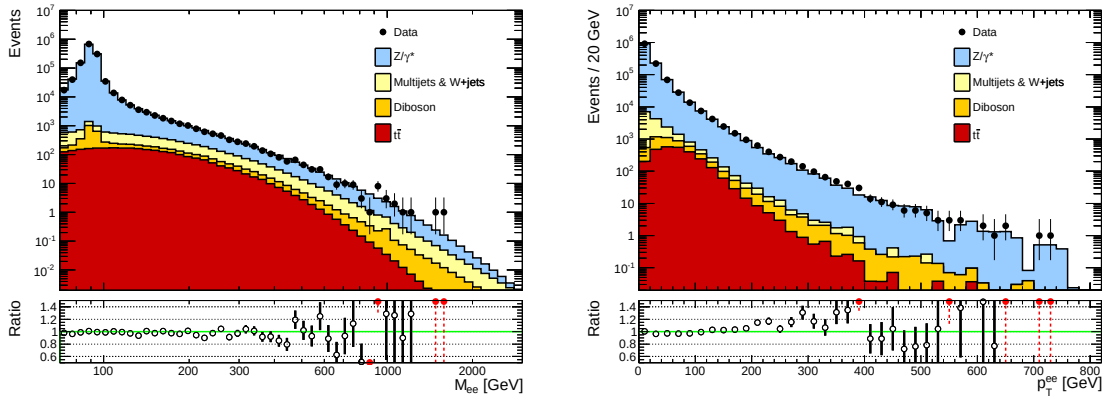

Figure 7.1: The left (right) plot shows the mass (p_T) distribution of the pair of electrons. Data is represented by the black markers, while the background expectation is drawn stacked on top of each other. The expectation is normalized to the number of data events in the mass range 70 GeV to 110 GeV. In the bottom panel, the ratio of the observed number of events in data over the expected number of events is shown.

Table 7.1: The expected total number of events in the SM together with their uncertainties is compared to the number of events observed in data in bins of the electron pair mass.

$m_{e^+e^-}$ [GeV]	70 - 110	110 - 130	130 - 150	150 - 170	170 - 200	200 - 240
Total	1236365 ± 54444	16871 ± 696	6716 ± 261	3613 ± 137	3044 ± 110	2047 ± 73
Data	1236365	16521	6611	3590	2969	1940
$m_{e^+e^-}$ [GeV]	240 - 300	300 - 400	400 - 800	800 - 1200	1200 - 2000	2000 - 3000
Total	1340 ± 47	767 ± 28	380 ± 16	16.6 ± 1.6	1.99 ± 0.35	0.066 ± 0.033
Data	1329	747	359	17	3	0

expectation value of B:

$$p\text{-value} = P(D \geq D_0, B) = \sum_{D'=D_0}^{\infty} \frac{B^{D'} e^{-B}}{D'!}. \tag{7.2}$$

Typically the p-value spans several orders of magnitude and is therefore transformed into a more illustrative quantity, the z-value. The transformation is defined via

$$p\text{-value} = \int_{z\text{-value}}^{\infty} \frac{1}{\sqrt{2\pi}} e^{-\frac{1}{2}x^2} dx \tag{7.3}$$

which relates the p-value to the value of the integral over a Gaussian distribution from the z-value to infinity expressed in standard deviations. This allows to interpret a p-value derived from Poisson statistics as if it was a fluctuation based on a Gaussian distribution. Fig. 7.2 shows the z-value as a function of the p-value. All p-values smaller than 0.5 are

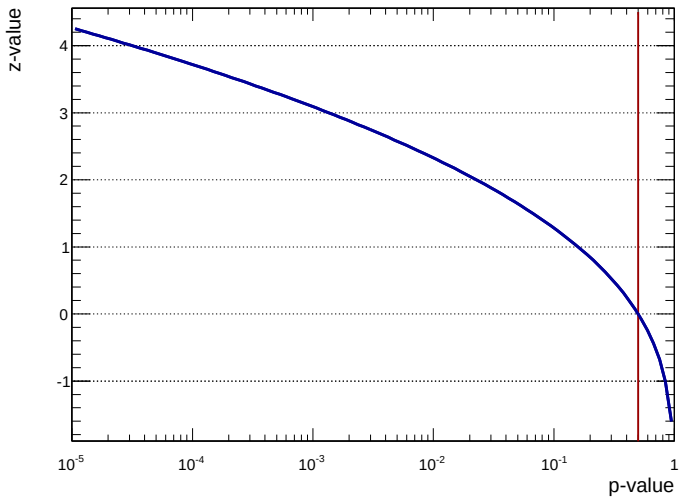

Figure 7.2: The blue curve shows how the z-value correlates with the p-value. The zero crossing at p-value $= 0.5$ is indicated by the red vertical line.

mapped to positive z-values, while p-values greater than 0.5 are not considered further, as they represent insignificant fluctuations (and because the sign of the z-value will be used to code another information).

To distinguish upward and downward fluctuations, the z-value has its sign flipped if an upward fluctuation occurred. With this method, upward fluctuations with a p-value < 0.5 are mapped to positive z-values and downward fluctuations with a p-value < 0.5 are mapped to negative z-values. This allows an intuitive interpretation of the fluctuations observed in data with respect to an expectation from a statistical point of view.

To judge the significance of a fluctuation, also systematic uncertainties need to be taken into account. They are implemented in a Bayesian way, that is the Poisson distribution is "smeared"[2] by convoluting it with a probability density that describes the total systematic uncertainty.

The definitions discussed for the z-value will be used to quantify the fluctuations observed in the mass distribution as shown in Fig. 7.3. The normalization region around the Z boson pole mass is not shown[3]. The only mass region that indicates a discrepancy is the first bin, which covers the mass range from 128.1 GeV to 136.9 GeV. A z-value of -4.1 is calculated for this bin, if only statistical uncertainties are taken into account. However if systematic uncertainties are taken into account, the z-value decreases to -1.5, which corresponds to a downward fluctuation of 1.5 standard deviations.

Fig. 7.4, which shows a zoom of the comparison of data to expectation in this mass region, indicates that this fluctuation is nothing to worry about; there are two bins with a width of 1 GeV where the ratio of the number of events in data over the number of events of the background expectation falls to 0.9 respectively 0.8.

Furthermore, the significances calculated with this method do not take the "look else-

[2]The total systematic uncertainty is treated as nuisance parameter, which is described by a Gamma density as probability density function. This choice allows to perform the convolution analytically and avoids the need to generate pseudo-experiments for this purpose. More details can be found in Ref. [106].

[3]In the default binning, which is equidistant on logarithmic scale, the first bin with $M_{ee} > 110$ GeV starts at 128.1 GeV.

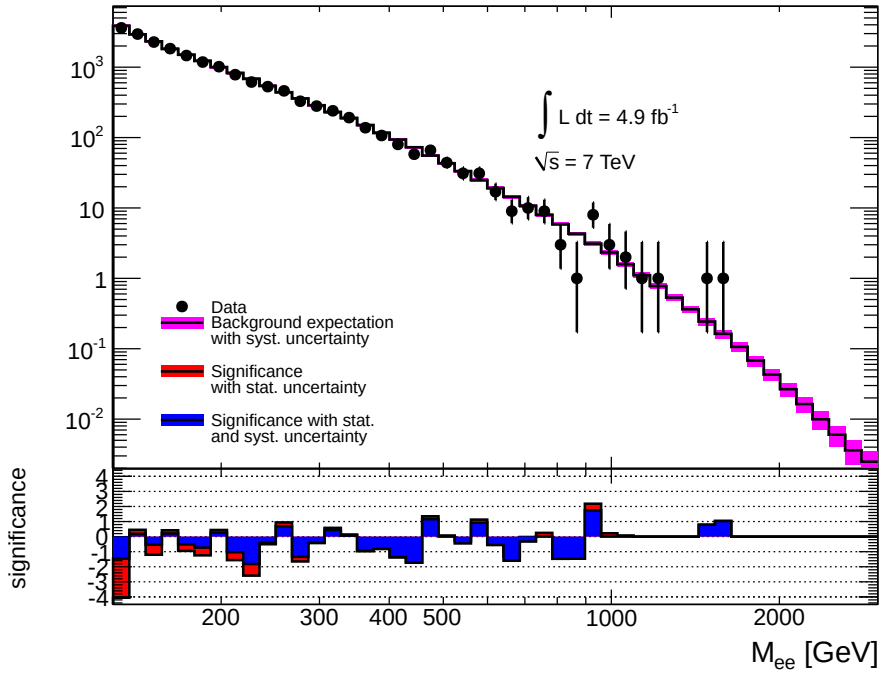

Figure 7.3: The invariant mass distribution for $M_{ee} > 128.1\,\text{GeV}$ is shown. Data is indicated by black markers, while the total background expectation is given by the black line. The violet area indicates the total systematic uncertainties assigned to the expectation. In the bottom panel, the local significance of the deviation of data from the expectation without the "look elsewhere effect" taken into account is shown. The significance in red considers statistical uncertainties only, while the one in blue takes the combined statistical and systematic uncertainty into account. If no statistical significance bar (red) is visible in a bin, the systematics are negligible and therefore both significances appear to be identical by eye.

where effect" (LEE) into account. The LEE describes the problem that the probability to observe a (locally) statistically significant fluctuation, increases with the number of tests performed. If a Gaussian distribution is used as a probability density function to draw from 20 times and a z-value of 4 is observed, this is significant. If 10^9 times is drawn, the same z-value of 4 is no rare outcome any more. In the next section, significances that take the LEE into account will be discussed.

7.2 Search using BumpHunter

A p-value determination, which takes the LEE into account is performed using BumpHunter [105]. BumpHunter compares data to an expectation by scanning over the mass distribution with search windows of various sizes. For each window size and position, the number of events in data (the number of events of the background expectation) is summed up and denoted by D_i (B_i). Using the Poisson distribution $P_i(D_i, B_i)$ (see Eq. 7.1), the corresponding p_i-value is calculated analytically. This is repeated for each unique combination of window size and position denoted by i. Finally the value of the BumpHunter test

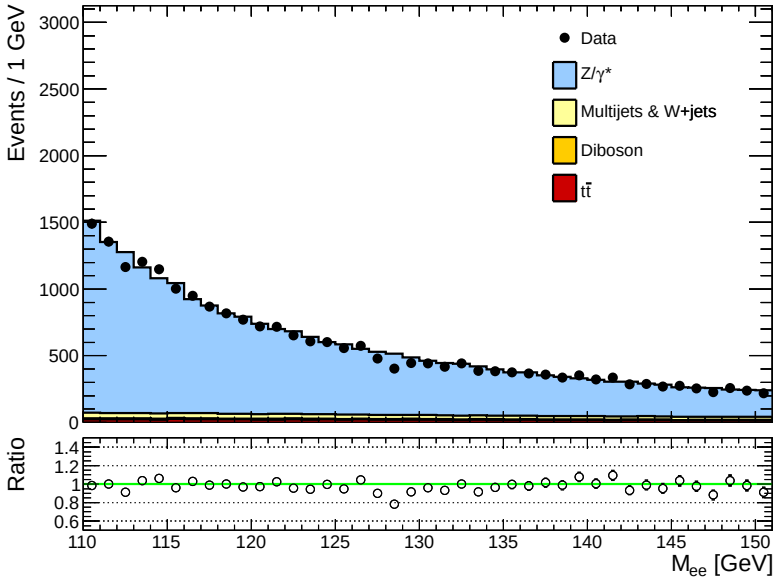

Figure 7.4: This plot shows the mass distribution in the mass range 110 GeV $\leq M_{ee} \leq$ 150 GeV. Data is shown in black and the individual background expectations are shown as a stack. The bottom inset shows the ratio of the number of events in data over the total number of events of the background expectation. In all plots, the background expectation is normalized to the number of events in data in the mass window 70 GeV to 110 GeV.

statistics for the observed data is calculated as

$$t = -\ln\left(min\left\{p_i\right\}\right). \tag{7.4}$$

The test statistic is basically a mapping of the agreement of the data with the expectation onto one single value. To judge the significance of this observed value t_0, pseudo-data spectra are derived using the background expectation values. For each of this pseudo-data spectrum, the above procedure to derive a BumpHunter test statistics value t is applied. With a sufficient number of pseudo-experiments, the probability density function of the BumpHunter test statistics is sampled and the final p-value can be derived as

$$p\text{-value} = \frac{N(t > t_0)}{N(all)}, \tag{7.5}$$

where $N(t > t_0)$ is the number of pseudo-experiments where the t value is greater than the value observed in data, t_0. The total number of pseudo-experiments is denoted by $N(all)$. The calculated p-value can be interpreted as the probability that upon repetition of the measurement, the same or a higher value of the test statistic is observed.

The particular choice of the test statistic naturally accounts for the LEE. Each combination of window size and position can be considered a "test". There is no favored test, because for each pseudo-experiment, the smallest p_i-value is taken. Each test has the same probability to have a significant fluctuation, that is to provide the lowest p_i-value. This behavior will be demonstrated with an example: Consider one test and 100 pseudo-experiments compared to 100 tests and 100 pseudo-experiments. The distribution of the

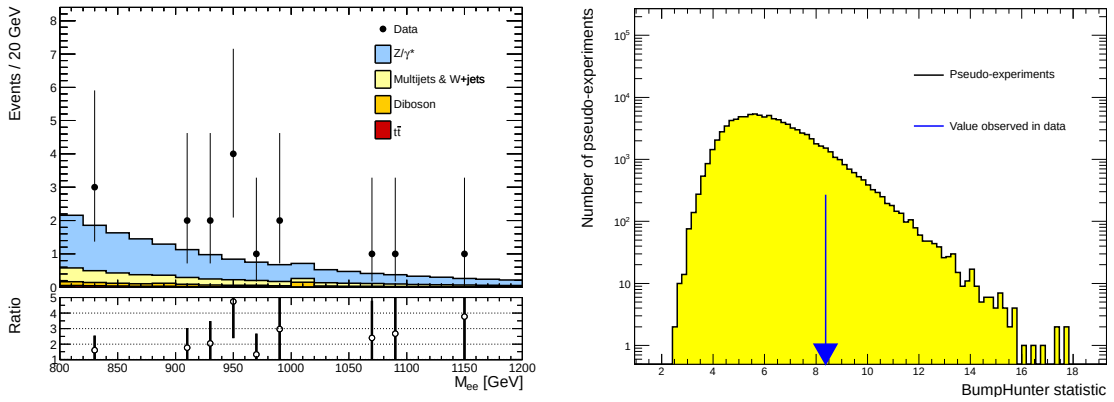

Figure 7.5: The left plot shows the mass distributions in the mass range around the region considered most deviant by BumpHunter (930 GeV to 960 GeV). Data is shown in black while the background expectation is shown as the colored stack of histograms. In the bottom panel, the ratio is shown of the number of events in data over the number of events of the background expectation. The background expectation is normalized to data in the mass region 70 GeV to 110 GeV. The right plot shows in yellow the distribution of the BumpHunter test statistics derived with 100,000 pseudo-experiments. The blue arrow indicates the value of the test statistic observed in data (8.37).

test statistic t in the latter case will be shifted a lot to smaller p-values because in each pseudo-experiment it is sufficient to have one "large" fluctuation. Therefore, an observed t_0 will be interpreted as less significant than in the case of only one test. Therefore it is important to quote the parameters chosen to allow transparent comparisons.

For the actual computations, the code as implemented by the author was used [105]. The histograms with the observed and expected mass distributions are provided in a equidistant 5 GeV binning ranging from 70 GeV to 3000 GeV. The minimum window size is chosen to be two bins, which corresponds to 10 GeV. Two maximum window sizes were evaluated[4], 50 GeV and 500 GeV. Each possible bin is considered as position seed for the search window. The program allows to include sideband information, which is not recommended for this type of search and therefore disabled. The type of deviation being searched for is an excess of data with respect to the expectation.

BumpHunter foresees to incorporate systematics, but it expects uncorrelated Poisson distributed systematics, while this analysis is dominated by correlated Gaussian distributed ones. Therefore, systematics are omitted when using BumpHunter; this leads to a bias towards lower p-values, but is nevertheless a good method to search for deviations of data with respect to expectation.

The result of the BumpHunter analysis is that the most deviant mass region is between 930 GeV and 960 GeV with a corresponding p-value of 0.078 (0.100) in case of a maximum window size of 50 GeV (500 GeV). The left plot of Fig. 7.5 shows the mass distribution measured in data compared to the expectation in the mass region quoted above. The right plot shows the BumpHunter test statistics and the value observed in data. These results show that data agrees well with the SM background expectations and indicates no

[4]Window sizes of 100 GeV or higher are larger than the expected width of signals. The second, large maximum window size was evaluated to give a feeling on the size of the LEE.

significant hint of new physics. Therefore, exclusion limits will be calculated and discussed in the next chapter.

8 Exclusion Limits

The statistical analysis performed showed no significant excess of data with respect to the SM prediction. Therefore exclusion limits will be calculated for two classes of models, the SSM Z′ and the E6 based Z′ models. The statistical aspects of the limit procedure will be described in the first section, followed by a discussion of the signatures of the actual Z′ models. Hereafter, the calculated limits will be discussed and compared to the results of other analyses from the ATLAS and CMS collaborations. The chapter will be closed with an outlook discussing possible sensitivity at higher LHC energies, e.g., at the design center-of-mass energy of 14 TeV and beyond.

8.1 The Limit Setting Procedure

In many limit setting procedures, new resonances need to have a narrow width in comparison to the detector resolution. In contrast, the limit setting procedure [107, 53] used here is designed to work with signatures that might consist of a broad signal distributed over a larger mass range. Therefore, the full shape of a signal needs to be taken into account by looking at all mass bins simultaneously.

A signal is parametrized via its cross-section times branching ratio, $\sigma_{sig}B_{sig}$, its mass-dependent acceptance[1], and its signal shape, which is the convolution of the line shape with the PDFs. This signal shape is normalized to unity and referred to as signal template in the following. It provides the information, which fraction of the signal is expected to be observed at which mass. This is important for broad signals. Additionally, the expected number of background events together with its uncertainty and the observed number of events in data are required, where all three quantities need to be binned in mass.

In the following, the maximum likelihood method used in this thesis will be described from a statistical point of view, followed by a discussion of the technical implementation.

The likelihood to observe n_i events in data in a mass bin i with a Poisson expectation of μ_i events is given by

$$\mathcal{L}(n_i|\mu_i) = \frac{\mu_i^{n_i} \cdot e^{-\mu_i}}{n_i!}. \tag{8.1}$$

The combined likelihood when considering all bins at once is defined as

$$\mathcal{L}(\vec{n}|\vec{\mu}) = \prod_i \mathcal{L}(n_i|\mu_i), \tag{8.2}$$

where $\vec{n}$ and $\vec{\mu}$ are vectors that contain the number of events observed and expected in each bin, respectively. For readability reasons, in the next part of the discussion the

[1] There are two conventions to define an acceptance. One way is to distinguish the pure geometrical acceptance on truth level from the efficiencies that describe the probability that an event within the geometrical acceptance passes the full selection on reconstruction level. The second way denotes the product of the geometrical acceptance and the efficiencies as one total acceptance, which is sufficient for the discussion of the sensitivity to Z' bosons. Therefore the second convention is used here.

component notation will still be used instead of the vector notation.

The expectation μ_i is the sum of the expected number of background events $\mu_i^{bkg}$and the expected number of signal events μ_i^{sig}:

$$\mu_i = \mu_i^{bkg} + \mu_i^{sig}. \tag{8.3}$$

Both expectation values have systematic Gaussian uncertainties, which are incorporated in a Bayesian way. Each uncertainty is described with a Gaussian probability density $G(\theta)$ with a mean value of zero and a standard deviation of one, which describes the probability that a fluctuation of amplitude $\theta \cdot \Delta$ occurs. Here Δ denotes the standard deviation of the uncertainty and θ is typically referred to as nuisance parameter. For example, $\theta = -2$ corresponds to a two standard deviation downward variation of the uncertainty. With this extension, the expected number of events is transformed to

$$\tilde{\mu}_i^{sig/bkg} = \mu_i^{sig/bkg} \prod_u^{N_{sys}} \left(1 + \theta_{iu}^{sig/bkg} \cdot \Delta_{iu}^{sig/bkg}\right), \tag{8.4}$$

where the uncertainties for background and signal are treated with the same ansatz indicated by a common "index" sig/bkg. The mass bin is denoted by i, and u denotes the u-th systematic uncertainty out of N_{sys} uncertainties in total. The likelihood defined in Eq. 8.2 can be written as

$$\mathcal{L}\left(\vec{n}|\vec{\mu}_{sig}, \vec{\mu}_{bkg}, \vec{\theta}_1, \vec{\theta}_2, \ldots \vec{\theta}_{N_{sys}}\right) = \prod_i \frac{\mu_i^{n_i} \cdot e^{-\mu_i}}{n_i!} \prod_u^{N_{sys}} G\left(\theta_{iu}^{sig/bkg}\right). \tag{8.5}$$

In case of fully correlated[2] uncertainties (over all bins i), $\theta_{iu}^{sig/bkg}$ becomes $\theta_u^{sig/bkg}$.

The reduced likelihood, which is a function of the parameter of interest only, is calculated by integrating over the nuisance parameters:

$$\mathcal{L}'\left(\vec{n}_{data}|\vec{\mu}_{sig}\right) = \int \mathcal{L}\left(\vec{n}_{data}|\vec{\mu}_{sig}, \vec{\mu}_{bkg}, \vec{\theta}_1, \vec{\theta}_2, \ldots \vec{\theta}_{N_{sys}}\right) d\vec{\theta}_1 d\vec{\theta}_2 \ldots d\vec{\theta}_{N_{sys}}. \tag{8.6}$$

The reduced likelihood is defined as a function of the number of signal events, while the actual limit is supposed to be a function of the cross-section times the branching-ratio into two electrons $\sigma_{sig}B_{sig}$, which is treated as one quantity. Therefore, μ_i^{sig} is expressed as

$$\mu_i^{sig} = \left(\sigma_{sig}B_{sig}\right) A_i^{sig} T_i L, \tag{8.7}$$

where L is the integrated luminosity, A_i^{sig} the acceptance for each mass bin, and T_i the fraction of signal events predicted in a mass bin i. In the limit of a an infinite mass resolution, an infinitesimal mass bin width, and a resonance width of zero, T_i would correspond to a delta distribution at the pole mass, and the acceptance A_i^{sig} would only be evaluated at the pole mass. For finite resolution and width, the full mass-dependent shape is taken into account. This will be discussed further in Section 8.2.

In the analysis, the total background expectation is normalized to data in the mass

[2]If a fully correlated systematic is varied up by one standard deviation in one bin, it is also varied up by one standard deviation in all other bins. Therefore the number of standard variations, $\theta_u^{sig/bkg}$, can be treated separate from the size of the standard deviation in a bin, $\Delta_{iu}^{sig/bkg}$.

region 70 GeV to 110 GeV. Therefore, the integrated luminosity can be expressed as the integrated luminosity derived from the Drell-Yan simulation after the number of events predicted is scaled to data:

$$L = \frac{N_{DY}}{\sigma_{DY} A_{DY}}. \tag{8.8}$$

The corresponding values of N_{DY} and A_{DY} are determined[3] for the phase space considered in the limit setting procedure, that is for masses above 128 GeV.

Using the discussed transformations, the reduced likelihood depends, in terms of free parameters, only on the number of events observed in data and on the cross-section times the branching-ratio of the signal: $\mathcal{L}'(\vec{n}_{data}|\sigma_{sig}B_{sig})$. To determine which values of $\sigma_{sig}B_{sig}$ can be excluded with the observed data, the likelihood $\mathcal{L}'(\sigma_{sig}B_{sig}|\vec{n}_{data})$ needs to be calculated. Those two likelihoods can be correlated by using Bayes' theorem [108]:

$$\mathcal{L}'(\sigma_{sig}B_{sig}|\vec{n}_{data}) = \frac{\pi(\sigma_{sig}B_{sig})}{\pi(\vec{n}_{data})}\mathcal{L}'(\vec{n}_{data}|\sigma_{sig}B_{sig}), \tag{8.9}$$

where $\pi(\sigma_{sig}B_{sig})$ and $\pi(\vec{n}_{data})$ denote the prior for $\sigma_{sig}B_{sig}$ and $\vec{n}_{data}$, respectively. Both priors are chosen to be constant[4], which expresses that there is no preference for any of the possible values of $\sigma_{sig}B_{sig}$ and $\vec{n}_{data}$. The corresponding posterior probability density for $(\sigma_{sig}B_{sig})$ given $\vec{n}_{data}$ is defined as

$$P(\sigma_{sig}B_{sig}|\vec{n}_{data}) = \frac{\mathcal{L}'(\sigma_{sig}B_{sig}|\vec{n}_{data})}{\int_0^\infty \mathcal{L}'(\sigma_{sig}B_{sig}|\vec{n}_{data})\, d(\sigma_{sig}B_{sig})}. \tag{8.10}$$

The value of $\sigma_{sig}B_{sig}$ that satisfies

$$0.95 = \int_0^{(\sigma_{sig}B_{sig})_{95}} P(\sigma_{sig}B_{sig}|\vec{n}_{data})\, d(\sigma_{sig}B_{sig}) \tag{8.11}$$

is denoted by $(\sigma_{sig}B_{sig})_{95}$. A signal with a cross-section times branching-ratio value[5] of $(\sigma_{sig}B_{sig})_{95}$ (or higher) has a probability to be contained in the observed data of $100\% - 95\% = 5\%$ (or lower), or can be excluded with 95% Confidence Level (C.L.).

The technical implementation is based on a tool written in C++ that has been developed for an earlier ATLAS dilepton resonance search [69]. It has been adapted by me and others for the needs of the ATLAS dilepton resonance search with the full data set taken in 2011 [24]. The Bayesian Analysis Toolkit [109] is used to perform the numerical integration of Eq. 8.6 via a Markov chain Monte Carlo method [110]. This way, the posterior defined in Eq. 8.10 is sampled numerically. Expected limits are calculated by generating pseudo-data that is used to derive the corresponding 95% C.L. limit. The median of the limits derived from pseudo-data is taken as the central value of the expected limit. Additionally, the 68% and 95% uncertainty bands, which correspond to one and two standard deviations of the Gaussian distribution of the expected limits, are extracted.

[3] $N_{DY} = 15155.5$ and $A_{DY} = 0.00321$, where the acceptance A_{DY} is derived with respect to all events generated for truth masses greater than 60 GeV. The corresponding Drell-Yan cross-section σ_{DY} at NNLO is 989 pb.

[4] Therefore, such priors are also called "flat" priors.

[5] This procedure depends on the exact modeling of signal shape and acceptance, which both enter in Eq. 8.7. These two parameters are considered as fixed input and therefore not listed as free parameters.

8.2 The Sequential Standard Model Z'

In this section, the SSM Z′ will be discussed in terms of properties and observables that are required for the limit setting procedure. Typically, to get predictions for a possible Z′ signal at multiple pole masses, Monte Carlo samples are generated at each pole mass. This approach demands a high amount of computing time to simulate a sufficient number of events at each pole mass.

Here a different approach was chosen. The formula to calculate the cross-section in Pythia was modified[6] such that it is approximately constant over the desired mass range from 200 GeV to 3000 GeV. The actual modification consists of two parts; the relativistic Breit-Wigner term, which describes the resonance, has been removed, and an enhancement term that approximately cancels the decreasing parton luminosity has been introduced.

When evaluating the prediction of a Z′ at a given pole mass, each event is weighted by

$$w(M) = \frac{1}{(M^2 - M_0^2)^2 + (M^2\Gamma_{M_0}^2)} e^{-aM}, \tag{8.12}$$

where M_0 is the desired pole mass and M the mass the event was generated with in the matrix element. The parton luminosity compensation constant a has been determined empirically for an earlier ATLAS dilepton resonance search [69]. The correlation between the pole mass M_0 and the width Γ_{M_0} has been evaluated and fitted by a polynomial in a Monte Carlo study for the ATLAS dilepton resonance search [53]. The relative width increases slowly with mass, e.g., from 3.09% at 1000 GeV to 3.15% at 2000 GeV. With this reweighting procedure, mass templates at various pole masses are derived. A selection of them is shown in the left plot of Fig. 8.1. The most prominent feature is the increase in the relative amount of events in the low mass tail with respect to the pole mass. This is caused by the decreasing probability to find two partons with sufficiently large Bjorken-x to produce such high mass bosons. The right plot of Fig. 8.1 shows two mass templates on top of the SM background expectation to demonstrate the signal strength.

The caveat of this low mass tail is a reduced acceptance for high pole masses. To understand this, the acceptance a_{mass} will be discussed first. It is defined as the probability for an event in a given truth mass bin[7] to pass all selection cuts. The left plot of Fig. 8.2 shows the distribution of a_{mass}. It rises rapidly for masses below 500 GeV and approximately forms a plateau for masses above 1000 GeV. The rapidity of particles produced in the s-channel becomes narrower with increasing mass, because the Bjorken-x values of the two initial partons become of similar size and approach unity for the limit of $Q^2 \to s$. As the boost along the beam-axis decreases for higher masses (Q^2), the probability for a particle to be produced outside of the η coverage of this analysis decreases significantly. Furthermore, the survival fraction of the electron E_T cut approaches unity for high masses.

However, the actual acceptance, a_{pole}, for a Z′ at a given pole mass is the convolution of a_{mass} with the corresponding mass template. The right plot of Fig. 8.2 shows the result of this convolution as a function of the pole mass. At masses above 1500 GeV, the acceptance starts to decrease due to the high number of events at low mass that enter with

[6] The described modifications were implemented in Pythia by colleagues (of the ATLAS collaboration), and a validated ATLAS Monte Carlo sample was generated for the ATLAS dilepton resonance search.

[7] Alternatively, this acceptance can be imagined as if it was calculated for a Z' with a line shape that is modeled by a delta distribution at the pole mass

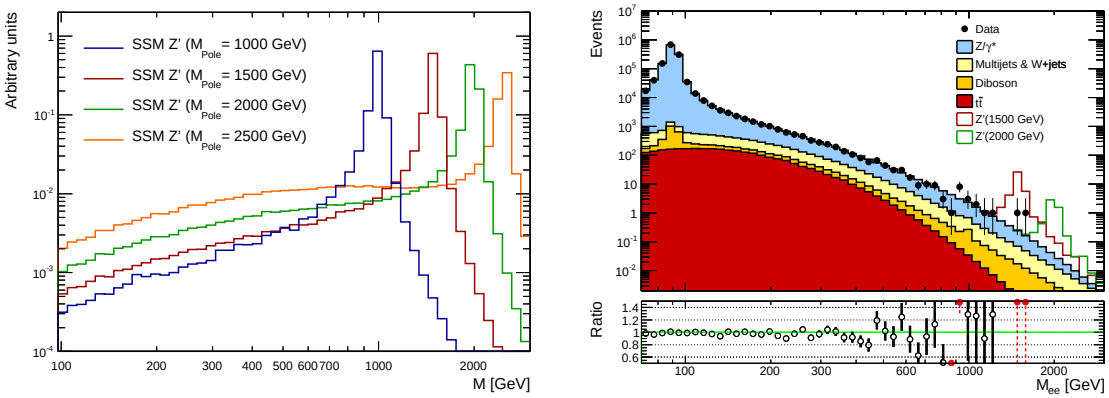

Figure 8.1: In the left plot, the reconstructed mass templates of the SSM Z′ at four different pole masses are shown. Here, each distribution is normalized to unity. The right plot shows the mass distribution of the pair of electrons as derived in Chapter 6. Data is represented by black markers, and the contributions to the background are drawn stacked on top of each other. Possible signals of a SSM Z′ with pole masses of 1500 GeV and 2000 GeV are drawn on top of the standard model expectation. The latter is normalized to the number of events in data in the mass range 70 GeV to 110 GeV. In the inset, the ratio of the number of events in data over the number of background events expected is shown.

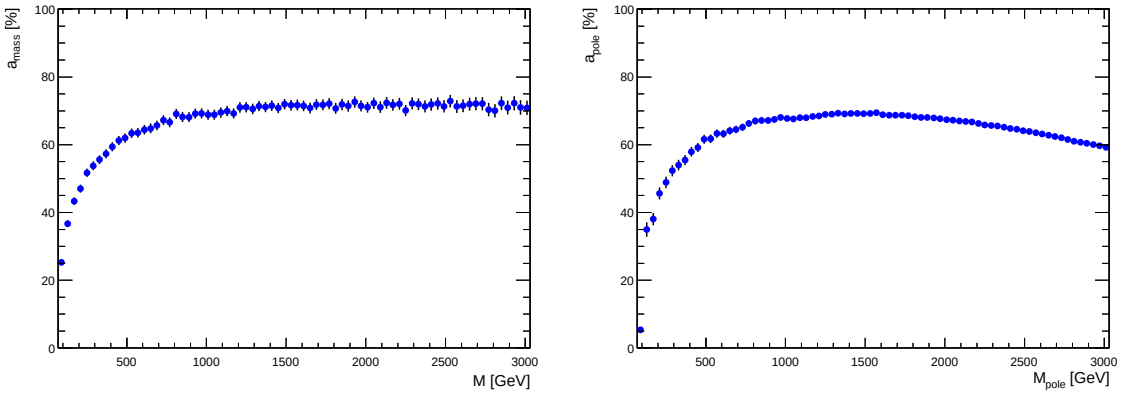

Figure 8.2: The left plot shows the acceptance a_{mass} as function of the SSM Z′ truth mass and the right one the acceptance a_{pole} as a function of the SSM Z′ pole mass. Note that for the right plot, for each value of M_{pole}, all events of the Monte Carlo sample are used, which leads to a lower statistical uncertainty at high pole masses.

a low acceptance weight a_{mass}. For example, the acceptance a_{pole} at 1500 GeV amounts to 69.2% while it is only 65.2% at 2500 GeV.

8.3 Exclusion Limits

Limits on the cross-section times branching ratio for the SSM Z' have been calculated using the procedure described in Section 8.1 with the background estimation as discussed in Section 6.6 and the signal templates for different pole masses as described in Section 8.2. Templates have been generated every 40 GeV in the pole mass range from 130 GeV to 2970 GeV, leading to 72 signal templates in total. For each pole mass, a total of 4000 pseudo-experiments have been carried out to estimate the expected limit at each point. As discussed in Section 2.5.3, interference of the Z' with the Drell-Yan process is neglected.

8.3.1 Systematic Uncertainties

For the uncertainties considered in the limit calculations of this thesis, the same approach was chosen as already used for the ATLAS Dilepton Search publication. The mass spectrum in the range 128 GeV to 3000 GeV is taken into account, which leaves out the mass region where the background prediction was normalized to data.

Fig. 8.3 shows the the relative impact of the evaluated uncertainties on the mass spectrum

$$\delta_{impact,j}(M_{ee}) = \frac{\Delta_{sys,j}(M_{ee})}{N_{tot}(M_{ee})}. \tag{8.13}$$

It describes the percentage by which the total background prediction, $N_{tot}(M_{ee})$, would change, if the total number of background events were increased or decreased by one standard deviation $\Delta_{sys,j}(M_{ee})$ of the considered uncertainty j. In the following, the individual uncertainties and the reasons for including or not including them as a nuisance parameter are discussed. Each individual uncertainty is treated as fully correlated over the whole mass spectrum.

The dominant systematic uncertainty at high masses is the uncertainty on the multijet and W+jets estimation. At[8] 2 TeV, the relative uncertainty itself amounts to 111%, which leads to an impact or uncertainty of 37% on the total background.

The uncertainty with the second largest impact at high masses is the combined PDF, α_s and scale uncertainty of the Drell-Yan contribution. The relative impact on the total background amounts to approximately 3% at low masses and increases to 12% at 2 TeV. The uncertainty on electroweak higher-order corrections to the Drell-Yan process does not affect the total background by more than 2.5%.

The relative impact of the extrapolation uncertainties for the diboson contribution on the total background prediction amounts to approximately[9] 1% at 1500 GeV and does not exceed 7% over the full mass range. The impact of the diboson cross-section uncertainty is even smaller than the extrapolation uncertainty.

[8] The uncertainties quoted here are evaluated for a bin from 2000 GeV to 2001 GeV, while the uncertainties quoted in, e.g., Table 6.7 are evaluated for the full bin listed in the table.

[9] The extrapolation for the diboson mass distribution starts at 1500 GeV. This threshold does not match the bin borders in the plot, which are 1434 GeV and 1534 GeV, therefore the relative impact of the bin starting at 1434 GeV is lower than 1%.

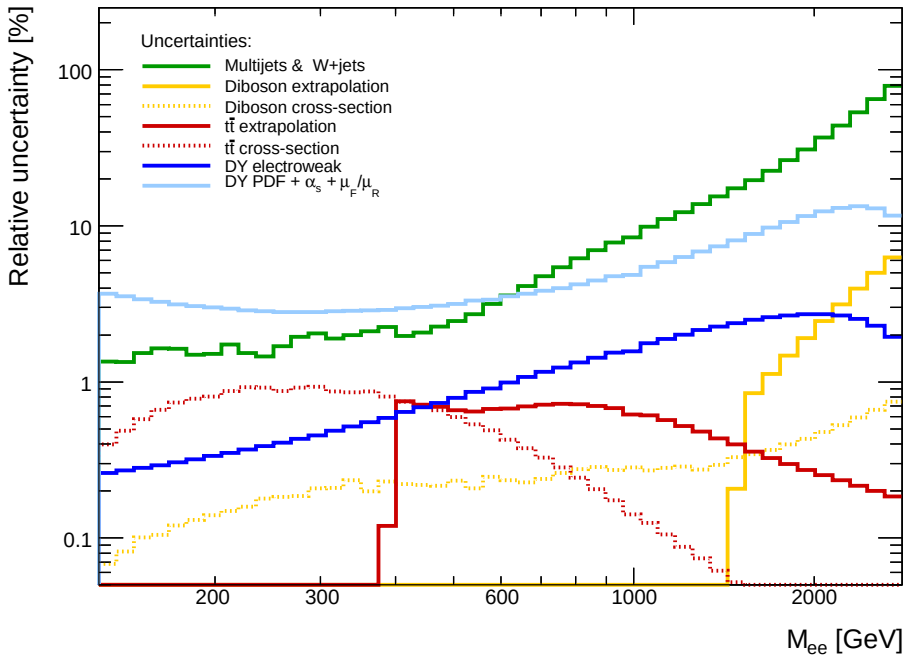

Figure 8.3: The impact of the individual systematic uncertainties, $\delta_{impact}(M_{ee})$, on the total number of background events predicted is shown. The turn on effects of the diboson and the $t\bar{t}$ extrapolation uncertainties are discussed in the text.

For the $t\bar{t}$ contribution, the impact of both, the extrapolation[10] and the cross-section uncertainty on the total background prediction, is below the per cent level.

To estimate the impact of the systematic uncertainties on the σB limits, expected limits with and without the uncertainties discussed so far have been calculated. The expected limit on the σB limits at 1 TeV worsened by 0.9%, whereas the decrease at 2.1 TeV amounts to 1.3%.

Furthermore, to estimate the minimum size of a systematic uncertainty to have an impact on the σB limits, expected limits have been calculated with and without the diboson extrapolation uncertainty included on top of the multijet and W+jets and Drell-Yan uncertainties. The difference is negligible, therefore the diboson extrapolation uncertainty and all further systematic uncertainties, which are smaller, are neglected for the limit calculations.

The efficiency scale factors are close to unity and their relative uncertainties are typically at the one per cent level. Therefore their impact on the final mass distribution is expected to be negligible. The luminosity uncertainty does not enter, because the background prediction is normalized to data in the mass range around the Z boson pole mass.

8.3.2 Results

Fig. 8.4 shows the calculated expected and observed 95% C.L. limits[11] on the cross-section

[10] The bin borders of the histogram do not match the mass threshold above which the extrapolation is used, see same comment on the diboson uncertainty.

[11] All limits derived in this thesis as well as all limits quoted from other analyses are 95% C.L. limits, therefore the confidence level is not quoted explicitly in the following.

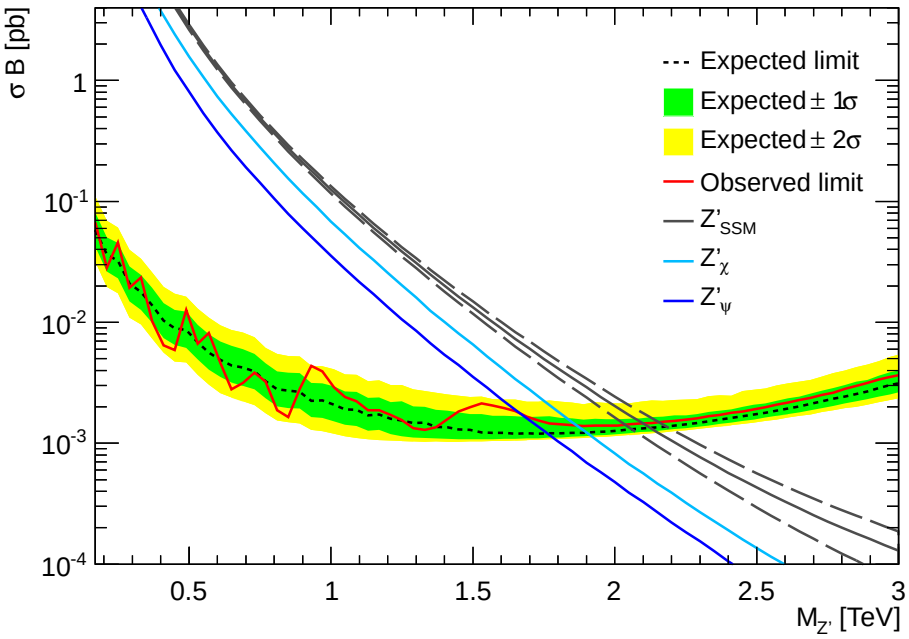

Figure 8.4: The calculated 95% C.L. limits on the cross-section times branching ratio are shown as a function of the pole mass of the SSM Z′. The expected limit is indicated by a dashed black line, which is surrounded by the one (two) sigma uncertainty band drawn in green (yellow), whereas the observed limit is shown as red line. For a given pole mass, all values of σB, which are above the value of the observed limit, are excluded with 95% C.L. For comparison some theoretical predictions are shown. The gray continuous line represents the theory prediction of the cross-section times branching ratio of the SSM Z′, while the dashed gray lines indicate the combined PDF, α_S and μ_F/μ_R scale uncertainties. The blue (cyan) curve shows the theory predictions for the $E6$-based Z′ boson with the lowest (highest) cross-section times branching ratio, the Z'_ψ (Z'_χ). The data used for the exclusion limits corresponds to an integrated luminosity of $4.9\,\mathrm{fb}^{-1}$.

times branching ratio σB for the SSM Z' as a function of the pole mass of the Z'. In total, 72 limits were calculated for the 72 templates at different pole masses discussed in Section 8.2. This leads to 72 results, each displayed in a separate mass bin in Fig. 8.4. It can be interpreted as follows: The lower the value of the expected limit on σB is in a mass bin, the larger is the sensitivity to an additional SSM Z' boson with a pole mass as denoted by the mass bin. The σB limits will be discussed first, then the conversion into mass limits and the corresponding results.

The shape of the expected σB limit can be explained with the shape of the acceptance as shown in the right plot of Fig. 8.2. At low masses, the acceptance increases as the survival fraction of the electron E_T and η cuts increases, and so does the sensitivity. For masses above approximately 1.6 TeV, the acceptance decreases due to the increasing low mass tail of the Z' mass distribution, which increases the fraction of events with lower acceptance. This leads to the decreasing sensitivity for masses above 1.6 TeV. For example, at a mass of 3 TeV, the sensitivity in terms of an expected limit on σB amounts

to only half the value expected[12] at 2 TeV.

The observed limits fluctuate within the 2σ uncertainty band of the expected limit, which is a further hint that there is no significant deviation from the SM expectation. At approximately 1 TeV and 1.6 TeV, two (small) local maxima are visible in the observed limit. The maximum at approximately 1000 GeV was already discussed in Section 7.2. The second, less significant maximum is caused by the 3 events observed between 1.2 TeV and 1.7 TeV, whereas 1.99 ± 0.35 are expected.

At higher Z' pole masses, where no events have been observed, the observed limit does not converge towards the expected limit, but is slightly above the expectation. This is due to the long low mass tail predicted for Z' bosons with pole masses beyond 1.64 TeV, which is compatible with the observed "excess" of approximately one event in data. As a sanity check, the two highest mass events observed in data at 1.47 TeV and at 1.64 TeV have been artificially removed. In this case, the observed limit converges quickly towards the expected limit, which shows that this effect has a physical reason and is not a bug or artifact of the limit setting procedure.

For a given pole mass, all values of σB, which are higher than the value of the expected σB limit, are expected to be excluded. The pole mass, where the predicted σB curve for the SSM Z' intersects with the expected σB limit, is thus the highest mass that can be expected to be excluded. For all pole masses below the intersection point, the predicted σB is higher than the value that is excluded. By generating and evaluating 4000 pseudo-experiments, an expected SSM Z′ mass limit of 2.13 TeV was calculated. The observed mass limit is calculated correspondingly from the intersection point of the theory prediction with the observed σB limit and amounts to 2.10 TeV, which is slightly below the expectation due to the slight "excess" in data.

As a cross-check, the expected limits have been calculated without any systematics included, which leads to slightly stricter limits on σB, namely 1.3% at 2.1 TeV. Due to the small amplitude of the deterioration and the small crossing angle between the theory cross-section and the σB limit, the impact on the SSM Z' mass limit is negligible. Both expected limits are identical, if quoted with three significant digits.

Exclusion limits have also been calculated for the E_6 based Z' models. Here, the same σB limits as for the SSM Z' were used, but they were converted into limits on a mass by using the σB of the corresponding E_6 Z' bosons. This approximation was also chosen in the ATLAS dilepton resonance search and assumes that the effect of the smaller relative width of the E_6 based Z' bosons, 0.5% to 1.3%, in comparison to the relative width of the SSM Z' boson of approximately 3% can be neglected. The mass resolution in the high mass regime was estimated to be approximately one percent (see Section 3.3.2). Therefore the approximation of the narrower E_6 based Z' signal templates with the wider SSM Z' templates is conservative, as it leads to a lower limit. More stringent limits for the E_6 based Z' bosos could have been achieved by calculating dedicated signal templates and acceptances as well as generating pseudo-experiments. Due to the small expected gain and the additional amount of computing power required, the approximation was used.

With this approximation, the excluded masses range from 1.67 TeV for the Z'_ψ, which has the lowest σB of the E_6 based Z' bosons, to 1.87 TeV for the Z'_χ, which has the highest σB of the E_6 based Z' bosons. In all cases, the observed limits are close to but lower than the expected limits. This behavior can be expected from Fig. 8.4.

[12] This interplay between parton luminosity, resulting low mass tails and acceptance does not allow to extrapolate results to higher integrated luminosities or center-of-mass energies directly. Instead, dedicated calculations are needed.

Table 8.1: This table shows expected and observed 95% C.L. limits derived for the SSM and E_6 based Z's. The data set analyzed corresponds to an integrated luminosity of $4.9\,\text{fb}^{-1}$.

Model	SSM Z'	Z'_ψ	Z'_N	Z'_η	Z'_I	Z'_S	Z'_χ
Expected mass limit [TeV]	2.13	1.76	1.78	1.81	1.81	1.85	1.90
Observed mass limit [TeV]	2.10	1.67	1.70	1.76	1.77	1.81	1.87

In Table 8.1, all expected and observed limits derived for the various Z' models are summarized. They depend on the coupling strength of the Z' bosons to fermions. For smaller couplings than the ones predicted in these models, the corresponding product of cross-section and branching ratio at a given pole mass is smaller and not excluded. Therefore, also in future searches for resonances beyond the SM, data ought to be compared carefully to the expectation over the whole mass spectrum, as the sensitivity to lower couplings increases with higher integrated luminosity and center-of-mass energy.

8.3.3 Comparison to other Analyses

In Section 2.5.4, results, which were derived from data taken before the data set of this thesis, were already discussed. Further results published during this analysis are summarized in Table 8.2 and will be discussed individually in the following.

The ATLAS collaboration has published results using a subset of the data taken in 2011 with an integrated luminosity of $1\,\text{fb}^{-1}$ in the di-electron and di-muon channel [94]. The expected and observed limits were identical within the quoted precision for both channels. SSM Z' masses below 1.70 TeV were excluded in the di-electron channel. In the di-muon channel, where the acceptance is significantly lower than in the di-electron channel, masses below 1.61 TeV were excluded. With the combination of both channels, masses up to 1.83 TeV were excluded.

The expected limit for the SSM Z' boson, derived in the official ATLAS dilepton resonance search analysis of the full 2011 data set [24] in the di-electron channel, is identical to the result of this thesis, while the observed limit in this thesis is slightly higher, 2.10 TeV in comparison to 2.08 TeV. As discussed in Section 6.6.1, the acceptance is identical in both analyses, and the total background estimations at high masses agree within uncertainties, whereas the background expectation derived in this analysis is slightly higher (11%). This leads to the very similar results, if the limits are rounded to three significant digits.

In the ATLAS dilepton resonance search, the results from the di-electron and the di-muon channel were also combined. In combination, masses up to 2.25 TeV were expected to be excluded, while the observed limit amounts to 2.22 TeV. For the E_6 based Z' models, only the combined results are public[13]. Since the limits using only the di-electron channel were calculated for the ATLAS dilepton resonance search, they could nevertheless be compared to the results of this thesis. The expected limits in both analyses are very similar, while the observed limits calculated in this thesis are slightly higher. This is

[13]For brevity, only the combined limits were published.

Table 8.2: Recent expected (exp.) and observed (obs.) 95% C.L. SSM $Z' \to ee$ limits as well as the combined 95% C.L. limits ($Z' \to ee$ and $Z' \to \mu\mu$) are shown. Results that were published previously are listed in Section 2.5.4. The data set size is expressed in terms of the associated integrated luminosity. Preliminary results are marked by "(*)". Unpublished results are marked by "n.p.", while limits that were not calculated are marked by "n.a." Expected limits marked by "n.p.n." were not published numerically but in form of plots only, which cannot be used to extract the expected limit with the desired precision.

Analysis by	Center-of-mass energy [TeV]	Data set size [fb^{-1}]	Z′→ *ee* limit [TeV] Exp.	Obs.	Comb. Z′ limit [TeV] Exp.	Obs.
This thesis	7 TeV	5	2.13	2.10	n.a.	n.a.
ATLAS [94]	7 TeV	1	1.70	1.70	1.83	1.83
ATLAS [24]	7 TeV	5	2.13	2.08	2.25	2.22
CMS [111]	7 TeV	5	n.p.n.	2.12	n.p.n.	2.33
ATLAS [112]	8 TeV	6	2.39(*)	2.39(*)	2.49(*)	2.49(*)
CMS [113]	8 TeV	4	n.p.n.	2.20(*)	n.p.	n.p.
CMS [113]	7+8 TeV	5+4	n.p.	n.p.	n.p.n.	2.59(*)

expected, because the same was observed for the SSM Z' limits.

The CMS collaboration has also performed an analysis of the 5 fb^{-1} of data taken in 2011 [111] and derived similar observed limits in the electron channel, namely 2.12 TeV in comparison to 2.10 TeV in this thesis. Expected limits of all relevant CMS dilepton analyses are published only in form of plots of similar style as in Fig. 8.4, which do not allow to derive the expected limits numerically with sufficient precision for comparisons on the 10 GeV level. However, the observed limits are, by eye, identical to the expected limits. This allows to conclude from the observed limits that the sensitivity of the CMS analysis with the 2011 data set is very similar to the sensitivity of the analysis of this thesis. In the following, only the observed limits of the CMS collaboration are discussed in terms of numerical results. The combined limit for the electron and muon channel derived by the CMS collaboration, is expected to be stricter than the limit calculated by the ATLAS collaboration, because the total muon acceptance is higher for CMS. In fact, the observed limit amounts to 2.33 TeV, which is stricter than the ATLAS limit of 2.22 TeV.

In 2012, the LHC was operated at a center-of-mass energy of 8 TeV. Parts of the data taken were already analyzed and published as preliminary results by both collaborations. The ATLAS collaboration has analyzed a data set with an integrated luminosity of 6 fb^{-1} and excludes Z′ masses below 2.49 TeV in the combination of the di-electron and di-muon results [112]. In this case, observed and expected limits are identical within the quoted precision. The CMS collaboration has analyzed a smaller data set with an integrated luminosity of 4 fb^{-1}, but has combined the results with the results derived from the 2011 data set. With the combination of both data sets in the electron and muon channel, Z′ masses below 2.59 TeV were excluded[14] [113]. This is the most stringent limit up to date

[14]The expected and observed limits in the plots are also judged as identical by eye, see the discussion on

on the mass of a SSM Z' boson, that is assuming SM-like couplings to fermions. For models that have a lower cross-section times branching ratio like the E_6 based Z' bosons, the exclusion limit in terms of masses is lower.

8.3.4 Discussion of possible Improvements

In the following, possibilities to increase the sensitivity to high mass resonances will be discussed. The sensitivity for a fixed data set size at a fixed center-of-mass energy depends mainly on the total acceptance, the size of the reducible (fake) background and the result of the convolution of the signal line shape with the PDFs at high pole masses. The ATLAS collaboration derived a new, optimized set of electron identification criteria, which provide an increased fake rejection while maintaining approximately the same signal efficiency. For high mass analyses, the new identification criteria need to be studied carefully, as they use, amongst others, additionally the information whether or not a particle emits transition radiation while traversing the transition radiation tracker. Already in the low momentum regime, e.g., at 25 GeV, electrons have a sufficiently high Lorenz factor and therefore emit transition radiation. In contrast, most jets consist primarily of pions and kaons, which do not emit transition radiation in this low momentum regime. This allows to discriminate between these jets and real electrons. For higher momenta of $\mathcal{O}(100\,\text{GeV})$, also pions emit transition radiation. This might introduce a discontinuity in the data-driven fake background estimate, which needs to be studied.

The electron isolation leakage correction, which corrects for energy deposited outside of the electron core region, has a decreasing efficiency as function of E_T and does not take into account the differences for leading and subleading electrons, see Section 5.2.4. With a sufficiently improved efficiency at high momenta, the isolation requirement could be tightened for the leading electron, and an isolation requirement could also be imposed on the subleading electron. Alternatively, the increased efficiency could be used to increase the signal acceptance slightly.

A further fake background reduction might be achieved by requiring that the selected pair of electrons is assigned to the same vertex. This means that both electrons were produced in the same proton-proton scatter. Then events can be suppressed, where only one prompt electron within the sensitive detector volume exists, which is combined with a jet from a second hard scatter in the same event, which fakes an electron signature. This cut is especially interesting for future analyses with data taken in a high pile-up environment, where the probability to find a high momentum jet from a second hard scatter is sufficiently high.

However, a higher fake background rejection has even more impact on data analysis. The fake background needs[15] to be estimated from data, and the number of events an estimate is based upon decreases with increasing fake rejection. This increases the sensitivity to statistical fluctuations as well as the size of the extrapolation uncertainty[16].

The impact of a higher fake background rejection is hard to judge. In the CMS analysis of the 2011 data set, a higher fake background rejection was achieved, e.g., by imposing

the CMS results of the 2011 data set.

[15] The higher the fake background rejection of the selection, the more Monte Carlo events need to be simulated to find one event that passes the selection. Further, to prove that the fake rate is correctly described in the simulation, a data-driven estimate is needed.

[16] Of course, this also depends on the availability of a dedicated support trigger, which might provide a sufficiently large data set of fake candidates.

the isolation requirement on the subleading electron. However, the limits derived by CMS are very similar to the limits derived by ATLAS, which might indicate that the effect of the fake background at highest masses is small.

The limit setting procedure itself is already quite sophisticated and takes into account the signal shape as a function of the reconstructed mass. The exclusion limits for the E_6 based Z' bosons could be enhanced by generating exact templates as it is done for the SSM Z'. For a given model respectively expected signal width, an optimization of the mass binning could be studied, e.g., the bin size adapted to the signal width, but no significant impact is expected.

Instead of optimizing the sensitivity to specific Z' models, a completely different ansatz could be evaluated, e.g. shape-insensitive limits in terms of cross-section times branching-ratio times acceptance for resonance models, where the width is small and the interference with the SM Drell-Yan process negligible. These limits could be interpreted by theorists, if they calculate the acceptance[17] of their signal in the phase space covered in the analysis. However, the sensitivity would be significantly lower and some popular models cannot be treated this way at all, e.g., the Randall-Sundrum gravitron [114], which has a very broad experimental signature for high coupling strengths, or Kaluza-Klein modes of electroweak bosons [115], whose main experimental signature is the strong destructive interference at approximately half the pole mass. With the shape sensitive limit setting procedure, the ATLAS dilepton resonance search has set the most stringent limits on Randall-Sundrum gravitrons up to date and, for the first time ever, limits on the existence of such Kaluza-Klein modes of electroweak bosons.

The largest increase of sensitivity can be achieved by increasing the center-of-mass energy. This does not only increase the parton-parton luminosity, but also the acceptance at high pole masses, see Sections 8.2 and 8.3.2. This leads to two effects. For a fixed pole mass, the sensitivity to lower coupling strengths will increase and higher pole masses will become accessible. Both effects will be discussed in detail in the next section.

8.4 Future Prospects

In 2012, the LHC was operated in the proton-proton mode at a center-of-mass energy of 8 TeV, and a data set with an integrated luminosity of $21.7\,\text{fb}^{-1}$ was recorded. Analyzing this data set, the ATLAS (and the CMS) collaboration will either observe hints on a new resonance, or calculate even stricter exclusion limits. For the ATLAS analysis, a first preliminary estimation of the combined expected limit for an integrated luminosity of $25\,\text{fb}^{-1}$ amounts to 2.87 TeV [116]. Extrapolated to an integrated luminosity of $21.7\,\text{fb}^{-1}$, masses below approximately 2.8 TeV are expected to be excluded. Of course, not yet implemented improvements in the analysis might improve the limits further.

For 2015, it is planned to operate the LHC at a center-of-mass energy of 13 TeV, slightly below the design energy of 14 TeV. To estimate limits that can be set with the data taken at these energies, the parton luminosities need to be discussed first. Fig. 8.5 shows the ratio of the parton luminosities at 8 TeV and 14 TeV with respect to 7 TeV, as predicted using the MSTW2008NLO PDF [117]. For the production of Z' bosons, the quark anti-quark parton luminosity summed up for all flavors is the relevant quantity. At a mass of 2 TeV (3 TeV), the parton luminosity increases by a factor of approximately 2 (3),

[17] On top of the geometrical acceptance, further efficiencies like electron reconstruction and identification efficiencies need to be taken into account.

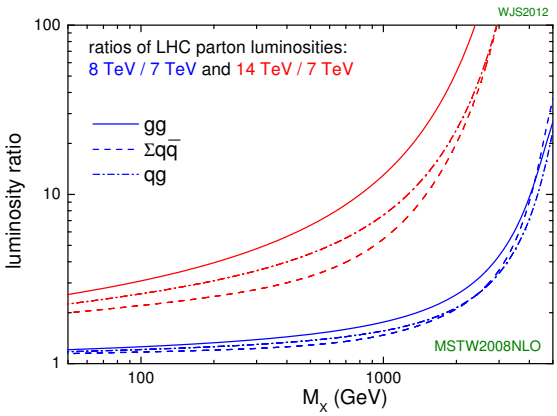

Figure 8.5: The ratios of the parton luminosities at 8 TeV (14 TeV) with respect to the ones at 7 TeV are shown in blue (red) as calculated with the MSTW2008NLO PDF. The ratios of the quark anti-quark luminosities (summed up for all flavors) are denoted by $\sum q\bar{q}$, whereas the ratios of the gluon-gluon luminosities are denoted by gg and the ratios of the quark-gluon luminosities by qg. The plot is taken from Ref. [117].

when increasing the center-of-mass energy from 7 TeV to 8 TeV. At 14 TeV, the parton luminosity for the same masses increases even by a factor of approximately 20 (100), which leads to a significantly enhanced sensitivity. On the other hand, when the LHC is operated at a center-of-mass energy of 13 TeV or 14 TeV and with the design luminosity of $10^{34}\,\mathrm{s}^{-1}\mathrm{cm}^{-2}$, new experimental challenges arise.

With the nominal 25 ns bunch spacing, on average 27 interactions per bunch-crossing are expected [118], which is above the original estimation of 23 interactions assumed during the ATLAS design phase. For comparison[18], in 2012 the average number of interactions amounted to 20, and in parts of the data an instantaneous luminosity close to the design luminosity was achieved.

To cope with this increased number of pile-up interactions, several upgrades will be installed in ATLAS during the long shutdown from spring 2013 to 2014. One important component is an additional layer of the inner tracking system, which will be inserted between the pixel detector and the beam pipe to measure charged particles as close as possible to the interaction point. This allows to separate tracks more precisely, which is important as the number of tracks will increase significantly due to the higher pile-up[19].

On the software side, the algorithms used to reconstruct and identify electrons need to be adapted, as the higher detector occupancy will lead to less well separated particle signatures in the calorimeters. Furthermore, the number of jets that could fake the signature of electrons will increase significantly, which requires a careful optimization

[18] In 2012, the bunch spacing was 50 ns, which results into approximately the double amount of interactions per bunch-crossing for the same instantaneous luminosity as with a 25 ns bunch spacing. The instantaneous luminosity was increased multiple times in 2012, so the average number of interactions as measured for the full 2012 does not correspond to a single value of the instantaneous luminosity, which makes it difficult to compare with the conditions planned for 2015.

[19] Furthermore, it allows to determine secondary vertices of long lived particles like b-hadrons more precisely

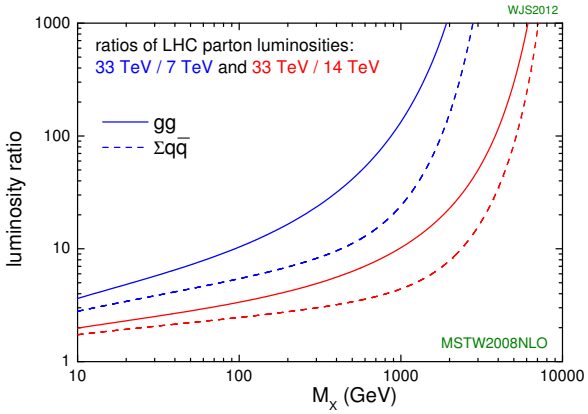

Figure 8.6: The ratios of the parton luminosities at 33 TeV with respect to the ones at 7 TeV (14 TeV) are shown in blue (red) as calculated with the MSTW2008NLO PDF. The ratios of the quark anti-quark luminosities (summed up for all flavors) are denoted by $\sum q\bar{q}$, whereas the ratios of the gluon-gluon luminosities are denoted by gg. The plot is taken from Ref. [117].

of the selection efficiency versus the background rejection for electrons.

At the higher nominal center-of-mass energy, electrons with a E_T of a few TeV might[20] not deposit their full energy in the em. calorimeter, but instead deposit a small fraction of their energy in the had. calorimeter. There are correction procedures in place to minimize the worsening of the energy resolution, but they need to be studied in detail.

The reach of future di-electron resonance searches has been estimated under the assumption that a real electron efficiency, resolution and fake rejection as for current analyses can be achieved. With a data set corresponding to an integrated luminosity of 300 fb^{-1} taken at a center-of-mass energy of 14 TeV, SSM Z' masses below 6.5 TeV are expected to be excluded [119].

For the future beyond this, several different scenarios are currently under discussion. One scenario, referred to as High Luminosity LHC (HL-LHC), foresees to take further data, approximately 3000 fb^{-1} at the design center-of-mass energy of 14 TeV, but with a higher instantaneous luminosity, e.g., $5 \cdot 10^{34}\,\mathrm{s}^{-1}\mathrm{cm}^{-2}$ [118]. The number of pile-up events per bunch-crossing is estimated to be 140 on average. Assuming a similar electron performance as in the 7 TeV or 8 TeV analysis can be achieved, an expected SSM Z' limit of 7.8 TeV has been calculated in the di-electron channel [119].

Another scenario is to further increase the center-of-mass energy to 33 TeV, which is referred to as High Energy LHC (HE-LHC). The sensitivity to high Z' masses is significantly increased due to the increased parton luminosity as shown in Fig. 8.6. For example, at a pole mass of 6 TeV, the parton luminosity increases by an factor of approximately 200. However, for this scenario no expected Z' exclusion limits have been calculated. As discussed before, limits are hard to extrapolate from, e.g., 14 TeV to 33 TeV, as both, the parton luminosity and the acceptance, need to be taken into account. From a generic approach made in Ref. [120], it was concluded that for Z' masses of 2.5 TeV a data set,

[20] The calorimeters are constructed such that typically electrons are stopped within the em. calorimeter. However, fluctuations of the shower depth are possible.

taken with an integrated luminosity of $300\,\mathrm{fb}^{-1}$ at the HE-LHC, has the same sensitivity as a data set taken with ten times the integrated luminosity at the HL-LHC. For higher Z' masses, the gain in sensitivity increases further for a fixed amount of data due to the significantly higher parton luminosity.

These two scenarios provide access to phase space regions that have not been accessible yet and which increases the sensitivity of direct searches for particles beyond the SM significantly. However, a completely different approach is also under discussion: Indirect searches in angular distributions of lepton-lepton final states at electron-positron colliders. A well studied scenario of this type is the International Linear Collider (ILC), a polarized electron-positron collider, which could be operated at center-of-mass energies between 0.5 TeV and 1 TeV. In contrast to proton-proton colliders, there are only few (photon-photon) pile-up interactions per bunch-crossing, which results into very clean event topologies and therefore allows much more precise cross-section measurements. Due to the low center-of-mass energy in comparison to the LHC, the reach in direct searches for Z' bosons is limited. However, by including the polarization information in measurements of angular asymmetries [121], the sensitivity to coupling strengths and types of Z' bosons is expected to be sufficient in order to distinguish between different models up to high pole masses, if a Z' was discovered. With an integrated luminosity of $500\,\mathrm{fb}^{-1}$ ($1000\,\mathrm{fb}^{-1}$) at a center-of-mass energy of 0.5 TeV (1 TeV), the SSM Z' boson, the E_6 based Z' bosons as well as further Z' models could be distinguished up to masses of approximately 3.3 TeV (6.5 TeV) [121]. In contrast, at the LHC, operated at a center-of-mass energy of 14 TeV and an integrated luminosity of $100\,\mathrm{fb}^{-1}$, the SSM and E_6 based Z' models can only be distinguished up to masses of 2.2 TeV, which are already excluded or about to be excluded, respectively [121].

The answer to the question, which scenario provides the richest physics perspectives, also depends largely on the discovery or not-observation of new particles in the data taken, when the LHC is finally operated at (or close to) design center-of-mass energy. If new heavy particles are discovered, especially beyond the direct kinematic reach of currently studied electron-positron colliders, scenarios with an upgraded LHC are favored. If no additional particles are discovered, the prospects of precision studies of the Higgs-like boson, which was discovered in summer 2012 by the ATLAS and CMS collaborations, will play an important role for the decision on a future collider. The couplings of this Higgs-like boson need to be measured with an relative precision of one per cent or better to distinguish a SM Higgs boson with sufficient significance from the Higgs bosons predicted by many beyond the SM extensions. And according to Ref. [122], the required precision can only be achieved with electron-positron colliders.

9 Conclusions and Outlook

Discoveries of so far unknown particles have always played a major role in the understanding of particle physics. Although the Standard Model (SM) of particle physics is very successful in describing most measurements with high precision, there are strong hints that the SM is an effective theory of a more complete theory. Many extensions of the SM predict heavy gauge bosons or other resonances that decay into a electron positron pair. They can be searched for with the LHC, where protons are collided at unprecedented center-of-mass energies. This allows to test the SM at electron pair masses, which have not been accessible at previous colliders like the Tevatron accelerator at the Fermilab.

This thesis reports on a search for high-mass resonances with the ATLAS detector at the LHC. The analyzed data set, which corresponds to an integrated luminosity of $4.9\,\mathrm{fb}^{-1}$, was taken in 2011, when protons were collided at a center-of-mass energy of 7 TeV. The di-electron mass spectrum has been measured and masses up to 1.64 TeV have been observed. The SM expectation has been carefully estimated using Monte Carlo simulations and data-driven methods. The main contributions at high mass are electron pairs from the Drell-Yan process, from diboson events, where two W and/or Z bosons were produced and decayed in final states with at least two electrons. Further, fake contributions from multi-jet production or associated jet production with a W boson, where a jet mimics the signature of an electron, have been estimated with a data-driven method and cross-checked with a partially data-driven method. The SM background estimate is an improved estimate with respect to the one I derived[1] for the ATLAS dilepton resonance search in the electron channel and also provided for the ATLAS search for contact interactions and large extra dimensions in dilepton events.

The main improvements in this thesis concern the SM expectation. The method to extrapolate mass distributions towards 3 TeV has been replaced by a method, which depends to a much lower degree on subjective choices for fit range variations to estimate the stability of the extrapolation. The estimation of the multijets and W+jets background with *method I* has been improved by refining the extrapolation method and performing detailed studies of systematic uncertainties. For the W+jets estimate with *method II*, the contribution of the mass distributions binned in the jet multiplicity has been studied in detail and different "slopes" as a function of mass have been found. Therefore the individual contributions have been extrapolated separately instead of extrapolating one merged mass distribution. Further, the (small) fake contribution of the $t\bar{t}$ background has been studied and corrected for explicitly.

This improved SM expectation has been used for a comparison with data. Possible deviations have been quantified in terms of local and global significances, but no significant deviation was found. Therefore, exclusion limits have been set on two classes of heavy

[1] In the ATLAS dilepton resonance search, I combined three methods that estimated the fake background, where two of them were the methods discussed here and the third method was derived by a colleague. For the third method, I also performed the extrapolation of the di-electron mass distribution to 3 TeV. Further the extrapolation (but not the derivation) of three Monte Carlo mass spectra was performed by another colleague due to time constraints.

gauge bosons, the Sequential Standard Model (SSM) Z' and the E_6 based Z' bosons. The limit setting procedure uses mass templates, which take into account the signal shape[2], but neglect interference of the SSM Z' with the SM Drell-Yan process. Limits in terms of the cross-section times branching ratio into electrons, σB, were derived as a function of the Z' pole mass, and converted into lower mass limits on the pole mass of the Z' boson. An expected limit of 2.13 TeV was calculated with 95% C.L.[3], whereas an observed limit of 2.10 TeV was derived. Further, exclusion limits on the lower mass of six Z' bosons as predicted by E_6 models were set, which range from 1.67 TeV for the Z'_ψ to 1.87 TeV for the Z'_χ.

In the frame of the ATLAS dilepton resonance search, very similar limits were derived, namely the expected limit for the SSM Z' boson is the same, because the acceptance, which drives the sensitivity to Z' bosons, is identical for both analyses. However, the observed limit of 2.10 TeV calculated in this thesis is slightly higher than the observed limit of 2.08 TeV derived in the ATLAS dilepton resonance search. Due to improvements with respect to the fake background estimation and with respect to the extrapolation to high masses, the total background expectation derived in this thesis is slightly higher (and closer to data) at high masses. This explains the higher observed limit.

The CMS collaboration also analyzed the 2011 data set and excluded SSM Z' masses below 2.12 TeV, which is a very similar result to the ones derived in this thesis.

In 2012, the LHC was operated at a center-of-mass energy of 8 TeV. The ATLAS collaboration has published preliminary results with a data set corresponding to an integrated luminosity of $6\,\text{fb}^{-1}$ out of the total $21.7\,\text{fb}^{-1}$. SSM Z' masses below 2.39 TeV were excluded in the di-electron channel, whereas in combination with the di-muon channel, masses below 2.49 TeV were excluded. The CMS collaboration analyzed a data set corresponding to an integrated luminosity of only $4\,\text{fb}^{-1}$, but combined the preliminary results with the ones from the analysis of the data set taken in 2011. With the combination of the di-electron and di-muon channel results, SSM Z' masses below 2.59 TeV were excluded, which is the most stringent limit up to date.

In 2015, the LHC center-of-mass energy is planned to be increased to 13 TeV initially, which is slightly below the design energy of 14 TeV. With a data set corresponding to an integrated luminosity of $300\,\text{fb}^{-1}$ at a center-of-mass energy of 14 TeV, SSM Z' masses below 6.5 TeV are expected to be excluded with the combined di-electron and di-muon data. This is a significant increase with respect to to what can be achieved with the data taken in 2012.

The sensitivity to high-mass resonances can not only be improved by upgraded colliders and detectors, but also slightly by improving the analysis itself, which will be summarized in the following. A new, optimized set of electron identification criteria has been derived by the ATLAS collaboration, which reduces the number of jets that are mis-identified as electrons, while maintaining the same electron efficiency as the set used in this analysis. Further studies are needed to show that the transition radiation cut used in the optimized set does not introduce discontinuities or biases in, e.g., the fake background mass distribution. An improved electron isolation leakage correction, which has a high efficiency at high transverse energies close to the barrel end-cap calorimeter transition region and which takes the differences between leading and subleading electrons into account, could be used to increase the signal acceptance by a small amount and/or to reduce the size

[2]The signal shape is governed by the convolution of the natural line shape and the Parton Density Functions (PDFs).

[3]All limits quoted, including those derived by other experiments, are 95% C.L. limits.

of the fake background. The fake background could be reduced further with the requirement that pairs of electron candidates need to be matched to the same vertex. The effect on an reduced fake background contribution is difficult to judge, but also no significant impact is expected. Furthermore, a consistency check of the fake factor method could be performed by studying the multijet and W+jets fake factor estimate without the $r = 1$ approximation.

The limit setting procedure itself is sophisticated and takes into account the signal shape as a function of the reconstructed mass for a maximum of sensitivity. The exclusion limits for the E_6 based Z' bosons could be enhanced by generating exact templates as it was done for the SSM Z'. For a given model respectively expected signal width, an optimization of the mass binning could be studied, but the impact on exclusion limits is expected to be small.

In conclusion, the sensitivity to high-mass resonances can be significantly improved by increasing the center-of-mass energy and the integrated luminosity. Improvements in the analysis methods on the other hand are expected to have little impact on the sensitivity, but can further enhance the quality of the background estimation.

Bibliography

[1] M. Gell-Mann, *A Schematic Model of Baryons and Mesons*, Phys.Lett. **8** (1964) 214–215.

[2] V. E. e. a. Barnes, *Observation of a Hyperon with Strangeness Minus Three*, Phys. Rev. Lett. **12** (1964) 204–206.

[3] PLUTO Collaboration, *Evidence for gluon bremsstrahlung in e^+e^- annihilations at high energies*, Physics Letters B **86** (1979) 418–425.

[4] TASSO Collaboration, *Evidence for planar events in e^+e^- annihilation at high energies*, Physics Letters B **86** (1979) 243–249.

[5] JADE Collaboration, *Observation of planar three-jet events in e^+e^- annihilation and evidence for gluon bremsstrahlung*, Physics Letters B **91** (1980) 142–147.

[6] MARK Collaboration, *Discovery of Three-Jet Events and a Test of Quantum Chromodynamics at PETRA*, Physical Review Letters **43** (1979) 830–833.

[7] UA1 Collaboration Collaboration, UA1 Collaboration, *Experimental Observation of Isolated Large Transverse Energy Electrons with Associated Missing Energy at $\sqrt{s} = 540\ GeV$*, Phys.Lett. **B122** (1983) 103–116.

[8] UA1 Collaboration, *Experimental Observation of Isolated Large Transverse Energy Electrons with Associated Missing Energy at $\sqrt{s} = 540\ GeV$*, Phys. Lett. **B122** (1983) 103–116.

[9] UA1 Collaboration, *Experimental observation of lepton pairs of invariant mass around 95 GeV/c^2 at the CERN SPS collider*, Physics Letters B **126** (1983) no. 5, 398 – 410.

[10] UA2 Collaboration, *Evidence for $Z^0 \to e^+e^-$ at the CERN anti-p p Collider*, Phys. Lett. **B129** (1983) 130–140.

[11] CDS Collaboration, *Observation of Top Quark Production in $p\bar{p}$ Collisions with the Collider Detector at Fermilab*, Physical Review Letters **74** (1995) 2626–2631.

[12] DØ Collaboration, *Search for High Mass Top Quark Production in $p\bar{p}$ Collisions at $\sqrt{s} = 1.8\ TeV$*, Physical Review Letters **74** (1995) 2422–2426.

[13] S. Glashow, *Partial Symmetries of Weak Interactions*, Nucl.Phys. **22** (1961) 579–588.

[14] A. Salam, *Weak and Electromagnetic Interactions*, Conf.Proc. **C680519** (1968) 367–377.

[15] S. Weinberg, *A Model of Leptons*, Phys.Rev.Lett. **19** (1967) 1264–1266.

[16] MINOS collaboration, *First direct observation of muon antineutrino disappearance*, Phys.Rev.Lett. **107** (2011) 021801.

[17] KamLand Collaboration Collaboration, M. P. Decowski, *KamLAND's precision measurement of neutrino oscillation parameters*, J.Phys.Conf.Ser. **136** (2008) 022005.

[18] N. Jarosik, C. Bennett, J. Dunkley, B. Gold, M. Greason, et al., *Seven-Year Wilkinson Microwave Anisotropy Probe (WMAP) Observations: Sky Maps, Systematic Errors, and Basic Results*, Astrophys.J.Suppl. **192** (2011) 14, 1001.4744.

[19] V. C. Rubin, W. K. J. Ford, and N. Thonnard, *Rotational properties of 21 SC galaxies with a large range of luminosities and radii, from NGC* 4605 *(R* = 4 *kpc) to UGC* 2885 *(R* = 122 *kpc)*, Astrophysical Journal **238** (1980) 471–487.

[20] A. D. Lewis, D. A. Buote, and J. T. Stocke, *Chandra observations of Abell 2029: The Dark matter profile at* $< 0.01R(VIR)$ *in an unusually relaxed cluster*, Astrophys.J. **586** (2003) 135–142.

[21] ATLAS Collaboration, *ATLAS Experiment at the CERN Large Hadron Collider*, JINST **3** (2008) S08003.

[22] P. Langacker, *The Physics of Heavy Z′ Gauge Bosons*, Rev. Mod. Phys. **81** (2009) 1199–1228.

[23] D. London and J. L. Rosner, *Extra Gauge Bosons in E(6)*, Phys. Rev. **D34** (1986) 1530.

[24] ATLAS Collaboration, *Search for high-mass resonances decaying to dilepton final states in pp collisions at a center-of-mass energy of* 7 *TeV with the ATLAS detector*, JHEP **1211** (2012) 138.

[25] ATLAS Collaboration, *Search for contact interactions and large extra dimensions in dilepton events from pp collisions at* $\sqrt{s} = 7$ *TeV with the ATLAS detector*, Phys.Rev. **D87** (2013) 015010.

[26] ATLAS Collaboration, *Observation of a new particle in the search for the Standard Model Higgs boson with the ATLAS detector at the LHC*, Phys.Lett. **B716** (2012) 1–29.

[27] CMS Collaboration, *The CMS experiment at the CERN LHC*, JINST **3** (2008) S08004.

[28] CMS Collaboration, *Observation of a new boson at a mass of 125 GeV with the CMS experiment at the LHC*, Phys.Lett. **B716** (2012) 30–61.

[29] Hanneke, D. and Fogwell, S. and Gabrielse, G., *New Measurement of the Electron Magnetic Moment and the Fine Structure Constant*, Physical Review Letters **100** (2008) no. 12, 120801.

[30] T. Aoyama, M. Hayakawa, T. Kinoshita, and M. Nio, *Tenth-Order QED Contribution to the Lepton Anomalous Magnetic Moment – Sixth-Order Vertices Containing an Internal Light-by-Light-Scattering Subdiagram*, Phys.Rev. **D85** (2012) 093013, arXiv:1201.2461.

[31] ALEPH, DELPHI, L3, OPAL, SLD Collaborations, the LEP Electroweak Working Group, the SLD Electroweak and Heavy Flavour Groups, *Precision Electroweak Measurements on the Z Resonance*, Phys. Rept. **427** (2006) 257.

[32] Tevatron Electroweak Working Group, CDF Collaboration, DØ Collaboration, *2012 Update of the Combination of CDF and DØ Results for the Mass of the W Boson*, arXiv:1204.0042.

[33] CDF Collaboration, DØ Collaboration, *Combination of the top-quark mass measurements from the Tevatron collider*, arXiv:1207.1069.

[34] Noether, E., *Invarianten beliebiger Differentialausdrücke.*, Gött. Nachr. (1918) 37–44.

[35] Noether, E., *Invariante Variationsprobleme.*, Gött. Nachr. (1918) 235–257.

[36] J. Goldstone, A. Salam, and S. Weinberg, *Broken Symmetries*, Phys. Rev. **127** (1962) 965–970.

[37] P. A. M. Dirac, *The Quantum Theory of the Emission and Absorption of Radiation*, Royal Society of London Proceedings Series A **114** (1927) 243–265.

[38] Halzen, F. and Martian, A. D., *Quarks & Leptons*, John Wiley & Sons, Inc. (1984) .

[39] J. Bjorken, *Asymptotic Sum Rules at Infinite Momentum*, Phys.Rev. **179** (1969) 1547–1553.

[40] J. C. Collins, D. E. Soper, and G. F. Sterman, *Factorization of Hard Processes in QCD*, Adv. Ser. Direct. High Energy Phys. **5** (1988) 1–91.

[41] M. Cacciari, G. P. Salam, and G. Soyez, *The Anti-k(t) jet clustering algorithm*, JHEP **0804** (2008) 063.

[42] G. Altarelli and G. Parisi, *Asymptotic Freedom in Parton Language*, Nucl. Phys. **B126** (1977) 298.

[43] A. Martin et al., *Parton distributions for the LHC*, Eur. Phys. J. **C63** (2009) 189–285.

[44] Particle Data Group, *The Review of Particle Physics*, J. Phys. **G37** (2010) 075021 and 2011 partial update for the 2012 edition.

[45] H.-L. Lai, M. Guzzi, J. Huston, Z. Li, P. M. Nadolsky, et al., *New parton distributions for collider physics*, Phys.Rev. **D82** (2010) 074024.

[46] H1 and ZEUS Collaboration Collaboration, F. Aaron et al., *Combined Measurement and QCD Analysis of the Inclusive $e^{\pm}p$ Scattering Cross Sections at HERA*, JHEP **1001** (2010) 109.

[47] H1 Collaboration, ZEUS Collaboration Collaboration, K. Lipka and Z. experiments, *Recent results from HERA and their impact for LHC*, EPJ Web Conf. **28** (2012) 02008, arXiv:1201.4486.

[48] NNPDF Collaboration Collaboration, R. D. Ball et al., *Unbiased global determination of parton distributions and their uncertainties at NNLO and at LO*, Nucl.Phys. **B855** (2012) 153–221, arXiv:1107.2652.

[49] G. Watt and R. Thorne, *Study of Monte Carlo approach to experimental uncertainty propagation with MSTW 2008 PDFs*, JHEP **1208** (2012) 052.

[50] R. D. Ball, S. Carrazza, L. Del Debbio, S. Forte, J. Gao, et al., *Parton Distribution Benchmarking with LHC Data*, arXiv:1211.5142.

[51] S. Dittmaier and M. Huber, *Radiative corrections to the neutral-current Drell-Yan process in the Standard Model and its minimal supersymmetric extension*, JHEP **01** (2010) 060.

[52] Mandelstam, S., *Determination of the Pion-Nucleon Scattering Amplitude from Dispersion Relations and Unitarity. General Theory*, Phys. Rev. **112** (1958) 1344–1360.

[53] ATLAS Collaboration, *Search for high-mass dilepton resonances in 5/fb of pp collisions at* $\sqrt{s} = 7$ *TeV*, ATL-COM-PHYS-2012-111, *unpublished* (2012).

[54] Y. Li and F. Petriello, *Combining QCD and electroweak corrections to dilepton production in FEWZ*, Phys.Rev. **D86** (2012) 094034.

[55] R. Hamberg, W. L. van Neerven, and T. Matsuura, *A Complete calculation of the order* α_s^2 *correction to the Drell-Yan K factor*, Nucl. Phys. **B359** (1991) 343–405.

[56] I. Antcheva et al., *ROOT – A C++ framework for petabyte data storage, statistical analysis and visualization*, Computer Physics Communications **180** (2009) no. 12, 2499 – 2512.

[57] C. M. Carloni Calame et al., *Precision electroweak calculation of the production of a high transverse-momentum lepton pair at hadron colliders*, JHEP **10** (2007) 109.

[58] P. Golonka and Z. Wąs, *PHOTOS Monte Carlo: a precision tool for QED corrections in* Z *and* W *decays*, Eur. Phys. J. **C45** (2006) 97–107.

[59] A. D. Martin, R. G. Roberts, W. J. Stirling, and R. S. Thorne, *Parton distributions incorporating QED contributions*, Eur. Phys. J. **C39** (2005) 155–161.

[60] T. G. Rizzo, *Z' phenomenology and the LHC*, SLAC-PUB-12129 (2006).

[61] M. Dittmar, A.-S. Nicollerat, and A. Djouadi, *Z' studies at the LHC: An update*, Phys. Lett. **B583** (2004) 111–120.

[62] E. Accomando et al., *Z' physics with early LHC data*, Phys. Rev. **D83** (2011) 075012.

[63] OPAL Collaboration, *Tests of the standard model and constraints on new physics from measurements of fermion pair production at* 189 *GeV to* 209 *GeV at LEP*, Eur. Phys. J. **C33** (2004) 173–212.

[64] DELPHI Collaboration, *Measurement and interpretation of fermion-pair production at LEP energies above the Z resonance*, Eur. Phys. J. **C45** (2006) 589–632.

[65] L3 Collaboration, *Measurement of hadron and lepton-pair production in* e^+e^- *collisions at* $\sqrt{s} = 192$ *GeV to* 208 *GeV at LEP*, Eur. Phys. J. **C47** (2006) 1–19.

[66] ALEPH Collaboration, *Fermion pair production in* e^+e^- *collisions at* $189 - 209$ *GeV and constraints on physics beyond the standard model*, Eur. Phys. J. **C49** (2007) 411–437.

[67] CDF Collaboration, *Search for High Mass Resonances Decaying to Muon Pairs in* $\sqrt{s} = 1.96$ *TeV* $p\bar{p}$ *Collisions*, Phys. Rev. Lett. **106** (2011) 121801.

[68] DØ Collaboration, *Search for a heavy neutral gauge boson in the dielectron channel with* 5.4 fb^{-1} *of* $p\bar{p}$ *collisions at* $\sqrt{s} = 1.96$ *TeV*, Phys. Lett. **B695** (2011) 88–94.

[69] ATLAS Collaboration, *Search for high mass dilepton resonances in pp collisions at* $\sqrt{s} = 7$ *TeV with the ATLAS experiment*, Phys. Lett. **B700** (2011) 163–180.

[70] CMS Collaboration, *Search for Resonances in the Dilepton Mass Distribution in pp Collisions at* $\sqrt{s} = 7$ *TeV*, JHEP **05** (2011) 093.

[71] ALICE Collaboration, *The ALICE experiment at the CERN LHC*, JINST **3** (2008) S08002.

[72] LHCb Collaboration, *The LHCb Detector at the LHC*, JINST **3** (2008) S08005.

[73] LHCf Collaboration et al., *LHCf detector at the CERN Large Hadron Collider*, JINST **3** (2008) S08006.

[74] TOTEM Collaboration Collaboration, G. Anelli et al., *The TOTEM experiment at the CERN Large Hadron Collider*, JINST **3** (2008) S08007.

[75] L. Evans and P. Bryant, *LHC Machine*, JINST **3** (2008) S08001.

[76] ATLAS Collaboration, *Luminosity Determination in pp Collisions at* $\sqrt{s} = 7$ *TeV Using ATLAS Detector at the LHC*, Eur.Phys.J. **C71** (2011) 1630.

[77] ATLAS collaboration. `https://twiki.cern.ch/twiki/bin/view/AtlasPublic/LuminosityPublicResults#2012_pp_Collisions`. Accessed: 2012/12/30.

[78] ATLAS Collaboration, *ATLAS liquid argon calorimeter: Technical design report*, CERN-LHCC-96-41 (1996) .

[79] Bazan, A. and others, *ATLAS liquid argon calorimeter read-out system*, IEEE Trans.Nucl.Sci. **53** (2006) 735–740.

[80] EGamma Performance Group. `https://twiki.cern.ch/twiki/bin/viewauth/AtlasProtected/EnergyScaleResolutionRecommendations`. Accessed: 2012/12/09.

[81] *ATLAS inner detector: Technical Design Report, 1*, CERN-LHCC-97-016 (1997) .

[82] ATLAS Collaboration, *Performance of the electronic readout of ATLAS liquid argon calorimeters*, JINST **5** (2010) P09003.

[83] ATLAS Collaboration, *Search for same-sign top-quark production and fourth-generation down-type quarks in pp collisions at* $\sqrt{s} = 7$ *TeV with the ATLAS detector*, JHEP **1204** (2012) 069.

[84] J.A. Aguilar-Saavedra et al., *Search for Same-Sign Top Pairs and Fourth Generation Bottom-like Quarks in Same-Sign Dilepton Final States with 1* fb^{-1} *of Data*, ATL-COM-PHYS-2011-710 (unpublished) (2011) .

[85] GEANT4 Collaboration, *GEANT4: A simulation toolkit*, Nucl. Instrum. Meth. **A506** (2003) 250.

[86] T. Sjöstrand, S. Mrenna, and P. Skands, *PYTHIA* 6.4 *physics and manual*, JHEP **0605** (2006) 026.

[87] G. Corcella et al., *HERWIG6: an event generator for hadron emission reactions with interfering gluons (including supersymmetric processes)*, JHEP **0101** (2001) 010.

[88] M. L. Mangano et al., *ALPGEN, a generator for hard multiparton processes in hadronic collisions*, JHEP **07** (2003) 001.

[89] S. Frixione and B. Webber, *Matching NLO QCD computations and parton shower simulations*, JHEP **0206** (2002) 029.

[90] A. Sherstnev and R. Thorne, *Different PDF approximations useful for LO Monte Carlo generators*, `arXiv:0807.2132`.

[91] ATLAS collaboration, *ATLAS Simulation Infrastructure*, European Physical Journal C **70** (2010) 823–874.

[92] ATLAS Collaboration, *Charged-particle multiplicities in pp interactions measured with the ATLAS detector at the LHC*, New J.Phys. **13** (2011) 053033.

[93] ATLAS Collaboration, *Measurements of underlying-event properties using neutral and charged particles in pp collisions at* 900 *GeV and* 7 *TeV with the ATLAS detector at the LHC*, Eur.Phys.J. **C71** (2011) 1636.

[94] ATLAS Collaboration, *Search for dilepton resonances in pp collisions at* $\sqrt{s} = 7$ *TeV with the ATLAS detector*, Phys.Rev.Lett. **107** (2011) 272002.

[95] EGamma Performance Group. `https://twiki.cern.ch/twiki/bin/viewauth/AtlasProtected/ElectronGamma`. Accessed: 2012/11/15.

[96] ATLAS Collaboration, *Charged particle multiplicities in pp interactions at $\sqrt{s} = 0.9$ and 7 TeV in a diffractive limited phase-space measured with the ATLAS detector at the LHC and new PYTHIA6 tune*, ATLAS-CONF-2010-031 (2010) .

[97] ATLAS collaboration, *ATLAS tunes of PYTHIA 6 and Pythia 8 for MC11*, ATL-PHYS-PUB-2011-009 (2011) .

[98] EGamma Performance Group, *Electron energy scale in-situ calibration and performance*, ATL-COM-PHYS-2012-263, *unpublished* (2012).

[99] ATLAS Collaboration, *ATLAS search for new phenomena in dijet mass and angular distributions using pp collisions at $\sqrt{s} = 7$ TeV*, `arXiv:1210.1718`. Submitted to JHEP.

[100] ATLAS Collaboration, J. M. Butterworth et al., *Single and Diboson Production Cross Sections in pp collisions at $\sqrt{s} = 7$* TeV, ATL-COM-PHYS-2010-695 (2010) .

[101] ATLAS Collaboration, *Combination of ATLAS and CMS results on the mass of the top quark using up to $4.9\,fb^{-1}$ of data*, ATLAS-CONF-2012-095 (2012) .

[102] CDF Collaboration, DØ Collaboration, *Combination of CDF and DØ measurements of the W boson helicity in top quark decays*, Phys.Rev. **D85** (2012) 071106.

[103] U. Langenfeld, S. Moch, and P. Uwer, *Measuring the running top-quark mass*, Phys.Rev. **D80** (2009) 054009, `arXiv:0906.5273`.

[104] R. J. Barlow and C. Beeston, *Fitting using finite Monte Carlo samples*, Comput.Phys.Commun. **77** (1993) 219–228.

[105] G. Choudalakis, *On hypothesis testing, trials factor, hypertests and the BumpHunter*, `arXiv:1101.0390v2 (2011)`.

[106] D. C. Georgios Choudalakis, *Data Analysis, Statistics and Probability*, Eur. Phys. J. Plus **127** (2012) .

[107] A. Abdelamin et al., *Limit Setting and Signal Extraction Procedures in the Search for Narrow Resonances Decaying into Leptons at ATLAS*, ATL-COM-PHYS-2011-085, *unpublished* (2010).

[108] G. Cowan, *Statistical Data Analysis*, Clarendon Press, Oxford (1994) .

[109] A. Caldwell, D. Kollar, and K. Kroninger, *BAT: The Bayesian Analysis Toolkit*, Comput. Phys. Commun. **180** (2009) 2197–2209.

[110] W.R. Gilks, S. Richardson, and D. Spiegelhalter (Eds.), *Markov Chain Monte Carlo in Practice*, Chapman and Hall (1996) .

[111] T. C. Collaboration, *Search for narrow resonances in dilepton mass spectra in pp collisions at $\sqrt{s} = 7$ TeV*, Physics Letters B **714** (2012) no. 2–5, 158–179.

[112] ATLAS Collaboration, *Search for high-mass dilepton resonances in 6.1/fb of pp collisions at $\sqrt{s}$= 8 TeV with the ATLAS experiment*, ATLAS-CONF-2012-129 (2012) .

[113] The CMS Collaboration, *Search for Resonances in the Dilepton Mass Distribution in pp Collisions at* $\sqrt{s} = 8\ TeV$, CMS-PAS-EXO-12-015 (2012) .

[114] L. Randall and R. Sundrum, *A large mass hierarchy from a small extra dimension*, Phys. Rev. Lett. **83** (1999) 3370–3373.

[115] I. Antoniadis, K. Benakli, and M. Quiros, *Direct collider signatures of large extra dimensions*, Phys. Lett. **B460** (1999) 176–183.

[116] F. Ellinghaus. Personal communication. 2012/12/20.

[117] W.J. Stirling. `http://www.hep.phy.cam.ac.uk/~wjs/plots/plots.html`. Accessed: 2012/12/13.

[118] L. Rossi, O. Brüning et al., *High Luminosity Large Hadron Collider*, European Strategy Preparatory Group - Open Symposium, Krakow (2012) .

[119] ATLAS-Collaboration, *Physics at a High-Luminosity LHC with ATLAS (Update)*, ATL-PHYS-PUB-2012-004 (2012) .

[120] O. Brning, B. Goddard, M. Mangano, S. Myers, L. Rossi, E. Todesco, and F. Zimmerman, *High Energy LHC Document prepared for the European HEP strategy update*, CERN-ATS-2012-237 (2012) .

[121] Osland, P. and Pankov, A.A. and Tsytrinov, A.V., *Identification of extra neutral gauge bosons at the International Linear Collider*, Eur.Phys.J. **C67** (2010) 191–204.

[122] J. R. Ellis et al., *High luminosity* e^+e^- *circular colliders for precise Higgs and other measurements*, European Strategy Preparatory Group - Open Symposium, Krakow (2012) .

A Appendix

A.1 General Electron Efficiency Scale Factors

In this section, the electron efficiency scale factors are shown quantitatively in form of distributions. They were derived by the ATLAS EGamma performance group (Fig. A.1 and Fig. A.2) [95] and the ATLAS dilepton search analysis team (Fig. A.3 to Fig. A.5) [53]. The methods, how the scale factors were derived, as well as their η and E_T dependence was already discussed in Section 5.2.

All efficiency scale factors that are relevant for the analysis of this thesis are close to unity. This demonstrates that the efficiencies are well modeled in the simulation.

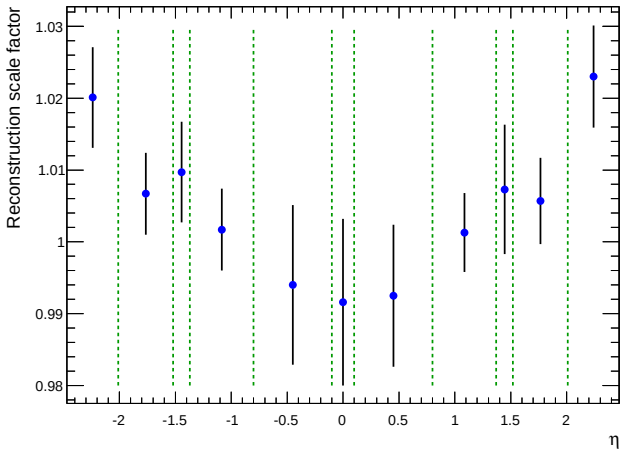

Figure A.1: The reconstruction efficiency scale factor is shown as a function of η. The vertical green lines indicate the ranges the scale factors were derived within. The values are taken from Ref. [95].

In the following, the technical recipe to combine the scale factors will be discussed. Efficiency scale factors are derived such that they are multiplicative in two ways. If an η and an E_T dependence is quoted for a scale factor, both scale factors need to be multiplied. Scale factors for different efficiencies, e.g., the trigger and the reconstruction efficiency, are also multiplicative.

The combined scale factor for leading electrons is calculated as the product of the reconstruction efficiency scale factor (Fig. A.1) times the medium identification efficiency scale factor (Fig. A.2) times the combined b-layer hit and isolation efficiency scale factor (Fig. A.3) times the trigger efficiency scale factor (Fig. A.5). For the subleading electron, the b-layer hit efficiency scale factor (Fig. A.4) is used instead of the combined b-layer hit and isolation efficiency scale factor (Fig. A.3).

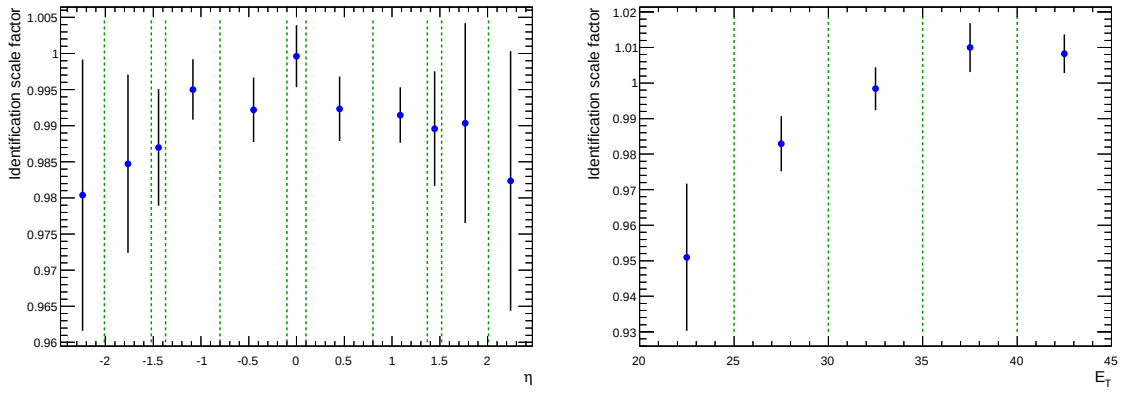

Figure A.2: The medium electron identification efficiency scale factor is shown as a function of η (E_T) in the left (right) plot. The vertical green lines indicate the ranges the scale factors were derived within. The values are taken from Ref. [95].

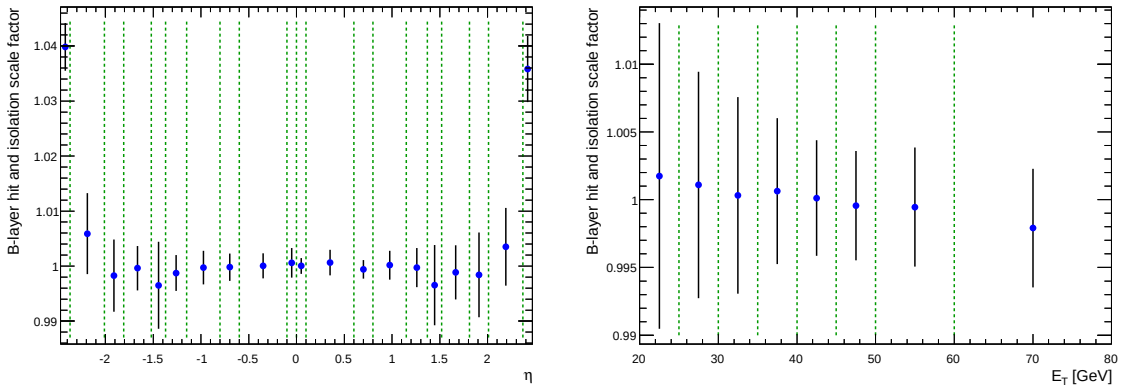

Figure A.3: The combined electron b-layer hit and isolation efficiency scale factor is shown as a function of η (E_T) in the left (right) plot. The scale factor is defined with respect to the medium electron identification scale factor. The vertical green lines indicate the ranges the scale factors were derived within. The values are taken from Ref. [53].

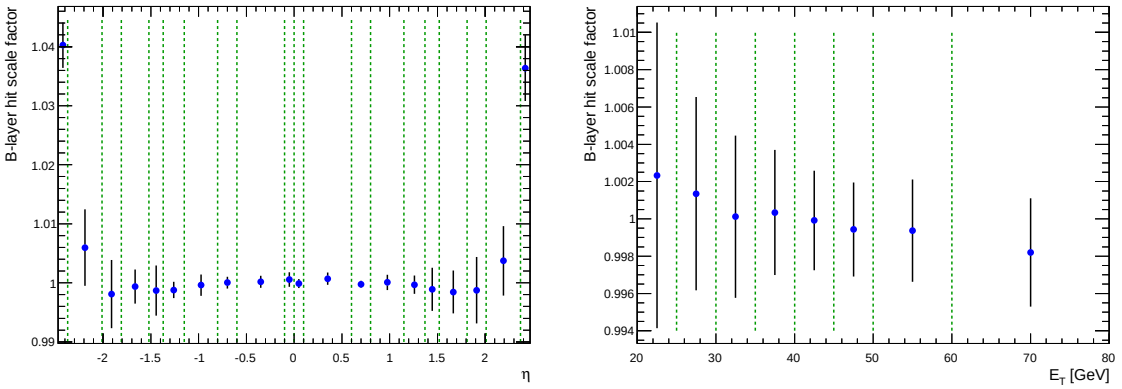

Figure A.4: The electron b-layer hit efficiency scale factor is shown as a function of η (E_T) in the left (right) plot. The scale factor is defined with respect to to the medium electron identification scale factor. The vertical green lines indicate the ranges the scale factors were derived within. The values are taken from Ref. [53].

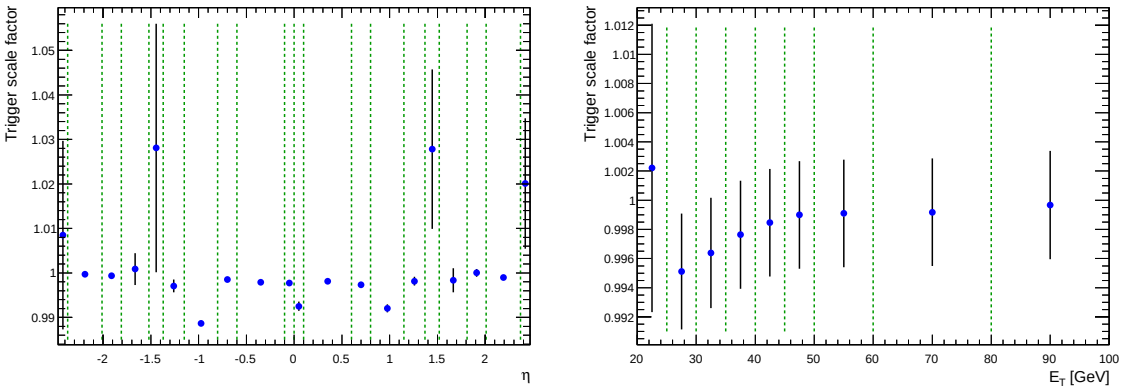

Figure A.5: The electron trigger efficiency scale factor is shown as a function of η (E_T) in the left (right) plot. The scale factor is defined with respect to to the product of the medium electron identification and the b-layer hit efficiency scale factor. The vertical green lines indicate the ranges the scale factors were derived within. The values are taken from Ref. [53].

A.2 Electron Isolation Efficiencies

This section provides additional plots for the discussion of the efficiency of the isolation requirement performed in Section 5.2.4. The efficiency for loose electrons to pass the medium identification level and the b-layer hit criterion is shown in Fig. A.6, while the efficiency including the isolation requirement is shown in Fig. A.7. From the distributions shown in the first figure, it can be concluded that the efficiencies for leading and subleading electrons are very similar. In contrast, from the second figure it can be concluded that the efficiency for subleading electrons is significantly lower, if the isolation requirement would be imposed. This effect is particularly pronounced in η regions around the barrel end-cap calorimeter transition region ($1.37 < |\eta| < 1.52$) and is also shown in a dedicated figure, see Fig. A.8. The reason for the different efficiencies is that the different signatures of leading and subleading electrons were not considered by the EGamma performance group, when the isolation variable was derived, see Section 5.2.4.

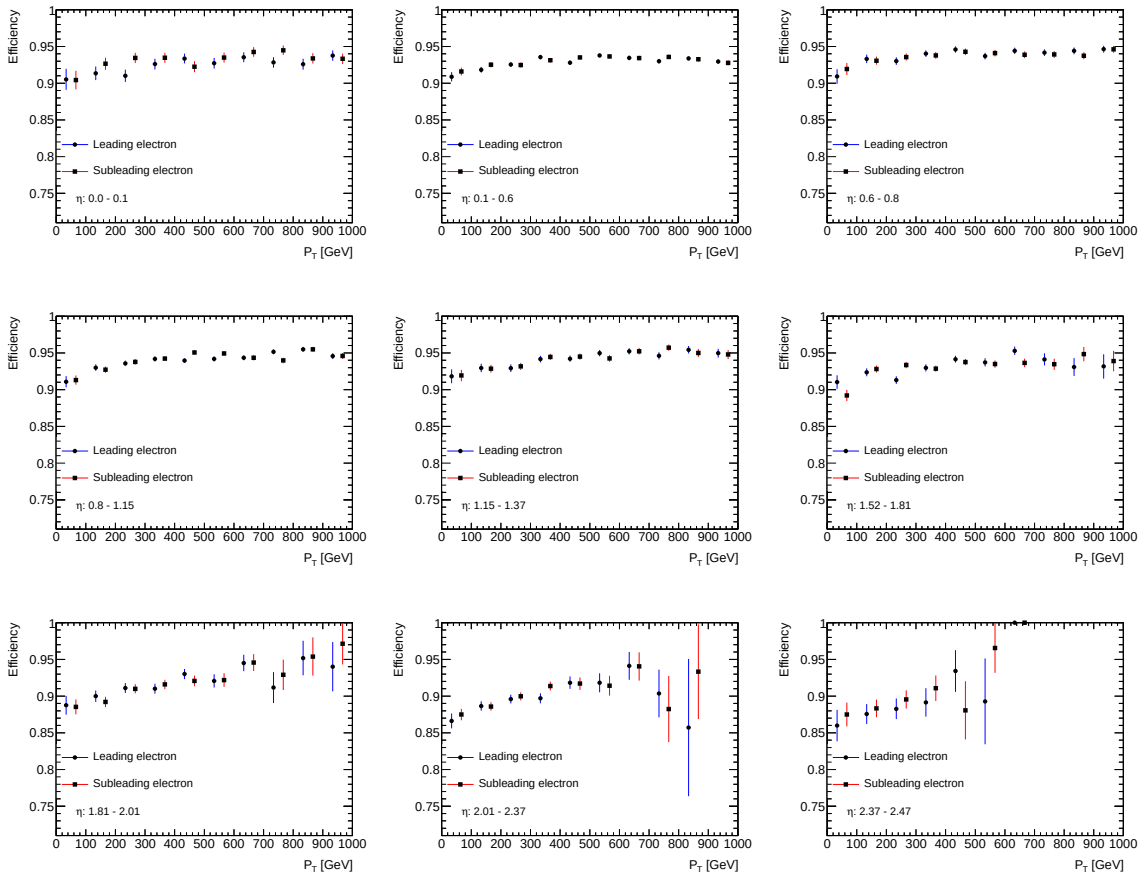

Figure A.6: The efficiency (or probability) for a loose electron candidate to pass the medium identification criteria and the b-layer hit criterion are shown as a function of electron E_T in nine bins of η. In blue (red) the efficiency for the leading (subleading) electrons is shown. The efficiencies were derived using Monte Carlo simulations with all efficiency scale factors applied.

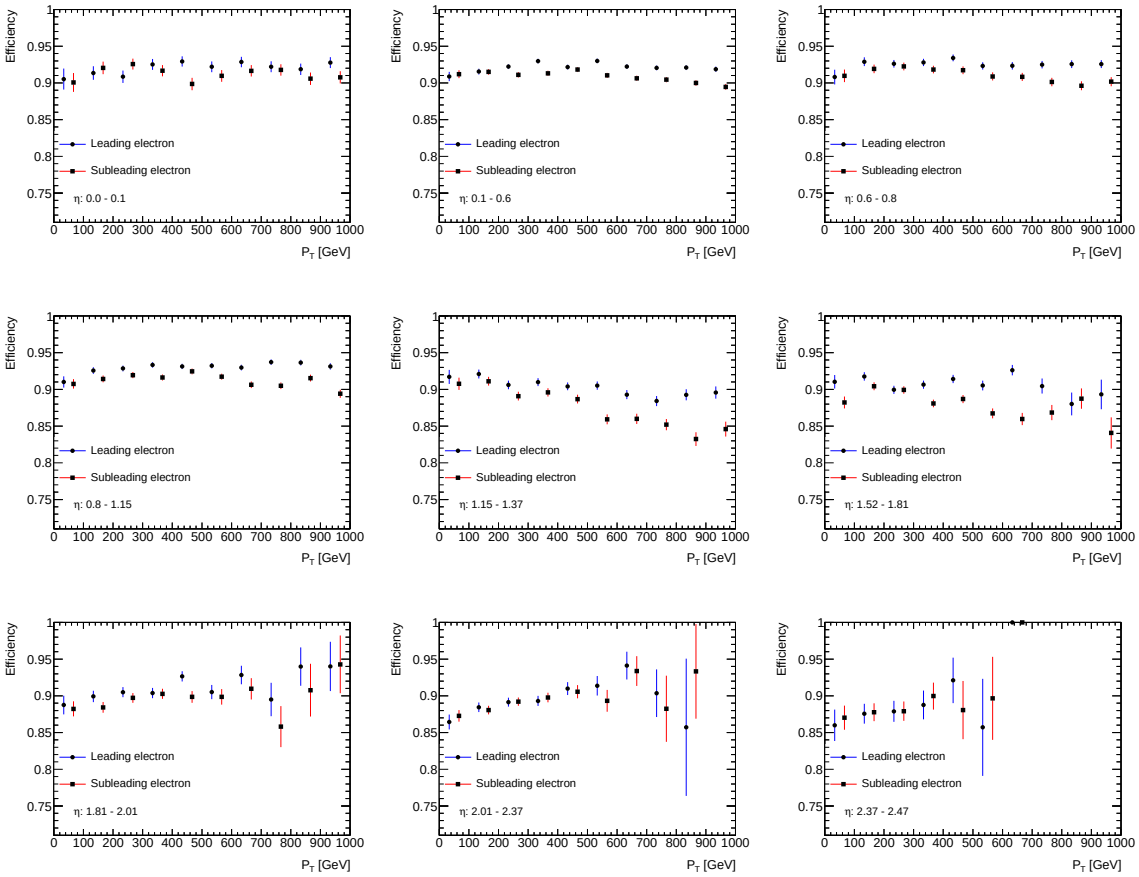

Figure A.7: The efficiency (or probability) for a loose electron candidate to pass the medium identification criteria, the b-layer hit criterion and the isolation requirement are shown as a function of electron E_T in nine bins of η. In blue (red) the efficiency for the leading (subleading) electrons is shown. The efficiencies were derived using Monte Carlo simulations with all efficiency scale factors applied.

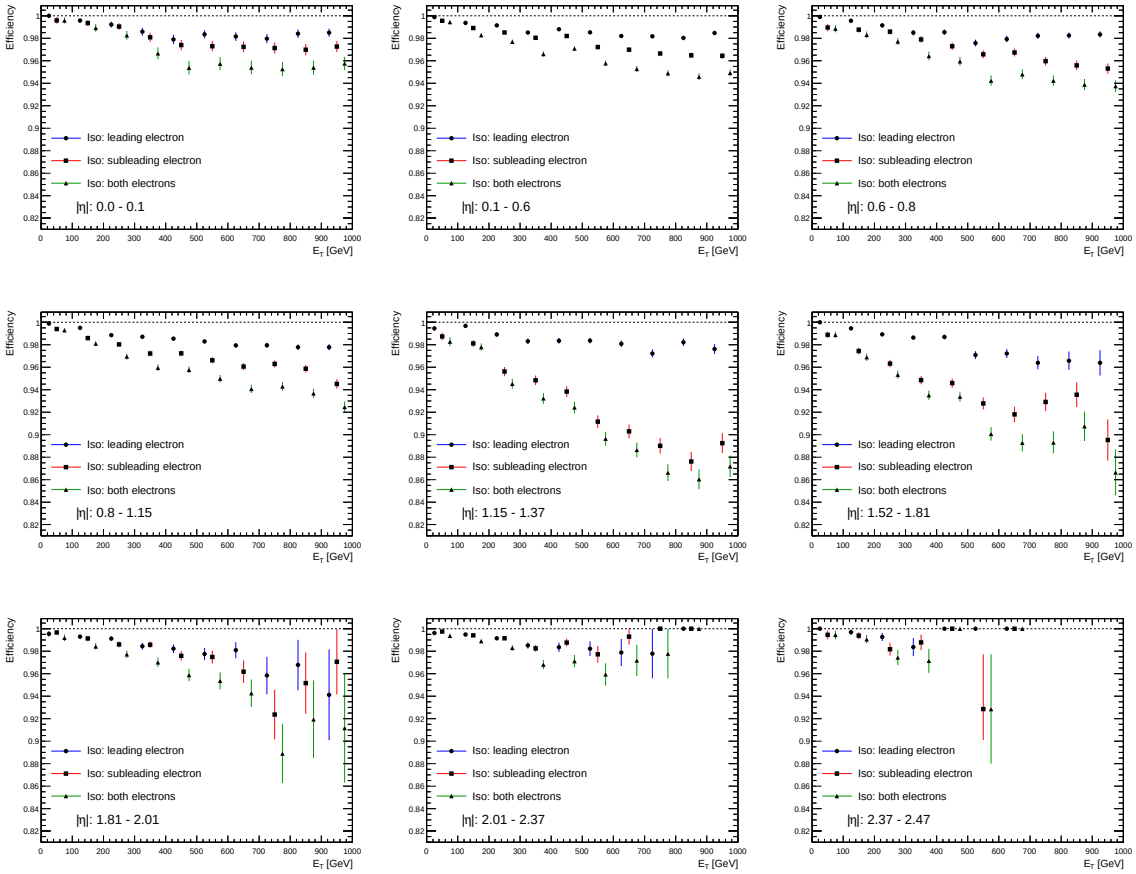

Figure A.8: The isolation efficiency ϵ_{iso} is shown as a function of the subleading electron E_T in nine bins of $|\eta|$. In blue the efficiency is shown in case only the leading electron is required to be isolated, while in red the corresponding case is shown, if only the subleading electron is required to be isolated. The case that both electrons are required to be isolated is shown in green. If an efficiency amounts to exactly one, that is numerator and denominator are identical, binomial statistics do not predict a meaningful uncertainty. Therefore the uncertainty is set to zero. The number of pairs in those bins never exceeds three.

A.3 Electron Transverse Energy Deposition

This section contains additional plots for the discussion in Section 5.2.1 about the defect FEBs for the third layer of the em. calorimeter. In Fig. A.9, the fraction of the total transverse energy that is deposited by electrons in each layer of the em. calorimeter is shown.

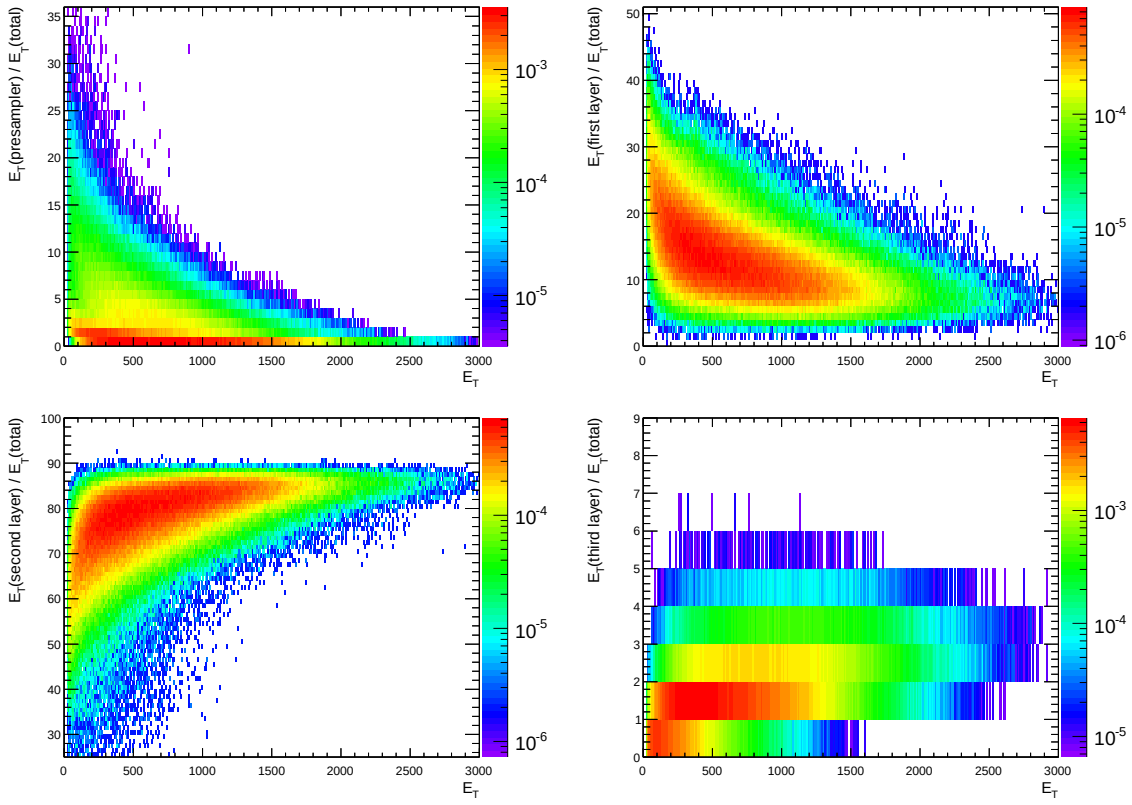

Figure A.9: The fraction of the total transverse energy that is deposited by electrons in each layer of the em. calorimeter is shown. From top to bottom and left to right, the layers are the presampler and the first to third regular calorimeter layer. The distributions were derived using Monte Carlo simulations.

A.4 Additional Cutflow Table

The cutflow for a simulated SSM Z' with a pole mass of 2 TeV is shown in Table A.1. For this cutflow, all calibrations and corrections described in Section 5.2 have been applied.

Table A.1: The cutflow derived from the SSM Z' sample with a pole mass of 2 TeV and interference with the SM Drell-Yan process is shown. The third column shows the survival fraction of the cut with respect to the previous one, while the survival fraction in the fourth column is calculated with respect to all events triggered. If a survival fraction is not defined, it is denoted by an N/A for not applicable. The numbers of the last cut are denoted by *, because this cut reduces the number of pairs per event to one, but does not reject events.

Cut name	Number of events after cut	Local cut efficiency	Total cut efficiency
Before cuts	20000	N/A	N/A
Trigger	18029	90.1 %	90.1 %
Loose electron identification	17690	98.1 %	88.5 %
Exclude barrel endcap transition	16509	93.3 %	82.5 %
Electron transverse momentum > 25 GeV	16102	97.5 %	80.5 %
Electron pair mass > 70 GeV	16088	99.9 %	80.4 %
Medium electron identification	15049	93.5 %	75.2 %
Electron b-layer hit	14705	97.7 %	73.5 %
Leading electron isolation (corr.) < 7 GeV	14430	98.1 %	72.2 %
Select highest p_T electron pair	14430*	100.0 %*	72.2 %*

A.5 Monte Carlo Samples

Table A.2: This table lists the simulated Monte Carlo samples for the Drell-Yan process together with their ATLAS internal run number, the σB used in PYTHIA the number of events generated N_{evt} in thousands and the integrated luminosity L_{int}. The numbers in parenthesis of the process column specify the selected mass ranges of the Z/γ^* exchange. If only one number is specified, there is only a lower mass threshold. The k-factors are listed and discussed in Section 2.4.1. The last row, denoted by a *, lists a Drell-Yan Monte Carlo sample generated with MC@NLO. This table is a extended version of the corresponding one in Ref. [53].

Process	Run number	σB [pb] (generated)	N_{evt} [k]	L_{int} [fb^{-1}]
$Z(60) \to ee$	106046	834.6	9986	10.
$Z(60) \to \tau\tau$	106052	834.6	495	0.5
$Z(120, 250) \to ee$	105467	8.53	298	35.1
$Z(250, 400) \to ee$	105468	0.410	100	243.
$Z(400, 600) \to ee$	105469	0.0664	100	1506.
$Z(600, 800) \to ee$	105470	0.01095	100	9128.
$Z(800, 1000) \to ee$	105471	0.002647	100	37778.
$Z(1000, 1250) \to ee$	105472	0.0008901	100	112340.
$Z(1250, 1500) \to ee$	105473	0.00023922	100	418025.
$Z(1500, 1750) \to ee$	105474	0.00007343	100	1361674.
$Z(1750, 2000) \to ee$	105475	0.00002464	100	4057947.
$Z(2000, 2250) \to ee$	145263	0.00000876	100	11413049.
$Z(2250, 2500) \to ee$	145264	0.00000322	100	31025068.
$Z(2500, 2750) \to ee$	145265	0.00000120	100	82829454.
$Z(2750, 3000) \to ee$	145266	0.00000045	100	223398789.
$Z(3000) \to ee$	145267	0.00000025	100	390838740.
$Z(60) \to ee^*$	106087	948.7	4973	1.9

Table A.3: This table lists the simulated Monte Carlo samples used for the diboson processes ($pp \to WW$, $pp \to WZ$, $pp \to ZZ$) and the $t\bar{t}$ process ($pp \to t\bar{t}$). The second column lists the ATLAS internal run number and the third column the filter efficiency. The fourth and fifth columns list the cross-section (times branching ratios) times filter efficiency first reported by the generator and second as calculated in [100, 103, 53]. The last two columns list the number of events generated and the corresponding integrated luminosity.
In the following, the applied filters are described. The first block of samples has a lepton filter applied that requires one lepton with $p_T > 10$ GeV and $|\eta| < 2.8$. For the second block, one electron with $p_T > 15$ GeV and $|\eta| < 2.6$ is required. Furthermore, both W bosons are forced to decay to electrons in the WW samples, whereas only one Z in each of the WZ and ZZ samples is forced to decay into electrons. Of all remaining events, each event is taken, where any pair of electrons forms an invariant mass in the specified range. For the third block, a semi-leptonic $t\bar{t}$ decay is required, that is either the W from the top or anti-top decay decays into two leptons. This table is a extended version of the corresponding one in Ref. [53].

Process	Run number	ϵ_f (filter efficiency)	$\sigma B \times \epsilon_f$ [fb] generated	calculated	N_{evt} [k]	L_{int} [fb^{-1}]
WW (1 lepton filter)	105985	0.38947	12115.	17487.	1000	57
WZ (1 lepton filter)	105987	0.31043	3565.	5743.	1000	180
ZZ (1 lepton filter)	105986	0.21319	975.	1271.	250	198.3
WW ($M_{ee} = 0.4 - 1$ TeV)	145487	0.00589	2.134	3.131	20	6388
WW ($M_{ee} = 1 - 1.6$ TeV)	145488	0.0000610	0.022	0.032	20	625000
WZ ($M_{ee} = 0.4 - 1$ TeV)	145493	0.00251	1.113	1.558	20	12836
WZ ($M_{ee} = 1 - 1.6$ TeV)	145494	0.0000725	0.032	0.045	20	444444
ZZ ($M_{ee} = 0.4 - 1$ TeV)	145499	0.00114	0.383	0.448	20	44643
ZZ ($M_{ee} = 1 - 1.6$ TeV)	145500	0.0000206	0.0069	0.0081	20	2469136
$t\bar{t} \to \ell X$	105200	0.54259	79.0	89.4	14995	168

Table A.4: This table lists the simulated Monte Carlo samples used to describe the $pp \to W + jets$ process. The generator, HERWIG, has a dedicated LO matrix element for each jet multiplicity, where the latter is defined on the number of final state partons, which have $p_T > 20\,\text{GeV}$. In the second column the ATLAS internal run number is listed and in the third and in the fourth the cross-section times branching ratio as reported by the generator and as calculated, respectively. In the last two columns the number of events generated and the corresponding integrated luminosity using the generated cross-section is reported. This table is a modified version of the corresponding one in Ref. [53]

Process	Run number	σB [pb] generated	σB [pb] calculated	N_{evt} [k]	L_{int} [fb^{-1}]
$W \to e\nu$ + 0 parton	107680	6933	8287	500	0.06
$W \to e\nu$ + 1 parton	107681	1305	1560	2500	1.6
$W \to e\nu$ + 2 partons	107682	378	452	2000	4.4
$W \to e\nu$ + 3 partons	107683	102	122	500	4.1
$W \to e\nu$ + 4 partons	107684	25.7	30.7	150	4.9
$W \to e\nu$ + 5 partons	107685	7.0	8.4	70	8.3
$W \to \tau\nu$ + 0 parton	107700	6933	8287	3418	0.4
$W \to \tau\nu$ + 1 parton	107701	1305	1560	2499	1.6
$W \to \tau\nu$ + 2 partons	107702	378	452	3751	8.3
$W \to \tau\nu$ + 3 partons	107703	102	122	1010	8.3
$W \to \tau\nu$ + 4 partons	107704	25	30.7	250	7.3
$W \to \tau\nu$ + 5 partons	107705	7.0	8.4	65	8.1

Table A.5: This table shows the simulated SSM Z' signal Monte Carlo samples. The first listed sample, denoted by run number 115494, is a special production with the SSM Z' process only. The generator cross-section for this sample is modified such that a flat Z' mass distribution from 10 GeV to approximately 3500 GeV is generated. The recipe to derive predictions with this sample is discussed in Section 8.2.
The other listed samples include the Drell-Yan process, starting at a mass of M_{min}, and the SSM Z' process, where the pole mass amounts to M_{pole}. The interference between the Drell-Yan process and the SSM Z' is simulated. The third column lists the width of the Z' resonance and the fourth column the branching ratio into electrons. It is followed by the ATLAS internal run number and the cross-section times branching ratio, the number of events generated and the corresponding integrated luminosity. Table taken from Ref [53].

M_{pole} [GeV]	M_{min} [GeV]	Γ [GeV]	$B(Z' \to e^+e^-)$ [%]	Run number	σB [fb] generated	N_{evt} [k]	L_{int} [fb^{-1}]
≥ 10				115494		388	
250	125	6.87	3.36	115272	35401	20	0.48
500	250	14.56	3.20	115273	2607	20	6.7
750	375	22.64	3.10	115274	473.5	20	37.5
1000	500	30.64	3.06	105603	124.7	20	143
1250	625	38.60	3.05	105549	39.89	20	469
1500	750	46.55	3.04	105624	14.38	20	1312
1750	875	54.49	3.03	105554	5.67	20	3597
2000	1000	62.43	3.03	105409	2.44	20	9091

Table A.6: The LO cross-sections times branching ratios into electrons are listed as a function of the pole mass for all Z' models used in the limit calculations. Table taken from Ref. [53].

M_{pole} [GeV]	$\sigma B(Z'_{\mathrm{SSM}})$ [fb]	$\sigma B(Z'_{\mathrm{S}})$ [fb]	$\sigma B(Z'_{\mathrm{N}})$ [fb]	$\sigma B(Z'_{\psi})$ [fb]	$\sigma B(Z'_{\chi})$ [fb]	$\sigma B(Z'_{\eta})$ [fb]	$\sigma B(Z'_{I})$ [fb]
250	27350.0	14710.0	9223.0	8132.0	15890.0	9566.0	13300.0
500	2038.0	1080.0	683.0	596.8	1163.0	694.6	951.8
750	366.8	188.5	119.7	106.9	210.1	123.2	170.0
1000	94.77	46.9	30.32	26.9	51.83	31.4	41.51
1250	29.6	13.63	9.069	8.171	15.56	9.704	11.87
1500	10.33	4.31	3.003	2.732	5.064	3.229	3.741
1750	3.876	1.44	1.037	0.9833	1.747	1.195	1.219
2000	1.579	0.509	0.3793	0.3706	0.641	0.455	0.4221
2250	0.6935	0.1911	0.144	0.1422	0.2493	0.1775	0.1571
2500	0.3296	0.08032	0.05754	0.05668	0.1044	0.07255	0.0653
2750	0.1729	0.03834	0.02464	0.02395	0.04888	0.03083	0.03066
3000	0.1000	0.02102	0.01151	0.01064	0.02591	0.01399	0.01690

A.6 Additional $t\bar{t}$ Material

The combined *type ee* and *type ef* $t\bar{t}$ estimation and the results of the extrapolation procedure are shown in Table A.7. The final *type ef* $t\bar{t}$ estimate and its uncertainties are shown in Table A.8.

Table A.7: The combined *type ee* and *type ef* estimation and the results of the extrapolation procedure are shown The number of events listed is scaled to an integrated luminosity of $4.9\,\mathrm{fb}^{-1}$.

Mass range [GeV]	70 - 110	110 - 130	130 - 150	150 - 170
Prediction (no extrapolation)	1092.1 ± 7.3	425.2 ± 4.4	329.6 ± 3.9	249.4 ± 3.3
Prediction (with extrapolation)	1262 ± 506	424 ± 106	316 ± 61	233 ± 35

Mass range [GeV]	170 - 200	200 - 240	240 - 300	300 - 400
Prediction (no extrapolation)	248.5 ± 3.3	190.9 ± 2.9	130.9 ± 2.5	70.3 ± 1.8
Prediction (with extrapolation)	238 ± 26	185 ± 14	131.5 ± 5.8	71.4 ± 1.8

Mass range [GeV]	400 - 800	800 - 1200	1200 - 2000	2000 - 3000
Prediction (no extrapolation)	25.4 ± 1.1	0.40 ± 0.14	0.067 ± 0.047	0.0 ± 0.0
Prediction (with extrapolation)	25.36 ± 0.93	0.332 ± 0.095	0.0140 ± 0.0083	0.00014 ± 0.00016

Table A.8: This table shows the predictions and uncertainties of the *type ef* $t\bar{t}$ background as a function of mass. The number of events listed is scaled to an integrated luminosity of $4.9\,\mathrm{fb}^{-1}$.

Mass range [GeV]	70 - 110	110 - 130	130 - 150	150 - 170
Number of events	90.9 ± 8.9	22.2 ± 2.4	15.5 ± 1.7	11.5 ± 1.1
Statistical uncertainty [%]	2 %	5 %	5 %	3 %
Fit uncertainty [%]	0 %	0 %	0 %	0 %
Cross-section uncertainty [%]	10 %	10 %	9 %	10 %
Normalization uncertainty [%]	0 %	0 %	0 %	3 %
Combined uncertainty [%]	10 %	11 %	11 %	11 %

Mass range [GeV]	170 - 200	200 - 240	240 - 300	300 - 400
Number of events	11.7 ± 1.2	8.86 ± 0.88	6.06 ± 0.61	3.32 ± 0.34
Statistical uncertainty [%]	0 %	0 %	0 %	0 %
Fit uncertainty [%]	11 %	8 %	4 %	3 %
Cross-section uncertainty [%]	9 %	9 %	9 %	9 %
Normalization uncertainty [%]	3 %	3 %	3 %	3 %
Combined uncertainty [%]	15 %	12 %	10 %	10 %

Mass range [GeV]	400 - 800	800 - 1200	1200 - 2000	2000 - 3000
Number of events	1.17 ± 0.12	0.0151 ± 0.0047	0.00063 ± 0.00039	0.0000063 ± 0.0000073
Statistical uncertainty [%]	0 %	0 %	0 %	0 %
Fit uncertainty [%]	4 %	29 %	60 %	115 %
Cross-section uncertainty [%]	9 %	10 %	10 %	10 %
Normalization uncertainty [%]	3 %	3 %	3 %	3 %
Combined uncertainty [%]	11 %	31 %	61 %	116 %

A.7 Additional Fake Factor Distributions

In Section 6.4.3, not all distributions used to calculate the fake factors were shown for space reasons. The distributions used to calculate the fake factors, which depend on η only, are shown in Fig. A.10. The distributions used to calculate the fake factors as a function of η and E_T are shown in Fig. A.11 and Fig. A.12. The corresponding factor factors themselves are shown in Fig. A.13.

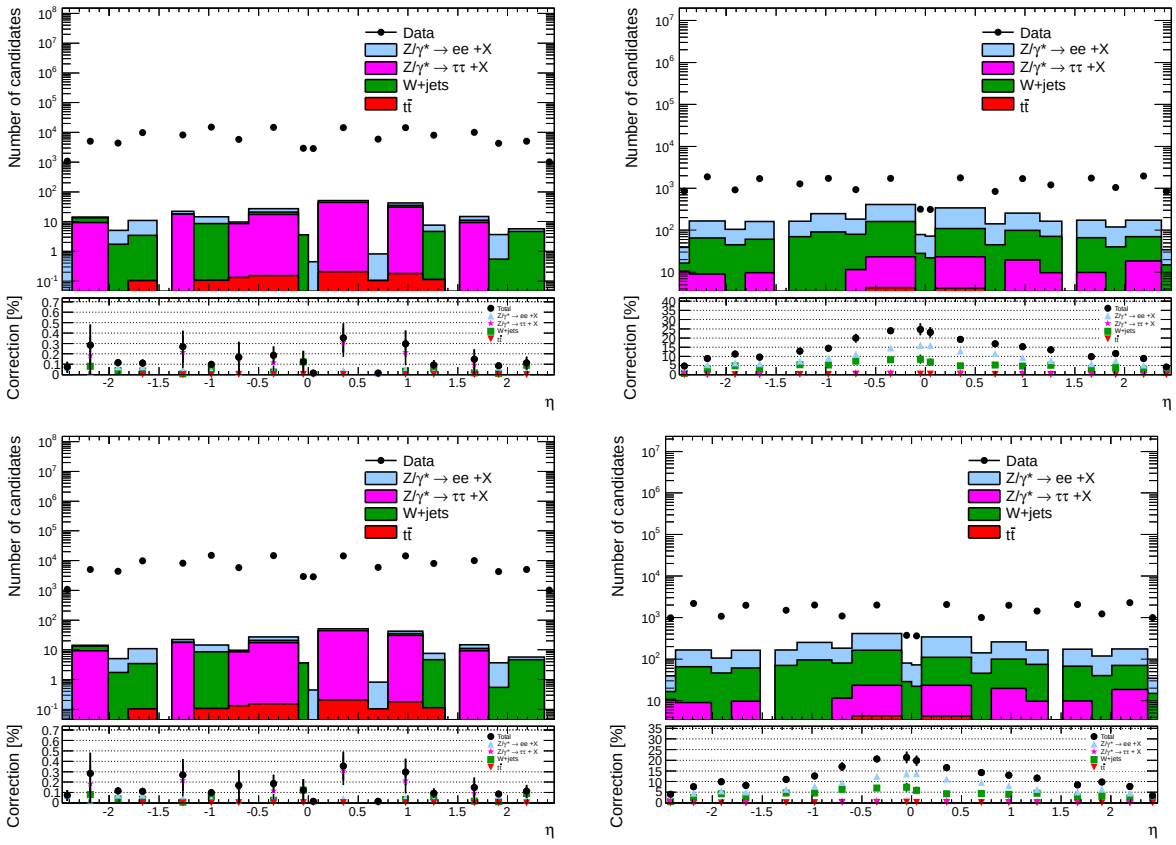

Figure A.10: The η distribution of the leading "loose fail tight" probes and the leading "tight" probes are shown in the top left and top right plot, respectively. The corresponding distributions for the subleading case are shown in the bottom left and right plots. Data is shown by black markers, and the corrections are shown as a colored stack of histograms. In the bottom panel, the relative size of the Monte Carlo corrections are shown. The distributions are scaled to an integrated luminosity of $4.9\,\mathrm{fb}^{-1}$.

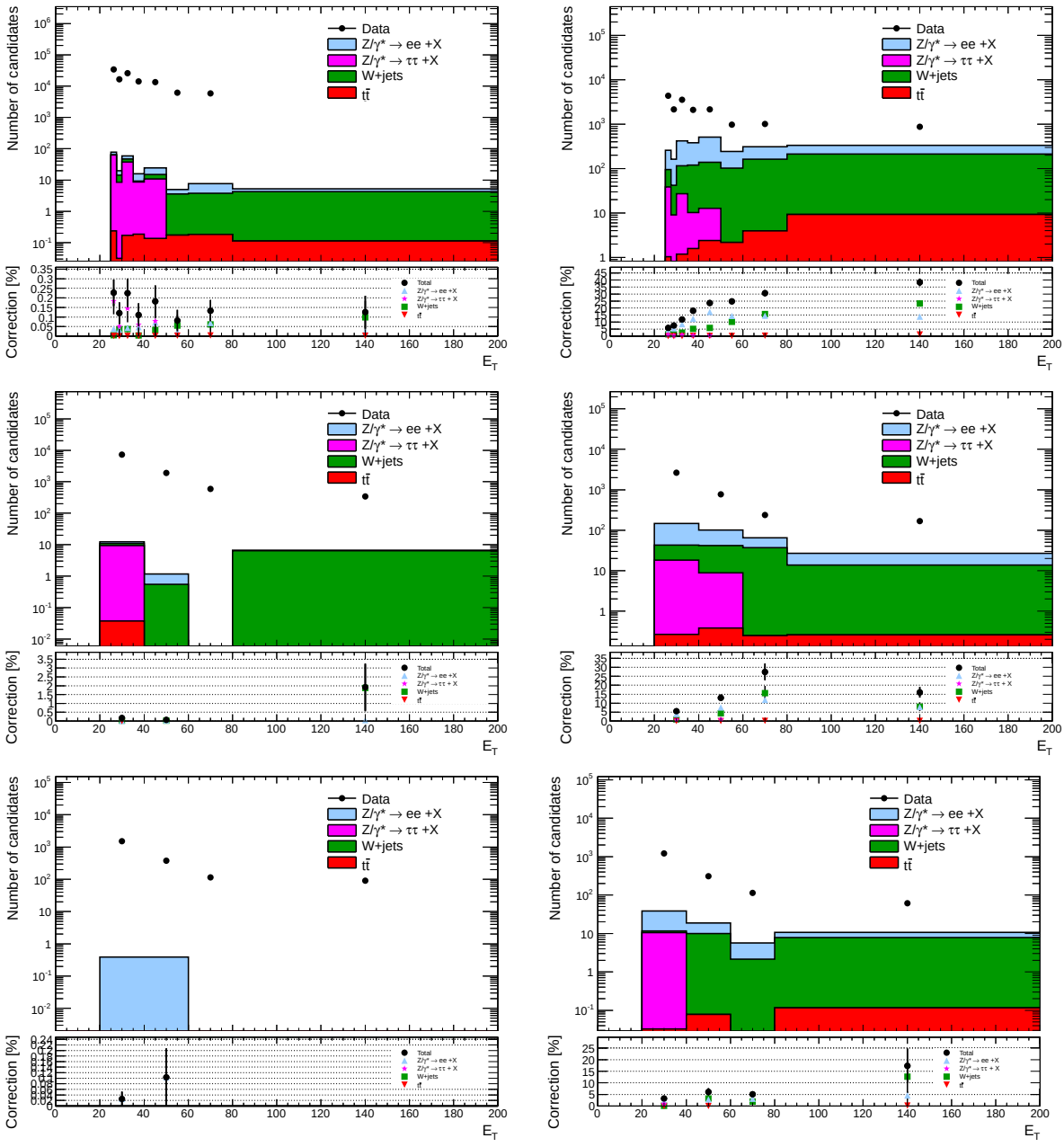

Figure A.11: The E_T distributions of the "loose fail tight" leading probes and of the "tight" probes are shown in the left and right columns, respectively. In both columns, the top plot covers $0 < |\eta| \leq 2.01$, the middle plot covers $2.01 < |\eta| \leq 2.37$ and the bottom plot covers $2.37 < |\eta| \leq 2.47$. Data is shown by black markers, and the corrections are shown as a colored stack of histograms. In the bottom panel, the relative size of the Monte Carlo corrections are shown. The distributions are scaled to an integrated luminosity of $4.9\,\mathrm{fb}^{-1}$.

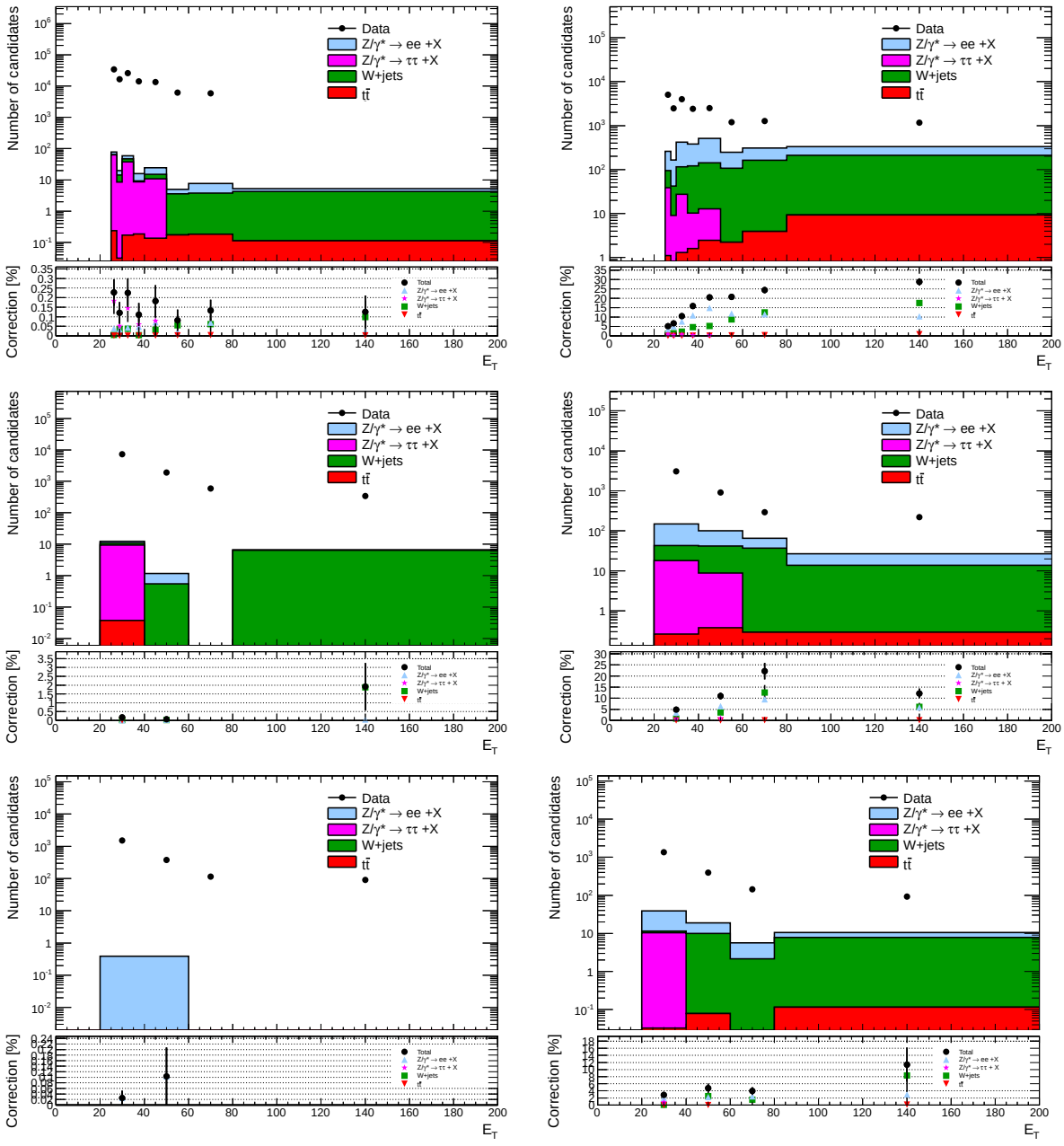

Figure A.12: The E_T distributions of the "loose fail tight" subleading probes and of the "tight" subleading probes are shown in the left and right columns, respectively. In both columns, the top plot covers $0 < |\eta| \leq 2.01$, the middle plot covers $2.01 < |\eta| \leq 2.37$ and the bottom plot covers $2.37 < |\eta| \leq 2.47$. Data is shown by black markers, and the corrections are shown as a colored stack of histograms. In the bottom panel, the relative size of the Monte Carlo corrections are shown. The distributions are scaled to an integrated luminosity of $4.9\,\mathrm{fb}^{-1}$.

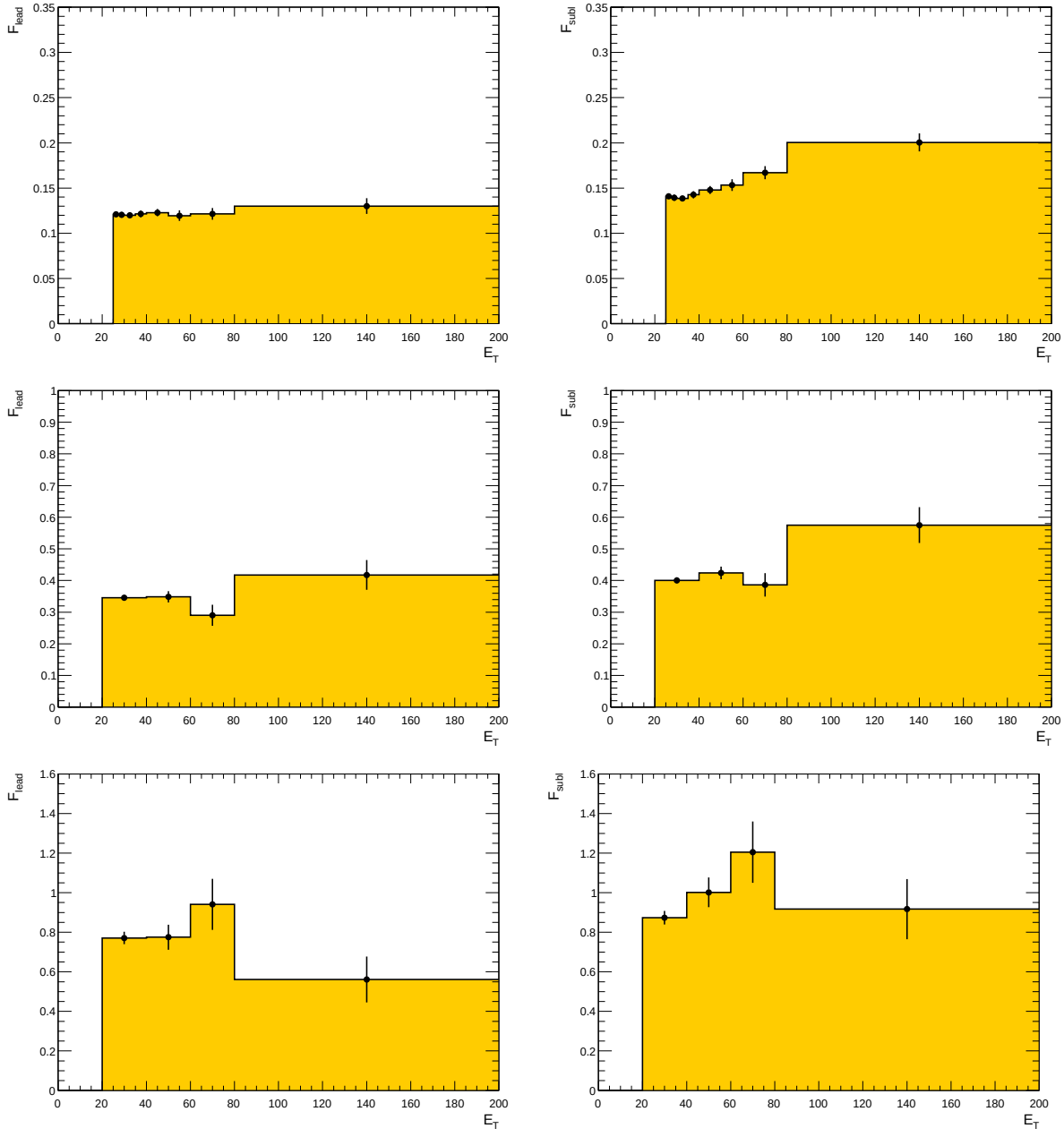

Figure A.13: The fake factor binned in E_T and η is shown for the leading electron in the left column and for the subleading electron in the right column. In both columns, the top plot covers $0 < |\eta| \leq 2.01$, the middle plot covers $2.01 < |\eta| \leq 2.37$ and the bottom plot covers $2.37 < |\eta| \leq 2.47$.

A.8 Additional Data Distributions

In Fig. A.14, the distribution of the isolation variable is shown. For the leading electron, the value of the isolation is required to be smaller than 7 GeV.

Fig. A.15 show the sames distributions as shown in Fig. 6.22, but with a logarithmic representation of the ordinate.

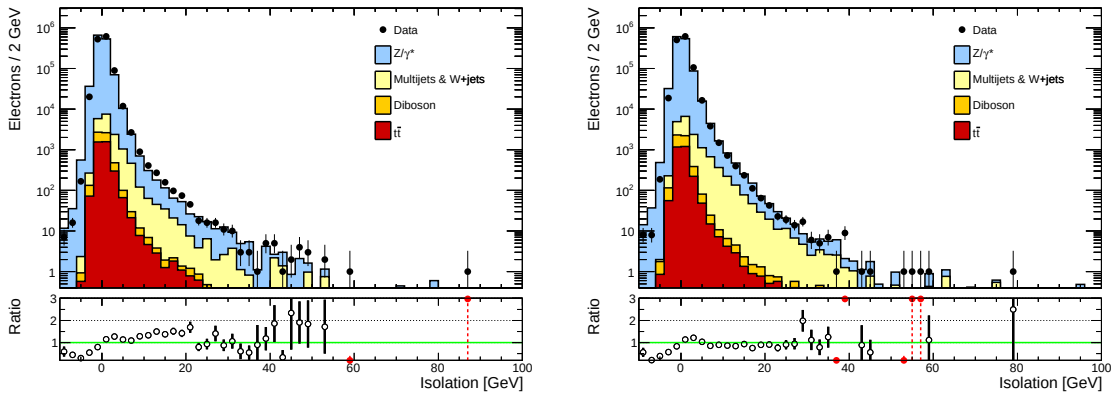

Figure A.14: The distribution of the isolation variable with all corrections applied is shown. Data is indicated by black markers, whereas the background expectation is shown as the colored stack of histograms. The background expectation is normalized to the number of events in data in the mass region 70 GeV to 110 GeV. In the bottom panel, the ratio of the number of events in data over the total number of events of the background expectation is shown. The green horizontal line indicates a ratio of one. Values of the ratio, which are outside of the range shown, are indicated in red.

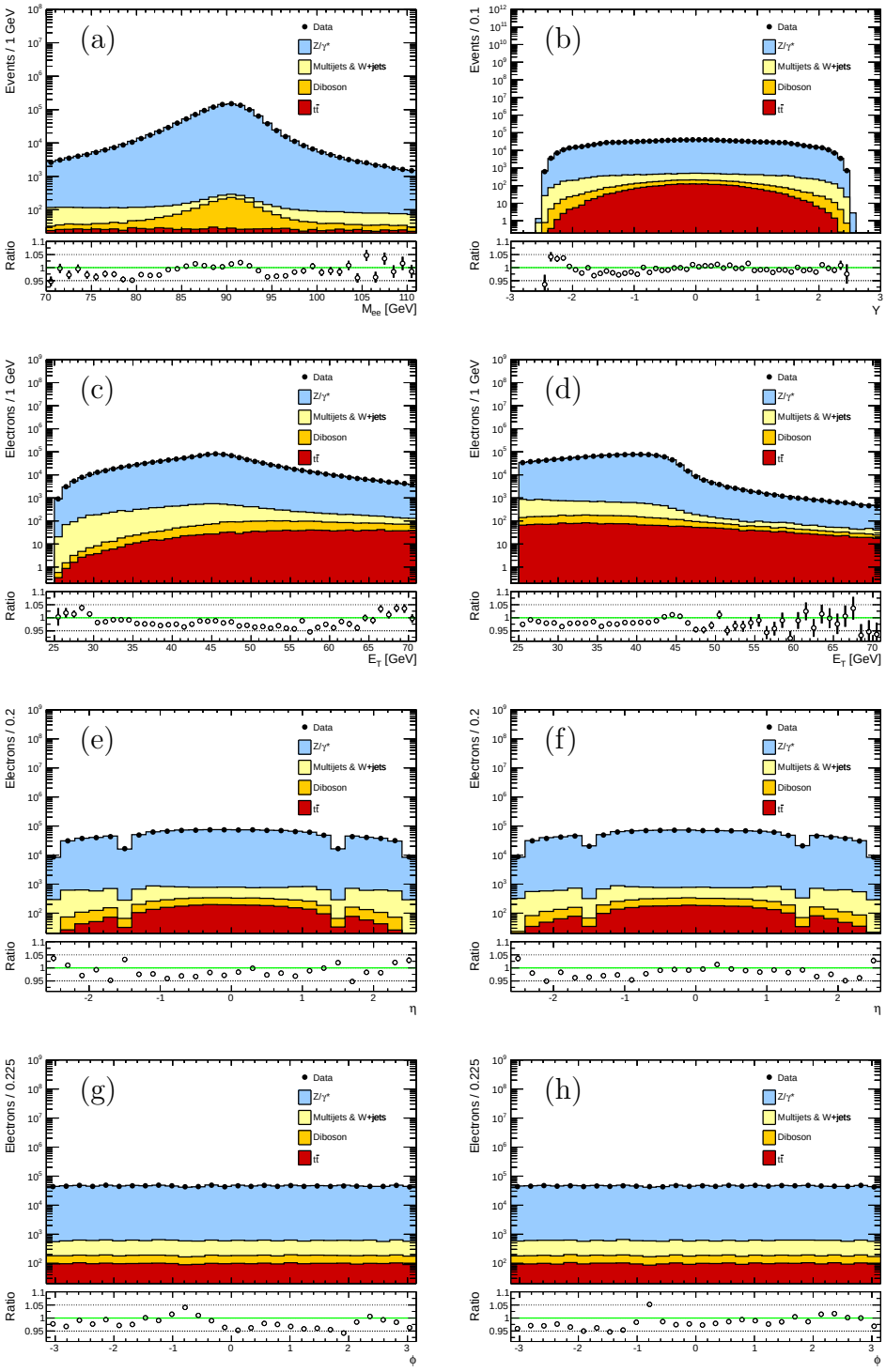

Figure A.15: This figure shows from top to bottom and from left to right the dielectron mass, dielectron rapidity, leading electron E_T, subleading electron E_T leading electron η, subleading electron η, leading electron ϕ and subleading electron ϕ distribution for masses greater than 70 GeV. In each plot, data is represented by black markers, while the background expectation is shown as the colored stack of histograms. The background expectation is normalized to the number of events in data in the mass region 70 GeV to 110 GeV. The bottom inset shows the ratio of the number of events in data over the total number of events of the background expectation and the green horizontal line indicates a ratio of unity.

Danksagung

Entfernt auf Grund datenschutzrechtlicher Bestimmungen.

Lebenslauf

Entfernt auf Grund datenschutzrechtlicher Bestimmungen.